THE UNIVERSITY *of* EDINBURGH

Globular clusters in the Local Group as probes of galaxy assembly

Jovan Veljanoski

Doctor of Philosophy
The University of Edinburgh
13 June 2014

Lay Summary

Understanding the formation and evolution of galaxies is one of the most active areas of research in astrophysics. Gradual build-up of matter by merging pre-galactic fragments is the current preferred model of constructing massive galaxies. A key prediction of this theory is that outskirts nearby galaxies should contain remnants of this assembly process in the form of fragmented stellar streams.

Found in all but the smallest of galaxies, globular star clusters (GC) are excellent probes for studying properties of galaxies. Having high luminosities, they are favourable targets in the outer regions of galaxies where the associated stellar surface brightness is low. GCs are thought to be amongst the oldest stellar systems in the Universe, and are likely born in the most significant phases of galaxy formation. Their metal abundances, ages, spatial positions and motions can be used to constrain the assembly history of their host galaxy.

In this thesis, I explore in great detail the motions and the light coming from GC systems in several nearby galaxies. The work is based on a major spectroscopic campaign, follow-up to the Pan-Andromeda Archaeological Survey (PAndAS), a large imaging program, designed to observe the Andromeda galaxy. Line-of-sight velocities are obtained for 78 GCs in the far outskirts of Andromeda, 63 of which were not studied before. In addition, GCs in the dwarf galaxies NGC 147, NGC 185 and NGC 6822 are also spectroscopically observed.

By conducting a detailed analysis, I find that GCs in the remote regions of Andromeda exhibit significant degree of rotation, which is in the same direction as for the GC located in the heart of the galaxy. My analysis of the GC motions located in the outskirts of Andromeda give further clues about how this galaxy got assembled through merging of smaller dwarf galaxies. I also estimate the total mass of Andromeda using the motions of its remote GC system.

I also characterize the GC systems of three dwarf galaxies in the Local Group: the dwarf elliptical satellites of M31, NGC 147 and NGC 185, and the isolated dwarf irregular NGC 6822. Using uniform optical and near-IR imagery, I constrain the age and metal abundance of their constituent GCs. The GCs around NGC 147 and NGC 185 are found to lack metals, as is typically the case for these type of objects, while their ages are more difficult to constrain. On the other hand, the GCs hosted by NGC 6822 are found to be very old, but with a variety of metal abundances. Finally, I analyse the motions of the GCs in these three systems, and use them to constrain the masses of the respective host galaxies.

Abstract

Understanding the formation and evolution of galaxies is one of the most active areas of research in astrophysics. Hierarchical merging of proto-galactic fragments to build more massive galaxies is the current preferred model. A key prediction of this theory is that haloes of nearby galaxies should contain remnants of this assembly process in the form of tidal debris.

Found in all but the smallest of dwarf galaxies, globular clusters (GC) are excellent probes of galaxy haloes. Having high luminosities, they are favourable targets in the outer regions of galaxies where the associated stellar surface brightness is low. GCs are thought to be amongst the oldest stellar systems in the Universe, and are likely born in the most significant phases of galaxy formation. Their metallicities, ages, spatial distributions and kinematics can be used to constrain the assembly history of their host galaxy.

In this thesis, I explore the photometric and kinematic properties of several GC systems in our cosmological backyard, the Local Group of galaxies. The work is based on a major spectroscopic campaign, follow-up to the photometric Pan-Andromeda Archaeological Survey (PAndAS), as well as additional optical and near-IR data sets. Radial velocities are obtained for 78 GCs in the halo of M31, 63 of which had no previous spectroscopic information. The GCs have projected radii between $\sim$ 20 and 140 kpc, thus sampling the true outer halo of this galaxy. In addition, GCs in the dwarf galaxies NGC 147, NGC 185 and NGC 6822 are also spectroscopically observed.

By conducting a detailed kinematic analysis, I find that GCs in the outer halo of M31 exhibit coherent rotation around the minor optical axis, in the same direction as their more centrally located counterparts, but with a smaller amplitude of 86 ± 17 km s^{-1}. There is also evidence that the velocity dispersion of the outer halo GC system decreases as a function of projected radius from the M31 centre, and this relation can be well described by a power law of index ≈ -0.5. I detect and discuss various velocity correlations amongst GCs that lie on stellar streams in the M31 halo. Simple Monte Carlo tests

show that such configurations are unlikely to form by chance, implying that significant fraction of the GCs in the M31 halo have been accreted alongside their parent dwarf galaxies. I also estimate the dynamical mass of M31 within 200 kpc to be $(1.2 - 1.6) \pm 0.2 \times 10^{12}$ $M_{\odot}$.

I also characterize the GC systems of three dwarf galaxies in the Local Group: the dwarf elliptical satellites of M31, NGC 147 and NGC 185, and the isolated dwarf irregular NGC 6822. Using uniform optical and near-IR photometry, I constrain the ages and metallicities of their constituent GCs. The metallicities of the GCs around NGC 147 and NGC 185 are found to be metal-poor ([Fe/H]$\lesssim -1.25$ dex), while their ages are more difficult to constrain. The GCs hosted by NGC 6822 are found to be old (>9 Gyr) and to have a spread of metallicities ($-1.6 \lesssim$ [Fe/H] $\lesssim -0.4$). I find close similarity between the mean optical $(V - I)_0$ colours of the GCs hosted by these three dwarf galaxies to those located in the M31 outer halo, consistent with the idea that dwarf galaxies akin to them might have contributed toward the assembly of the M31 outer halo GC population. Analysing their kinematics, I find no evidence for systemic rotation in either of these three GC systems. Finally, I use the available GC kinematic data to calculate the dynamical masses of NGC 147, NGC 185 and NGC 6822.

Declaration

I declare that this thesis was composed by myself, that the work contained herein is my own except where explicitly stated otherwise in the text, and that this work has not been submitted for any other degree or professional qualification except as specified.

Parts of this work have been published in

Veljanoski, J. et al., 2013, ApJL, 768, 33L

Veljanoski, J. et al., 2013, MNRAS, 435, 3654

Veljanoski, J. et al., 2014, MNRAS, in press.

(*Jovan Veljanoski, 13 June 2014*)

Acknowledgements

First of all, I would like to thank my supervisor, Annette Ferguson both for the fantastic opportunity you have given me, and for your guidance throughout this journey. You have shown me what it means to be a top-notch and yet a humble researcher, have given me the best example of academic excellence and professionalism, and I can not describe how much I have learned from you.

I would like to thank my friends and colleagues Edouard Bernard and Denija Crnojević for the countless talks, support and encouragement, inside and outside the office. You were there every time for me, for work and for fun.

A big thanks to Dougal Mackey; although I am yet to meet you in person, working together with you was a great experience and I am thankful for all of your e-mails with detailed explanations and comments. Many thanks to Mike Irwin, Avon Huxor, Pat Côté and the rest of the PAndAS collaboration for making this project possible. I would like to thank Jorge Peñarrubia for teaching me the art of statistics, and Alexander Rogers for teaching me how to python with style. In addition, I would like to thank Jim Dunlop, Ross McLure, Ken Rice, Philip Best, John Peacock and all the rest former and present IfA staff members for their help and support throughout my studies in Edinburgh. I am also grateful to the postdocs and fellow Ph.D. students with whom I had many interesting discussions. Thanks to José Sabater Montes, Sylvain de la Torre, Fernando Buitrago, Massimo Viola, Isaac Roseboom, Eric Tittly, Ami Choi, Emma Curtis-Lake, Esther Marmol-Queralto, Michal Michalowski, Mike Barker, Victoria Bruce, Duncan Forgan, Tom Target, Pratika Dayal, Maciej Koprowski, Joao Ferreira, Rebecca Bowler, Vinod Arumugam, Marika Asgari, Chris Duncan, Alexandar Mead, Jack Mayo, Henry Pearce and all the rest of the team. Thanks to Ignacio Trujillo and Michele Cirasuolo for their advice and encouragement. Very special thanks to the IfA computing support staff lead by Horst Meyerdierks and John Barrow, as well as world best administrators Paula Wilkie, Nathalie Dupin and Jane Patterson.

So many people have helped me stay focused and motivated during the last four years, for which I am humbled and very grateful. But I also had many fiends by my side who helped me relax, forget my worries for a few hours and helped me recharge my batteries to be ready to give 100% the next day. Thanks to my basketball team mates, especially Craig Morris, Mike, Ben and Dominic Clarke, Scott Howell and all players from our “Prestige” club. I want to thank Fernando and Ignacio for introducing me to the wonderful world

of salsa dancing, through which I met many terrific people. Thanks to the entire Edinburgh salsa community and especially to Karolina Brzozowska, Katarzyna Gasiorowska, Marta Bajerska and Maria Dokova for all the lovely moments and many memorable dances, and to our classy teacher Sagi Iluz for making everything possible. Thanks to my dear friends Robyn Donnelly and Michael Kepa, your work ethic have inspired me greatly, and have motivated me to push hard for the top. Special thanks to my beloved friends around the world: Kristina Krstić-Joksimović, Ana Škvorc, Marija Librenjak, Lovro Palaversa, Nadia Blagoródnova; your love and continuous support meant a lot to me. Many thanks to my old friends from back home: Miroslav and Darko Todorovski, Tome Tomovski, Marko Marcikić, Jordan Palikrušev, Vlado and Sanja Kragujevski, Bojan Aleksoski (in memoriam), Filip Tanturovski, Mite Mitreski, Marija Grunćeska and Vladislav Bidikov. When we are all together, it is the best time anyone can ask for. Thank you for all the fun moments, every summer and winter that you have helped me unwind, for making me laugh breathlessly, for all the little things. I want to share this achievement with all of you.

Finally, and most importantly, I want to thank my parents Krste and Lidija Veljanoski, and my sister Hristina Veljanoska. You are the real reason behind all my accomplishments. Your lifelong hard work, dedication and sacrifice is what has granted me the possibility of doing this work, the result of which is this book. You have always been there for me, supporting me with everything you have got. And seeing you smile is the best reward I will ever get. With all my love, I dedicate this work to thee.

This research has made use of the NASA/IPAC Extragalactic Database (NED), which is operated by the Jet Propulsion Laboratory, California Institute of Technology, under contract with the National Aeronautics and Space Administration; NASA's Astrophysics Data System Bibliographic Services; open source scientific tools for Python (NumPy & SciPy, Oliphant, 2007; Matplotlib, Hunter, 2007 and IPython, Pérez & Granger, 2007).

The *Kitt Peak National Observatory* is operated by the Association of Universities for Research in Astronomy (AURA) under cooperative agreement with the National Science Foundation. The *William Herschel Telescope* is operated on the island of La Palma by the Isaac Newton Group in the Spanish Observatorio del Roquede los Muchachos of the Instituto de Astrofísíca de Canarias.

Partly based on observations obtained at the Gemini Observatory, which is operated by the Association of Universities for Research in Astronomy, Inc., under a cooperative agreement with the NSF on behalf of the Gemini partnership: the National Science Foundation (United States), the National Research Council (Canada), CONICYT (Chile), the Australian Research Council (Australia), Ministério da Ciência, Tecnologia e Inovação (Brazil) and Ministerio de Ciencia, Tecnología e Innovación Productiva (Argentina).

This work made use of the Pan-STARRS1 Surveys (PS1) which have been made possible through contributions of the Institute of Astronomy, the University of Hawaii, the Pan-STARRS Project Office, the Max-Planck Society and its participating institutes, the Max Planck Institute for Astronomy, Heidelberg and the Max Planck Institute for Extraterrestrial Physics, Garching, The Johns Hopkins University, Durham University, the University of Edinburgh, Queen's University Belfast, the Harvard-Smithsonian Center for Astrophysics, the Las Cumbres Observatory Global Telescope Network Incorporated, the National Central University of Taiwan, the Space Telescope Science Institute, the National Aeronautics and Space Administration under Grant No. NNX08AR22G issued through the Planetary Science Division of the NASA Science Mission Directorate, the National Science Foundation under Grant No. AST-1238877, and the University of Maryland.

Contents

List of Figures

List of Tables

Chapter 1

Introduction

Galaxy assembly is one of the fundamental processes in astrophysics which is not fully understood. Yet, the knowledge of how galaxies form and evolve plays a key role in our understanding of the formation and evolution of the large scale structure, and through that, of the Universe itself. Our current best description of the Universe is through the ΛCDM cosmological model. Consistent with the majority of observations, the growth of structure according to this model is primarily a hierarchical process. The pristine overdensities of matter, both visible and dark, collapse under their own gravity forming the first proto-galaxies. These proto-galaxies are not entirely isolated, and mutual gravitational attraction causes them to merge together forming ever larger systems. This process continues to give rise to a fully formed, massive galaxy like those observed today. The process does not end here. Massive galaxies are in gravitational contact as well, forming galaxy groups and galaxy clusters. These also attract the neighbouring clusters forming superclusters, which form the large-scale structure of the Universe.

The ΛCDM model provides an excellent description of the growth of structure throughout the Universe, starting all the way from its most infant stages. However, we still have only a limited understanding of galaxy formation on small scales, and the processes that govern such events. For instance, it is uncertain when a star-burst is expected to ignite after a dark matter halo has started to collapse. There is also a considerable lack of understanding of the rate at which galaxies grow and transform from one morphological type into another.

Our study of galaxy assembly can be greatly aided if we can track the formation and evolution of these systems using probes that are sensitive to

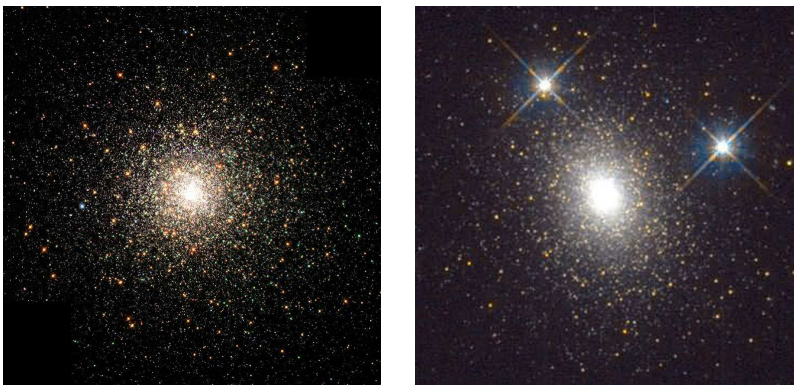

Figure 1.1 *Two globular clusters observed through the* Hubble Space Telescope. *The left panel displays the Galactic GC M80, while on the right shown is G1, a globular located in the halo of M31.*

their earliest, most significant star-burst phases, as well as major and minor mergers. Probes through which we can infer various galaxy properties that can not be measured directly, and yet are important for our understanding of structure formation. Luckily, such probes exist!

1.1 Globular Clusters

Globular clusters (GCs) are spherical collections of stars commonly found orbiting around galaxies. Their name is derived from the Latin word *"globulus"*, meaning a small sphere. Consisting of $10^4 - 10^6$ stars, they are tightly bound by gravity which gives them their spherical form, with the stellar density increasing towards the centre of each cluster. This makes them quite compact, with typical half-light radii of a few parsecs. The mass is entirely dominated by stellar material, with minimal evidence for dark matter. Being such dense concentrations of stars, GCs are bright objects with luminosities between $M_V \sim -5$ to -10, which makes them readily observable in external galaxies, and especially in galaxy haloes, where they are significantly brighter than the underlying stellar field component. Example images of GCs are shown in Figure 1.1. Globular clusters tend to have lower than solar metal abundance, although typically their [Fe/H][1] values range from ~ -2.5 to 0.5 dex.

With ages older than 10 Gyr, GCs are likely amongst the oldest stellar systems to have formed in the Universe. GCs are believed to form in the early, most violent phases of galaxy formation (e.g. West et al., 2004), thus tracing the bulk of the star formation history of the early universe. There is evidence that

[1] In astrophysics there are a few different ways in which metallicity is defined. In this case, [Fe/H] is the logarithm of the ratio between the amount of iron and the amount of hydrogen in an object, relative to that of our Sun, i.e. $[\mathrm{Fe/H}] = \log_{10}(\mathrm{Fe/H})_\star - \log_{10}(\mathrm{Fe/H})_\odot$

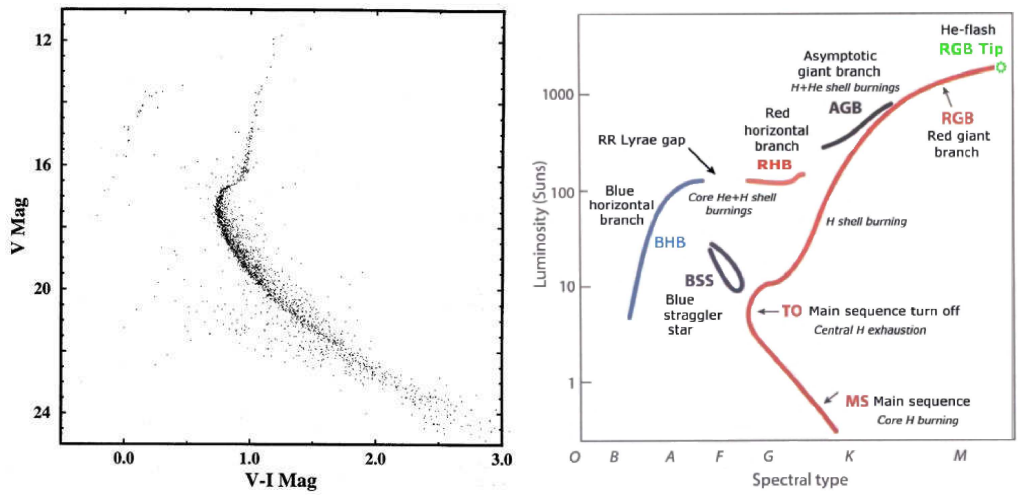

Figure 1.2 *Left panel: classical CMD of the Milky Way GC NGC 6752 (Rubenstein & Bailyn, 1997), illustrating the idea of GC as simple stellar populations. Right panel: a schematic of a typical GC Hertzsprung-Russell diagram (Fusi-Pecci & Clementini, 2000), on which the main phases of stellar evolution are marked.*

massive galaxies can increase their GC census by accreting smaller cluster bearing systems (e.g. Bellazzini et al., 2003; Mackey et al., 2010b). Furthermore, GCs may form during star formation events induced by major galaxy mergers. This is supported by several observations of young massive clusters around interacting galaxies (e.g. Whitmore & Schweizer, 1995; Miller et al., 1997; Trancho et al., 2007). However, it remains unclear whether these young massive clusters, after evolving for several Gyr, will have the same properties as GCs observed today.

Early studies of colour-magnitude diagrams (CMD) of GCs, indicated that they are composed of a single stellar population, meaning that their stars are coeval and have the same metal abundance (e.g Hesser et al., 1987; Stetson, 1993). The left panel in Figure 1.2 shows a classical CMD of the Milky Way GC, NGC 6752 (Rubenstein & Bailyn, 1997). The small spread of the stars comprising the main sequence and the red giant branch (RGB) gives the idea that clusters such as this one are simple stellar populations. For reference, the right panel in this figure shows a schematic view of a typical GC Hertzsprung-Russell diagram (Fusi-Pecci & Clementini, 2000), on which the main phases of stellar evolution are labelled. This is similar to a CMD where the magnitude is a proxy for luminosity while the colour is a proxy for the temperature.

However, more recent studies of CMDs that use high quality data have found a spread of ages and metallicities amongst the stars of some GCs, pointing towards the existence of multiple populations (e.g. Ferraro et al., 2004; Piotto et al., 2007, 2012; Milone et al., 2008). The multiple populations

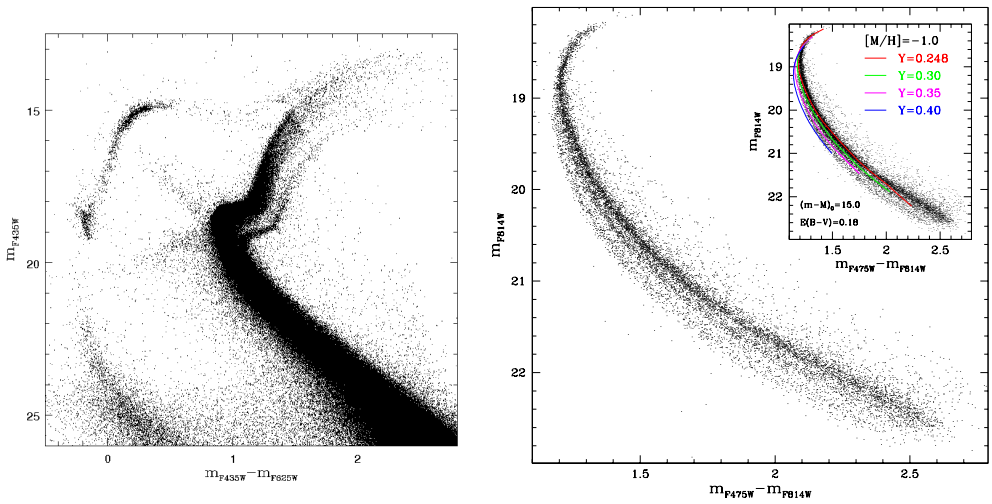

Figure 1.3 *Left panel: CMD of ωCen (Villanova et al., 2007). Multiple sub-giant branches are observed, corresponding to populations of stars with different ages. Right panel: CMD of the main sequence of NGC 2808 from Piotto et al. (2007). The multiple main sequences are well-fit by isochrones of a single age (12.5 Gyr), but with different Helium abundances.*

are commonly seen to have different main sequence turn-off points, hence different ages, or to be coeval but have different Helium abundances. Such observations are displayed in Figure 1.3, which shows recent, high quality CMDs of Milky Way GCs. The left panel is a CMD of ω-Cen (Villanova et al., 2007), where up to four different main sequence turn-off points are visible, corresponding to stellar populations of different ages. The right panel shows a CMD of the Milky Way GC NGC 2808 from Piotto et al. (2007), on which multiple main sequences are visible. The different main sequences are well fit by a set of isochrones having the same age but different Helium content. Given the difficultly of detecting these subtle features in Milky Way GCs, they are not an obstacle when discussing extragalactic GC systems in relation to their host galaxy properties or assembly histories, as done in this thesis.

GC research can provide valuable, and sometimes unique constraints on galaxy properties and formation mechanisms. Studies of GC systems in distant galaxies have uncovered a number of correlations with host galaxy properties (e.g. Brodie & Strader, 2006; Pota et al., 2013). For example, a strong correlation has been found between the mean colour of red GCs (see Section 1.3.2) and host galaxy velocity dispersion, which is a proxy for galaxy mass (e.g. Forbes & Forte, 2001). The total number of GCs around a galaxy has also been used to constrain its stellar mass and luminosity (e.g. Rhode, 2012; Harris et al., 2013), as well as put limits on the total mass of a galaxy (e.g. Hudson et al., 2014). Furthermore, the GC luminosity function can be used as a distance indicator (e.g. Richtler, 2003). Together with dwarf galaxies, GCs

are arguably the best kinematic tracers of dark matter haloes of galaxies at large galactocentric radii. Hence, they are often used to estimate the total mass of galaxies (e.g. Woodley et al., 2010; Schuberth et al., 2012). The kinematics of GCs associated the bulge of a galaxy can be used to constrain the properties, such as the mass, of the super-massive black hole in the centre of that galaxy (e.g. Burkert & Tremaine, 2010; Pota et al., 2013; Harris et al., 2014).

Metallicity studies of GC systems provide insight into the early phases of formation and chemical enrichment of the host galaxy. For instance, determining the $[\alpha/\mathrm{Fe}]$[2] ratio sets a limit on the duration of a star formation event. It is generally thought that the α-elements and approximately one third of Fe are produced in Type II supernovae. These explosions occur within tens of Myr of the onset of the star burst. The remaining Fe comes from Type Ia supernovae which occur over Gyr time-scales. Hence, super-solar $[\alpha/\mathrm{Fe}]$ ratios indicate that GCs formed within < 1 Gyr of the onset of star formation in the galaxy, while sub-solar $[\alpha/\mathrm{Fe}]$ values indicate they formed later from polluted gas (e.g. Kuntschner et al., 2002; Beasley et al., 2004; Puzia et al., 2005; Woodley et al., 2010).

1.2 The globular cluster system of the Milky Way

The GC system that has been studied the longest, and in the greatest detail, is that of our Galaxy, the Milky Way. This system comprises 157 GCs, the physical and orbital properties of which are summarized in a regularly updated catalogue (Harris, 1996, 2010 edition)[3]. A detailed review of the Galactic GC system has been presented in Harris (2001). Here I will briefly summarize its properties, which set the context for the extragalactic work that is the focus of this thesis.

[2] $[\alpha/\mathrm{Fe}]$ is the logarithm of the ratio between the amount of alpha elements (O, Mg, Ti, Si) and the amount of iron in a star, relative to that of our Sun.

[3] The on-line description of the catalogue can be found at http://physwww.mcmaster.ca/∼harris/mwgc.dat, while the corresponding bibliography can be found at http://physwww.mcmaster.ca/∼harris/mwgc.ref.

1.2.1 The bimodal nature of the Milky Way GC system

Metallicity and colour bimodality

The metallicity of the Milky Way GCs can be established by either fitting isochrones to high quality CMDs, or via spectroscopy of individual stars. It has been known for a long time that the Galactic GCs have a range of metallicities (e.g. Morgan, 1959; Kinman, 1959), and these early studies attempted to group clusters together based on the similarity of their spectral features. Modern observations have made it possible to reliably determine the metal content for most of the Milky Way GCs (e.g. Koch & McWilliam, 2008, 2010; Koch & Côté, 2010; Da Costa et al., 2009; Carretta et al., 2009).

The left panel in Figure 1.4 displays a histogram of [Fe/H] values for the Galactic GC system, constructed with data from the catalogue compiled by Harris (1996, 2010 edition). The [Fe/H] values are weighted means from all individually available metallicity measurements coming from both spectroscopic and photometric studies, as explained by Harris (1996). This figure shows that the distribution of [Fe/H] is bimodal with clear prominent peaks at ~ -1.5 and at ~ -0.5. Hence, the clusters that have $[\mathrm{Fe/H}] < -0.8$ are typically referred to as metal-poor, while those that have $[\mathrm{Fe/H}] > -0.8$ are referred to as metal-rich.

In addition, the right panel in Figure 1.4 shows the distribution of the optical $(V-I)_0$ colours. This distribution shows much weaker evidence for bimodality, with a dominant peak occurring at ~ 1.0, and a possible secondary peak at 1.5. It is often assumed that the cause of the colour bimodality is the metallicity bimodality, at least to first order.

Spatial distributions

In their classic work, Morgan (1956, 1959) and Kinman (1959) were amongst the first ones to point out the link between the metal content of Milky Way GCs and their distance from the Galactic centre. Indeed, today we know that the metal-rich and metal-poor GCs occupy different regions of the Galaxy and have different spatial distributions (e.g. Ashman & Zepf, 1998).

Figure 1.5 shows the spatial distribution of the metal-rich and metal-poor Galactic GCs in the YZ plane[4], again constructed with data compiled by

[4]Galactocentric rectangular coordinate system (X,Y,Z), centred on the Sun: X points from

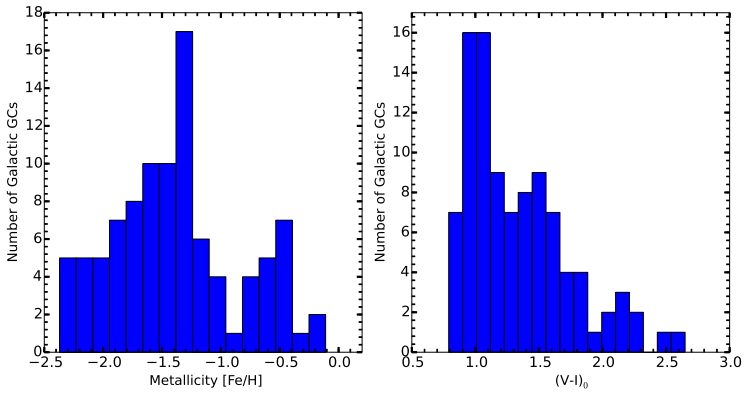

Figure 1.4 *The left panel shows a histogram of [Fe/H] values, which are on the Zinn & West (1984) scale, for the Galactic GCs. The right panel displays a histogram of $(V-I)_0$ colours. The clear bimodal distributions provide the first hint of the existence of multiple formation channels or epochs. The data was taken from Harris (1996, 2010 edition).*

Harris (1996, 2010 edition). It is evident from this figure that the metal-rich GCs, plotted on the left panels with red symbols, are much more centrally concentrated than their metal-poor counterparts, plotted on the right panels with blue symbols. In fact, the metal-rich GCs form a structure that might resemble the bulge, with all but two clusters having $|Z| < 4$ kpc. In contrast, the metal-poor GCs have an extended spatial distribution which is approximately spherical in shape, exhibit a large range of $|Z|$ values and appear to be associated with the Galaxy halo.

However, it is worth mentioning that there is a significant problem when observing Galactic GCs. More than half of the Milky Way population is located near or on the opposite side of the Galactic centre with respect to our location. Thus, observations of these objects are heavily affected by foreground dust clouds in the Galactic disc. One needs to take special care in order to correctly account for the interstellar reddening, especially prior to determining their distance, which is a very important parameter when studying the Milky Way GC system.

Kinematics

A number of past studies have tried to use the kinematics of the Milky Way GCs in order to learn more about its origin and formation (e.g. Zinn, 1985; Côté, 1999). It has been found that the metal-rich GCs, that are generally

the Sun towards the Galactic centre; Y points towards the direction of the Galactic rotation; Z points northward, perpendicular to the Galactic plane. In this notation, the Sun is centred at (0,0,0) kpc, while the Galactic centre is approximately at (8,0,0) kpc.

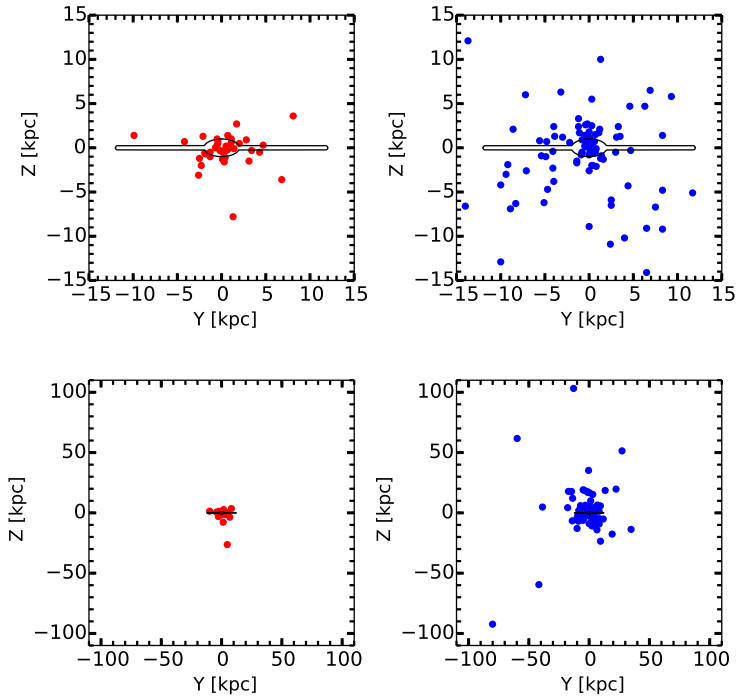

Figure 1.5 *Spatial distribution of the metal-rich (left panel, red coloured symbols) and metal-poor (right panels, blue coloured symbols) GCs. It shows that the metal-rich GCs are much more centrally concentrated and lie near the Galactic disc, while their metal poor counterparts have a much more extended, roughly spherical spatial distribution The data was taken from Harris (1996, 2010 edition).*

confined to the inner regions of the Galaxy, exhibit a significant pro-grade rotation. In contrast, the metal-poor population as a whole is dynamically hot, and exhibits little if any rotation. Naturally, the velocity dispersion of the metal-poor GCs is higher than that of their metal-rich siblings. Various past studies have attempted to dissect the Galactic GC system in smaller groups when studying its kinematics and this has resulted in some success. The main results from these past efforts are presented in Table 1.1, taken from Harris (2001).

A particularly interesting finding was the split of the metal-rich globulars into two distinct kinematic groups. The first group comprises clusters that have Galactocentric distances (R_{gc}) between 0 - 4 kpc, and is typically referred to as the 'inner group'. The 'outer group' consists of clusters with R_{gc} between 4 - 8 kpc.

The inner metal-rich group has been found to rotate with velocity of $\sim$ 80 km s^{-1}. Minniti (1995) and Zinn (1996) have shown that the motions of the GCs that are part of this group match well with the motions exhibited by the RGB bulge stars. Thus this group is interpreted as a flattened rotating bulge population. Studying the orbits of the metal-rich GCs, Burkert & Smith (1997)

Table 1.1 *Kinematics of the Milky Way GC system (Harris, 2001). Even though the census of GCs in the Milky Way increased with time, its kinematic properties remained the same.*

Sample	Subgroup	Number of GCs	V[km s^{-1}]	σ[km s^{-1}]
Metal-rich GCs	All [Fe/H] > -1	33	111 ± 26	89 ± 11
Metal-rich GCs	R_{gc} = 0-4 kpc	20	86 ± 40	99 ± 15
Metal-rich GCs	R_{gc} = 4-9 kpc	13	147 ± 27	66 ± 12
Metal-poor GCs	All [Fe/H] < -1	91	30 ± 25	121 ± 9
Metal-poor GCs	R_{gc} = 0-4 kpc	28	56 ± 37	122 ± 16
Metal-poor GCs	R_{gc} = 4-8 kpc	19	12 ± 31	79 ± 12
Metal-poor GCs	R_{gc} = 8-12 kpc	12	26 ± 63	122 ± 16
Metal-poor GCs	R_{gc} = 12-20 kpc	14	-97 ± 110	79 ± 12
Metal-poor GCs	$-2.30 <$ [Fe/H] < -1.85	17	139 ± 57	114 ± 19
Metal-poor GCs	$-1.85 <$ [Fe/H] < -1.65	19	41 ± 55	142 ± 22
Metal-poor GCs	$-1.65 <$ [Fe/H] < -1.50	21	-35 ± 59	134 ± 20
Metal-poor GCs	$-1.50 <$ [Fe/H] < -1.32	17	-12 ± 56	106 ± 17
Metal-poor GCs	$-1.32 <$ [Fe/H] < -1.00	17	31 ± 32	80 ± 13

found that the innermost members form an elongated bar-like structure.

The clusters comprising the outer metal-rich group have been found to rotate much faster with an amplitude of $\sim$ 150 km s^{-1}, and also exhibit lower velocity dispersion than those in the inner group. Zinn (1985), Armandroff (1989) and Burkert & Smith (1997) have studied the kinematic and orbital properties of this group, and found that it is similar to a thick disc population. If this is indeed true, it would mean that these GCs formed together with the stars of the thick disc. This in turn would enable us to age-date the formation epoch of the thick disc via chronology of GCs belonging to this group. However, the rotation speed of this group is less than that of the thick disc, which is found to be $\sim$ 180 km s^{-1} (Armandroff, 1989). It is therefore attractive to propose that the GC members of the outer metal-rich group are remnants of the pre-disc star formation epoch during which the proto-galactic gas fragments have yet to settle into a disc configuration and still had substantial random motions.

The metal-poor GCs dominate the Milky Way system in terms of numbers, as there are nearly 3 times more metal-poor clusters as there are metal-rich ones. When this sample is split into arbitrary radial bins, it is found that none of the bins exhibit a net rotation. This is shown in Table 1.1 adopted from Harris (2001). However, when the sample is split in arbitrary metallicity subgroups, a strong pro-grade rotation of $\sim$ 150 km s^{-1} is detected for the clusters falling in the most metal-poor subgroup. It is found that this effect is driven by metal-poor clusters located in the inner halo of the Galaxy (Harris, 2001).

1.2.2 The age-metallicity relation of the Galactic GC system

In their seminal paper, Searle & Zinn (1978) were the first to recognise the significance of considering the metallicities and ages of GCs in relation to galaxy formation models. They derived the metal content of 19 Galactic GCs from low resolution spectra of 119 red giant branch stars in total. These authors found that the clusters outside the solar circle exhibit no metallicity abundance gradient as a function of Galactocentric radius (Eggen et al., 1962). This led Searle & Zinn (1978) to exclude the slow pressure supported collapse as a possible mode of formation for these cluster since in that case a metallicity gradient with Galactocentric distance will necessarily form in both metal-rich and metal-poor populations. On the other hand, if GCs form while the gas is at free fall, it is expected their kinematic properties not to be dependent on their abundances, and so no abundance gradient is formed. Hence Searle & Zinn (1978) require that the Milky Way halo GCs formed in a way that allows their kinematics to be uncorrelated with their metallicity abundances when they come into a dynamical equilibrium with the Galactic system. One possible way to achieve this is to form the clusters in a number of small proto-galaxies which then amalgamate to form the present Galactic halo.

These ideas were expanded considerably by exploring the age-metallicity relations exhibited by the Milky Way GCs. Amongst the first works that searched for such a relation in the Galactic GC system is that conducted by Sarajedini & King (1989). They derived ages for 32 GCs using the difference in magnitude between the horizontal branch and main sequence turn off stars in their CMDs. These authors found that the age-metallicity trend exhibited by the clusters having $R_{gc} < 15$ kpc is much shallower compared to that of clusters with $R_{gc} > 15$ kpc. This led Sarajedini & King (1989) to deduce that the inner halo GCs formed in a region of high gas density thus accelerating the formation of GCs and their chemical enrichment, based on the work of Larson (1972) and Tinsley & Larson (1978). In contrast, the GCs residing in the outer halo of our Galaxy formed in lower density sub-galactic fragments, in a slower and more chaotic manner similar to the accretion scenario proposed by Searle & Zinn (1978) which features in ΛCMD galaxy formation models.

One of the most recent studies on the age-metallicity relation in the Milky Way GC system relied on uniform photometric data obtained with the Advanced Camera for Surveys (ACS) mounted on the Hubble Space Telescope (HST) (Marín-Franch et al., 2009). This high quality data set provides deep photometry which reaches $\sim$ 7 magnitudes below the main sequence turn

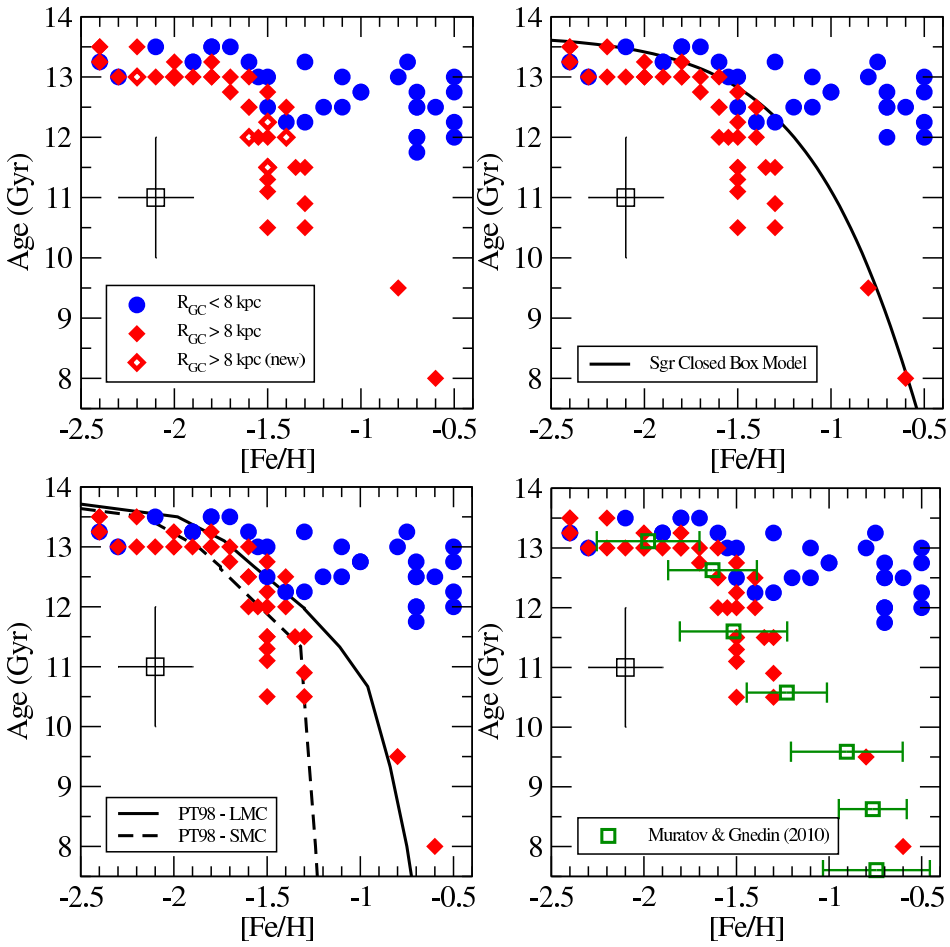

Figure 1.6 *Each panel shows the two age-metallicity relations exhibited by the Galactic GCs. The circles and diamonds correspond to GCs comprising the flat and steep age-metallicity relation, respectively. Top right: the Sagittarius closed box model (Siegel et al., 2007) is overlaid over the age-metallicity relations The models for the Magellanic Clouds (Pagel & Tautvaisiene, 1998) are over-plotted in the bottom left panel, while the semi-analytic GC formation model from Muratov & Gnedin (2010) is over-plotted in the bottom right panel. Figure taken from Dotter et al. (2011).*

off (Anderson et al., 2008). With a careful analysis, Marín-Franch et al. (2009) showed that the age-metallicity relation features two distinct branches, as shown on Figure 1.6. This result was further reinforced by Dotter et al. (2010, 2011), with each study increasing the number of analysed GCs. The authors of these studies deduced that the splitting of the age-metallicity relation is due to distinct stages of galaxy formation.

The age range of the GCs which are members of the shallow age-metallicity relation (blue circles on Figure 1.6) is compatible with the collapse of a proto-galaxy having the same mass and scale length as the Milky Way dark matter halo. In this scenario the GCs formed in a relatively brief star burst episode due to the collapse of the initial cloud, hence having uniform old ages.

The GCs which comprise the steeper age-metallicity relation (red diamonds on Figure 1.6) formed during the second phase of star formation that spanned a time interval of $\sim$ 6 Gyrs. To make matters more interesting, Marín-Franch et al. (2009) found that a significant number of the GCs that constitute the steeper age-metallicity relation are associated with the Sagittarius dwarf galaxy or the Monoceros ring (Newberg et al., 2002). The Sagittarius dwarf galaxy is currently being accreted onto the Milky Way and is observed to be donating at least 5 GCs to the Galactic halo (e.g. Ibata et al., 1994, 1995; Martínez-Delgado et al., 1999; Cohen, 2004; Law & Majewski, 2010). This observation was the first direct evidence that at least some GCs in the Galactic halo have an external origin and were donated by accreted dwarf galaxies. Dotter et al. (2011) further examined this link by comparing it to various model predictions. The top right panel in Figure 1.6 compares the age-metallicity relations to the results for the closed-box chemical evolution model of a Sagittarius dwarf galaxy by Siegel et al. (2007). A closed-box chemical evolution model assumes that the gas of the galaxy is well mixed, no gas escapes or is added to the galaxy, and that the high mass stars return their nucleosynthetic products much faster than the time it takes for a significant number of stars to form. Assuming such a model, Siegel et al. (2007) showed that the age-metallicity relation of the GCs is similar to that predicted for the Sagittarius dwarf galaxy. A similar comparison was also made with the Magellanic Clouds, the ages and metallicities of which were derived via the evolutionary models of Pagel & Tautvaisiene (1998). The bottom left panel of Figure 1.6 implies that a variety of dwarf galaxies could have contributed towards the build up of the Galactic halo GC system and thus the steeper age-metallicity relation.

Hence, it is tempting to argue that the GCs which constitute the steeper age-metallicity relation in Figure 1.6 have formed within satellite galaxies which only got accreted onto the Milky Way at later times. However, one potential problem with this interpretation is that clusters from the same progenitor dwarf galaxy, Sagittarius, are all part of the same steep age-metallicity relation.

1.3 Extragalactic globular cluster systems

To better understand how GCs fit into the scheme of galaxy formation, it is necessary to study many GCs systems hosted by galaxies with different morphologies and residing in different environments. Hence, studies outside the Local Group are required. Advancement of instrumentation, and especially the launch of the *HST*, has made the detection of GCs up to $\sim$ 100 Mpc possible

(e.g. Peng et al., 2011). In this case, the standard method of identifying GCs is by subtracting the diffuse light of the host galaxy, following which they are seen as a centrally concentrated overdensity of point sources (e.g. Blom et al., 2012). Further colour and magnitude cuts are typically used to clean candidate samples of pollutants (e.g. Gómez & Richtler, 2004). At intermediate distances of $\sim$ 20 Mpc, GCs can be partially resolved when observed with the *HST*, and thus their shape can serve as another constraint when candidates are selected (e.g. Jordán et al., 2004).

In recent years, ground based studies have also resulted in prolific detections of GCs outside the Local Group out to distances of $\sim$ 30 Mpc (e.g. Blom et al., 2012; Usher et al., 2013; Kartha et al., 2014). The advantage of ground based telescopes is the ability to use wide-field imagers, thus covering a significantly larger area around galaxies than space based observations. The candidate GCs are selected based on colour, magnitude and size criteria. Whenever possible, follow-up radial velocity surveys can help eliminate contaminants (e.g. Strader et al., 2011)

Observations of GC systems outside the Local Group are affected by a number of problems. Identification of GCs in distant galaxies is not unambiguous and samples can suffer from contamination. The main contaminants are unresolved background galaxies and faint Milky Way halo stars which can have colours and apparent magnitudes such that they are not eliminated by magnitude and colour cuts. An additional bias comes from the final depth of the imaging, which can greatly affect the faint end of the GC luminosity function. The most common way to try to quantify this magnitude incompleteness is through artificial cluster tests (e.g. Puzia et al., 2002; Faifer et al., 2011). With this method, a large number of artificially generated clusters having a range of colours, magnitudes and sizes are added to the images. Then, an attempt is made to recover them via the same methods applied to the real candidates, effectively giving the completeness limits of the data. An additional problem is the spatial incompleteness. Most surveys tend to focus on the central regions of galaxies, often leaving large extents of their haloes, where significant populations of GCs may reside, incomplete. Examples of this type of bias are shown on Figure 1.7.

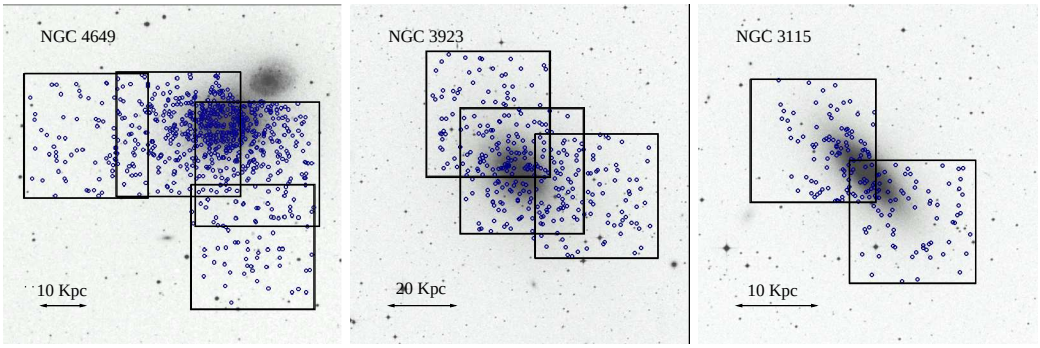

Figure 1.7 *Images of two elliptical galaxies (NGC 4649 and NGC 3923) and one S0 type galaxy (NGC 3115), observed with the Gemini telescopes. The surveyed fields and the GC candidates are marked. This is a clear example of a spatial bias, as most likely many GCs remain uncharted in the outer halo regions not covered by the imaging. Figure taken from Faifer et al. (2011).*

1.3.1 Specific frequency

An often used statistic when comparing the richness of GC systems hosted by different galaxies is the GC specific frequency,

$$S_N = N_{\rm GC} \times 10^{0.4(M_V+15)} \tag{1.1}$$

where $N_{\rm GC}$ is the total number of GCs in the system, and M_V is the integrated absolute V magnitude of the host galaxy (Harris & van den Bergh, 1981). This quantity can be thought of as the formation efficiency of GCs relative to field stars, although the interpretation is more complicated if one considers that fractions of these populations may have been accreted rather than formed *in situ*. The relation between S_N and galaxy luminosity is shown in Figure 1.8. The relation has a characteristic U-shape: the S_N is large for galaxies with very high or very low luminosities, but it settles down to a value of ~ 1 for typical massive galaxies. Harris et al. (2013) proposed that this trend is due to different types of feedback that occur during the galaxy formation phase. For dwarf galaxies having low mass, formation of field stars is inhibited by radiative feedback and gas ejection before it is completed. In giant galaxies, star formation is inhibited by active galactic nuclei (AGN) activity, after the GCs have formed. The creation of central dominant (cD) galaxies by accretion of a number of massive galaxies can significantly boost the total number of GCs and the luminosity of that galaxy, creating the extreme cases at the bright end of Figure 1.8.

Past studies (e.g. Peng et al., 2008; Spitler et al., 2008; Spitler & Forbes, 2009; Georgiev et al., 2010) have explored a number of correlations between the size

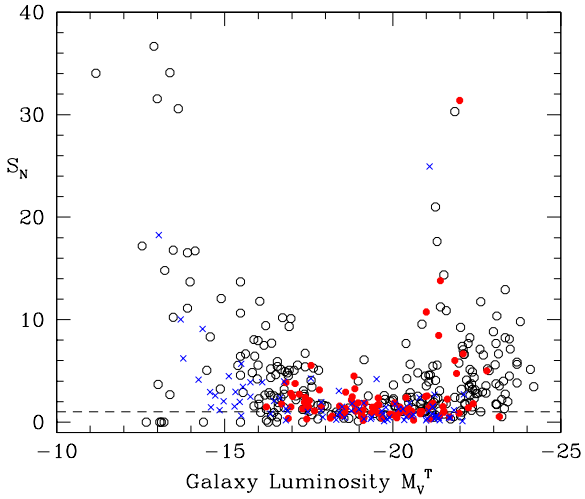

Figure 1.8 *The relation between specific frequency (S_N) and galaxy luminosity. Different symbols represent different morphological type of galaxies. The characteristic U-shape is seen. The horizontal line marks $S_N = 1$, a well defined value for typical massive galaxies. Figure from Harris et al. (2013).*

of a GC system and its host galaxy. Recently, Harris et al. (2013) created the most complete compilation to date of GC populations hosted by 422 galaxies from published data. These authors find a tight correlation between the $N_{\rm GC}$ and the dynamical mass $M_{\rm dyn}$[5] of the host galaxy, graphically shown in Figure 1.9. For galaxy masses larger than 10^{10} $M_\odot$, the number of GCs appears to increase almost linearly with the mass of the host (Harris et al., 2013).

After exploring several empirical relations, Harris et al. (2013) found that a simple product between the bulge velocity dispersion ($\sigma_{\rm e}$) and the effective radius of a galaxy ($R_{\rm e}$) accurately predicts the size of the GC system hosted by that galaxy. The empirical solution for Elliptical galaxies has the form:

$$N_{\rm GC} = (600 \pm 35) \left[\left(\frac{R_{\rm e}}{10{\rm kpc}}\right) \left(\frac{\sigma_{\rm e}}{100{\rm km/s}}\right) \right]^{1.29\pm0.03} \tag{1.2}$$

The same relation can be made valid for both Lenticular and Spiral galaxies by introducing a zero-point offset of -0.2 dex and -0.3 dex, respectively. These relations, separately illustrated for each morphological type, are shown in Figure 1.10.

[5]The dynamical mass is defined as $M_{\rm dyn} = 4\sigma_{\rm e}^2 R_{\rm e}/G$ where R_e is the effective radius of the galaxy light profile and σ_e is the central velocity dispersion.

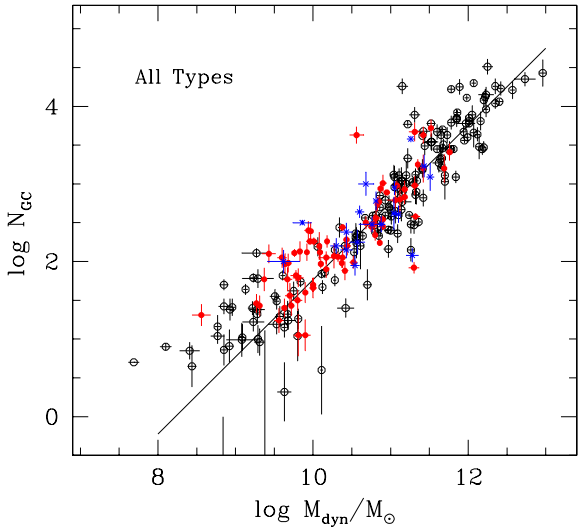

Figure 1.9 *Number of GCs vs. the dynamical mass of the host galaxy. Different galaxy types are plotted with different symbols. The solid line represents the best fit solution for all galaxies with $M_{\rm dyn} > 10^{10} M_{\odot}$. Figure from Harris et al. (2013).*

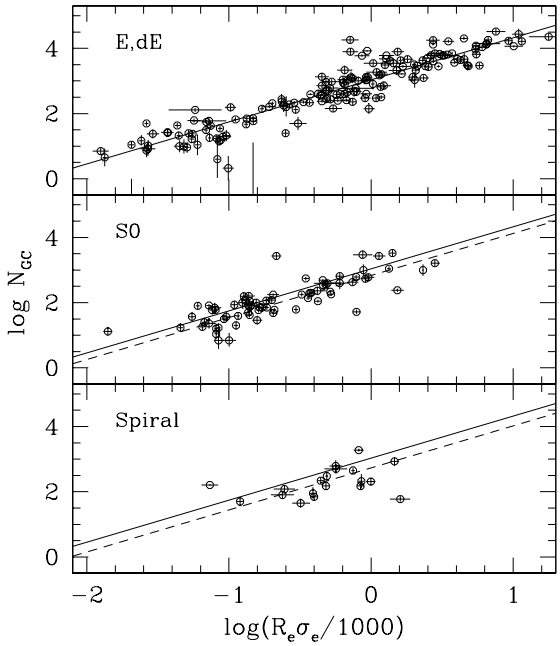

Figure 1.10 *Number of GCs vs. the $R_{\rm e}\sigma_{\rm e}$ factor (see text for details). The correlations are shown separately for elliptical, lenticular and spiral galaxies. In each panel, the solid line represents the best fit solution for elliptical galaxies, where both massive and dwarf constituents area included. The dashed lines in the middle and bottom panels are offset from the solid line by -0.2 dex and -0.3 dex respectively, in order to fit their respective samples. Figure taken from Harris et al. (2013).*

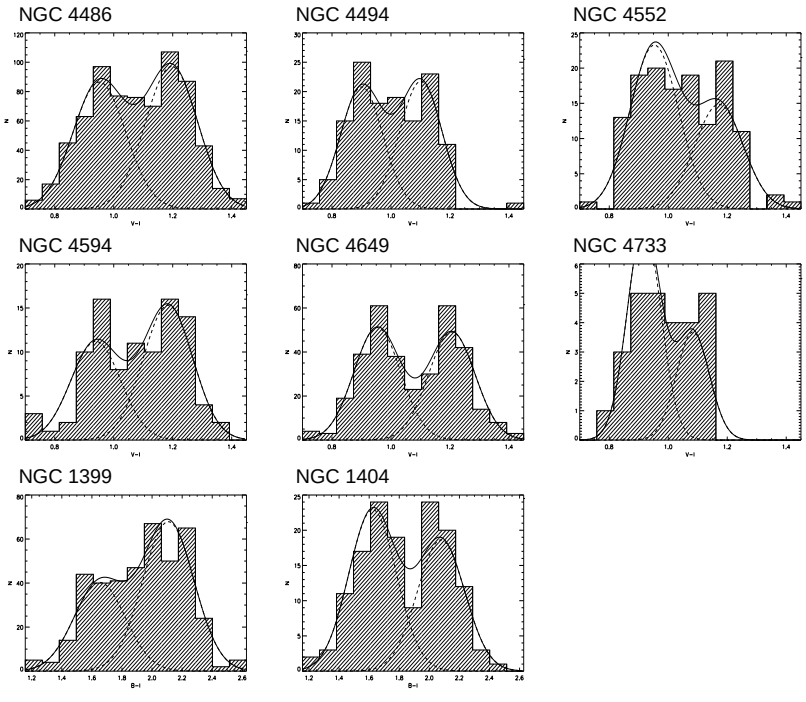

Figure 1.11 *Examples of bimodal $V - I$ and $B - V$ colour distributions of GCs in a sample of early type galaxies. Gaussian functions corresponding to the two colour peaks are over-plotted with dashed lines, while their sum is plotted with a solid line. Figure taken from Larsen et al. (2001).*

1.3.2 Colour bimodality

One of the first large photometric surveys exploring extragalactic GC systems which employed the *HST* was performed by Gebhardt & Kissler-Patig (1999). These authors surveyed 50 galaxies of which 43 were of type S0 or earlier. Gebhardt & Kissler-Patig (1999) found that nearly 50% of the observed galaxies hosted GC systems which were bimodal in colour. Further *HST* surveys with deeper imaging showed that colour bimodality is a common phenomenon even amongst distant galaxies (e.g. Larsen et al., 2001; Kundu & Whitmore, 2001; Faifer et al., 2011; Hargis & Rhode, 2012; Kim et al., 2013). In fact, there is no known massive elliptical galaxy which does not host multiple subpopulations of GCs (Brodie & Strader, 2006). Figure 1.11 shows GC colour distributions of a sample of early type galaxies observed with the *HST*. Even thought they do not occur exactly at the same place, the red and blue GC colour distributions peak typically at $V - I \sim 1.2$ and ~ 0.95, respectively (Larsen et al., 2001).

Spiral galaxies are also found to host subpopulations of GCs (e.g. Goudfrooij et al., 2003; Chandar et al., 2004; Young et al., 2012). Observations of such systems are more challenging due to extinction effects, since spiral galaxies contain significant amounts of gas and dust. Despite this, Larsen et al. (2001) found

that the peak of the colour distributions can be similar in both early and late type galaxies.

Various studies have found that, as in the Milky Way, red GCs are spatially concentrated toward the centre of their hosts, and that these clusters are good tracers of the underlying galaxy light. Conversely, the blue GCs have more extended spatial profiles and are generally associated with the haloes of their host galaxies (e.g. Pota et al., 2013).

It is generally accepted that colour bimodality is a result of a bimodal metallicity distribution in the GC system considered, such that the metal-rich globular clusters have red colours while their metal-poor counterparts feature blue optical colours. Recent spectroscopic studies of massive galaxies have shown that metallicity bimodality is a common phenomenon (e.g. Usher et al., 2012; Brodie et al., 2012), and that this is the most likely cause for the observed colour bimodality. Figure 1.12 presents such evidence for NGC 3115. If bimodal distributions of both colour and metallicity are indeed real, this would imply at least two distinct GC formation channels, or different formation epochs, which can be of great aid to galaxy formation models.

However, some studies have claimed that the colour bimodality is a result of a strong non-linear colour-metallicity relation (e.g. Yoon et al., 2006, 2011; Blakeslee et al., 2010). These studies claim that the shape of the metallicity distribution function is peaked in the metal-rich domain and has a characteristic metal-poor tail. Yoon et al. (2011) interpreted this to be due to continuous chemical enrichment with a short time-scale. The relation between the colour and metallicity distributions of GC systems is still an area of much active research and debate.

1.3.3 Kinematics

Studies of GC systems hosted by elliptical galaxies indicate that each one has its own unique kinematic system, connected to how the galaxy and its GC system formed and evolved (e.g. Zepf et al., 2000; Woodley et al., 2010; Strader et al., 2011). Pota et al. (2013) presented a kinematic study of 12 early type galaxies containing over 2500 GCs in total out to a projected radius of $\sim$ 65 kpc. Augmenting their sample with additional 10 GC systems hosted by early type galaxies from the literature, these authors determined several common kinematic features. It was found that red GC populations exhibit a rotation signature consistent with that of stars and planetary nebulae of the

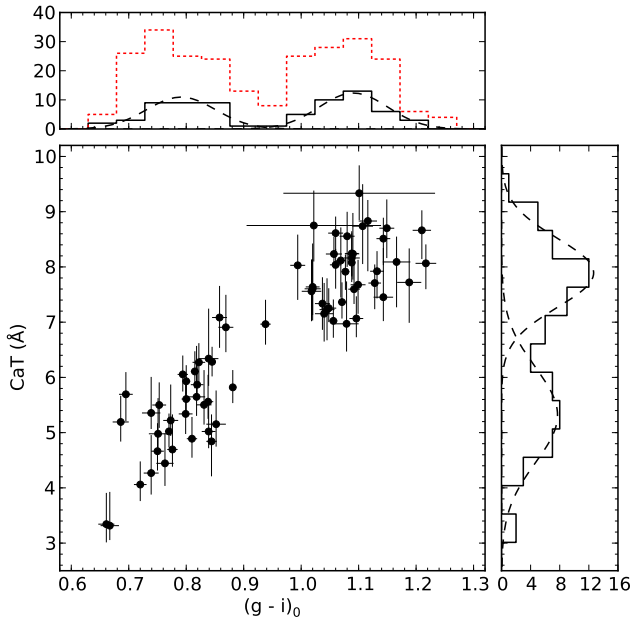

Figure 1.12 *Calcium triplet based metallicities are plotted vs.* $(g-i)_0$ *colours for the GC system of NGC 3115. Their distributions are also shown. The solid and dotted histograms correspond to the spectroscopic and background-decontaminated photometric samples, respectively. In every case, the presence of a bimodal distribution is obvious. The best fit Gaussian profiles are plotted over the histograms. Bimodality is preferred over unimodality at the* $>$ *99.9% and 99.8% for the colour and metallicity distributions respectively. Figure taken from Brodie et al. (2012).*

host galaxy. In addition, the red GCs were typically found to rotate around the major photometric axis of their host galaxy. On the other hand, the rotation of blue GCs was typically consistent with zero. However, individual cases were found in which the blue GCs were rotating, but in a way completely uncorrelated with the stars of the host galaxy.

Studying the velocity dispersion, Pota et al. (2013) found that red GCs follow the trend set by the host galaxy stars and planetary nebulae. Conversely, the velocity dispersion of blue GC populations is uncorrelated with that of the stars, and is found to be generally larger compared to that of red GCs. These authors found the velocity dispersion to be decreasing as a function of radius for galaxies having $M_K > -25$. For the brighter galaxies the dispersion profile was often found to be flat or even increasing. It was found that the effect of an increasing dispersion profile is induced solely by blue GC populations, while the red GCs always have either flat or decreasing velocity dispersion profiles.

Additional analysis has revealed that the root-mean-squared velocity of blue GCs hosted by massive early type galaxies increases as a function of galactocentric distance, while red GCs have much shallower profiles. Examining the velocity kurtosis for GC systems in their galaxy sample, Pota et al. (2013)

deduced that red GCs have in general radially-biased orbits, while blue GCs appear to be isotropic or tangentially-biased. These differences in the kinematics between red and blue populations of GCs have led the authors to deduce that colour bimodality is indeed a real feature, and it is not induced by a strong non-linear colour metallicity relation.

Unfortunately, the kinematics of GC systems hosted by spiral galaxies has been investigated in only few systems. The most notable contributions are those by Olsen et al. (2004), who derived radial velocities for 6 spiral galaxies in the Sculptor group out to a projected radius of $\sim$ 35 kpc around each galaxy, and Nantais & Huchra (2010) who performed spectroscopic observations on the GC system hosted by M81 out to projected radius of $\sim$ 22 kpc. GCs in the inner regions of spiral galaxies generally exhibit strong rotation signatures, driven by the red subpopulation, often associated with the HI discs or bulges in those galaxies. The blue GCs are assumed to form a halo system, with little if any rotation. So far little data has been obtained for GCs residing in haloes of spiral galaxies outside the Local Group, and the motions of those clusters are largely uncertain.

1.3.4 The origin of bimodality and galaxy formation models

At present, most observations show that massive galaxies host at least two distinct populations of GCs. This is reflected in the colours, metallicities, spatial distributions, and in many cases in the kinematics of the GCs. This means that they were formed at different times, at different locations or via different mechanisms. Galaxy formation models can greatly benefit from these observations since explaining how or when different populations of GCs formed also puts limits on the galaxy assembly scenarios.

The major merger model

With what is now known as the major merger model, Ashman & Zepf (1992) predicted the existence of metallicity bimodality in giant early type galaxies before it was observed. In this model, two spiral galaxies merge to form a resulting elliptical. The metal-rich GCs are formed by the gas mainly residing in the discs of the two progenitor spirals, which has been enriched by the birth and death of previous generations of stars. Conversely, the metal-poor GCs formed in the haloes of the spiral galaxies. In this model, the younger red GCs are more concentrated in the centre of the newly-

formed galaxy, while the older blue clusters have more extended spatial distribution. Numerical simulations support this idea as they are able to reproduce the properties of the elliptical galaxies and the metal-rich GCs that are formed through such mergers (e.g. Barnes & Hernquist, 1996; Bekki et al., 2002; Bekki, 2010). Additional support for this model is provided by HST observations of merging spiral galaxies and the discovery of young massive clusters around them (e.g. Whitmore & Schweizer, 1995; Miller et al., 1997; Trancho et al., 2007). Furthermore, the major merger model predicts that the young red globulars should exhibit little rotation compared to the blue GCs because the angular momentum would be transferred to the outer regions of the galaxy as a result of the merging process.

There are a number of problems associated with the major merger model. In the currently accepted view, GCs are formed in high pressure environments. However, the gas pressure in haloes of spiral galaxies is not sufficiently high for the required number of blue GCs to be formed (e.g. Ashman & Carr, 1988). In addition, it is known that spiral galaxies host multiple GC populations of their own, and it is difficult to explain this via the major merger model as it is unclear how the result of a merger between two spiral galaxies can also be a spiral galaxy. Another problem is the number of metal-poor GCs hosted by spirals, which is too low to explain the number of such clusters observed in early type galaxies. A proposed hypothetical solution for this problem is that ellipticals are much more efficient in accreting metal-poor GCs than spirals are. There is still no explanation for why this would be the case. The different ages for the metal-rich and metal-poor GC populations predicted by the major merger model represents yet another problem. Various spectroscopic studies have shown that, in many galaxies, the metal-poor (blue) and metal-rich (red) GCs are coeval (e.g. Forbes et al., 2001; Cohen et al., 2003; Beasley et al., 2004; Pierce et al., 2005). Finally, this model can not explain the rotation of red GCs, especially those located in the inner regions of elliptical galaxies such as NGC 5128 or M87 for example (Woodley et al., 2010; Strader et al., 2011).

The multiphase collapse model

An alternative scenario for explaining the observed bimodal nature of GC systems in massive galaxies was put forward by Forbes et al. (1997). Dubbed the "*in situ* multiphase collapse model", it predicts that most GCs were formed in the galaxy they inhabit, but at different times. This model requires at least two distinct stages of gas collapse and hence star formation. The metal-poor GCs are formed in the initial phase. The metal-rich clusters are then formed

in the subsequent phases after the interstellar medium has been enriched by previous generations of stars. A correlation between the luminosity of the parent galaxy and the metallicity of the metal-poor GCs is used in support of the *in situ* formation model (Brodie & Strader, 2006). If a galaxy is indeed formed through this process, it is expected its red GCs show some degree of rotation, while its blue GCs are expected to have high velocity dispersion with no rotation signature. This is because the blue GCs are formed in the initial free-fall phase, out of clumps of gas which are not necessarily related to one another. Conversely, their metal-rich counterparts are formed from the same giant gas cloud and thus retain a portion of its angular momentum.

Similarly to the major merger scenario, the primary problem with the multiphase collapse model is that it predicts different ages for different GC populations. In addition, this model relies on some effective mechanism which can halt and restart the gas collapse and hence the star formation at appropriate times.

The dissipationless accretion model

Côté et al. (1998) constructed the dissipationless accretion model to be consistent with the hierarchical formation of large-scale structure. In this model, the red GCs are formed in a monolithic collapse of a giant proto-galactic cloud, roughly half the size of a fully formed massive galaxy. They are predicted to be centrally concentrated, as the highest points of gas density and star formation are expected to occur in the central regions of the proto-galaxy. The high star formation and rapid self enrichment causes these clusters to have a higher metal abundance. The blue GCs are then captured via the accretion of dwarf galaxies and other sub-galactic fragments. Since the gas density and star formation rates are lower in such sub-galactic fragments, the self enrichment rate of the interstellar medium is also much lower, and thus the GCs formed in these environments are more metal-poor than their counterparts formed in the more massive proto-galaxy. In addition, given that the accretion of dwarf galaxies is meant to be a chaotic process, blue GCs are not expected to exhibit any rotation signature. This model is supported by the observations of kinematic substructures exhibited by groups of GCs present in some galaxies (Woodley & Harris, 2011; Strader et al., 2011).

The major assumption of the dissipationless accretion models is that all metal-poor (blue) GCs entered the system of their massive host galaxy through dissipationless mergers or accretion events. If this is indeed true, galaxy haloes

should be abundant with various stellar tidal debris as a result of the numerous past accretion events. As discussed before, the first direct observation of such an event was the discovery of the Sagittarius dwarf elliptical galaxy, which is donating at least 5 GCs to the Milky Way system while being accreted (e.g. Ibata et al., 1994, 1995; Martínez-Delgado et al., 1999; Cohen, 2004). However, one such event, even with the addition of all the discovered tidal remnants in the "Field of streams" (Belokurov et al., 2006), is not sufficient to explain the existence of the large number of metal-poor GCs in the Galaxy, and this issue is even more pronounced in galaxies with richer GC systems. However, it is worth noting that such stellar streams have very low surface brightness and their detection is challenging in both the Milky Way and galaxies outside the Local Group.

In reality, it is possible that a combination of the above mentioned models is responsible for the assembly of a GC system hosted by a massive galaxy. It is clear however that knowing various properties of a given GC system, such as its colour, metallicity and spatial distribution, as well as its kinematics, can constrain its origin and be of great aid to galaxy formation models.

Cosmological formation of GCs

With the success of the ΛCDM cosmological model, it is important to understand the formation of GCs within the grand picture of hierarchical galaxy assembly. In this cosmological framework, Peebles (1984) suggested that GCs are formed in collapsing dark matter haloes that have a total mass between $10^8 - 10^{10}$ $M_\odot$ and contain $\sim 10^6$ $M_\odot$ of gas. This process occurred at a very high redshift ($z = 10 - 20$), after which the dark matter halo was stripped without disturbing the cluster within. The increase of computing power and sophistication of N-body numerical simulations have allowed for this idea to be examined in a much greater detail. Even though such simulations still can not resolve individual GCs, they are an excellent tool for studying their formation. In such simulations, GCs are typically assumed to form in high density giant molecular clouds when the dynamical time-scale exceeds the cooling time (e.g. Kravtsov & Gnedin, 2005; Muratov & Gnedin, 2010).

Kravtsov & Gnedin (2005) performed a sophisticated high resolution numerical simulation, containing both dark matter and gas components, in which they studied the formation of GCs around a Milky Way type galaxy down to redshift $z = 3$ (see Figure 1.13). The GCs were created out of giant molecular clouds which assembled during gas rich mergers of proto-galaxies.

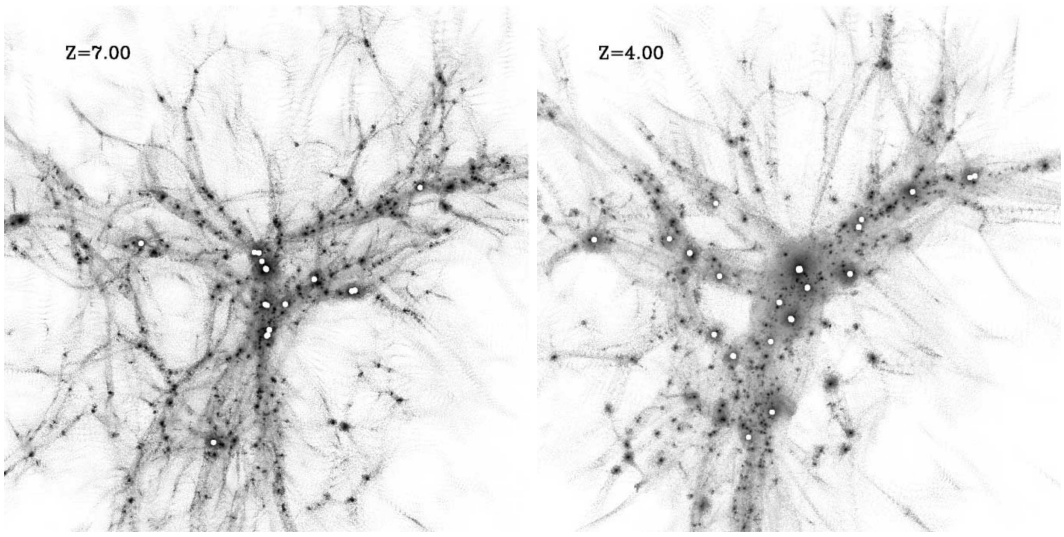

Figure 1.13 *Snapshots of the highest mass region in the N-body simulation run by Kravtsov & Gnedin (2005). The region has a co-moving size of* $1h^{-1}$*Mpc. The density of dark matter particles have a gray-scale colouring scheme on a logarithmic scale. The white circles show locations favourable for GC formation. Each white circle may contain multiple GCs. Figure taken from Kravtsov & Gnedin (2005).*

The gas formed a cold self-gravitating disc, which fragmented into spiral arms composed of molecular clouds. Most clusters formed in proto-galaxies having virial masses greater than 10^9 $M_\odot$. As seen on Figure 1.13, such proto-galaxies were found to be highly clustered which is consistent with the spatial concentration of GCs compared to the extended dark matter distribution profiles observed today. In this simulation, cluster formation started at $z \sim 12$, and the best conditions for GC formation occurred at $z \sim 3-5$. Kravtsov & Gnedin (2005) found that the mass function of the newly-formed GCs in their simulation closely matched that of the young massive clusters observed in the Antennae system. In addition, these authors found the mass and size distributions of the simulated GCs at the end of their simulation to be remarkably similar to those for the observed clusters in the Milky Way. The metallicity bimodality was not recovered, however.

Recently, Muratov & Gnedin (2010) presented a model in which they successfully reproduced the bimodality in GC systems, while forming GCs via a single mechanism – merging of gas rich proto-galaxies. The metallicity of the newly-formed GCs was linked to the mean galaxy metallicity in a one-to-one relation. With this prescription, these authors found that the metallicity distribution of all simulated clusters that survived until $z = 0$ is remarkably similar to that of the GCs around the Milky Way, thus successfully reproducing the observed bimodality, as shown in Figure 1.15. Hence, Muratov & Gnedin (2010) found that bimodality in GC systems is a natural product of hierarchical galaxy

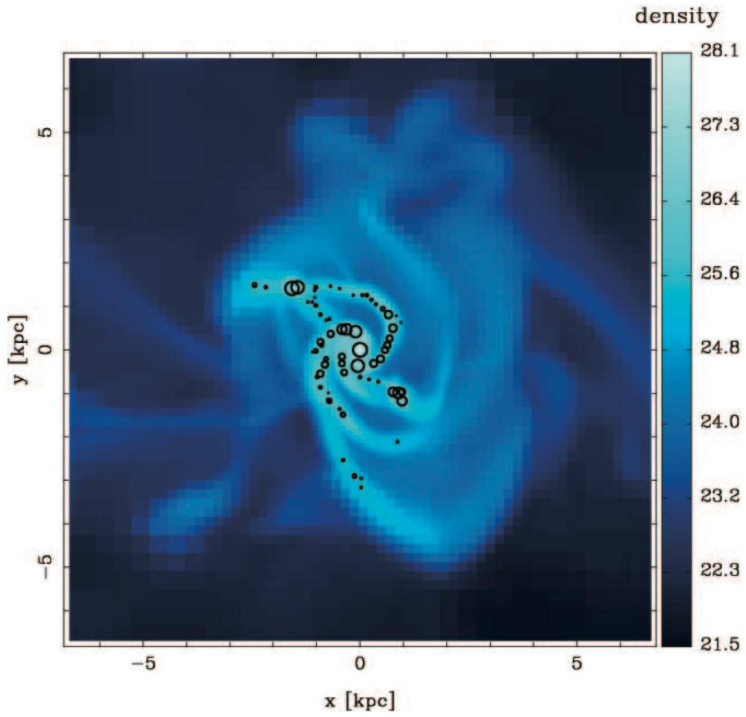

Figure 1.14 *Gas density of the most massive disc at $z = 4$ from the simulation by Kravtsov & Gnedin (2005). The white circles show the identified GCs, with the radius of each circle corresponding to the mass of each cluster. Figure taken from Kravtsov & Gnedin (2005).*

assembly and is dependent on the rate of mergers and the amount of cold gas in the merging proto-galaxies. Mergers of proto-galaxies with relatively low mass were found to produce mainly metal-poor clusters. Red GCs were formed in mergers involving more massive progenitors, but those happen much less frequently. Since the number of created clusters was proportional to the mass of the parent galaxies, only a few such mergers were required to produce a significant number of metal-rich GCs. A consequence of this GC formation method is a age-metallicity relation, such that metal-poor GCs are older than their metal-rich counterparts, since they form earlier in the merging phase. This is inconsistent with observations of Milky Way GCs which found that portions of metal-poor and metal-rich clusters are coeval, as shown in Figure 1.6 (Marín-Franch et al., 2009; Dotter et al., 2011).

1.4 The globular cluster system of M31

Located at a distance of ~ 780 kpc the Andromeda galaxy (M31) is more than a desirable target, since in many ways it bridges the positive aspects of observing our Galaxy to those of distant systems. The close proximity makes M31 the

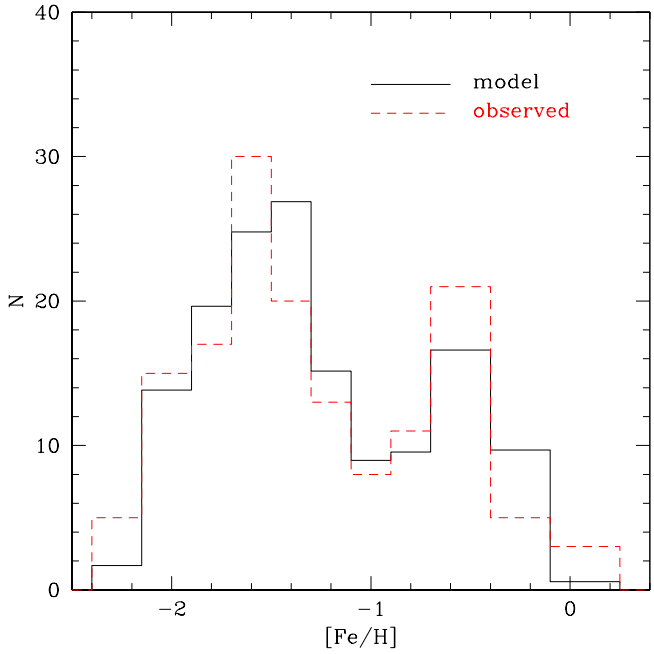

Figure 1.15 *Comparison between the metallicities of the Galactic GCs to the simulated clusters that survived dynamical disruption until the present day. Figure taken form Muratov & Gnedin (2010).*

only massive galaxy for which ground based observations of the resolved stellar populations of both the disc and halo are possible. Subtending a large angle on the sky, it provides a much better view of a spiral galaxy halo than the Milky Way, where one needs to observe vast angular regions and battle with projection and extinction effects.

1.4.1 The GCs in the inner regions of M31

Studying the GC system of the Andromeda galaxy has been a popular topic in astronomy for nearly a century. Hubble conducted the first GC search and detected 140 GC candidates in the disc of this galaxy from photographic plate observations (Hubble, 1932). Just over a decade later, similar efforts continued and the M31 GC sample grew considerably (e.g. Seyfert & Nassau, 1945; Vetešnik, 1962; Baade & Arp, 1964; Mayall & Eggen, 1953; Alloin et al., 1976; Sargent et al., 1977; Battistini et al., 1987). With the advent of modern CCD detectors in the early 1990s, which made observations more efficient and the GC identification more robust, the searches reignited and continued to bear fruit (e.g. Auriere et al., 1992; Battistini et al., 1993; Mochejska et al., 1998; Barmby & Huchra, 2001; Galleti et al., 2004; Huxor et al., 2005, 2008, 2014; Lee et al., 2008; di Tullio Zinn & Zinn, 2013). Today it is known that M31 hosts a rich GC system with over 500 confirmed members, listed in the

Revised Bologna Catalogue (RBC, Galleti et al., 2004), effectively making it over 3 times larger than the one hosted by our Galaxy. Thus, we are able to study a statistically significant sample of GCs, spread over the full extent of M31, and use it to probe in great detail the properties of a massive spiral galaxy similar to our own.

Metallicity

Similar to the Galactic GC system, the metallicity distribution of the GCs hosted by M31 is also bimodal in nature. Using a sample of 301 clusters out to ~ 22 kpc in projection, Perrett et al. (2002) confirmed the existence of a bimodal metallicity distribution in this GC system, by employing the KMM algorithm (Ashman et al., 1994). This algorithm assumes that the data is drawn from an underlying distribution that is the sum of multiple Gaussian distributions. Perrett et al. (2002) tested the probability of the parent metallicity distribution being bimodal rather than unimodal, which was assumed to be the null hypothesis. They found that bimodality is preferred with 97% confidence. The resulting bimodal distribution, shown in the top panel of Figure 1.16, features [Fe/H] peaks at -0.5 ± 0.13 for the metal-rich distribution and -1.44 ± 0.22 for the metal-poor GCs. These findings are consistent with those of Ashman & Bird (1993) and Barmby et al. (2000) who used smaller data sets comprised of 144 and 221 GCs respectively. Perrett and colleagues also found that out of the 301 GCs in their sample, 231 were determined to be metal-poor while 70 belonged to the metal-rich population according to the posterior probability of group membership resulting from their KMM test.

A number of early studies using small samples suggested the presence of a shallow metallicity gradient in the M31 GC system (Sharov, 1988; Huchra et al., 1991). Using the running histogram algorithm to robustly estimate the mean metallicity of their large GC sample in radial bins, Perrett et al. (2002) uncovered the presence of a more significant [Fe/H] gradient. This is displayed in the bottom panel in Figure 1.16. These authors found that the gradient disappeared when they repeated their analysis on the metal-rich subsample alone, while it remained prominent when only the metal-poor GCs were considered. However, it needs to be noted that in all cases when present, the metallicity gradient was observed to extend out to projected radius of ~ 60 arcmin (~ 30 kpc), outside of which the analysis become unreliable due to small number statistics.

It is also worth mentioning that, similar to the Galactic GC system, the metal-

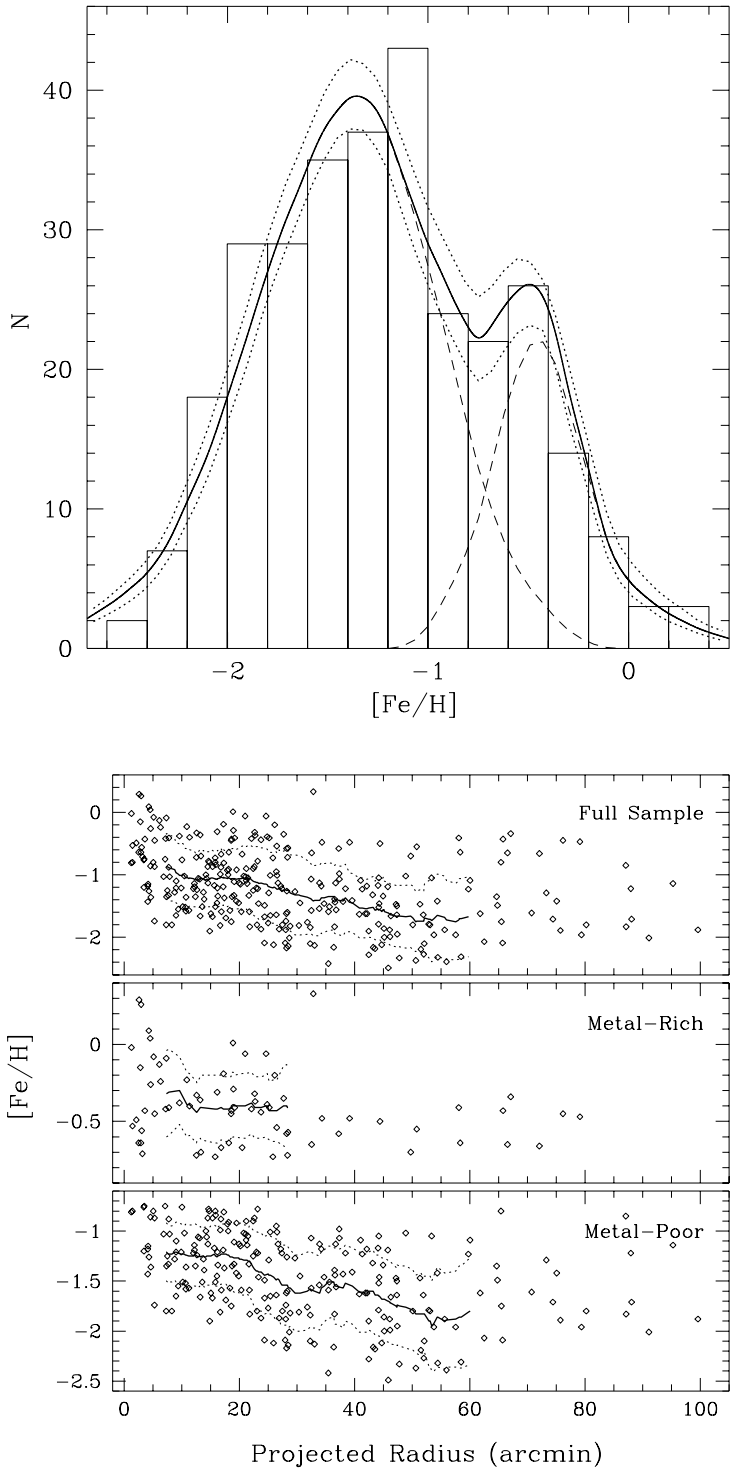

Figure 1.16 *Top: Metallicity distribution of the M31 GCs. The dashed curves represent Gaussian functions corresponding to the metal-rich and metal-poor GC distributions, the solid curve represents their sum, while the dotted curves mark the 90% confidence intervals. Bottom: [Fe/H] vs. projected radius for the M31 GCs. A running histogram algorithm was used to compute the mean (black curve), and the root-mean-square (dotted curve). Figures taken from Perrett et al. (2002).*

rich GCs hosted by M31 are concentrated towards the centre of the galaxy, while their metal-poor counterparts have a more extended spatial distribution. Lee et al. (2008) found the radial distribution of the metal-rich GCs to be highly peaked with a narrow half width of $\sim$ 2 kpc, suggesting that they are associated with the bulge of M31. Conversely, inspecting the spatial distribution of the metal-poor clusters, these authors found it to be extended along the major optical axis having a similar ellipticity as the M31 disc.

Kinematics

The kinematics has been of a particular interest when studying the GC system of M31. The first radial velocities for M31 GCs were obtained by van den Bergh (1969). Later, Hartwick & Sargent (1974) used the available data to estimate the mass of M31 using its GCs as tracers. A number of radial velocity studies followed (Huchra et al., 1982, 1991; Federici et al., 1990, 1993), each increasing the GC velocity data, while also updating the M31 mass estimate and providing velocity dispersion values for different subsamples.

Using higher precision data for their sample of 301 GCs, all having projected radii $\lesssim$ 22 kpc, Perrett et al. (2002) showed that the M31 GC system exhibits a strong rotation signature around the minor optical axis of this galaxy, with an amplitude of 138 ± 13 km s^{-1}. These authors also claim that the metallicity bimodality of the M31 GC system also extends to a kinematic bimodality. They measured the rotation amplitude of the metal poor GCs alone to be 131 ± 13 km s^{-1}, while that of the metal-rich population was determined to be higher at 160 ± 19 km s^{-1}. Furthermore, this study found that the metal poor GCs have mean heliocentric velocity of -290 ± 10 km s^{-1} with a velocity dispersion of 115 ± 7 km s^{-1}. Conversely, the metal-rich subsample featured mean heliocentric velocity of -260 ± 18 km s^{-1}. with a velocity dispersion of 146 ± 12 km s^{-1}. These differences in the kinematics of the metal-rich and metal-poor GCs have been used to suggest that the two populations might have undergone different formation mechanism (Perrett et al., 2002).

Six years later, Lee et al. (2008) revisited the kinematics of the M31 GC system, and performed detailed analysis using an updated sample comprising 504 GCs from Kim et al. (2007) with measured radial velocities, all of which lie at distances less than 25 kpc from the M31 centre. This work confirmed the rapid rotation of the GC system around the minor optical axis, and found the corresponding amplitude to be much higher than any previous study at 188^{+34}_{-28} km s^{-1}. The rotation corrected velocity dispersion was found to be

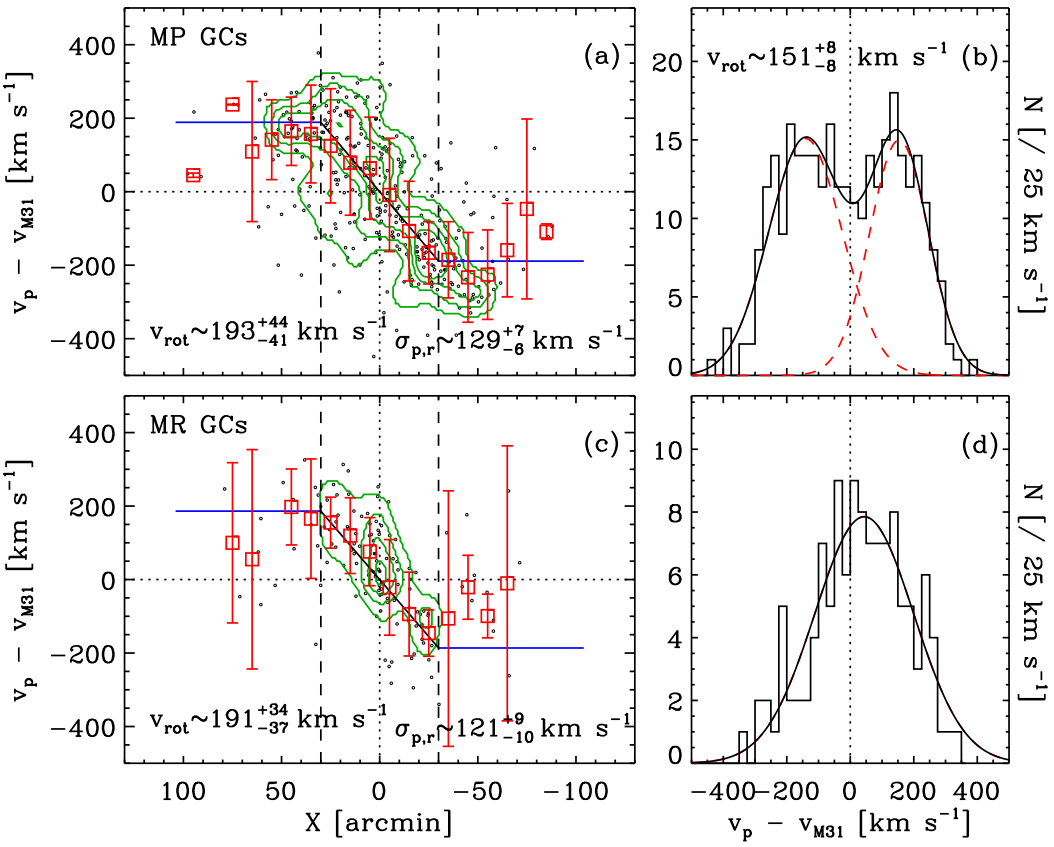

Figure 1.17 *On the left panels the dots mark the radial velocities of the metal poor (a) and metal-rich (c) GCs vs. their projected distances along the major axis of M31 (X). The open squares mark the mean velocities in 10′ bins, while their error bars represent the velocity dispersion of the clusters in each bin. The contours mark the number densities in the radial velocity vs. X space, and their levels are the same in panels (a) and (c). Panels (b) and (d) show the velocity histograms for the metal-poor and metal-rich GCs respectively. The solid line is the sum of individual Gaussian fits, plotted as dashed curves. However, note that Peacock et al. (2010) found the data sample used by Lee et al. (2008) to be significantly affected by contamination, rendering their results unreliable. Figure taken from Lee et al. (2008).*

134 ± 5 km s^{-1}. This latter value was found to rise with increasing distance along the minor axis of M31, thus showing that the M31 GC system is more pressure supported at larger scaleheights.

Figure 1.17 shows that, unlike Perrett et al. (2002), the study conducted by Lee et al. (2008) found essentially no difference between the motions of the metal-poor (amplitude of 193^{+44}_{-41} km s^{-1}; rotation corrected velocity dispersion of 129^{+7}_{-6} km s^{-1}) and the metal-rich clusters (amplitude of 191^{+34}_{-37} km s^{-1}; rotation corrected velocity dispersion of 121^{+9}_{-10} km s^{-1}).

Lee et al. (2008) made another interesting test. They split their GC sample

in two parts: bright GCs ($T_1 < 17$) and faint GCs ($T_1 > 17$)[6]. Re-applying their kinematic analysis on these newly-created subsamples, perhaps unsurprisingly, found that both exhibit strong rotation around the minor optical axis of M31. However, they found that the rotation of the faint GCs is stronger (amplitude of 178 ± 23 km s^{-1}; rotation corrected velocity dispersion of 107 ± 8 km s^{-1}), than that of the brighter clusters (amplitude of 129 ± 35 km s^{-1}; rotation corrected velocity dispersion of 146 ± 7 km s^{-1}). It is thought that this difference in rotation is closely related to how these subsamples are distributed spatially, as the faint GCs are more extended along the major axis than the bright GCs. This in turn would imply a gradient in the rotational velocity which is not surprising: a GC system is not a rigid body, and some degree of differential rotation is expected to occur naturally.

However, all the results presented by Lee et al. (2008) need to be treated with great caution. Using Sloan Digital Sky Survey (SDSS) imaging, Peacock et al. (2010) found that many of the sources classified by Kim et al. (2007) as genuine GCs were in fact stars. This was especially true for objects with fainter magnitudes. The reclassification was based on the superior spatial resolution of the SDSS data compared to the data obtained by Kim et al. (2007). This implies that the results of Lee et al. (2008) are significantly affected by contamination, making their validity impossible to judge.

It is also very important to discuss the effort of past studies (e.g. Ashman & Bird, 1993; Perrett et al., 2003; Perina et al., 2009), that used available kinematical data to search for and detect possible velocity sub-clustering amongst the M31 GCs. Ashman & Bird (1993) made the first significant attempt at detecting GC groups in the inner regions of M31. These authors used a technique in which groups of GCs were isolated based on deviations of the global mean velocity and velocity dispersion between each cluster and N nearest companions. Although this technique yielded a number of groupings, Ashman & Bird (1993) warned that their method may produce false positives if the GC system were to exhibit significant rotation, which was later found to be indeed the case.

Using an improved and enlarged data set, Perrett et al. (2003) searched for sub-clustering in the inner M31 GC system as evidence of past merger remnants. These authors employed a modified "friends-of-friends" algorithm, which can detect the elongated groups that are expected to be found along tidal debris

[6]The Washington photometric system, featuring the bands C, M, T_1, T_2, was specifically designed to obtain accurate temperatures and metallicities for G and K giant stars. The T_1 band has an effective wavelength of 6330 Å, with a width of 800 Å.

streams. Perrett et al. (2003) detected 10 unique groups, each consisting of at least 4 GCs, all of them lying in the complex region within 11 kpc from the centre of M31 in projection. They performed additional tests and found that even though the majority of these might be chance groupings, there was a high probability that at least some might be genuine dynamically linked units.

Most recently, Perina et al. (2009) attempted to identify clusters in the inner parts of M31 that sit away from the global trend in metallicity vs. position, as such objects might have an external origin. Out of the clusters that satisfied their initial criteria, three were found to have similar projected radii and similar radial velocities, which were quite distinct from the kinematics of the M31 disc. Moreover, Perina et al. (2009) found these three clusters to have similar metallicities and velocities as the underlying local stellar populations, indicative that these clusters are likely to be physically part of a coherent substructure.

It still needs to be emphasized that all above attempts at finding coherent GC groups in M31 were undertaken for clusters lying at projected distances smaller than 30 kpc from the M31 centre. At these locations, such searches are quite challenging. It is difficult, if not impossible, to trace a single stellar debris stream reliably in these regions due to the presence of many intertwined stellar substructures, as well as the comparatively high stellar densities of the M31 spheroid. In addition, the high number density and the wide range of GC properties makes it difficult for distinct kinematic groups to be reliably detected. Furthermore, since the dynamical time-scales in the inner parts of M31 are short, it is possible that any accreted objects presently found in these regions are now well mixed with the host populations of stars, and clusters no longer retain their initial dynamical links.

1.4.2 The Pan-Andromeda Archaeological Survey

Until less than a decade ago, almost everything known about the M31 GC system came from studies that extended less than $\sim$ 30 kpc in radius. When studying galaxy assembly, it is crucial to investigate galaxy haloes. This is because even though they contain only a small fraction of the total galaxy mass, it is only in the haloes of galaxies that remnants of past mergers or accretion events can be detected due to the long dynamical time-scales.

The first homogeneous survey of the M31 halo was done with the *Wide Field Camera (WFC)* mounted on the *Isaac Newton Telescope (INT)* (Ferguson et al.,

2002; Ibata et al., 2007). Comprising 164 individual pointings, this survey – see Figure 1.18 – covers an area of $\sim$ 40 deg^2, extending $\approx$ 55 kpc along the semi-major and $\approx$ 34 kpc along the semi-minor axis of M31. Analysis of these data revealed that beyond a radius of $\approx$ 20 kpc, the halo of M31 is dominated by various stellar overdensities in the form of loops, shells and streams (Ferguson et al., 2002), which are thought to be the remnants of accreted and tidally disrupted galaxies. The most noteworthy feature is the Giant Stellar Stream (Ibata et al., 2001), located in the south-east region of M31, roughly parallel to its semi-minor axis. With the same data set, Ibata et al. (2005) detected the presence of an extended stellar structure resembling a disc and spanning radii between $\sim$ 15 and 40 kpc in projection. Based on a spectroscopic follow-up of over 2800 RBG stars in the disc, these authors found that the stars have velocities consistent with them being in circular orbits in the plane of the M31 HI disc, with a typical velocity dispersion of $\sim$ 30 km s^{-1}. Moreover, the disc was found to irregularly extend out to $\sim$ 70 kpc, where its composed of various substructures, and thus Ibata et al. (2005) argued for an accretion origin.

Further examination of the *INT* data led to the discovery of many new GCs, including a new type of extended luminous star clusters (Huxor et al., 2005, 2008), which were later found to exhibit the same features as the classical GCs, save for their structural properties (Mackey et al., 2006). In addition, a dwarf spheroidal galaxy, satellite of M31 (And VII, Irwin et al., 2008), was also discovered.

The result of the *INT* survey discussed above served as a motivation to initiate the "Pan-Andromeda Archaeological Survey" (PAndAS, McConnachie et al., 2009), imaging the resolved stellar populations of M31 and its lesser companion M33 on a much grander scale. PAndAS is a state-of-the-art modern survey employing the MegaCam instrument (Boulade et al., 2003), mounted on the 3.6-m *Canada-France-Hawaii Telescope (CFHT)*. The detector consists of a mosaic of 36 2048 $\times$ 4612 pixel CCDs, with a pixel scale of 0.187 arcsec per pixel, giving a total field of view of $\approx$ 1 deg^2. This survey comprised $\approx$ 400 distinct pointings, covering an area of $\sim$ 380 deg^2 and extending to a projected radius of $\sim$ 150 kpc from the centre of M31. PAndAS was undertaken in two optical bands, g and i. The observations were taken in good photometric conditions with typical seeing < 0.8, reaching a depth down to $\sim$ 25.5 in g, and $\sim$ 24.5 in the i band, with a signal-to-noise ratio (S/N) of 10.

The *MegaCam* data were initially reduced by *CFHT* staff using the ELIXIR pipeline which performs the standard bias, flat-field and fringe corrections,

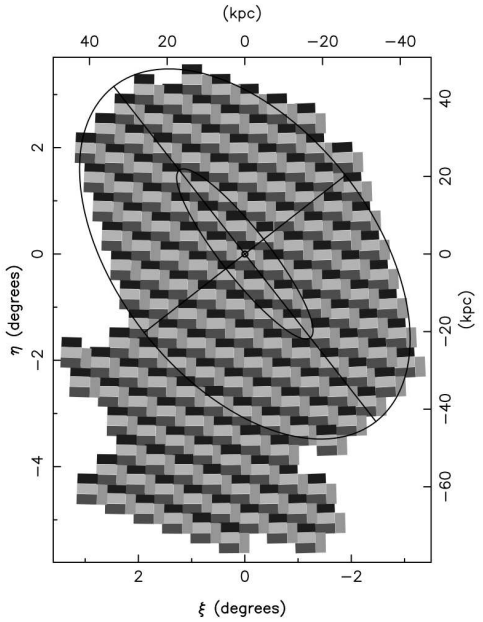

Figure 1.18 *The area observed with the* INT/WFC *survey of M31, spanning* ≈ 40 *deg*^{2}*. The inner ellipse has a semi-major axis of 27 kpc and approximately marks the extent of the HI disc of M31. The larger ellipse features a semi-major axis of 55 kpc. Figure taken from Ibata et al. (2007).*

and determines the photometric zero-point. The typical night-to-night variations of the zero-point is around 1-2% (Regnault et al., 2009). The data were further processed by the Cambridge Astronomy Survey Unit[7], and the full details of this process are described in McConnachie et al. (2010).

Building on the results from the *INT* survey, PAndAS found that the various stellar substructures extend far in the outer halo of M31, out to the edge of the survey at projected distance of $\sim$ 150 kpc. The number of streams revealed by both surveys implies that M31 had a rich accretion history. In a recent contribution, Ibata et al. (2014) used PAndAS data to study the properties of the resolved stellar halo of M31, including the substructure morphology as a function of metallicity. Assuming the stars are 13 Gyr old and have $[\alpha/\mathrm{Fe}] = 0$, photometric metallicities were derived by interpolating between stellar population model isochrones (Dotter et al., 2008), with varying metallicities for each star. To minimize contamination coming from Galactic disc stars, only those having $(g-i)_0 < 1.8$ were selected. Ibata et al. (2014) found a substantial metallicity gradient in the M31 halo, with the mean metallicity decreasing from $[\mathrm{Fe/H}] = -0.7$ at $\sim$ 30 kpc to $[\mathrm{Fe/H}] = -1.5$ at 150 kpc in projection. These authors find that the halo is almost entirely dominated by the Giant Stellar Stream when a metallicity cut of $[\mathrm{Fe/H}] > -1.1$ is applied, as shown in Figure 1.19. The numerous intermediate to low mass accretions are best

[7]http://casu.ast.cam.ac.uk

visible in the metallicity range of $-1.7 < [\mathrm{Fe/H}] < -1.1$, while the most metal-poor cut $-2.5 < [\mathrm{Fe/H}] < -1.7$ revealed a predominantly smooth halo. It is interesting to note that no spatial correlation was found between stellar substructures and HI content in the halo of M31, apart from the location of the Giant Stellar Stream (Lewis et al., 2013).

Data from this survey also led to the discovery of new dwarf galaxies, satellites of M31 (Martin et al., 2009; Richardson et al., 2011). Ibata et al. (2013) found that about half of the M31 satellites lie in a thin plane, and appear to be rotating with the rotation axis being inclined by ~ 45 deg with respect to the minor axis of this galaxy.

In addition to the 40 GCs discovered by Huxor et al. (2008), careful examination of the high quality PAndAS imaging resulted in the discovery of 59 new GCs, most of which lie in the outer halo of M31 (Huxor et al., 2014). Amongst these, is the most remote currently known GC in the Local Group, with a deprojected distance of 200 kpc from the M31 centre (Mackey et al., 2010a). Because this sample forms the basis of much of the work presented in this thesis, I will discuss its construction in detail. The clusters were detected by visual examination of objects classified as non-stellar in the final PAndAS photometric catalogue that had $-10.5 < M_{V_0} < -3.5$ and $0 < (V-I)_0 < 1.7$. The classification is unambiguous since the GCs are partially resolved in the images, and as a result there is virtually no contamination. The search was complemented by a visual inspection of the complete area covered by the survey, as well as by using an adapted automated method, originally designed to search for dwarf galaxies and stellar overdensities (Martin et al., 2013). The newly-discovered GCs are displayed in Figure 1.20.

To better quantify the success of the GC search, Huxor et al. (2014) presented a detailed analysis regarding the two sources of incompleteness that affected their work. One source was the spatial incompleteness, arising from the many gaps between the imaging CCDs in the MegaCam focal plane, and the gaps due to the imperfect tiling of the observations. GCs are sufficiently small on the sky that they could be missed were they to land in such a gap. The other source of incompleteness was associated with the one's ability to visually detect GCs, and is related to the final depth of the imaging.

The quantification of the spatial incompleteness required a calculation of the total area lost due the gaps in the imagery. First, the WCS information in the image headers are used to determine the RA and DEC boundaries of each of the 36 CCDs in a given MegaCam pointing. Then, sets of randomly

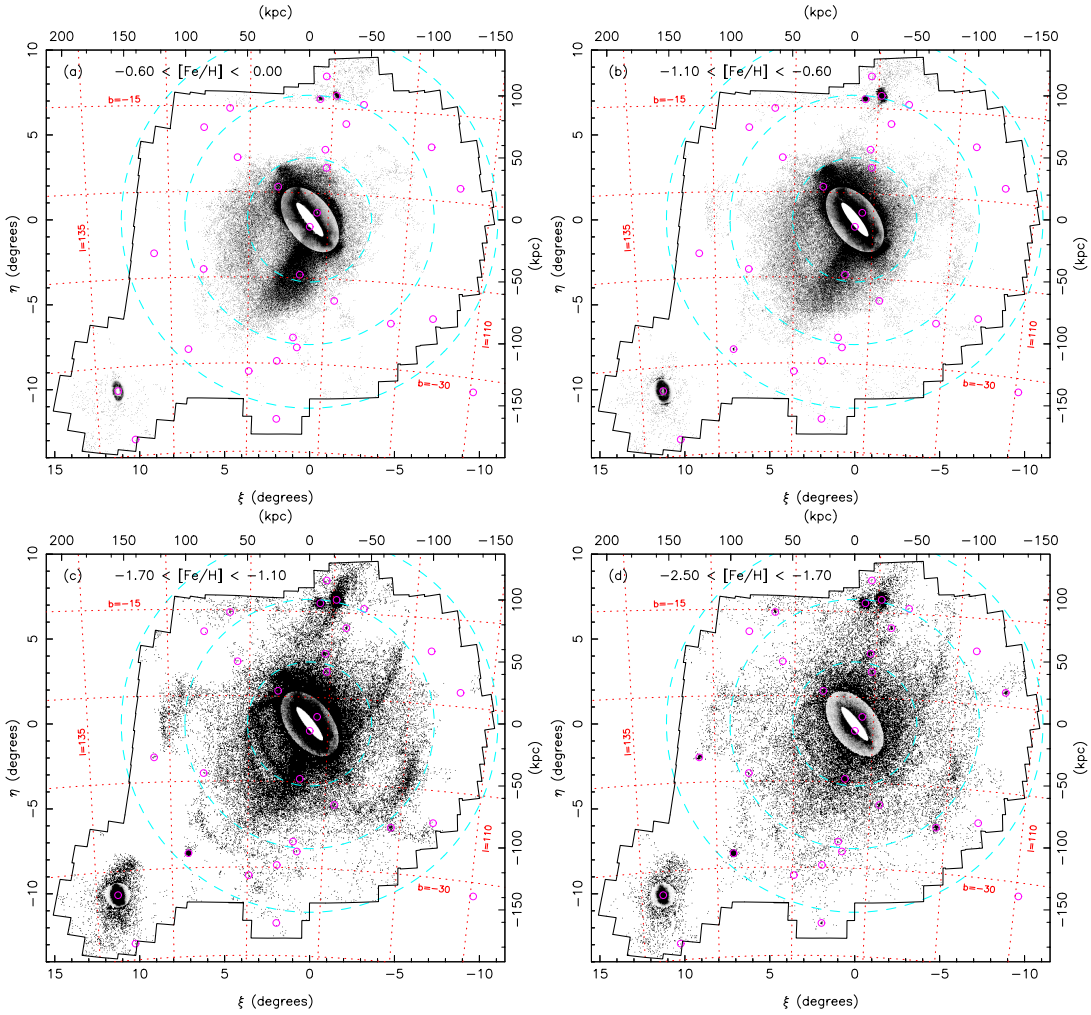

Figure 1.19 *Maps of stars with* $(g-i)_0 < 1.8$*. Each panel shows a different metallicity cut. The highly crowded regions around the centres of M31 and M33 are shown as gray-scale density images. The positions of known satellite galaxies are marked with the pink circles. The upper two panels show that the higher metallicity halo is dominated by the giant stream. The many substructures are most prominent on panel (c) featuring a* $-1.7 < [\mathrm{Fe/H}] < -1.1$ *metallicity cut. In the most metal-poor cut, displayed on panel (d), the halo appears smooth to first order. Figure taken from Ibata et al. (2014).*

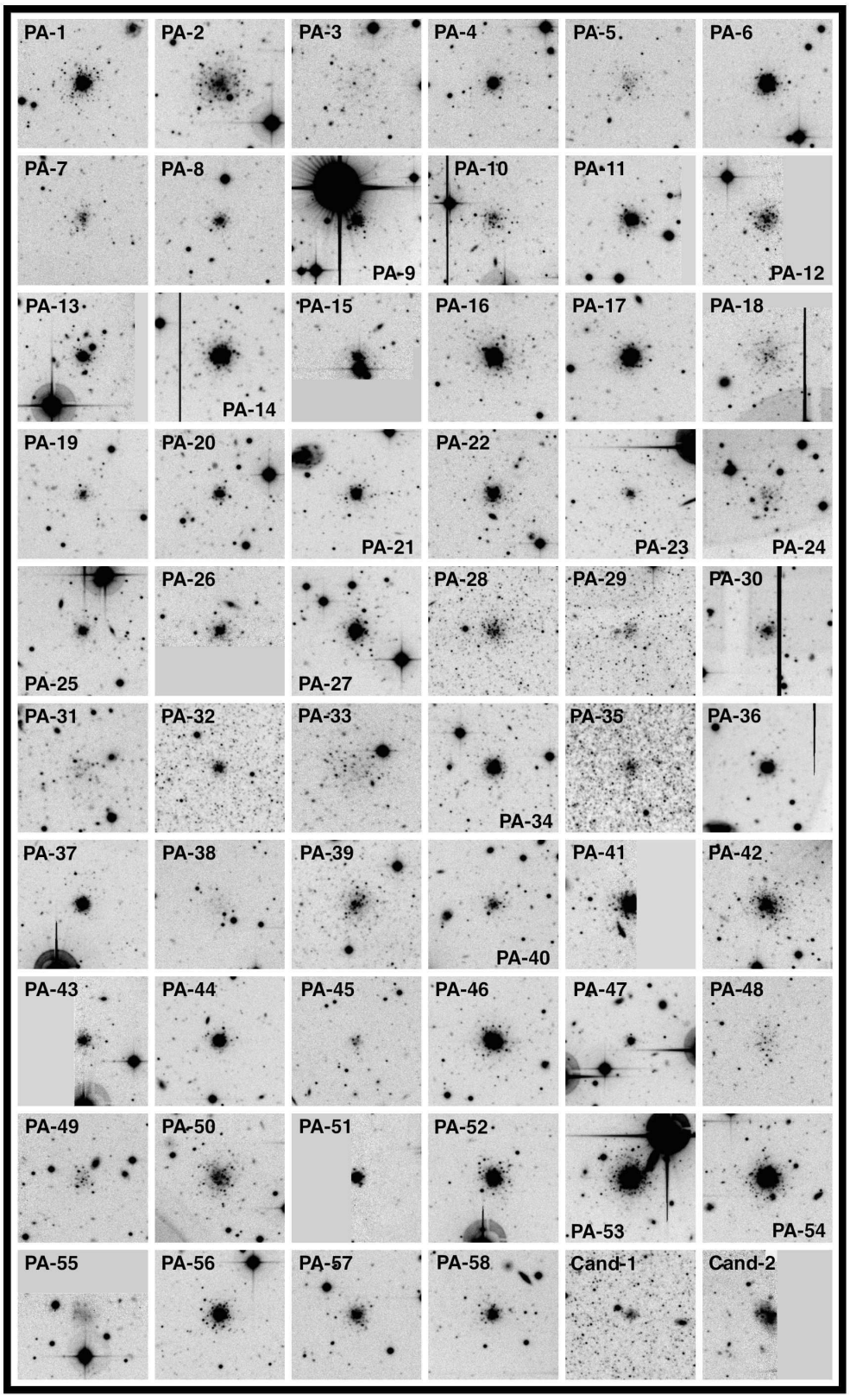

Figure 1.20 *PAndAS g-band images of the new GCs discovered in the M31 halo. Each frame is* 1×1 *arcmin in size. North is up and east is left. Figure taken from Huxor et al. (2014).*

located points area generated, with each set falling between two circular annuli separated by 0.5 kpc at the distance of M31, and centred on it. The number of generated points in each annulus was high enough to reach a density of at least $\sim$ 100 arcmin^{-2}. The “observed" area was simply calculated by dividing the number of points which fell within the RA and Dec boundaries by the total. Huxor et al. (2014) found that the spatial completeness is 96% 150 kpc, falling down to $\sim$ 80% at 130 kpc and further to $\sim$ 20% at 150 kpc in projection.

To quantify ones ability to detect GCs through visual inspection, a suite of artificial GCs was generated using the SIMCLUST (Deveikis et al., 2008) and SKYMAKER (Bertin, 2009) software packages. The clusters were constructed with a range of luminosities and concentrations[8] and were embedded within field star backgrounds of a varying density. Thumbnails of these generated clusters were then visually inspected by Avon Huxor who decided if a cluster was present or not based on the same criteria that was applied to the real data. It was found that the search is 100(50)% complete down to $M_V \approx -6.0(-4.1)$. For reference, these limits indicated that, if present, most if not all of the Milky Way Palomar type clusters would be detected. Indeed, of the thirteen such objects known in the Milky Way that have available absolute integrated V magnitudes, ten of them are brighter than -5.0, while eleven are brighter than -4.0 (Harris, 1996). The Koposov clusters, which have $M_V \sim -1$ (Koposov et al., 2007), would not be detected, which is unsurprising since the detection of these objects is quite challenging even in the Milky Way. The full details on the incompleteness assessment is presented in Huxor et al. (2014).

Carefully inspecting the spatial position of the GCs in the M31 halo, shown in Figure 1.21, one gets the sense that most of the GCs lie projected on top of stellar substructures, or are clustered together. Mackey et al. (2010b) was the first to quantify these observations, demonstrating that over 80% of the GCs in the M31 halo preferentially lie projected onto stellar streams. Monte Carlo simulations showed that the probability of such alignment arising by chance is less than 1%. These observations suggest that the majority of the M31 halo GCs were not formed *in situ*, but have an external origin, i.e. were donated to the M31 system by accreted dwarf galaxies. Further support for the accretion arguments comes from the finding that at least two GCs that lie on a prominent stellar overdensity are at least 2 Gyr younger than the oldest GCs in the Milky Way (Mackey et al., 2013). This is consistent the ages determined for the GCs associated with the Sagittarius stellar stream in our Galaxy, as shown in Figure 1.6. Given the apparent rich accretion history of M31, it is possible

[8]The concentration is defined as $c = \log(r_t/r_c)$; where r_t and r_c are the cluster tidal and core radii respectively, assuming a King (1962) profile for its radial surface density.

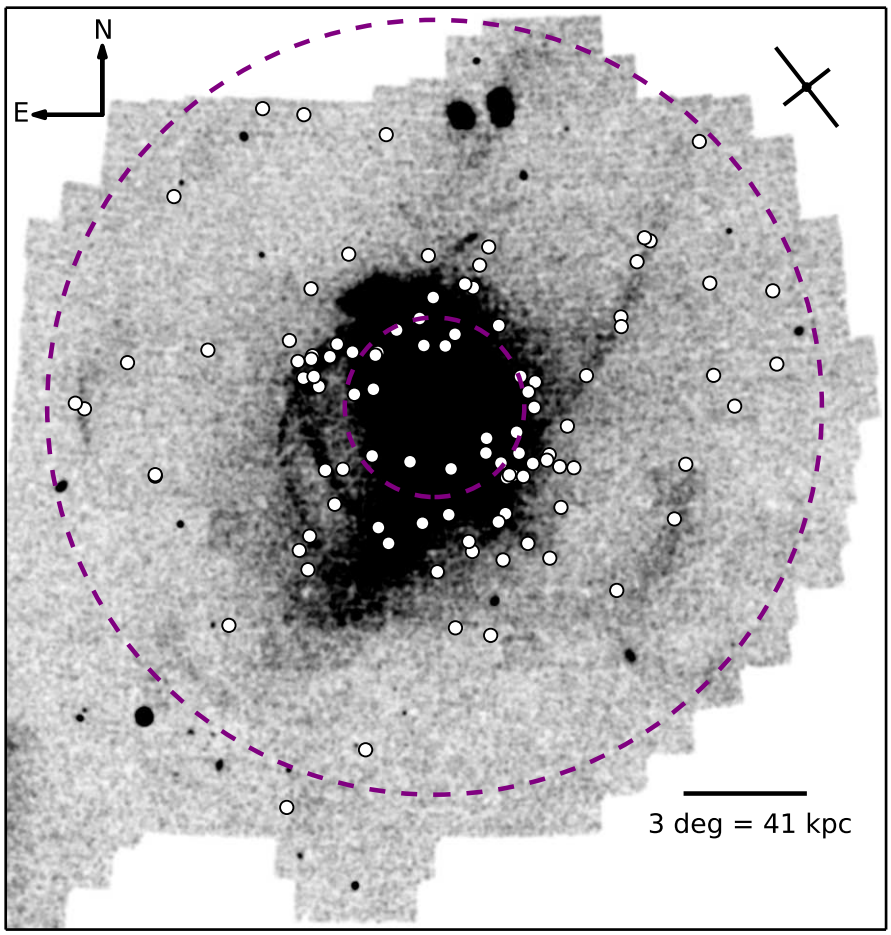

Figure 1.21 *Metal-poor ([Fe/H]$\lesssim -1.4$) RGB stellar density map of M31 from PAndAS. The variety of stellar streams and other tidal debris, thought to be the remnants of accreted dwarf galaxies, are clearly visible. To guide the eye, the purple dashed circles have projected radii of 30 and 100 kpc. The positions of the GCs discovered by PAndAS as well as those lying at projected radii larger than 30 kpc are marked with white dots.*

that all of its halo GCs lie on stellar debris features, but not all such features are visible with the currently available imaging. It is also interesting to note the apparent lack of GCs projecting on the Giant Stellar Stream given its size and complexity. Many of the other dominant stellar streams, albeit appearing less massive, are observed to have more GCs (see Section 3.4).

Investigating the global properties of the M31 GC system, Huxor et al. (2011) found tentative evidence that the GC luminosity function is bimodal. Using the final PAndAS GC catalogue, Huxor et al. (2014) found that the GC luminosity function is indeed bimodal when considering only halo clusters having projected radii larger than 30 kpc (see Figure 1.22. The authors claim that the secondary peak, located at $M_{V_0} \sim -6$ is driven by GCs that were accreted along with their parent dwarf galaxies. This is consistent with the observation of the Milky Way GCs associated with the Sagittarius dwarf

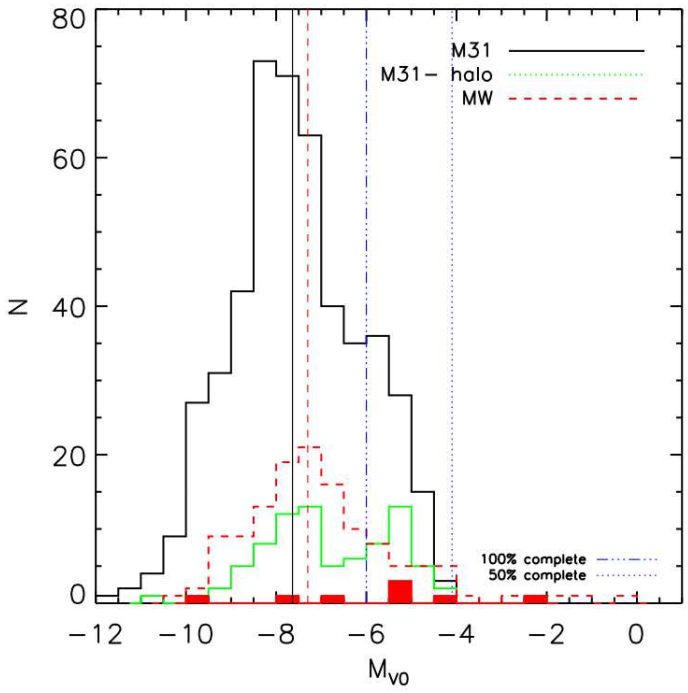

Figure 1.22 *Histogram of M_{V_0} for the entire M31 GC system. The sample of GCs having projected radii larger than 30 kpc (green histogram), as well as the M31 GC system (red histogram) are also shown. The red regions show the clusters associated with the Sagittarius dwarf galaxy. The blue vertical lines indicate the 100% and 50% completeness limits for the PAndAS GC search. Figure taken from Huxor et al. (2014).*

galaxy, 5 of which have $M_{V_0} < -6$. Further support comes from the study by Mackey & van den Bergh (2005) who detected a similar faint peak in the luminosity function of young halo GCs in the Milky Way which have also most likely an accretion origin.

Examining the GC radial number density profile, shown in Figure 1.23, Huxor et al. (2011) and Mackey et al. (2014 in prep), found it to be well described by a power law, up until an irregular bump occurring at $\approx$ 30 kpc. Huxor et al. (2011) found a break at the same point in the stellar luminosity function of M31. Numerical simulations have shown that such a change in the luminosity function is expected for a galaxy that forms through a combination of *in situ* star formation and accretion: the break in the luminosity function marks the point outside of which the bulk of the matter has been accreted (Abadi et al., 2006). Thus, if similar, the bump in the GC luminosity function naturally divides the clusters into a inner region sample, and an outer halo population. Hence, throughout this thesis, the label "outer halo GCs" stands for those that have projected radii larger than 30 kpc.

Finally, it is important to note that PAndAS also improved the census of GCs

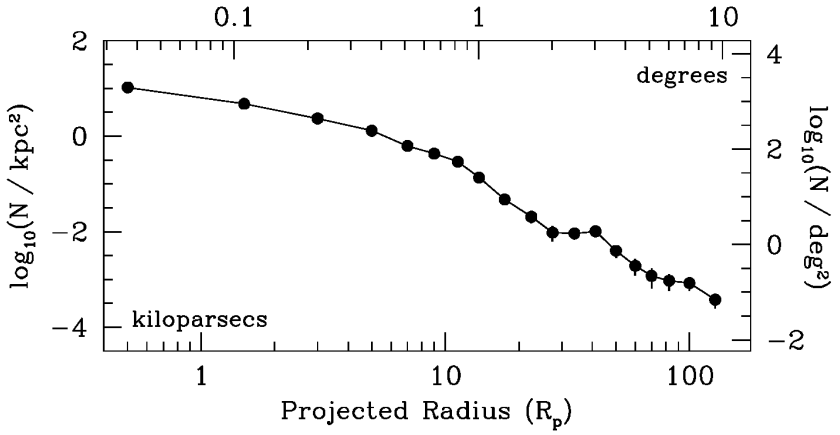

Figure 1.23 *Radial number density profile of the M31 GCs. Notice the characteristic bump at* $\sim$ *30 kpc, after which the GCs are thought to have primarily an accretion origin (Abadi et al., 2006). Figure taken from Mackey et al. (2014, in prep).*

around M33, NGC 147, and NGC 185 (for the latter two, see Chapter 4). Since the PAndAS imaging is superior to most previous wide-field surveys of M31, it is also used to clean the RBC catalogue of contaminants (Huxor et al., 2014).

Henceforth, building on these results, in this thesis I further explore the M31 halo GC system via the study of its kinematic properties. The bulk motions, and the kinematic properties of GC associated with stellar overdensity features are used to constrain the origin of the GC system. I also constrain the total mass of M31, using the halo GCs as dynamical tracers. The attention then turns towards the GC bearing dwarf galaxies NGC 147 and NGC 185, located in the outer halo of M31, as well as towards the isolated Local Group dwarf galaxy NGC 6822. I characterize these systems by performing photometric and spectroscopic analysis of their GC systems, with the goal being to put additional constraints on their properties as well as on the formation of the M31 halo.

Chapter 2

Observations, data reduction and velocity measurements

The contents of this chapter are published in Veljanoski et al. (2014)

2.1 The observed sample

Compared to the Milky Way, M31 has a considerably more extended and populous halo GC population. Of particular interest is the finding that a significant number of the halo clusters in M31 appear to be spatially correlated with underlying stellar substructures. Acquiring spectroscopic data is a major step towards understanding the processes that have governed the formation of the halo GC system of M31, as well as for establishing important properties of M31 itself. For instance, kinematic information derived from spectroscopic data of these outer halo GCs will provide not only information about their bulk motions, but also rule out any random alignments between the GCs and the substructure. GCs may be used as kinematic tracers, thus providing an estimate of the total mass of M31 out to a large radius. In addition, they can also provide strong constraints of the infall trajectories of the progenitor satellites, which is critical when modelling the assembly history of the halo of this galaxy.

This served as the motivation to launch a major spectroscopic follow-up campaign to the PAndAS photometric survey. The data were acquired over the course of eight separate observing runs conducted with three different telescope/instrument combinations: the *ISIS* spectrograph mounted on the 4.2-m *William Herschel Telescope (WHT)*, the *RC* spectrograph mounted on and the 4.0-m *Kitt Peak National Observatory (KPNO)* telescope, and the *GMOS*

Table 2.1 *Observing log showing the instruments used, the observation dates, the program numbers, the observation modes and the number of GCs observed in each run. Note that certain GCs were repeatedly observed in different observing runs.*

Instrument	Date of obs.	Program Number	Obs. mode	No. GCs
WHT/ISIS	29/09-02/10 2005	.	Visitor	19
WHT/ISIS	16/08-18/08 2009	.	Visitor	12
WHT/ISIS	09/09-11/09 2010	.	Visitor	13
KPNO/RC	13/08-17/08 2009	.	Visitor	17
Gemini/GMOS-N	20/07-02/09 2010	GN-2010B-Q-19	Service	4
Gemini/GMOS-N	02/08-05/09 2011	GN-2011B-Q-61	Service	11
Gemini/GMOS-N	29/07-13/09 2012	GN-2012B-Q-77	Service	7
Gemini/GMOS-N	02/08-31/08 2013	GN-2013B-Q-66	Service	7

instrument installed on the 8-m *Gemini-North* telescope. The targets were selected from the catalogue of outer halo M31 GCs comprised mainly of objects discovered in the PAndAS survey (Huxor et al., 2014), but also including clusters found in previous efforts (Martin et al., 2006; Huxor et al., 2008), as well as a few additional objects listed in the RBC. In total, the list of possible targets contains 83 GCs situated at projected radial distances ($R_{\rm proj}$) larger than 30 kpc, plus many at smaller radii. Table 2.1 shows the observation log for all eight observing runs. Altogether 90 GC observations were made which lead to the acquisition of spectra for 78 unique clusters, of which 63 had no previous spectroscopic information. Repeated observations of some GC were made primarily to facilitate consistency checks but also to supplement lower quality data in a few instances.

Throughout the campaign, priority was given to clusters lying on top of stellar substructures, and to those having larger $R_{\rm proj}$. The final observed sample consists of GC with $R_{\rm proj}$ between 18 and 141 kpc. Most, however, lie beyond 30 kpc in projection from the M31 centre – a region which throughout the remainder of this thesis will be refer to as the "outer halo". As discussed in Section 1.4.2 and shown in Figure 1.23, this radius corresponds to the clear break in the GC radial number density profile observed by (Huxor et al., 2011, see also Mackey et al. 2014 in prep). In total, spectra were acquired for 71 clusters with $R_{\rm proj} > 30$ kpc, corresponding to 85.5% of the known GCs in the M31 outer halo. Of these, 20 are located beyond 80 kpc including 10 beyond 100 kpc in projection. Figure 2.1 shows a PAndAS map on which the observed GCs are marked, while Figure 2.2 shows the radial completeness of the observed sample.

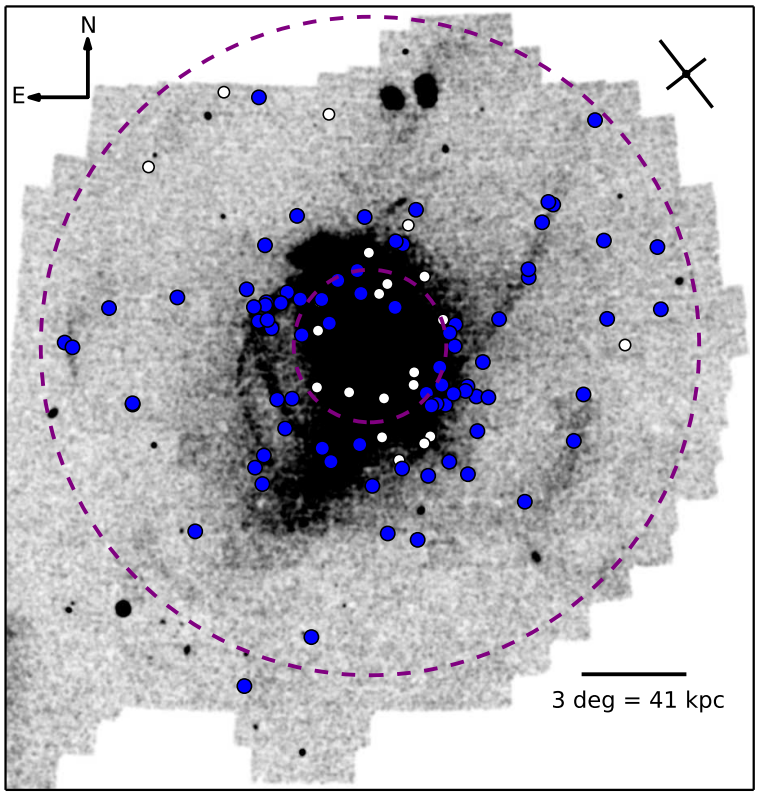

Figure 2.1 *The PAndAS map as in Figure 1.21. The blue points, represent the GCs for which spectroscopic data were obtained.*

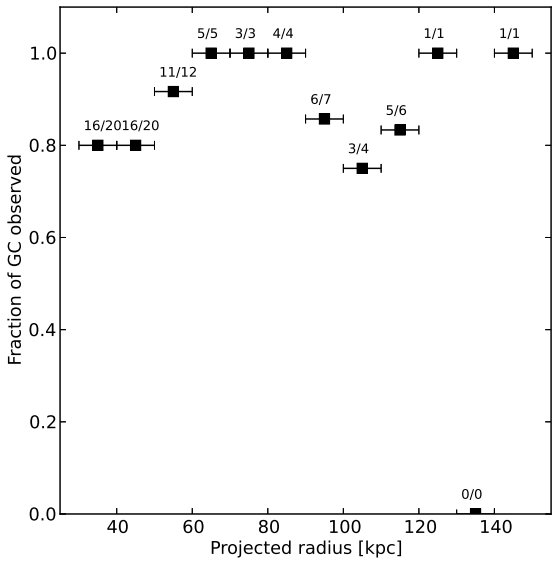

Figure 2.2 *The fraction of GCs between 25 and 145 kpc that has been spectroscopically observed as a function of R_{proj}. The bins are 10 kpc wide. In total the observed sample represents 85.5% of the known GCs lying beyond 30 kpc in projection.*

2.2 The Data reduction

2.2.1 *WHT* and *KPNO* data

Data description

The *ISIS* instrument mounted on the 4.2-m *WHT* was used for three observing runs, performing longslit spectroscopic observations of 41 different GCs in my sample. *ISIS* has two detectors ("arms"), that independently sample two separate wavelength ranges, a blue and a red one. In all runs, the slit width was set to be between 1.5 - 2 arcsec. For the blue arm the EE12 detector together with the R600B grating were used to cover the wavelength range between $\sim$ 3500 and 5000 Å, with a dispersion of 0.45 Å pixel^{-1}. The resolving power was R $\sim$ 1500. For the red arm, the RED-PLUS camera along with the R600R grating were used to cover the wavelength range between $\sim$ 7500 - 9200 Å achieving a dispersion of 0.49 Å pixel^{-1}. The resolving power in this case was R $\sim$ 2700. The only exception to this set up was for the observing run conducted in 2005, when only the blue arm of *ISIS* was used. Each GC was observed as a series of short exposures, with the total integration time varying between 600 and 7200 s depending on the cluster brightness. The data were unbinned in both the spatial and wavelength direction. The typical S/N of the spectra is $\sim$ 7 - 20 per Å, while reaching $\sim$ 70 per Å for the brightest targets.

For the lone observing run conducted with the *KPNO* telescope in 2009, the *RC* spectrograph was employed in single slit mode to obtain spectra of 17 GCs. During these observations the slit width was set to 2 arcsec. The T2KB detector was used, along with the KPC007 grating selecting the wavelength range between $\sim$ 3500 - 6500 Å with a dispersion of 0.139 Å pixel^{-1} and resolving power of R $\sim$ 1300. A similar observing strategy to that used for the *WHT* observations was also adopted here. Each target cluster was observed with multiple exposures, and the total exposure time ranged between 600 and 6400 s, depending on the brightness of the target GCs. There was no binning in the data in either the wavelength or the spatial dimension. The typical S/N of the spectra is 25-60 per Å.

Data reduction and calibration

I reduced the data obtained with the *WHT* and *KPNO* telescopes using standard IRAF[1] procedures. For the basic reduction of the spectra (bias and overscan subtraction, flat-fielding, illumination correction), I employed dedicated standard tasks, which are part of the CCDRED package. I used the *apall* task in the KPNOSLIT package to extract one-dimensional spectra from two-dimensional frames. The extraction apertures had radii between 2-2.5 arcsec. With the same task I was able to interactively select the appropriate background sky regions and to find the trace. The sky was fit with a 2nd order Chebyshev polynomial and subtracted. The spectra were traced using a 3rd order cubic spline function, and were extracted using the optimal variance weighting option in *apall*. A significant advantage of *apall* is that it produces an error spectrum based on the Poisson noise of the spectrum that is being extracted.

The wavelength calibration was based on Cu-Ne-Ar and He-Ne-Ar lamps for *WHT* and *KPNO* spectra respectively. Comparison "arcs" were obtained before and after each program target exposure. I extracted the arc spectra using the same *apall* parameters as the target GCs they were obtained to calibrate. Following this, I used the *identify* task to identify ~ 50 *RC*, ~ 90 *ISIS* blue and ~ 25 *ISIS* red lines in the arc spectra, and fit the dispersion solution with a 3rd order cubic spline function. The root-mean-square residuals of the fits were 0.08 ± 0.01 Å 0.05 ± 0.01 Å and 0.02 ± 0.01 Å for the data obtained with the *RC*, *ISIS* blue arm and *ISIS* red arm instruments respectively. Since two wavelength solutions were found for each target from the 'before' and 'after' arcs, they were averaged and assigned to the appropriate GC spectrum via the *dispcor* task. To check whether the wavelength calibration is reliable, I measured the positions of sky emission lines in separately extracted sky spectra. I found that the wavelength calibration is accurate to 0.08 Å with no systematic shifts for all data observed with the 4-m class telescopes.

Given that each GC observation consisted of a number of separate exposures, I stacked them in the following manner. First, all exposures are interpolated onto a common wavelength scale, and then combined together as described by

[1] IRAF is distributed by the National Optical Astronomy Observatories, which are operated by the Association of Universities for Research in Astronomy, Inc., under cooperative agreement with the National Science Foundation.

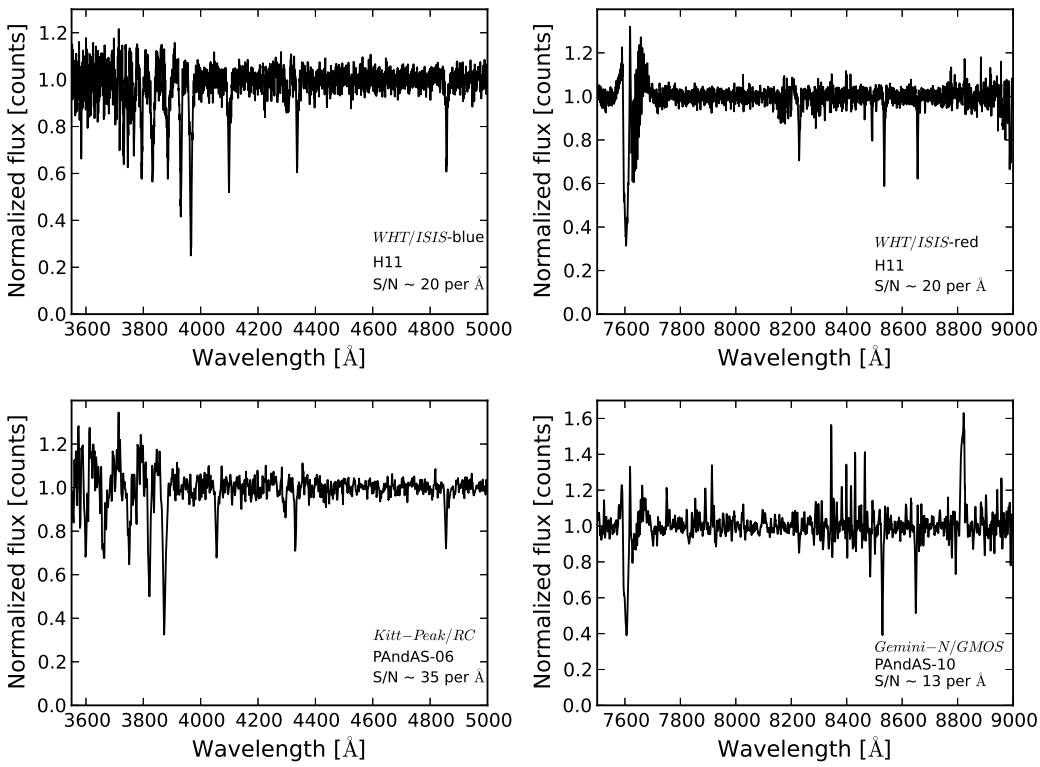

Figure 2.3 *Typical continuum normalised spectra obtained with each of the employed instruments. The spectra are shown as observed and they are not shifted to the heliocentric frame. Note that the sky subtraction residuals in the* GMOS *spectra are larger in a relative sense due to the faintness of those targets.*

Equation 2.1:

$$S_i = \frac{\sum_j \frac{S_{i,j}}{\eta_{i,j}^2}}{\sum_j \frac{1}{\eta_{i,j}^2}} \tag{2.1}$$

where S represents a spectrum, while η is the corresponding error spectrum. The index i corresponds to a particular pixel in an exposure j. Finally, the resulting spectra were continuum subtracted for the purpose of measuring radial velocities. Several examples of the fully reduced spectra are shown in Figure 2.3. The displayed spectra are continuum normalized rather than continuum subtracted in order to preserve the relative strengths of the absorption features for better visualization. At short wavelengths between $\sim$ 3600 and $\sim$ 3800 Å the continuum is not always well determined due to very low numbers of photon counts, and this region is avoided in the subsequent velocity determination process in order to avoid any additional uncertainties.

2.2.2 *Gemini* Data

Data description

To observe the fainter, as well as the more extended and diffuse GCs in the M31 halo, which typically have lower surface brightness compared to a classical compact globular cluster, the *GMOS* instrument mounted on the *Gemini-North* telescope was used. Spectra were taken for 29 objects over the course of four separate observing runs executed in service mode between 2010 and 2013. The observations were conducted using a longslit mask with a slit width of 0.75 arcsec. The grating of choice was R831, which was used to select the wavelength range between $\sim$ 7450 and 9500 Å. To account for the gaps between the chips of the GMOS detector, two or three sets of three exposures were taken with slightly different grating angles, effectively slightly moving the central wavelengths. For each science exposure in each set, the telescope was dithered by $\pm$15 arcsec along the spatial direction of the slit. This strategy helped to minimise any effects coming from the imperfections in the detector, as well as any systematic effects due to the background sky subtraction. The typical total integration time was $\sim$ 5700 s. The data were binned by a factor of two in the wavelength direction obtaining a resolution of 0.68 Å pixel^{-1}. This was also repeated in the spatial direction as well, achieving a spatial resolution of $\sim$ 0.147 arcsec pixel^{-1}. The resolving power achieved with this setup was R $\sim$ 4000. The average S/N of these data is $\sim$ 15 per Å.

Data reduction and calibration

I reduced the data obtained with the Gemini-North telescope using IRAF, but employing tasks from the dedicated GEMINI/GMOS package. I carried out the reduction separately for data sets observed with different central wavelengths. First of all, I created a master bias frame with the *gbias* task from $>$ 30 raw bias frames acquired near the times of the program observations. The standard overscan and bias subtraction, flat-fielding and mosaicking of the three chips of the detector into a single frame was done with the *gsreduce* task.

Unlike the data taken with the 4-m class telescopes, here I calibrated the two-dimensional frames before one-dimensional spectra were extracted. This was done in order to remove the geometrical distortions due to the slit not being exactly parallel to the optical array. Such distortions, like tilts or bends in the spatial axis, are more common for larger telescopes and were not present in

the 4-m data. The wavelength calibration is based on Cu-Ar arcs, and such frames were taken before and after each set of program target exposures, with the central wavelength of the arcs matching the central wavelength of the observed GCs in a specific set. I employed the *wavelength* task to identify ~ 16 emission lines in the arc spectra and to fit a dispersion solution using a fourth order Chebyshev polynomial. The root-mean-square of the fits was ~ 0.02 Å. Following this I assigned the appropriate wavelength solution to each GCs frame via the *gstransform* task.

I extracted one-dimensional spectra with the standard *apall* package within IRAF. As the *Gemini* observations primarily targeted faint and diffuse clusters, I often needed to use multiple apertures to extract the light coming from individual bright stars within the cluster. The typical effective aperture radii ranged from 0.7 to 2.5 arcsec. The internal velocity dispersion of extended and low luminosity clusters is smaller than the measured radial velocity uncertainty of each star in such a cluster, which makes this approach appropriate. The *apall* task was once again used to carefully subtract the background sky, and to find the trace in a similar way as for the 4-m data. The extraction was done with the variance weighting option turned on. Finally, I stacked all exposures for a given GC observation in the same manner as for the 4-m telescope data. If multiple extraction apertures were used, they were also stacked together following the prescription in Equation 2.1, producing a final one-dimensional science spectrum. The science spectra were then continuum subtracted as required for better radial velocity measurements. An example of a representative, fully reduced spectrum is shown in Figure 2.3.

2.3 Radial velocity measurements

For the purpose of determining the radial velocities of the GCs, multiple observations of 6 different radial velocity standard stars were also conducted throughout the spectroscopic campaign. The standard stars were chosen to have stable and accurately known radial velocities, to be of certain spectral type so that their spectra would be similar to the GC spectra, and to be sufficiently bright so that a high S/N spectrum could be obtained with a very short exposure. In addition, I also used two luminous M31 GCs, G1 and MGC1, as radial velocity templates. These GC have high precision radial velocity obtained from high resolution spectra (Galleti et al., 2004; Alves-Brito et al., 2009), and possess metallicities spanning the expected range for outer halo GCs $-2.3 \lesssim [\mathrm{Fe/H}] \lesssim -1.0$. These properties allow for high

S/N spectra to be observed with relatively short integration times. Table 2.2 displays the relevant data regarding the radial velocity standard stars and template GCs.

I derived heliocentric radial velocities via a customized routine that performed χ^2 minimisation between a target and a template spectrum. First, the template is adjusted to the wavelength scale of the target spectrum. The template spectrum is then Doppler shifted by an input velocity, which is systematically varied between -1000 and 500 km s^{-1}, in increments of 1 km s^{-1} in the heliocentric frame. The chosen velocity search range is large enough to comfortably encompass the expected velocities of all GCs that belong to the M31 system. The χ^2 match between the target and template spectra is then calculated via:

$$\chi^2 = \sum_i \frac{(d_i - kM(\triangle v, \sigma)_i)^2}{\eta_i^2 + \delta_i^2} \tag{2.2}$$

where i is the pixel index, d is the spectrum of the target GC ('the data' in the statistical sense), and M is the template spectrum ('the model' against which the data are tested). The uncertainties in the target and template spectra are η and δ respectively. The model M is a function of two free parameters. The first is the input velocity $\triangle v$. The second parameter, σ, is due to the different widths of the absorption lines in the target cluster and the template star spectrum, caused by the internal velocity dispersion of the stars that comprise a certain GC. However, as the resolution of the spectrographs is not sufficient to probe the internal velocity dispersions of the GCs, this parameter can be safely ignored. The parameter k accounts for the flux difference between the target and the template spectra. It is not independent, and can be calculated via:

$$k = \frac{\sum_i \frac{d_i M_i}{\eta_i^2 + \delta_i^2}}{\sum_i \frac{M_i^2}{\eta_i^2 + \delta_i^2}} \tag{2.3}$$

where the symbols are as in Equation 2.2. The input velocity corresponding to the minimum of the χ^2 function is the measured velocity of the GC. In order to remove the large telluric features, any regions of higher sky subtraction residuals, and the edges of the spectra were the S/N is low, I selected certain wavelength ranges over which the χ^2 function is calculated. For the data observed with the *GMOS-N* and the red arm of *ISIS*, the χ^2 window selects

Table 2.2 *Information regarding the radial velocity standard stars and globular clusters used. (1) Star/Cluster ID, (2) Right Ascension, (3) Declination, (4) Spectral type of the stars, (5) Heliocentric radial velocity, (6) number of exposures, (7) Instrument used, (8) Year of observation and (9) Source of the heliocentric radial velocity.*

ID	RA (J2000) [h:m:s]	DEC (J2000) [d:m:s]	Spec. Type	V_{helio} [km s^{-1}]	# Exp.	Instrument	Year	Reference
HD 4388	+00:46:27.0	+30:57:05.6	K3III	-27.5 $\pm$ 0.3	4	*KPNO/RC*	2009	Udry et al. (1999)
					1	*WHT/ISIS*	2009	
					3	*WHT/ISIS*	2010	
HD 12029	+01:58:41.9	+29:22:47.7	K2III	38.5 $\pm$ 0.3	4	*KPNO/RC*	2009	Udry et al. (1999)
HD 145001	+16:08:04.5	+17:02:49.1	G8III	-10.3 $\pm$ 0.3	4	*KPNO/RC*	2009	Udry et al. (1999)
HD 149803	+16:35:54.3	+29:44:43.3	F7V	-7.5 $\pm$ 0.7	1	*KPNO/RC*	2009	Udry et al. (1999)
HD 154417	+17:05:16.8	+00:42:09.2	F9V	-18.6 $\pm$ 0.3	7	*KPNO/RC*	2009	Udry et al. (1999)
					5	*WHT/ISIS*	2009	
					5	*WHT/ISIS*	2010	
HD 171391	+18:35:02.4	-10:58:37.9	G8III	7.4 $\pm$ 0.2	5	*KPNO/RC*	2009	Udry et al. (1999)
G1	+00:32:46.8	+39:34:42.6		-332 $\pm$ 3	1	*KPNO/RC*	2009	Galleti et al. (2004)
					2	*WHT/ISIS*	2005	
					4	*WHT/ISIS*	2009	
					3	*WHT/ISIS*	2010	
					9	*Gemini/GMOS-N*	2010	
MGC1	+00:50:42.4	+32:54:58.7		-355 $\pm$ 2	2	*WHT/ISIS*	2009	Alves-Brito et al. (2009)
					3	*WHT/ISIS*	2010	
					9	*Gemini/GMOS-N*	2011	

just the region around the Ca II triplet (CaT) lines with a range of $8400 - 8750$ Å. For the blue arm of *ISIS* the χ^2 window was in the range of $3900 - 4900$ Å, and for the data observed with the *KPNO* the corresponding χ^2 window was $3831 - 6000$ Å.

This technique is an improvement over the standard cross correlation method because it uses the uncertainties of both the template and target spectra. This can be very useful as it helps to eliminate spurious peaks in the in the χ^2 function that might arise due to imperfectly subtracted skylines, which are especially strong for the faint GC around the CaT.

For GCs observed in a single observing run, the final radial velocity and its corresponding uncertainty are given by the mean and standard deviation of all the individually obtained velocities resulting from the χ^2 minimisation between the spectrum of that cluster and all available template spectra, respectively. The averaging is not error weighted since all templates yield the same uncertainty. Regarding the GCs which were observed with the *WHT* in 2009 and 2010, two independent radial velocities were measured from the blue and red arms of *ISIS*. It is important to note that these measurements are consistent with each other, and there is no systematic offset between them. A comparison between these two independent sets of measurements is shown in Figure 2.4. The mean offset from the ideal 1:1 line is 1.0 km s^{-1}, while the root-mean-square is 18 km s^{-1} Because of the excellent consistency, final velocity values for objects in the 2009 and 2010 *WHT* runs, I simply computed the the error weighted average of the blue and red arm measurements.

There are 7 clusters that were repeatedly observed in different observing runs. For the radial velocity of these objects I adopt the error weighted mean of the velocities measured in each run individually, including the measurements with the two *ISIS* arms if available.

A total of 15 objects in my sample have known radial velocities in the literature, listed in Table 2.3. Figure 2.5 shows the heliocentric radial velocities measured in my work versus measurements from the RBC and Mackey et al. (2013). Excluding the two most deviant points from Federici et al. (1993), I find an excellent agreement between the velocities derived in this study and those present in the literature. This is represented by the linear fit, which has the form $Y = 1.01(\pm 0.05) \times X + 2(\pm 16)$, and is plotted as a dotted line in Figure 2.5. The 13 points used to make the fit have an RMS scatter of 15 km s^{-1} around the ideal 1:1 relation, which for comparison is plotted as a solid line in Figure 2.5. This figure also shows that there are no offsets between my radial

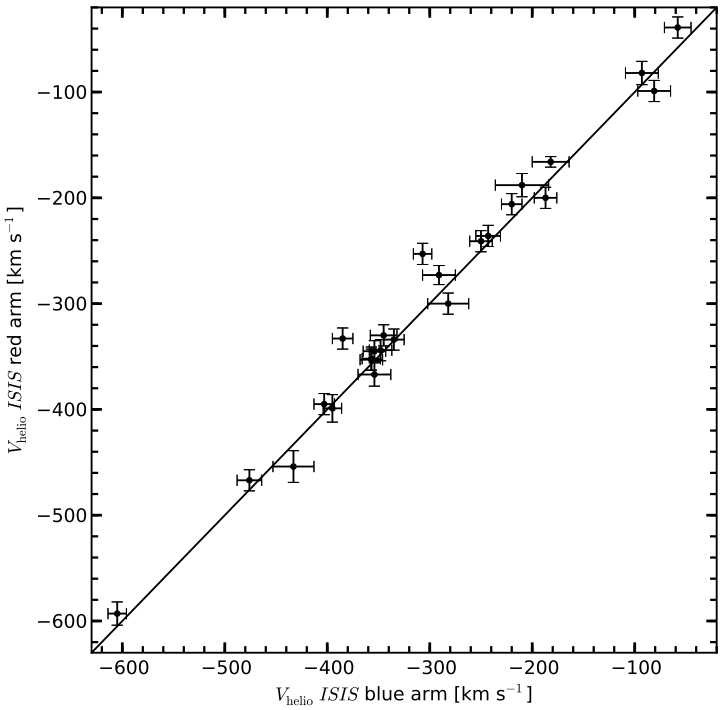

Figure 2.4 *Comparison between the radial velocities determined via the red and blue arms of the* ISIS *spectrograph. The solid black line represents the 1:1 relation. It is seen that there is good agreement without any systematic offsets between the two independent sets of measurements.*

velocity measurements and those collated in the RBC.

To assess the reliability and the robustness of my χ^2 minimisation method, I also derived the radial velocities for the GCs in my data sample with the standard cross correlation method (Tonry & Davis, 1979). I find an excellent agreement between the two techniques, with the χ^2 approach producing marginally lower uncertainties in the GC velocity measurements. The comparison between these two techniques is presented in Appendix A.

2.3.1 Corrections for perspective

Because my GC data sample is spread over a large area of sky spanning $\sim$ 20 deg, I converted the radial velocity measurements from the heliocentric to the Galactocentric frame in order to remove any effects the solar motion could have on the kinematic analysis. The conversion was computed via the relation found in Courteau & van den Bergh (1999), with updated values of the solar

Table 2.3 *Literature heliocentric radial velocities for the 15 GCs in my sample that where previously observed as part of other studies.*

ID	alternative ID	$V_{\rm helio}$ [km s^{-1}]	Reference
G1	Mayall-II	-332 ± 3	average, see Galleti et al. (2004)
G2	Mayall-III	-313 ± 17	average, see Galleti et al. (2006)
B514	MCGC4	-458 ± 23	Galleti et al. (2007)
B517	.	-272 ± 54	Galleti et al. (2009)
G339	BA30	33 ± 30	Federici et al. (1993)
EXT8	.	-152 ± 30	Federici et al. (1993)
H1	MCGC1/B520	-219 ± 15	Galleti et al. (2007)
H10	MCGC5	-358 ± 2	Alves-Brito et al. (2009)
H14	MCGC7	-248 ± 24	Caldwell et al. (2011)
H23	MCGC8	-381 ± 15	Galleti et al, in preparation
H24	MCGC9	-147 ± 20	Galleti et al, in preparation
H27	MCGC10	-291 ± 2	Alves-Brito et al. (2009)
MGC1	.	-355 ± 2	Alves-Brito et al. (2009)
PAndAS-07	PA-7	-433 ± 8	Mackey et al. (2013)
PAndAS-08	PA-8	-411 ± 4	Mackey et al. (2013)

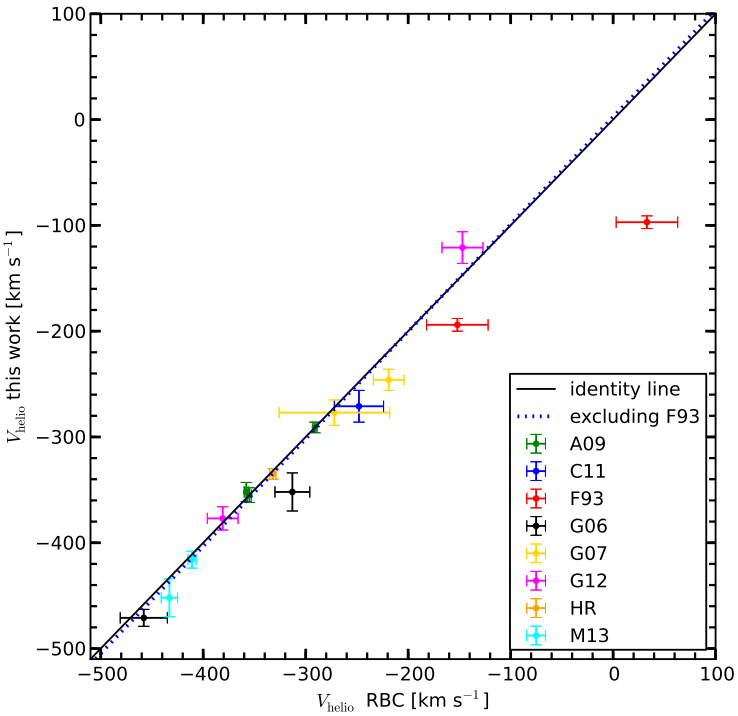

Figure 2.5 *Comparison between the heliocentric radial velocities measured here to those found in the literature. The ideal 1:1 relation is shown by the black solid line. Excluding the two most deviant points from Federici et al. (1993), a near perfect agreement is obtained. The best fit line has the form $Y = 1.01(\pm 0.05) \times X + 2(\pm 16)$. The RMS scatter of the 13 points around the identity line is 15 km s^{-1}. The legend key is: A09 = Alves-Brito et al. (2009); C11 = Caldwell et al. (2011); F93 = Federici et al. (1993); G06 = Galleti et al. (2006); G07 = Galleti et al. (2007); G12 = Galleti et al, in preparation; HR = Peterson (1989) and Dubath & Grillmair (1997); M13 = Mackey et al. (2013).*

motion from McMillan (2011) and Schönrich et al. (2010):

$$v_{\rm gal-raw} = v_{\rm helio} + 251.24\sin(l)\cos(b) + 11.1\cos(l)\cos(b) + 7.25\sin(b) \quad (2.4)$$

where l and b are the Galactic latitude and longitude respectively.

The wide angular span of the GC sample on the sky introduces additional factors that must be considered. As per van der Marel & Guhathakurta (2008), the observed (Galactocentric) line-of-sight velocity for a target that is part of the extended M31 system, but separated from its centre by an angle ρ on the sky, can be decomposed as:

$$V_{\rm gal} = V_{\rm M31,r}\cos(\rho) + V_{\rm M31,t}\sin(\rho)\cos(\phi - \theta_{\rm t}) + V_{\rm pec,los} \quad (2.5)$$

Here, M31 it taken to have a systemic radial velocity (along the line-of-sight to its centre) of $V_{\rm M31,r}$, and a systemic transverse velocity $V_{\rm M31,t}$ in a direction on the sky given by a position angle $\theta_{\rm t}$. The position angle of the target with respect to the centre of M31 is ϕ, while $V_{\rm pec,los}$ is its peculiar line-of-sight velocity.

The first two terms in Eq. 2.5 state that with increasing separation ρ, a decreasing fraction of the systemic M31 radial velocity is observed along the line-of-sight to the target, but an increasing fraction of the transverse motion is carried on this vector. This induces the appearance of a solid body rotation for targets at wide separations from the centre of the system, around an axis sitting 90 deg away from the direction of the transverse velocity on the sky.

One of the main goals of this thesis is the kinematic analysis of the outer halo GC system of M31, which includes testing for possible systemic rotation. It is therefore important to consider whether a correction is needed for the "perspective rotation" described above. The most precise measurement of the M31 transverse velocity to date comes from van der Marel et al. (2012) who found $V_{\rm M31,t} = 17.0$ km s^{-1} with respect to the Milky Way, at a position angle $\theta_{\rm t} \approx 287$ deg east of north. Their 1σ confidence region is $V_{\rm M31,t} \leq 34.3$ km s^{-1}, consistent with M31 being on a completely radial orbit towards our Galaxy. The small transverse velocity of M31 means that the induced perspective rotation for my GC sample is negligible – at most a few km s^{-1} even for the most remote objects (which have $\rho \approx 10$ deg). This is smaller than the typical measurement uncertainties. In principle one could, for completeness, still use

Eq. 2.5 to correct for the rotation. However, the formal uncertainties on the individual components of the van der Marel et al. (2012) transverse velocity, namely the components in the north and west directions on the sky, are ≈ 30 km s^{-1} each. Hence making the correction would introduce significantly larger random uncertainties into the final velocity measurements than ignoring the small induced rotation entirely.

I use Eq. 2.5 with the second term set to zero to obtain the peculiar line-of-sight velocity of each GC in my sample. Thus, I remove the component due to the radial systemic motion of M31 by solving for $V_{\rm pec,los}$. In my thesis, I adopt a heliocentric velocity of -301 ± 1 km s^{-1} for M31 (van der Marel & Guhathakurta, 2008), which corresponds to a Galactocentric radial velocity $V_{\rm M31,r} = -109 \pm 4$ km s^{-1} (see also van der Marel et al., 2012).

One remaining effect to consider is that each of the final corrected velocities lie along a slightly different vector due to the different lines-of-sight to the individual GCs. In principle, the velocities need to be corrected for as if their vectors were parallel. However to make this correction for a given GC requires knowledge of its peculiar proper motion, as a small component of this transverse velocity is carried onto the new vector. In the absence of this information I choose to leave my measurements unaltered. Doing so is not an issue, since for most targets the correction is smaller than the random uncertainties on their measured velocities.

2.4 Summary

Table 2.4 lists the radial velocity measurements for all GCs in my sample. For each object the raw heliocentric velocity $V_{\rm helio}$ is reported, followed by the Galactocentric velocity $V_{\rm gal}$ from Eq. 2.4, and the peculiar line-of-sight velocity in the M31 frame obtained by solving Eq. 2.5 as described towards the end of Section 2.3.1. I hereafter refer to this latter velocity as $\rm V_{M31corr}$. As seen in Table 2.3, some previously observed GCs have more precise radial velocities found in the literature. In those cases, the velocities with smaller accompanying uncertainties are used in the forthcoming analysis.

The results of my measurements are also shown in Figure 2.6, where the observed GCs from this study are overlaid as coloured points on top of the most recent PAndAS metal-poor ([Fe/H] $\lesssim -1.4$) red giant branch stellar density map. The colour of each marked GC corresponds to its measured $\rm V_{M31corr}$.

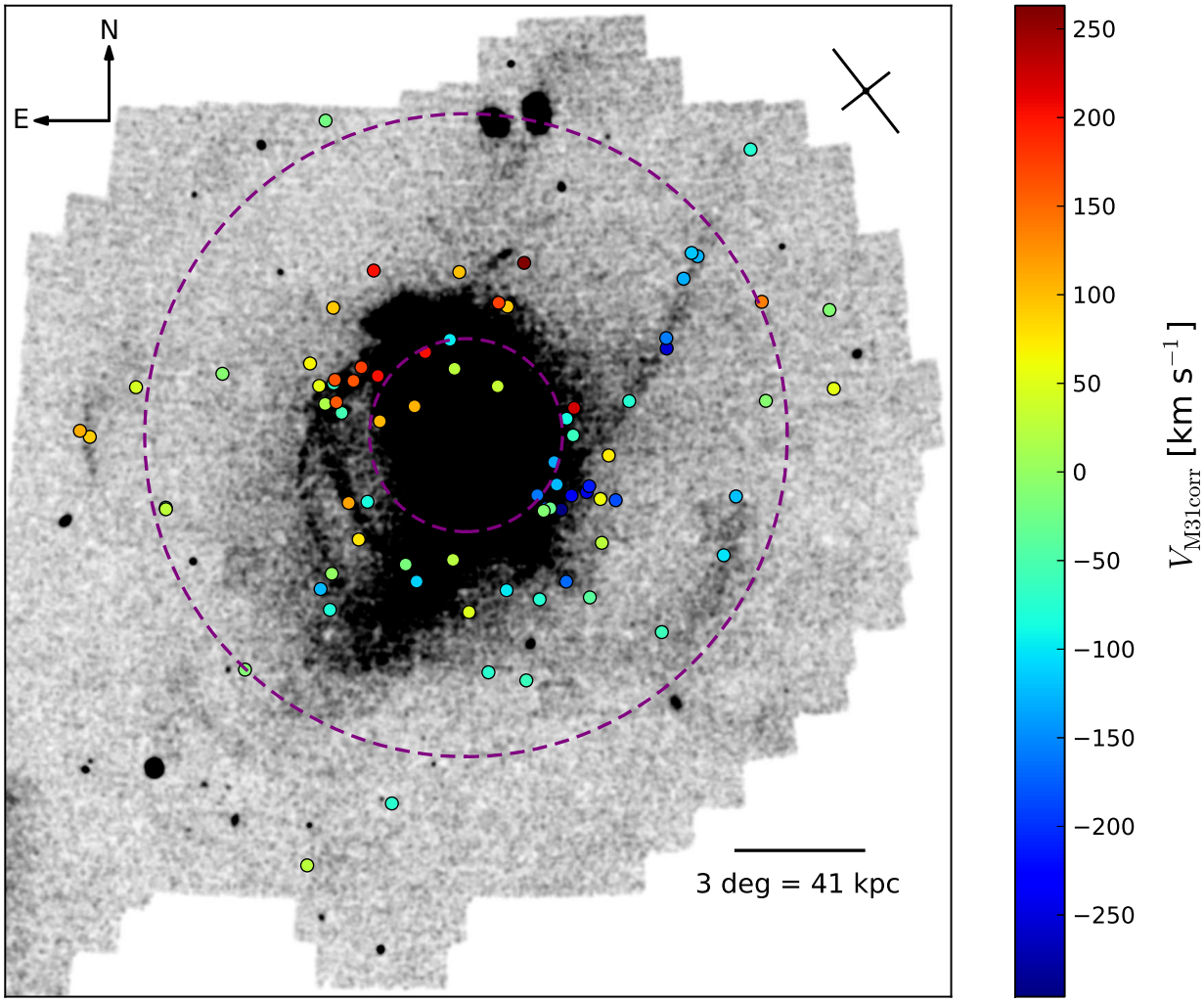

Figure 2.6 *The metal-poor stellar density map of M31 from PAndAS. Positions of the observed GCs are marked with coloured dots which correspond to their Galactocentric radial velocities in units of km s^{-1}. The velocities have been corrected for the systemic motion of M31, which is -109 ± 4 km s^{-1} in the Galactocentric frame. The purple dashed circles correspond to projected radii of 30 and 130 kpc. The small schematic on the top right corner represents the orientation of the major and minor axes of M31.*

Searching through the RBC, I found that there is only one cluster with $R_{\mathrm{proj}} >$ 25 kpc that has not been observed or re-observed throughout my spectroscopic campaign, but which has a known velocity in the literature. To improve statistics, I have added this cluster, dubbed HEC12, or alternatively named MCEC4 in the RBC (Collins et al., 2011), to my data sample and show it also in Figure 2.6. Its relevant data is also listed in Table 2.4.

Table 2.4 *Coordinates, projected radius, position angle, GC type, heliocentric and Galactocentric velocities for the GCs in my sample. Clusters for which more precise radial velocity measurements exist in the literature are marked: (1) in the RBC; (2) in Mackey et al. (2013); (⋆) object not observed in any of the runs.*

Cluster ID	RA (J2000) [hh:mm:ss]	DEC (J2000) [dd:mm:ss]	$R_{\rm proj}$ [kpc]	PA [deg]	GC type	$V_{\rm helio}$ [km s^{-1}]	$V_{\rm Gal}$ [km s^{-1}]	$V_{\rm M31corr}$ [km s^{-1}]	Prominent substructure
B514	00:31:09.8	+37:54:00	55	214	GC	-471 ± 8	-279 ± 8	-169 ± 8	.
B517	00:59:59.9	+41:54:06	45	78	GC	-277 ± 13	-93 ± 13	16 ± 13	Stream C/D (overlap)
EXT8	00:53:14.5	+41:33:24	27	81	GC	-194 ± 6	-7 ± 7	102 ± 7	.
G001[1]	00:32:46.5	+39:34:40	35	229	GC	-335 ± 5	-141 ± 6	-31 ± 6	Association 2
G002[1]	00:33:33.7	+39:31:18	34	226	GC	-352 ± 19	-158 ± 19	-49 ± 19	Association 2
G268	00:44:10.0	+42:46:57	21	10	GC	-277 ± 8	-84 ± 8	25 ± 8	.
G339	00:47:50.2	+43:09:16	29	26	GC	-97 ± 6	95 ± 6	204 ± 6	.
H1	00:26:47.7	+39:44:46	46	245	GC	-245 ± 7	-48 ± 7	61 ± 7	.
H2	00:28:03.2	+40:02:55	42	248	GC	-519 ± 16	-322 ± 16	-212 ± 16	Association 2
H3	00:29:30.1	+41:50:31	35	284	GC	-86 ± 9	113 ± 9	222 ± 9	.
H4	00:29:44.9	+41:13:09	33	270	GC	-368 ± 8	-170 ± 8	-61 ± 8	.
H5	00:30:27.2	+41:36:19	32	279	GC	-392 ± 12	-194 ± 12	-85 ± 12	.
H7	00:31:54.5	+40:06:47	32	242	GC	-426 ± 23	-231 ± 23	-121 ± 23	Association 2
H8	00:34:15.4	+39:52:53	29	230	GC	-463 ± 3	-269 ± 4	-160 ± 4	Association 2
H9	00:34:17.2	+37:30:43	56	204	GC	-374 ± 5	-184 ± 6	-74 ± 6	.
H10[1]	00:35:59.7	+35:41:03	78	194	GC	-352 ± 9	-165 ± 9	-56 ± 9	.
H11	00:37:28.0	+44:11:26	42	342	GC	-213 ± 7	-15 ± 7	93 ± 7	.
H12	00:38:03.8	+37:44:00	50	195	GC	-396 ± 10	-207 ± 10	-978± 10	.
H14	00:38:49.4	+42:22:47	18	327	GC	-271 ± 15	-76 ± 15	33 ± 15	.
H15	00:40:13.2	+35:52:36	74	185	GC	-367 ± 10	-182 ± 10	-73 ± 10	.
H17	00:42:23.6	+37:14:34	55	181	GC	-246 ± 16	-60 ± 16	48 ± 16	.
H18	00:43:36.0	+44:58:59	51	2.4	GC	-206 ± 21	-10 ± 21	99 ± 21	.
H19	00:44:14.8	+38:25:42	39	174	GC	-272 ± 18	-85 ± 18	24 ± 18	.
H22	00:49:44.6	+38:18:37	44	155	GC	-311 ± 6	-127 ± 6	-17 ± 6	.
H23	00:54:24.9	+39:42:55	37	124	GC	-377 ± 11	-193 ± 11	-84 ± 11	Stream D
H24	00:55:43.9	+42:46:15	39	57	GC	-121 ± 15	66 ± 15	175 ± 15	Stream C/D (overlap)
H25	00:59:34.5	+44:05:38	57	46	GC	-204 ± 14	-16 ± 14	93 ± 14	.
H26	00:59:27.4	+37:41:30	66	137	GC	-411 ± 7	-233 ± 7	-124 ± 7	Stream C
H27[1]	01:07:26.3	+35:46:48	100	137	GC	-291 ± 5	-121 ± 6	-12 ± 6	.
HEC1	00:25:33.8	+40:43:38	45	262	EC	-233 ± 9	-34 ± 9	74 ± 9	.
HEC2	00:28:31.5	+37:31:23	63	217	EC	-341 ± 9	-148 ± 9	-39 ± 9	.
HEC6	00:38:35.4	+44:16:51	42	346	EC	-132 ± 12	65 ± 12	174 ± 12	.
HEC10	00:54:36.4	+44:58:44	59	29	EC	-98 ± 5	93 ± 6	202 ± 6	.
HEC11	00:55:17.4	+38:51:01	47	134	EC	-215 ± 5	-33 ± 6	76 ± 6	Stream D
HEC12⋆	00:58:15.4	+38:03:01	60	136	EC	-288 ± 2	-109 ± 4	0 ± 4	Stream C
HEC13	00:58:17.1	+37:13:49	69	142	EC	-366 ± 5	-188 ± 6	-79 ± 6	Stream C
MGC1[1]	00:50:42.4	+32:54:58	116	169	GC	-355 ± 7	-181 ± 7	-73 ± 7	.

Table 2.4 *Continued*

Cluster ID	RA (J2000) [hh:mm:ss]	DEC (J2000) [dd:mm:ss]	$R_{\rm proj}$ [kpc]	PA [deg]	GC type	$V_{\rm helio}$ [km s^{-1}]	$V_{\rm Gal}$ [km s^{-1}]	$V_{\rm M31corr}$ [km s^{-1}]	Prominent substructure
PAndAS-01	23:57:12.0	+43:33:08	119	289	GC	-333 ± 21	-119 ± 21	-11 ± 21	.
PAndAS-02	23:57:55.6	+41:46:49	115	277	EC	-266 ± 4	-54 ± 4	53 ± 4	.
PAndAS-04	00:04:42.9	+47:21:42	125	315	GC	-397 ± 7	-183 ± 7	-75 ± 7	NW stream
PAndAS-05	00:05:24.1	+43:55:35	101	294	EC	-183 ± 7	28 ± 7	136 ± 7	.
PAndAS-06	00:06:11.9	+41:41:20	94	277	GC	-327 ± 15	-119 ± 15	-10 ± 15	.
PAndAS-07[2]	00:10:51.3	+39:35:58	86	257	EC	-452 ± 18	-248 ± 18	-139 ± 18	SW cloud
PAndAS-08[2]	00:12:52.4	+38:17:47	88	245	GC	-416 ± 8	-215 ± 8	-106 ± 8	SW cloud
PAndAS-09	00:12:54.6	+45:05:55	91	308	GC	-444 ± 21	-235 ± 21	-126 ± 21	NW stream
PAndAS-10	00:13:38.6	+45:11:11	90	309	EC	-435 ± 10	-226 ± 10	-117 ± 10	NW stream
PAndAS-11	00:14:55.6	+44:37:16	83	306	GC	-447 ± 13	-239 ± 13	-130 ± 13	NW stream
PAndAS-12	00:17:40.0	+43:18:39	69	296	EC	-472 ± 5	-267 ± 5	-157 ± 5	NW stream
PAndAS-13	00:17:42.7	+43:04:31	68	293	GC	-570 ± 45	-365 ± 45	-256 ± 45	NW stream
PAndAS-14	00:20:33.8	+36:39:34	86	225	EC	-363 ± 9	-167 ± 9	-58 ± 9	SW cloud
PAndAS-15	00:22:44.0	+41:56:14	52	282	GC	-385 ± 6	-183 ± 6	-74 ± 6	NW stream
PAndAS-16	00:24:59.9	+39:42:13	51	247	GC	-490 ± 15	-292 ± 15	-183 ± 15	.
PAndAS-17	00:26:52.2	+38:44:58	54	232	GC	-279 ± 15	-84 ± 15	25 ± 15	.
PAndAS-18	00:28:23.2	+39:55:04	42	245	EC	-551 ± 18	-354 ± 18	-245 ± 18	Association 2
PAndAS-19	00:30:12.2	+39:50:59	38	240	GC	-544 ± 6	-348 ± 6	-239 ± 6	Association 2
PAndAS-21	00:31:27.5	+39:32:21	38	232	GC	-600 ± 7	-405 ± 7	-296 ± 7	Association 2
PAndAS-22	00:32:08.3	+40:37:31	29	253	GC	-437 ± 1	-241 ± 3	-132 ± 3	Association 2
PAndAS-23	00:33:14.1	+39:35:15	34	228	GC	-476 ± 5	-282 ± 6	-172 ± 6	Association 2
PAndAS-27	00:35:13.5	+45:10:37	57	341	GC	-46 ± 8	154 ± 8	262 ± 8	.
PAndAS-36	00:44:45.5	+43:26:34	30	9	GC	-399 ± 7	-205 ± 7	-96 ± 7	.
PAndAS-37	00:48:26.5	+37:55:42	48	161	GC	-404 ± 15	-220 ± 15	-111 ± 15	.
PAndAS-41	00:53:39.5	+42:35:14	33	56	GC	-94 ± 8	94 ± 8	203 ± 8	Stream D
PAndAS-42	00:56:38.0	+39:40:25	42	120	GC	-176 ± 4	7 ± 5	115 ± 5	Stream D
PAndAS-43	00:56:38.8	+42:27:17	39	64	GC	-135 ± 6	52 ± 7	160 ± 7	Stream D
PAndAS-44	00:57:55.8	+41:42:57	39	80	GC	-349 ± 11	-164 ± 11	-54 ± 11	Stream D
PAndAS-45	00:58:37.9	+41:57:11	42	76	GC	-135 ± 16	50 ± 16	159 ± 16	Stream D
PAndAS-46	00:58:56.3	+42:27:38	44	67	GC	-132 ± 16	54 ± 16	162 ± 16	Stream D
PAndAS-47	00:59:04.7	+42:22:35	44	69	GC	-359 ± 16	-174 ± 16	-64 ± 16	Stream D
PAndAS-48	00:59:28.2	+31:29:10	141	160	EC	-250 ± 5	-83 ± 6	25 ± 6	.
PAndAS-49	01:00:50.0	+42:18:13	48	72	EC	-240 ± 7	-55 ± 7	53 ± 7	Stream D
PAndAS-50	01:01:50.6	+48:18:19	107	24	EC	-323 ± 7	-131 ± 7	-22 ± 7	.
PAndAS-51	01:02:06.6	+42:48:06	53	65	GC	-226 ± 5	-41 ± 6	67 ± 6	Stream D
PAndAS-52	01:12:47.0	+42:25:24	78	76	GC	-297 ± 9	-118 ± 9	-9 ± 9	.
PAndAS-53	01:17:58.4	+39:14:53	96	104	GC	-253 ± 10	-82 ± 10	26 ± 10	.
PAndAS-54	01:18:00.1	+39:16:59	96	104	GC	-336 ± 8	-165 ± 8	-56 ± 8	.
PAndAS-56	01:23:03.5	+41:55:11	103	82	GC	-239 ± 8	-66 ± 8	42 ± 8	.
PAndAS-57	01:27:47.5	+40:40:47	116	90	GC	-186 ± 6	-18 ± 7	90 ± 7	Eastern Cloud
PAndAS-58	01:29:02.1	+40:47:08	119	89	GC	-167 ± 10	1 ± 10	109 ± 10	Eastern Cloud
SK255B	00:49:03.0	+41:54:57	18	61	GC	-191 ± 10	-1 ± 10	107 ± 10	.

Chapter 3

Kinematics of the M31 halo globular clusters

The contents of this chapter are published in Veljanoski et al. (2013b) and Veljanoski et al. (2014)

Studying the kinematics of the M31 outer halo GCs is one of the main goals of this thesis. Given the well known rapid rotation exhibited by the GCs located in the inner regions of this galaxy, it is interesting to investigate if any such global motion is present in the halo population as well. Indeed, carefully examining Figure 2.6, one can notice a hint of rotation: the GCs in the north-east region have systematically higher velocities compared to the clusters in the south-west region. Thus, one of my goals in this chapter is to quantify this possible rotation, and determine whether such overall motion, if indeed present, is significant in a statistical sense. In addition, given that the halo GCs span a large area, many of which are remote, I will explore the behaviour of the velocity dispersion as a function of projected radius from the M31 centre. To achieve this, I will construct a kinematic model which will best describe the properties of the M31 outer halo GCs.

3.1 Bayesian inference

Bayesian inference is a powerful statistical tool for estimating a set of parameters Θ in a model $\mathcal{M}$, as well as discriminating between different models. Given some data D and certain prior information I, the mathematical form of

Table 3.1 *The scale devised by Jeffreys (1961) for discriminating between models – in this case evaluating $\mathcal{M}$ over $\mathcal{N}$ – via the Bayes factor.*

$\log B_{\mathcal{MN}}$	$B_{\mathcal{MN}}$	Strength of evidence
< 0	< 1	Negative (supports $\mathcal{N}$)
0 to 0.5	1 to 3.2	Barely worth mentioning
0.5 to 1	3.2 to 10	Positive
1 to 1.5	10 to 32	Strong
1.5 to 2	32 to 100	Very strong
> 2	> 100	Decisive

the Bayes theorem is:

$$p(\Theta|DI) = \frac{p(\Theta|I)p(D|\Theta I)}{p(D|I)} \tag{3.1}$$

where $p(\Theta|DI)$ is the posterior probability distribution function (pdf) of the model parameters, $p(\Theta|I)$ is the prior, and $p(D|\Theta I)$ is the likelihood function. The expression $p(D|I)$, sometimes also labbeled simply as E, is the Bayesian evidence which is the average value of the likelihood weighted by the prior and integrated over the entire parameter space. It is mathematically expressed as:

$$p(D|I) = E = \int p(D|\Theta I)p(\Theta|I)d\Theta \tag{3.2}$$

When more of a model's parameter space has high likelihood values, the evidence is large. However, the evidence is very small for models with large parameter spaces having low likelihood values, even if the likelihood function itself is highly peaked. This Bayesian quantity is key when one wants to discriminate between two different models, $\mathcal{M}$ and $\mathcal{N}$. The typical question that one needs to answer in this case is which model is a better fit to the data. This can be done via the Bayes factor B, which is essentially the ratio between the evidence of the models that are considered, and formally defined as:

$$B_{\mathcal{MN}} = \frac{\int p_{\mathcal{M}}(D|\Theta_{\mathcal{M}} I_{\mathcal{M}})p_{\mathcal{M}}(\Theta_{\mathcal{M}}|I_{\mathcal{M}})d^m\Theta_{\mathcal{M}}}{\int p_{\mathcal{N}}(D|\Theta_{\mathcal{N}} I_{\mathcal{N}})p_{\mathcal{N}}(\Theta_{\mathcal{N}}|I_{\mathcal{N}})d^n\Theta_{\mathcal{M}}} \tag{3.3}$$

Model $\mathcal{M}$ describes the data D better than model $\mathcal{N}$ if $B_{\mathcal{MN}} > 1$. A frequently used interpretation scale is the one set up by Jeffreys (1961), presented in Table 3.1.

The Bayes factor is a powerful tool for model selection, especially since it does not depend on any single set of parameters as the integrations are over the entire parameter space in each model. This allows for significantly different models to be compared. In addition, the Bayesian model comparison

implicitly guards against overfitting (Kass & Raftery, 1995).

3.2 Kinematic models

One of the main goals of this chapter is to constrain the overall kinematic properties of the M31 outer halo GC population. Working in the Bayesian framework provides the ability to discriminate between different kinematic models, while simultaneously deriving probability distribution functions for the free parameters in each model.

I construct two kinematic models, $\mathcal{M}$ and $\mathcal{N}$. The model $\mathcal{M}$ comprises two components: an overall rotation of the M31 outer halo GC system, and the velocity dispersion of the GCs. The $\mathcal{N}$ model contains only the velocity dispersion of the GC population. By considering both rotating and non-rotating models, I can quantify the statistical significance of any detected rotation of the M31 outer halo GCs.

The rotation component in $\mathcal{M}$ is modelled as prescribed in Côté et al. (2001):

$$v_{\rm rot}(\theta) = v_{\rm sys} + A\sin(\theta - \theta_0) \tag{3.4}$$

where $v_{\rm rot}$ is the rotational velocity of the GC system at position angle θ, measured east of north, and θ_0 is the position angle of the rotation axis of the GC system. The rotation amplitude is labelled as A, while the systemic radial motion of the GC system, taken to be the Galactocentric systemic motion of M31 itself, is denoted as $v_{\rm sys}$. As detailed in Côté et al. (2001), this method assumes that the GC system being investigated is spherically distributed, that its intrinsic angular momentum is constant on spherical surfaces, and that the rotation axis is perpendicular to the line of sight – i.e., it lies in the plane of the sky.

The velocity dispersion is assumed to have a Gaussian form and to decrease as a function of projected radius from the M31 centre in a power law manner. The observed dispersion (σ) comprises two components – the intrinsic dispersion of the GC system, and the effect of the measurement uncertainties in the GC radial velocities. This is mathematically described in Equation 3.5, where Δv is the aggregate uncertainty of the Galactocentric velocities, $R_{\rm proj}$ is the projected radius, and γ is the power law index describing how the velocity dispersion

changes as a function of $R_{\rm proj}$:

$$\sigma^2 = (\Delta v)^2 + \sigma_0^2 \left(\frac{R_{\rm proj}}{R_0} \right)^{2\gamma} \tag{3.5}$$

The scale radius R_0 is fixed at 30 kpc, as this is the point at which the M31 halo begins to dominate; σ_0 is the corresponding intrinsic velocity dispersion at $R_{\rm proj} = 30$ kpc.

Joining Equations 3.4 and 3.5 results in the creation of a rotation enabled model $\mathcal{M}$:

$$p_{i,\mathcal{M}}(v_i, \Delta v_i | v_{\rm rot}, \sigma) = \frac{1}{\sqrt{2\pi\sigma^2}} \; e^{-\frac{(v_i - v_{\rm rot})^2}{2\sigma^2}} \tag{3.6}$$

where $v_{\rm rot}$ is the systemic rotation described by Equation 3.4, v_i are the observed Galactocentric radial velocities of the GCs as presented in Table 2.4, and σ is a velocity dispersion case as prescribed by Equation 3.5.

Similarly, the model $\mathcal{N}$ which is a special case of model $\mathcal{M}$, does not contain an overall rotation component is simply constructed as :

$$p_{i,\mathcal{N}}(v_i, \Delta v_i | \sigma) = \frac{1}{\sqrt{2\pi\sigma^2}} \; e^{-\frac{v_i^2}{2\sigma^2}} \tag{3.7}$$

Hence, the likelihood function for each of the above defined kinematic models is:

$$p_{\mathcal{M}}(D|\Theta) = \mathcal{L}_{\mathcal{M}} \left(v, \Delta v, R_{\rm proj}, \theta | A, \theta_0, \sigma_0, \gamma \right) = \prod_i p_{i,\mathcal{M}} \tag{3.8}$$

$$p_{\mathcal{N}}(D|\Theta) = \mathcal{L}_{\mathcal{N}} \left(v, \Delta v, R_{\rm proj} | \sigma_0, \gamma \right) = \prod_i p_{i,\mathcal{N}} \tag{3.9}$$

in which v, Δv, $R_{\rm proj}$, θ are the observed properties of the GCs, and A, θ_0, σ_0, γ are the free parameters of the models I am trying to determine. Here, the index i loops over each individual data point. Any prior information is left out from Equations 3.8 and 3.9 because in all models I assume flat priors. Previous studies (e.g, Lee et al., 2008) have found the velocity dispersion and the overall rotation of the M31 GCs in both the halo and the disc to have the same order of magnitude. Thus, it is important to note that in my proposed model $\mathcal{M}$, I am attempting to describe the overall rotation and velocity dispersion simultaneously rather than separately as has been the case in the majority of past studies. This is done in order to avoid any possible bias that can arise

from measuring these quantities in succession, because in such cases the latter measurement will depend on the first one

As a reminder, the input sample of GCs is defined by the 72 objects in Table 2.4 with $R_{\rm proj} > 30$ kpc. The vast majority of the velocities used are those derived from the observations presented in this thesis, apart from a handful of cases where previous measurements in the literature are more precise. The areal coverage of the input sample is high but non-uniform (see Figure 2.1 and 2.2), and the sample is biased towards GCs that project onto visible substructures in the field halo and lie at larger $R_{\rm proj}$.

It is numerically very challenging to calculate the likelihood function, the evidence and the posterior probability distributions, as described by Equations 3.8, 3.9, 3.2 and 3.1. Various Monte Carlo algorithms (e.g. Lewis & Bridle, 2002; Skilling, 2004; Feroz & Hobson, 2008; Feroz et al., 2009) have been introduced to make the calculation of these quantities more efficient. Even though these methods greatly reduce the computation time, and have been thoroughly tested and widely applied, they do not fully sample the entire parameter space and there is always danger that a secondary peak in a posterior distribution might remain undetected, or that the algorithm might get stuck in a local maximum. Because my models contain a low number of free parameters, I choose to fully sample the parameter space via a brute-force exploration method. In general, this approach is not possible with more contrived models. The likelihood function is systematically calculated for each combination of the free parameters stated in Equations 3.8 and 3.9. In this calculation the amplitude A ranges between 0 and 200 km s^{-1} with a step size of 3 km s^{-1}, θ_0 ranges between 0 and 2π rad with an interval of 0.1 rad, σ_0 ranges between 50 and 600 km s^{-1} with a 5 km s^{-1} increment, and γ ranges between -1.5 and 0.5 with a step size of 0.025. Careful testing has shown that this combination of parameters and sampling gives excellent balance between computational speed and resolution of the likelihood function and the posterior probability distributions. Finally, the integral in Equation 3.2 is evaluated by applying the Simpson rule in multiple dimensions.

3.3 Overall halo kinematics

I use the Bayesian tools described in Section 3.1 to derive posterior probability distribution functions for the free parameters of each kinematic model. Since these distributions are not necessarily Gaussian, or symmetric, I report their

Table 3.2 *Expectation value of the free parameters for each kinematic model, accompanied by the corresponding 68% confidence limits. The Bayesian evidence along with the number of GCs used for the statistics are also displayed.*

Kinematic model	$< A >$ [km s^{-1}]	$< \theta_0 >$ [deg]	$< \sigma_0 >$ [km s^{-1}]	$< \gamma >$	$\log_{10}(E)$	N_{GC}
$\mathcal{M}$	86 ± 17	135 ± 11	136^{+29}_{-20}	-0.45 ± 0.22	-191	72
$\mathcal{N}$			222^{+48}_{-32}	-0.37 ± 0.21	-218	72

expectation values, accompanied with the 68% confidence limits, in Table 3.2. This table also displays the logarithm of the Bayesian evidence for each model, which is used to discriminate between them. I find that the rotating model $\mathcal{M}$ is decisively preferred over the non-rotating one, $\mathcal{N}$, with $\log_{10}(B_{\mathcal{MN}}) \sim 30$.

The posterior probability distribution functions for the free parameters of model $\mathcal{M}$ are shown in Figure 3.1, along with the 68% confidence limits around the respective expectation values. The strong preference for the favoured model $\mathcal{M}$ over the non-rotating model $\mathcal{N}$ can clearly be seen from the upper left panel. As model $\mathcal{N}$ is just a special case of model $\mathcal{M}$, it is reassuring that the upper left panel of Figure 3.1 shows the probability of measuring a rotation amplitude of zero is entirely excluded.

The position angle of the M31 optical minor axis is 128 deg measured East of North, closely matching the inferred rotation axis of the M31 outer halo GC system. In addition, the rotation of the M31 outer halo globulars is in the same direction as their inner region counterparts albeit with a smaller amplitude. This is best seen in Figure 3.2, which shows the Galactocentric radial velocities of the GCs in my sample, corrected for the systemic motion of M31, versus their projected radii along the major (top panel) and minor axis (bottom panel). The top panel of Figure 3.2 clearly shows that the rotation is observed even for the GCs with the largest projected distances, and is not driven either by clusters projected onto major halo substructures or clusters not lying on any visible substructure.

When modelling the rotation of the outer halo GC population, I assumed that the rotation axis lies in the plane of the sky – i.e., perpendicular to the line of sight. Thus, so far I have determined the *projected* rotation amplitude, and there is an additional unknown factor $\sin i$ to account for, where i is the inclination angle of the rotation axis to the plane of the sky. Since the rotation axis of the M31 outer halo GC population coincides with the minor optical axis of this galaxy, it is reasonable to assume that the rotation axis lies perpendicular to the disc of M31. In this case, taking the inclination of M31 with respect to the line of sight to be 77.5 deg (Ferguson et al., 2002), the mean of the deprojected

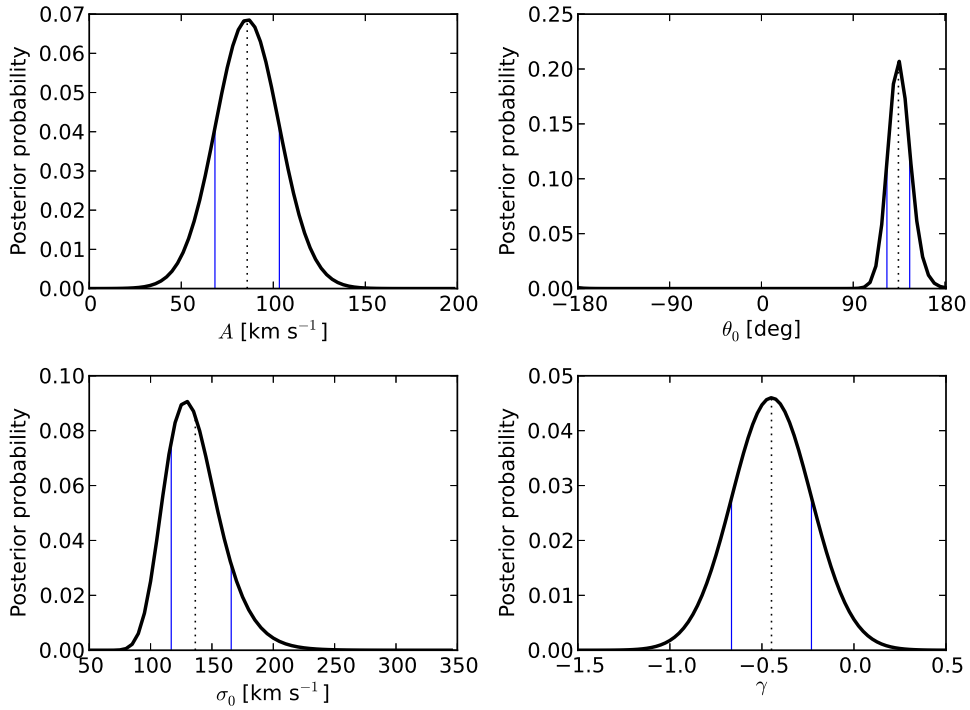

Figure 3.1 *Marginalized posterior probability distribution functions for A, θ_0, σ_0, and γ for model $\mathcal{M}$, which best represents the observed data. The vertical dotted line represent the expectation value for the respective distribution, while the accompanying vertical solid blue lines mark the 68% confidence limits around it.*

rotation amplitude posterior probability distribution function would be 88 ± 17 km s^{-1}, which is barely different from the projected values.

I also find substantial evidence for decreasing velocity dispersion with increasing $R_{\rm proj}$. Looking at the bottom right panel of Figure 3.1, it is seen that the expectation value of the γ posterior probability distribution function is inconsistent with $\gamma = 0$. In fact, the posterior probability to measure $\gamma = 0$ is less than 1%. This is shown in more detail in Figure 3.3, which shows the 1, 2 and 3-σ levels of the likelihood in γ-σ_0 space. It can easily be seen that a constant velocity dispersion as a function of $R_{\rm proj}$ can be discarded at approximately a 2-σ level.

Figure 3.4 shows the Galactocentric radial velocities of the outer halo GCs, corrected for both their bulk rotation as per model $\mathcal{M}$ as well as for the systemic motion of M31, as a function of their projected radii. Different groups of GCs that lie along specific stellar streams are marked (see Section 3.4). The GC halo dispersion profile is plotted with a solid line as described by Equation 3.5 using the best fit parameters from Table 3.2. The stellar velocity dispersion profile determined by Chapman et al. (2006) is also displayed. The fit is for metal-poor giant stars in the range between $\sim$ 10 and 70 kpc in

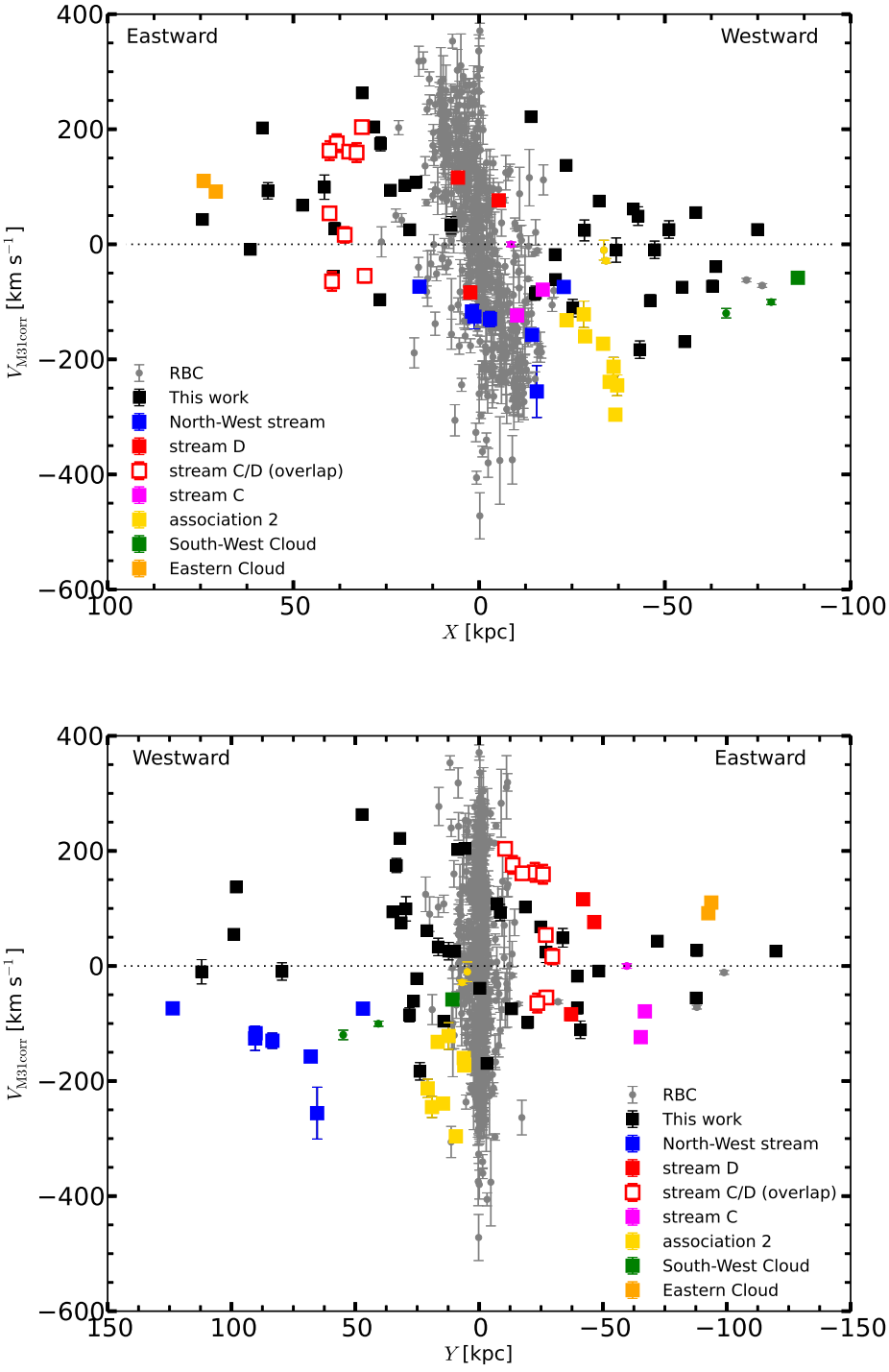

Figure 3.2 *Galactocentric velocities, corrected for the systemic motion of M31, versus projected distance along the major (top panel) and minor optical axis of M31 (bottom panel). The colours mark GCs that lie on specific stellar debris features, further discussed in Section 3.4. The top panel clearly displays the rotation of the outer halo GCs, which is found to be in the same sense as for their inner region counterparts, but with a smaller amplitude. Notice that the rotation is observed even for the most distant GCs in projection in my sample. Since there is no clear pattern observed in the bottom panel, this is a good indication that the minor axis is consistent with being the rotation axis of GCs located in both the inner regions and the outer halo of M31.*

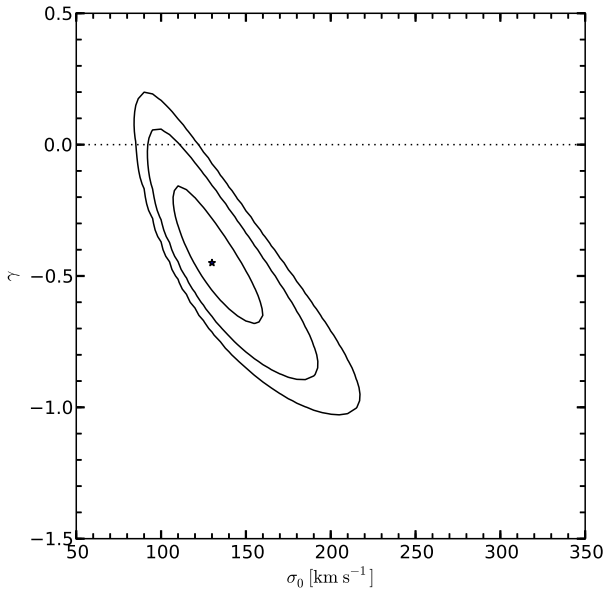

Figure 3.3 *Likelihood contours corresponding to the 1, 2 and 3-σ intervals in the γ-σ_0 plane. The expectation value is marked with the star. The posterior probability of measuring $\gamma = 0$, $p(\gamma = 0) < 1\%$. Thus, a constant velocity dispersion as a function of $R_{\rm proj}$ can be almost entirely rejected.*

projection, with the majority of the data points lying between ~ 10 and 50 kpc. The stellar velocity dispersion profile was modelled to be linear in shape, and beyond 70 kpc the fit is extrapolated. Figure 3.4 shows a close similarity between the velocity dispersions of the M31 halo stars and GCs, despite being fit by different models, at least out to $\sim$80 kpc in projection. This similarity might hint that the spatial density profiles of the M31 halo stars and GCs may be similar. Huxor et al. (2011) has indeed shown this to be the case by comparing the radial number density profile of the M31 GCs to that of the metal-poor ($-3.0 < [\mathrm{Fe/H}] < -0.7$) stars (see their Figure 9).

3.4 Globular cluster groups on streams

The M31 halo is rich with various field substructures in the form of stellar streams, loops and filaments. Many remote GCs appear spatially correlated with prominent features that are visible in the stellar maps (Mackey et al., 2010b), including a significant number of clusters in my spectroscopic sample. Careful examination of Figure 2.6 reveals that such objects tend to exhibit clear velocity correlations. It might naively be expected that coherent velocity patterns amongst GC groups would be quite unlikely to arise in the case where the GCs are essentially randomly distributed members of a pressure-

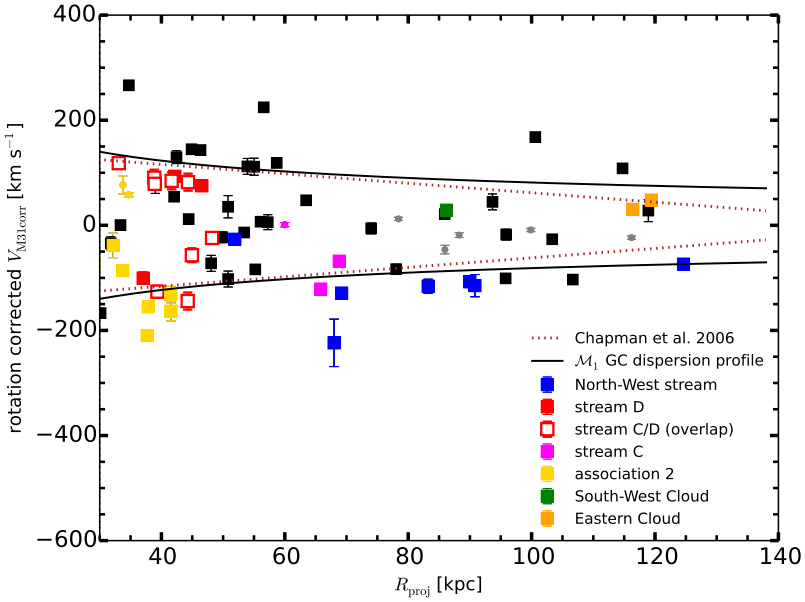

Figure 3.4 *Galactocentric radial velocities for my GC sample, corrected for the measured rotation and the systemic motion of M31, versus projected radius from the M31 centre. The different coloured symbols mark groups of GCs projected on various stellar streams as indicated. The solid line corresponds to the most-likely velocity dispersion profile for the outer halo GCs. The dotted line describes the velocity dispersion of kinematically selected metal-poor giant stars as measured by Chapman et al. (2006). Note that in the latter case, the fit beyond 70 kpc is a linear extrapolation.*

supported halo, even if a substantial rotation component is also present, but would be unsurprising in the case where these clusters are associated with underlying kinematically cold stellar debris features. In this section I consider a number of GC groups that appear projected on top of stellar streams and overdensities, as marked on Figure 3.5, and attempt to quantitatively assess the probability of the various observed velocity trends or correlations arising randomly.

I proceed by constructing simple Monte Carlo experiments similar to the one devised by Mackey et al. (2013). Although these tests are tailored to each specific instance, they all share a common basis. Using the most likely global kinematic model M derived earlier in this chapter, I know what halo velocity dispersion and rotation amplitude to expect at each GC position. For the N GCs in a given group, I first subtract the global rotation signal from the observed velocities, which have already been corrected for the M31 systemic motion, and then generate 10^6 sets of N GCs with positions matching those of the real set, but with each individual velocity randomly drawn from a Gaussian distribution centred on zero and with a width set by the dispersion model described by Equation 3.5 at the appropriate projected radius. This way I aim to quantify how unusual the observed velocity patterns exhibited

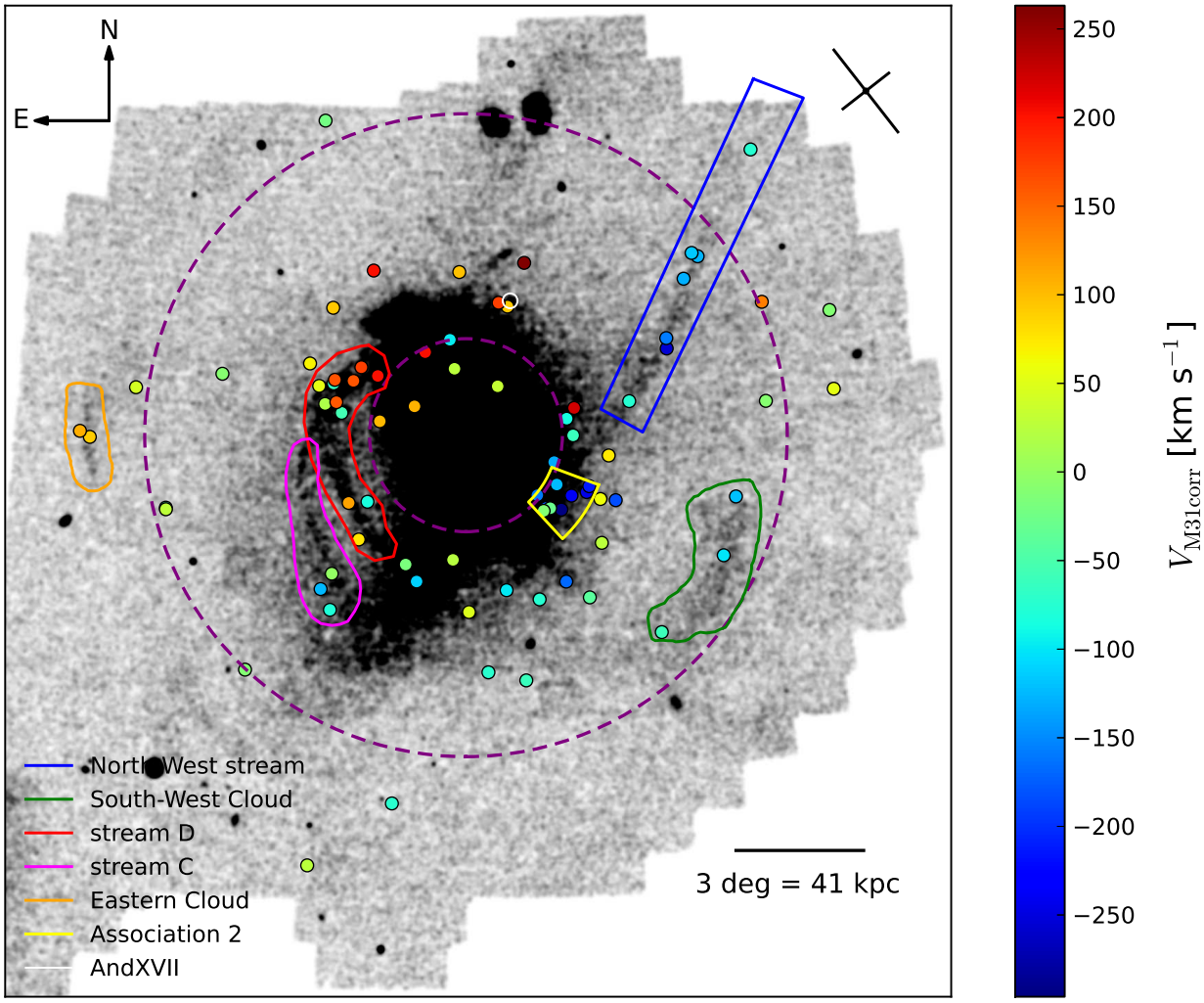

Figure 3.5 *Metal-poor stellar density map of M31 from PAndAS. Points are as in Figure 2.6. Coloured contours mark the cold stellar features of interest (see text for details).*

by clusters which project onto specific features might be, given the null hypothesis that all N GCs are independent (uncorrelated) members of the M31 halo.

Ideally, the best way to establish or refute an association between GCs and underlying streams would be to directly demonstrate that the GC velocities match those of stars in the substructures. However, determining velocities for these extremely low surface-brightness features is a challenging observational problem and at present few such measurements exist. In what follows, I highlight the few cases where it is possible to make such direct comparisons using extant data.

3.4.1 The North-West stream

One of the most prominent and interesting stellar debris features in the M31 halo is the North-West (NW) stream. Marked with a blue rectangle on Figure 3.5, it extends over a range $\sim$ 30 to 130 kpc in projected radius. This is a clear example of a now-disrupted dwarf galaxy being accreted onto M31. Projected on top of the NW stream lie 7 GCs for which I have measured velocities. As the stream extends almost radially from the M31 centre, in close to a straight line on the sky, it is interesting to see how the velocities of these 7 GCs behave as a function of $R_{\rm proj}$. This is shown in Figure 3.6, where the Galactocentric velocity is plotted, corrected for the measured rotation and systemic motion of M31, against projected radius.

Six of the 7 NW stream GCs share a clear trend in corrected radial velocity as a function of $R_{\rm proj}$, in that the velocity becomes more strongly negative the closer a GC is to the centre of M31. However the innermost GC, PA-15, deviates substantially from this trend and, assuming its measured velocity is correct, it is difficult to see how this object could be associated with the NW stream despite the fact that its position projects precisely onto the feature.

It is interesting that, as marked in Figure 3.6, the relationship between the outermost five GCs on the stream is very close to linear, with a gradient of 1.0 ± 0.1 km s^{-1} per kpc, a free index of -199 ± 9 km s^{-1}, and a Pearson correlation coefficient $\mathcal{R} = 0.98$. This is quite a remarkable observation, and there is no compelling reason to expect a highly linear correlation between velocity and radial distance. Indeed I ascribe no important physical insight into this specific form of the relationship – fitting a straight line to the data is merely the simplest means of quantifying the observed trend.

The linear parametrisation is, however, very useful for assessing the likelihood that the 5 outermost NW stream GCs could be independent members of the M31 halo. Conducting a Monte Carlo experiment to consider the outermost five GCs on the NW stream, I conservatively counted what fraction of the mock GC sets satisfied $\mathcal{R} < -0.9$ or $\mathcal{R} > 0.9$, which is considered an indicator of high (anti)correlation. Around 3% of the simulated sets satisfy this criterion. If I only consider cases of infall, meaning the sets only need to satisfy $\mathcal{R} > 0.9$, the probability of finding such a pattern falls to 2%.

It is also notable that the NW stream clusters lie substantially displaced by a magnitude $\gtrsim 100$ km s^{-1} from zero velocity, which is where the mean of the distribution of corrected halo velocities should sit. This is somewhat larger

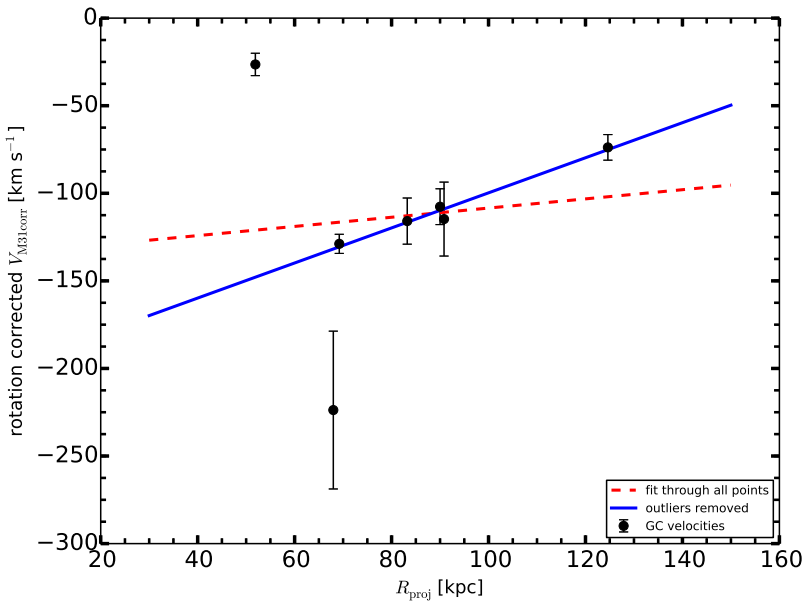

Figure 3.6 *Galactocentric radial velocity, corrected for the measured rotation and systemic motion of M31, as a function of projected radius for the 7 GCs that lie projected on top of the North-West stream. The dashed red line is a linear fit through all the data points, while the solid blue line is the fit after excluding the two innermost GCs. This latter fit has a slope of* 1.0 ± 0.1 *km s*$^{-1}$ *per kpc and a free index of* -199 ± 9 *km s*$^{-1}$.

than the measured dispersion of the GC system at commensurate radii (see Figure 3.4). This inspired me to search through the 10^6 mock sets to see in how many cases all five GCs fell outside either $\pm 1\sigma$ from the mean. I found this to be an unusual configuration, occurring only 0.02% of the time.

In combination, these two simple tests show that the kinematic properties of these 5 NW stream GCs are almost certainly not due to a chance occurrence among independent halo GCs, providing additional convincing evidence, beyond their spatial alignment, for an association with each other and the underlying stellar stream. While final confirmation will require a direct comparison between the GC kinematics and velocities measured for stars belonging to the stream, note that the observed velocity gradient amongst the GCs – a more negative velocity the closer a GC is to the centre of M31 – likely represents the infall trajectory of the progenitor satellite. In addition, the scatter of the five GC velocities about the best-fit line is very small, suggestive of a dynamically cold system with a dispersion consistent with zero.

Although the sixth NW stream cluster, PA-13, does share in the trend of increasingly negative velocity with smaller $R_{\rm proj}$, it is quite displaced from the linear relationship describing my measurements for the outer 5 GCs. Note however, that this object has the lowest S/N spectrum in my entire GC sample,

and its velocity is thus accompanied by a rather large uncertainty such that it lies, rather ambiguously, $\sim 2\,\sigma$ from the best-fit line. It might be that the velocity of PA-13 is indicating that this object is unrelated to the NW stream. On the other hand, if the cluster *is* associated with the stream, the possibility of a deviation to even more negative velocities than expected from my simple linear fit to the outermost GCs might indicate *accelerating* infall along the stream. In this context a more precise velocity measurement for PA-13 would indeed be valuable.

3.4.2 The South-West Cloud

The South West (SW) Cloud is a large diffuse overdensity found near the major axis of M31 at a distance of ~ 90 kpc, and is marked with a green contour on Figure 3.5. The properties of this stellar debris feature have been studied in detail by Bate et al. (2013) (see also Lewis et al., 2013). There are three GCs projected on top of the SW Cloud. In a recent paper, Mackey et al. (2013) presented radial velocities for two of these objects, PA-7 and PA-8. Applying a simple statistical test, the authors showed that it is very likely that these two clusters are associated with each other, and with the SW Cloud itself.

In this thesis I have measured a radial velocity for the third cluster projected on top of the SW Cloud, PA-14, as well as confirming the velocity measurements for PA-7 and PA-8 from Mackey et al. (2013). Unlike the NW stream, the SW Cloud is not a radial feature, but more closely resembles an arc tracing a roughly constant projected radius. All three GCs projected onto the SW Cloud have $R_{\rm proj}$ between 86 and 88 kpc. In Figure 3.7, I have plotted the Galactocentric velocity for these GCs, again corrected for the measured rotation and systemic motion of M31, as a function of position angle relative to the M31 centre. There is a clear velocity gradient along the arc, in that the corrected velocities become more negative with increasing position angle (i.e., in the anti-clockwise direction on Figure 3.5, or from south to north along the arc of the stream).

Once again, a linear fit does an excellent job of describing this trend. The best-fit line has a gradient of -2.32 ± 0.02 km s^{-1} per deg, a free index of 550 ± 6 km s^{-1}, and a correlation coefficient $\mathcal{R} = -0.99$. As for the NW stream clusters, I do not ascribe any particular significance to this assumed form for the relationship – a linear fit is just the simplest means of quantifying the observed trend in velocity with position angle.

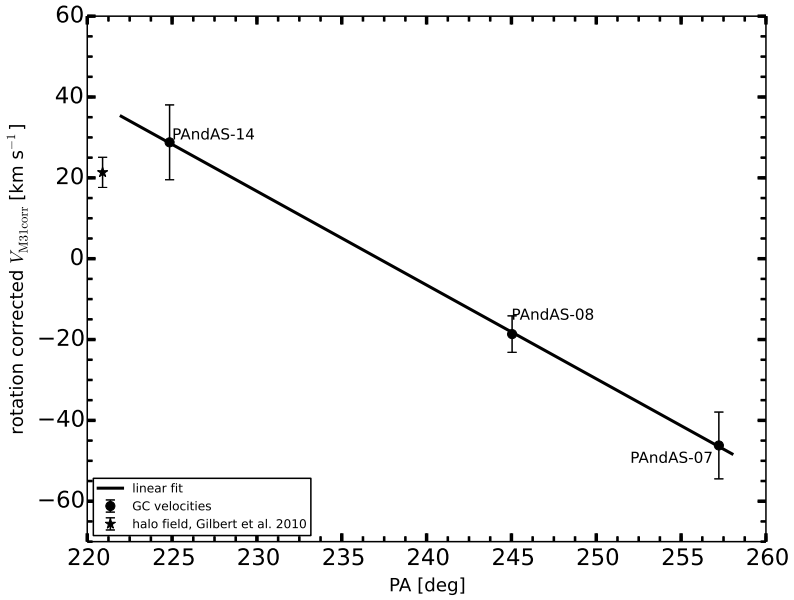

Figure 3.7 *Galactocentric radial velocity, corrected for the measured rotation and systemic motion of M31, as a function of position angle (east of north) relative to the M31 centre, for the 3 GCs that lie projected on top of the South-West Cloud. The solid line represents the best fit, having a gradient of* -2.32 ± 0.01 *km s*$^{-1}$ *per degree and a free index of* 550 ± 6 *km s*$^{-1}$*. The halo field measured by Gilbert et al. (2012), in which they detected a cold kinematic peak with* $V_{\rm helio} = -373 \pm 3$ *km s*$^{-1}$ *and an intrinsic dispersion* $\sigma = 6.1^{+2.7}_{-1.7}$ *km s*$^{-1}$ *is also marked.*

To assess the likelihood that such a trend could arise amongst a group of unrelated halo clusters, I ran a Monte Carlo experiment to consider the three SW Cloud GCs, and assessed what fraction of the mock sets exhibit a linear correlation with $\mathcal{R} > 0.9$ or $\mathcal{R} < -0.9$. I find that this is actually moderately common, arising 29% of the time. Note that this calculation supersedes that of Mackey et al. (2013), as their model did not include any correction for the systemic rotation because its existence was not known at that time. However, since the SW Cloud lies near the M31 major axis, the rotation signal is at a maximum and it is important to take this into account.

By itself, this finding is not sufficient to conclude that the three GCs discussed here are indeed associated with the SW Cloud; in addition, unlike the NW stream clusters, the three SW Cloud objects do not have corrected velocities strongly offset from the expected mean of zero. However one must also recall that the chance of all three GCs being projected directly onto the SW Cloud in the first place is quite small ($\sim$ 2.5%, Mackey et al., 2010b). In addition, Bate et al. (2013) have noted that spectroscopic measurements of the M31 field halo near to PA-14 by Gilbert et al. (2012) revealed a cold kinematic peak at a very similar velocity to that of the clusters: $\mathrm{V_{helio}} = -373 \pm 3$ km s^{-1}, and an intrinsic dispersion $\sigma = 6.1^{+2.7}_{-1.7}$ km s^{-1}. In the corrected Galactocentric

frame, this corresponds to a velocity of $+21 \pm 4$ km s^{-1}, as compared with my measured velocity for PA-14 of 29 ± 9 km s^{-1} (see Figure 3.7). In making this comparison, I have assumed that the M31 field halo exhibits the same rotation as the GCs projected onto the SW Cloud.

Together these facts paint a convincing picture; however, as before, final confirmation will require a direct comparison between field kinematics and GC velocities at a number of points along the stream. It is interesting to note that, if real, the radial velocity gradient along the SW Cloud would likely imply substantial motion in the plane of the sky, and hence a significant line-of-sight depth to the feature – as tentatively detected by both Mackey et al. (2013) and Bate et al. (2013).

3.4.3 Streams C and D

Directly to the east of M31 lie two well-defined arc-like overdensities, named stream C and stream D (see Ibata et al., 2007; Richardson et al., 2011). These are, respectively, marked with magenta and red contours on Figure 3.5. This is a complex part of the M31 halo – the streams appear to overlap in projection at their northern end; in addition, stream C is known to split into two kinematically distinct constituents (Chapman et al., 2008) – a metal-poor component, Cp, which is the narrow stream visible in Figure 2.6 and 3.5, and a metal rich component, Cr, which overlaps Cp in projection but is spatially much broader. This latter feature is not evident in Figure 2.6 and 3.5 because its member stars fall above the metal-rich cut-off used in the construction of these plots; see however, e.g., Martin et al. (2013); Ibata et al. (2014).

There are a total of 15 GCs projected on top of streams C and D, and I have measured radial velocities for all of them. The northern area of overlap is particularly rich in clusters, with 9 contained inside a relatively small region on the sky; indeed, as noted by Mackey et al. (2010b), this represents the second highest local density enhancement of GCs, relative to the azimuthal average, seen in the M31 halo (the highest being "Association 2" – see below). The observed velocities for these 9 clusters suggest that they split into two distinct kinematic subgroups. I employ the biweight location and scale estimators (Beers et al., 1990) to determine the mean velocity and velocity dispersion of these two groups. These two robust statistics were specifically designed to be applied to small kinematic samples, and are resistant to the presence of outliers. The first group appears to contain 5 GCs, has a mean rotation corrected Galactocentric velocity of 84 ± 4 km s^{-1} and dispersion

of 8^{+15}_{-8} km s^{-1}, while the second features 3 GCs and has a mean rotation corrected Galactocentric velocity of -111 ± 49 km s^{-1} and a dispersion of 39^{+54}_{-39} km s^{-1}. The ninth cluster in the region, PA-49, possesses a rotation corrected Galactocentric velocity of -24 ± 7 km s^{-1}, and hence cannot be robustly identified with either kinematic subgroup.

It is interesting to note that the mean velocities of the two GC subgroups fall on either side of zero. Thus the two GC groups, and, in all likelihood, two of the three underlying streams, are in counter-rotating orbits about the M31 centre. Also of interest here is the work of Perina et al. (2009) who identified a possible kinematic subgrouping of GCs near to the stream C/D overlap region at a projected radius $R_{\rm proj} \approx 20$ kpc. The Galactocentric velocity of this subgroup is $V_{\rm Gal} \approx -160$ km s^{-1}, and when corrected for the systemic motion of M31, I find that this velocity is consistent with one of the GC groupings in the overlap area. This additional subgroup might therefore represent the inward extension of stream Cp, Cr or D. Unfortunately however, it is not possible to trace these streams within ~ 30 kpc of the M31 centre due to the loss of contrast against the high stellar densities of the M31 spheroid, and the presence of numerous additional substructures.

I conduct a Monte Carlo experiment for each of the two GC subgroups I have identified above, to assess the likelihood that they are chance assemblies of unrelated GCs. At $R_{\rm proj} \approx 40$ kpc the expected velocity dispersion is $\sigma \sim 115$ km s^{-1}. For the first subgroup, the fraction of mock sets where all five GCs lie $\pm 0.7\sigma$ away from zero, but with an internal velocity dispersion less than 10 km s^{-1}, is extremely small at 0.02%. For the second subgroup, the configuration where 3 GCs all sit outside either $\pm 0.8\sigma$ while having an internal dispersion of 39 km s^{-1} is somewhat more frequent, occurring 2% of the time. Thus I can conclude that the GC groups are very likely associated with two of the underlying substructures.

Following the streams anti-clockwise in Figure 3.5, both stream C and stream D have three GCs projected onto their southern regions (see Mackey et al., 2010b). Unlike in the northern overlap area, where the field halo has not been studied kinematically, there are some literature measurements of the stream velocities nearby to each of these two southern locations.

I consider stream D first. The three GCs projected onto the southern part of this feature have velocities encompassing a range of ≈ 200 km s^{-1}, thus these objects do not appear to form a kinematic subgroup. One GC, PA-42, lies very precisely on the narrow stream D, and it is natural to hypothesize that this

cluster (with $V_{Gal} = 7 \pm 5$ km s^{-1}) would be the most likely stream member. However, (Chapman et al., 2008) tentatively measured the velocity of stream D to be $V_{Gal} \approx -205$ km s^{-1} in a field less than a degree away from PA-42; this instead matches quite closely with the velocity of one of the other lower stream D clusters, H23 ($V_{Gal} = -193 \pm 11$ km s^{-1}). Additional secure measurements of the stream velocity from field stars are required to positively identify which GCs, if any, are associated with this overdensity.

Moving to stream C, it is seen that the three GCs projected onto the southern part of this stream have quite disparate velocities and are thus unlikely to form a kinematic subgroup, much like the lower stream D clusters. One of these clusters, HEC12, is quite well studied. It lies precisely on the narrow metal-poor component Cp, and previous work (Chapman et al., 2008; Collins et al., 2009) has clearly demonstrated that it shares a common velocity with the underlying stream – in the Galactocentric frame HEC12 has $V_{Gal} = -109 \pm 3$ km s^{-1}, while surrounding stars from stream Cp have $V_{Gal} = -106 \pm 3$ km s^{-1}. The clusters H26 and HEC13 lie less than a degree to the south-east of HEC12. It is interesting to note that my velocity measurement for HEC13 ($V_{Gal} = -188 \pm 6$ km s^{-1}) is very similar to the velocity measured by (Chapman et al., 2008) for the metal-rich component of stream C surrounding HEC12, $V_{Gal} = -171 \pm 3$ km s^{-1}; i.e., HEC13 is plausibly associated with Cr. The velocity of H26 is ≈ 55 km s^{-1} more negative than that of HEC13, such that this object does not appear to be a member of either component of stream C.

It is tempting to try to use the measured field and GC velocities from the southern parts of stream C and stream D to deduce which of the GC subgroups in the northern overlap region might be associated with which underlying stream. However, doing this correctly requires knowledge of the velocity gradient along each stream, and such a robust measurement does not exist at present, and any such discussion must be deferred until additional measurements of the field star velocities at well spread points along the various streams become available.

3.4.4 The Eastern Cloud

The Eastern Cloud is a small arc-like stellar debris feature located at a projected radius of $\sim$ 118 kpc due east of M31. This overdensity is marked with an orange line in Figure 3.5. There are two GCs projected onto the Eastern Cloud (PA-57 and PA-58), which have a velocity difference of less than 20 km s^{-1} and

a mean velocity that sits ≈ 100 km s^{-1} away from the M31 systemic velocity. These properties are suggestive of an association between the two GCs and the underlying stellar overdensity.

I once again use simple probabilistic arguments to explore the plausibility of this hypothesis. First, noting that although the mean velocity of the two clusters lies well separated from the M31 systemic velocity, just over half of this separation can be accounted for by the systemic rotation which I have observed for the outer halo GC population. Correcting for the rotation, it is found that both GCs sit outside 0.5σ from the mean (i.e., zero velocity) where σ is the inferred velocity dispersion of the GC system at the appropriate radius. As before, I generated 10^6 pairs of GCs with velocities drawn from a Gaussian probability distribution, centred on zero and with a width σ. I then counted the number of mock pairs that, conservatively, have both members sitting outside 0.5σ of zero velocity but with an absolute velocity difference between them smaller than 30 km s^{-1}. I find that this is not a very common occurrence, arising 10% of the time.

Nonetheless, one must also bear in mind that the Eastern Cloud is a comparatively small overdensity in terms of its projected surface area. Mackey et al. (2010b) did not consider this feature as it was undiscovered at the time of their work. The overdensity subtends a position angle of ≈ 15 deg and spans, generously, the radial range $115 - 120$ kpc ($\approx 8.4 - 8.8$ deg). Its projected surface area is hence ≈ 0.9 deg^2. It is also known that the surface density of GCs at this radius in the M31 halo is very close to 0.1 deg^{-2} (Mackey et al. 2014, in prep.). Applying simple Poisson statistics makes it possible to infer that the probability of observing two or more GCs falling in this region by chance is $\sim 0.4\%$. The chance that they also have very similar velocities, as per the discussion above, is smaller still at 0.04%.

It can thus be concluded that it is very unlikely for the two GCs that lie on top of the Eastern Cloud to be unrelated M31 outer halo members, but rather they are almost certainly associated with the substructure they project on. As usual, final verification will require measurements of the stream velocity from field stars, for direct comparison with the GC observations.

3.4.5 Association 2

Mackey et al. (2010b) identified a spatial overdensity of GCs, dubbed "Association 2", close to the western major axis of M31 at a distance of $R_{\rm proj} \sim 40$

kpc. This group numbers a total of 10 clusters[1] sitting within a small area, constituting the single highest local density enhancement of GCs, relative to the azimuthal average, seen in the M31 halo. Association 2 sits in a complex region where the stellar halo and outer disc of M31 overlap, and it is difficult to assess whether there might be one or more distinct underlying stellar features (see Figure 2.6). It has previously been noted that the very luminous cluster G1, which is a member of Association 2, does overlap spatially with a stellar overdensity known as the G1 clump. However, this label is a misnomer as Faria et al. (2007) have demonstrated that there is no kinematic link between the two and concluding that the G1 clump is likely a fragment of the outer disc of M31.

Using the biweight location and scale estimators (Beers et al., 1990), it is found that the entire Association 2 ensemble has a mean Galactocentric velocity – corrected for the systemic motion of M31 and the rotation of the outer halo GC population – of -83 ± 38 km s^{-1}, and a velocity dispersion of 92 ± 25 km s^{-1}. This dispersion would suggest that Association 2 does not, in its entirety, form some kinematically coherent unit. Nonetheless, there is the possibility of distinct sub-groupings of GCs. For instance, there are four objects with corrected Galactocentric velocities below -130 km s^{-1}; three of these (H2, PA-18 and PA-19) sit within 30 km s^{-1} of each other near -150 km s^{-1}, while the fourth (PA-21) has a velocity of -210 km s^{-1}. Formally, the biweight estimators give a mean velocity of -162 ± 18 km s^{-1} and a dispersion of 30 ± 28 km s^{-1} for this subgroup. Similarly, there are another four GCs (H7, H8, PA-22, and PA-23) with corrected Galactocentric velocities lying within $\approx$ 40 km s^{-1} of each other in the range 0 to -100 km s^{-1}. The biweight estimators suggest a mean velocity -63 ± 17 km s^{-1} and dispersion 19 ± 13 km s^{-1} for these objects.

To assess the plausibility of these two apparently coherent sub-units forming by chance I conducted a Monte Carlo experiment for each. I find that the occurrence of 4 random GCs all lying outside either $\pm 1.1\sigma$ away from zero, but having an internal dispersion less than 30 km s^{-1}, as per the first observed subgroup, is very rare at 0.04%. Regarding the second subgroup, the chance for all 4 members sit to $\sim 0.4\sigma$ away from zero, while having an inter-group dispersion smaller than 20 km s^{-1} is also very small and arises 0.05% of the time in my model.

In summary, I find that Association 2 is very unlikely to be a chance grouping

[1]Two additional GCs were discovered in this region since the analysis by Mackey et al. (2010b).

of GCs even though there is no evident underlying field substructure. The ensemble, in its entirety, does not constitute a kinematically coherent group of clusters; however, there are two distinct sub-groups, numbering 8 objects in total, possessing kinematic properties that are difficult to explain unless the clusters in these sub-groups are associated with each other. In this sense, Association 2 may represent the projected convergence of two (or more) disrupted relic systems, similarly to the overlapping northern region of streams Cp/Cr/D. In this context, it is interesting that Association 2 sits very close to the projected base of the North-West stream. The first GC sub-group, which has $R_{\rm proj} \sim 40$ kpc and a corrected velocity of ≈ -162 km s^{-1}, matches very closely to an extrapolation of the linear velocity gradient along the NW stream described in Section 3.4.1 (see Figure 3.6), and it is tempting to speculate that this sub-group may be linked to the stream. Similarly, the second sub-group sits very close, position-wise, to the G1 clump. Reitzel et al. (2004) have shown the velocity of this overdensity to sit near $V_{hello} \approx -450$ km s^{-1}, which matches very well with the heliocentric velocities of the GC sub-group members as reported in Table 2.4 – the weighted mean for which is ≈ -441 km s^{-1}. It is thus possible that these GCs may be associated with the outer disc of M31.

3.4.6 The case of And XVII

Apart from the GC groups that project onto the obvious stellar substructures, there is another case that is worth considering. Marked with a white open circle in Figure 3.5 is the And XVII dwarf spheroidal galaxy (dSph) discovered by Irwin et al. (2008). These authors note that relatively close to this galaxy located are 3 GCs: H11, HEC6 and HEC3. The projected distances to H11, HEC6 and HEC3 from the centre of And XVII are 2 kpc, 3.7 kpc and 5.9 kpc respectively. Irwin et al. (2008) showed that the probability of this spatial configuration occurring by chance is $\approx 0.2\%$, suggesting that at least one of these clusters may be associated with the dwarf. If this is true, And XVII would become the lowest luminosity galaxy ($M_{V_0} = -8.7$, McConnachie, 2012) that is known to host a GC. Since I have obtained radial velocities for both H11 and HEC6, and the radial velocity of And XVII is also well known (-251 ± 2 km s^{-1}, Collins et al., 2013), I attempt to investigate whether this is plausible based on the measured velocities.

The cluster HEC6 has a heliocentric radial velocity of -132 ± 12 km s^{-1}. The large discrepancy between its velocity and that of And XVII means that it is

most likely not associated with the dSph. For H11, the situation is a little more interesting. It is not only much closer to And XVII, but the velocity difference between them is 38 ± 7 km s^{-1} in the heliocentric frame, and hence there is a higher chance it might be bound to the dSph. I investigate this via a simple Newtonian escape velocity argument:

$$v = \sqrt{\frac{2GM}{r}} \tag{3.10}$$

where v is the escape velocity, G is the gravitational constant, M is the total mass of the system and r is the radial distance between the two objects. Assuming true distance between the two objects of 2 kpc, and a total mass of 10^7 M$_\odot$ for the And XVII + H11 system – note that Collins et al. (2014) measured a mass of 0.13×10^7 M$_\odot$ within the half-light radius of And XVII – the escape velocity is found to be ~ 7 km s^{-1}, which is smaller than the observed velocity difference. Conversely, And XVII is required to have a total mass of $\sim 3 \times 10^8$ M$_\odot$ in order for the dSph and H11 to form a bound system, given their observed velocity difference of 38 ± 7 km s^{-1}. Thus it seems unlikely that And XVII hosts any GCs despite the close proximity of 3 such objects.

3.5 The dynamical mass of M31

It is of particular importance to accurately know the mass of M31. For example, it is necessary for constraining the dynamics of the Local Group, and for testing various cosmological models and predictions. Even though M31 is the closest massive galaxy to our own, it is striking that its mass is still not measured with high precision. Indeed, the debate as to whether M31 or the Milky Way is more massive is still very much active. A number of studies have employed a variety of methods in order to estimate the mass of M31. Some of the more recent such estimates are displayed in Table 3.3. Older mass estimates are summarized in Federici et al. (1990, 1993) and Evans & Wilkinson (2000). One way to measure the M31 mass is to use its outer halo GCs as dynamical mass tracers. Given that the halo population is spatially very extended, this enables the total mass to be calculated within a large radius.

Assuming the outer halo GC system is spherically symmetric, the total mass of M31 can be estimated by solving the Jeans equation (Binney & Tremaine, 1987). The Jeans equation for a tracer population with a constant anisotropy β

Table 3.3 *Estimates of the total mass of M31 found in the recent literature. For reference, the virial radius of M31 is assumed to be* $\sim$ *260 kpc (Seigar et al., 2008).*

Reference	Mass [10^{12} $M_\odot$]	$R_{\rm max}$	Method
Peñarrubia et al. (2014)	$1.5^{+0.5}_{-0.4}$	constraints out to 3.5 Mpc	Dynamics of LG galaxies
Hudson et al. (2014)	3.9 ± 1.8	200 times the critical density	The total number of GCs
Fardal et al. (2013)	1.9 ± 0.2	200 times the critical density	Used the Giant stream
van der Marel et al. (2012)	1.5 ± 0.4	within the virial radius	Timing argument
Tollerud et al. (2012)	$1.2^{+0.9}_{-0.7}$	within the virial radius	19 dwarf galaxies
Watkins et al. (2010)	1.5 ± 0.4	within 300 kpc	23 dwarf galaxies
Lee et al. (2008)	$1.9 - 2.4$	within 100 kpc	504 inner region GCs
Evans et al. (2003)	~ 1.2	within 100 kpc	89 inner region GCs

about a mean rotation velocity $\langle v_\phi \rangle$ is:

$$\frac{GM(r)}{r} = \langle v_\phi \rangle^2 - \sigma_{\rm r}^2 \left(\frac{\partial \ln(\rho {\sigma_{\rm r}}^2)}{\partial \ln(r)} + 2\beta \right) \tag{3.11}$$

where G is the gravitational constant, ρ is the density distribution and $\sigma_{\rm r}$ is the velocity dispersion along the line of sight of the tracer population. The first and second terms in Equation 3.11 describe the contribution of rotation and pressure of the tracer population to the total mass M. Because I have found the M31 halo GC system to exhibit a significant rotation signature, the first term is used directly applying the mean rotational amplitude to calculate the total contribution to the mass due to rotation, $M_{\rm r}$, simply via:

$$M_{\rm r} = \frac{R_{\rm max} v_{\rm max}^2}{G} \tag{3.12}$$

where v_{max} is the rotation amplitude of the GC system considered, R_{max} is the projected radius of the outermost GC in the sample.

In order to determine the pressure supported mass, M_p, once can in principle try to solve the right hand side of Equation 3.11 numerically while marginalizing over β. However, the integration may become problematic depending on the exact form of ρ. Instead, I use the solution[2] of the non-rotating Jeans equation proposed by Evans et al. (2003), dubbed the Tracer Mass Estimator

[2]For a general solution to the Jeans equation please see e.g. Mamon & Łokas (2005).

(TME):

$$M_{\rm p} = \frac{C}{GN} \sum_{i=1}^{N} \left(v_i - v_{\rm sys}\right)^2 R_i \tag{3.13}$$

where R is the projected radius from the M31 centre of a given GC, v is the radial velocity of that GC with the rotational component removed, $\rm v_{sys}$ is the systemic velocity of M31, and N is the total number of clusters in the sample considered. The index i loops over each GC in the sample. The constant C is dependent on the shape of the underlying gravitational potential, the radial distribution of the mass tracers and the anisotropy of the system. Here I assume that the M31 outer halo system is spherical and isotropic, and therefore C takes the form of (Evans et al., 2003):

$$C = \frac{4(\alpha+\gamma)}{\pi} \frac{4-\alpha-\gamma}{3-\gamma} \frac{1-(r_{\rm in}/r_{\rm out})^{3-\gamma}}{1-(r_{\rm in}/r_{\rm out})^{4-\alpha-\gamma}}. \tag{3.14}$$

In the above definition of C, $r_{\rm in}$ and $r_{\rm out}$ are the smallest and largest deprojected radii of the GCs in the sample respectively. The value for $r_{\rm in}$ is taken to be the distance at which the halo begins to dominate, i.e. 30 kpc, while $r_{\rm out}$ is taken to be 200 kpc assuming MGC1 is the the most remote cluster that belong to the M31 halo (Mackey et al., 2010a). The constant α is related to the shape of the underlying gravitational field, which is assumed to be scale free between $r_{\rm in}$ and $r_{\rm out}$. For a NFW profile (Navarro et al., 1996), Watkins et al. (2010) found $\alpha \approx 0.55$. In the case of an isothermal halo potential, where the system has a flat rotation curve at large radii, $\alpha = 0$. The TME assumes that the volume density distribution of the tracer population is well described by a power law, and the constant γ in Equation 3.14 is the power law index of that distribution. Assuming spherical symmetry, it is found that $\gamma \approx 3.34$ for the GCs with $R_{\rm proj} > 30$ kpc (Mackey et al. 2014, in prep). In addition, it is worth clarifying that the TME calculates the total enclosed mass even though it is based on observations of GCs within a spherical shell.

Applying the above method in the case of an isothermal halo potential, I find the total mass enclosed within 200 kpc from the centre of M31 to be $M_{200} = 1.6 \pm 0.2 \times 10^{12}$ $\rm M_\odot$. Assuming a NFW profile for the M31 halo (Navarro et al., 1996), I find $M_{200} = 1.2 \pm 0.2 \times 10^{12}$ $\rm M_\odot$. The uncertainties are estimated via the statistical bootstrapping technique. The results of the mass estimation, along with the relevant parameters, are also displayed in Table 3.4.

Table 3.4 *Estimates of the M31 mass within 200 kpc using the present sample via the TME (Evans et al., 2003). The quoted errors incorporate the statistical uncertainties only. The mass estimates are highly dependent on the various assumptions made, such as isotropic orbits for the GCs, power law form for the GC volume density distribution and the underlying gravitational field.*

N_{GC}	α	γ	M_p $[M_\odot]$	M_{rot} $[M_\odot]$	M_{total} $[M_\odot]$
72	0	-3.34	$1.4 \pm 0.2 \times 10^{12}$	$0.2 \pm 0.01 \times 10^{12}$	$1.6 \pm 0.2 \times 10^{12}$
72	0.55	-3.34	$1.0 \pm 0.2 \times 10^{12}$	$0.2 \pm 0.01 \times 10^{12}$	$1.2 \pm 0.2 \times 10^{12}$

Although this estimate of the dynamical mass of M31 is consistent with the majority of the dynamical mass estimates found in the literature that sample a similar radial range (e.g. Watkins et al., 2013; Peñarrubia et al., 2014), it is worth noting that Hudson et al. (2014) found $\sim$ 3 times larger mass based on the number of GCs present around M31. It is also important to state that that there are a number of caveats in TME when used in the present situation. This mass estimator assumes that the tracer population is in a steady state equilibrium, while throughout this chapter I have shown that this is not true for the majority of the M31 halo GCs, which appear to be spatially correlated with apparent cold stellar debris features and are thus likely to be new arrivals in the M31 halo. In addition, many of the GCs that lie on distinct stellar features have correlated velocities as described in Section 3.4. This in turn implies that it is almost certainly not appropriate to treat all 72 outer halo GCs that were used for the mass estimate as independent data points. In this case some data points are weighted more heavily than others, thus introducing a bias which is not known for this specific case. However it is important to note that studies which explored the presence of substructure in tracer populations found results to be biased only by 20% (Yencho et al., 2006; Deason et al., 2012). I also assumed, due to a lack of information to the contrary, that the velocity anisotropy of the GC orbits is zero, while in reality this is unlikely to be true for the whole halo population. Nonetheless, Di Cintio et al. (2012) found the anisotropy parameter to have negligible effect on mass estimates for which only radial velocity information is available. Finally, there is no theoretical motivation to assume that the entire dark matter halo of a massive galaxy follows a single power law, and thus fixing α to a single number might introduce additional biases. These caveats give rise to systematic uncertainties in the M31 mass estimate that are not incorporated in the quoted errors, which only contain the statistical uncertainty. Given the complex nature of the M31 halo GC population, a more reliable mass estimation will require a method specifically tailored to this system – an attempt I defer for my future work.

3.6 Discussion

The high quality PAndAS data made exploring the true outer halo of M31 ($30 \lesssim R_{\rm proj} \lesssim 150$ kpc) in a continuous and complete fashion possible for the first time. The the presence of numerous stellar substructures (e.g. McConnachie et al., 2009; Ibata et al., 2014) are consistent with the predictions of the ΛCDM galaxy formation model, according to which massive galaxies are built hierarchically via accretion and merging of smaller clumps of matter. In addition, a significant portion of the GCs discovered in the outer halo appear to preferentially lie projected on top of the tidal debris (Mackey et al., 2010b) implying that the halo GC system of M31 was also assembled in a similar manner.

Using the radial velocity measurements derived in Chapter 2, I demonstrated that various discrete groups of GCs – specifically those projecting onto the most luminous halo streams and overdensities – exhibit clear kinematic patterns. The global kinematic measurements of the M31 outer halo GC system were used in conjunction with simple Monte Carlo experiments to indicatively assess how frequently these velocity trends or correlations might occur in the cases where all GCs in a given groups are independent members of the M31 halo. Each instance that I examined, save for the ostensible And XVII association, showed clear evidence of non-random behaviour, indicative of a dynamical linked between the GCs and the streams they project onto. These results strongly reinforce the notion from Mackey et al. (2010b) that a substantial fraction of the outer halo GC population of M31 consists of objects accreted along with their now-defunct host galaxies. A striking feature of many of the considered ensembles is the coldness of their kinematics – cluster groups on the NW stream, SW Cloud, and Eastern Cloud, as well as sub-groups in the stream C/D overlap area and in Association 2 – all exhibit velocity dispersions consistent with zero. At measurements of stream velocities directly from the constituent stars are available only in a handful of cases. However, I demonstrated that these few instances largely support the presented assertions.

In light of these results, the discovery of the high overall degree of rotation exhibited by the outer halo GCs in M31 is particularly surprising. It is relevant to note that this rotation is not predominantly driven by either the subset of remote clusters clearly associated with underlying stellar streams, or the complement of this subset. The is clearly evident from inspection of the left-hand panel in Figure 3.2. To make matters more interesting, I have found that

the outer halo GCs share the same rotation axis as the inner halo GCs; indeed, the rotation of these two subsystems is virtually indistinguishable save for the difference in amplitude. This is in contrast with observations in the Milky Way where there is almost no net rotation exhibited by the halo GC population (Harris, 2001; Brodie & Strader, 2006). It is unfortunate that to date there is little opportunity to compare the kinematics of the M31 outer halo GCs to that of other massive spiral galaxies apart from the Milky Way. Olsen et al. (2004) derived kinematic properties for 6 spiral galaxies in the Sculptor group. However, there are only 6 GCs per galaxy on average, and they all lie in the inner regions of their hosts, likely making the results of their study affected by small number statistics. Nantais & Huchra (2010) presented a discovery of rapid rotation in the GC system of M81. However, all of the GCs with available radial velocity data in that galaxy lie at projected radii of less than 20 kpc. In elliptical galaxies, it is common to find rotating GC populations towards the more central regions, but finding significant rotation beyond a few tens of kpc appears to be a rare occurrence (e.g. Woodley et al., 2010; Strader et al., 2011; Blom et al., 2012; Pota et al., 2013).

It is worth considering how to reconcile the discovery of significant rotation in the outer halo of M31 with the chaotic accretion of dwarf galaxies implied by hierarchical models. One way this phenomenon might arise is through the major merger of two spiral galaxies. For example, the numerical simulations of Bekki (2010) suggest that a major merger between M31 and a similar spiral galaxy could give rise to the rapid rotation observed in the inner GC system of M31, including the rotation of the halo populations. In a not-entirely unrelated scenario, a large fraction of the halo GC subsystem might have been brought into the potential well of M31 via a single moderate-mass satellite. In this event, the satellite seeds its GCs in the halo as it spirals in towards the centre of M31. However, in order for such a satellite to be able to deposit several tens of GCs it would need to have a considerable mass – perhaps akin to the Large Magellanic Cloud, which possesses 16 old GCs, and many young massive clusters. If an encounter between M31 and such a massive satellite did occur, the question must arise as to how disruptive such an event would have been on the M31 disc. In addition, in this scenario it may also be difficult to explain the observed correlations between the outer halo GCs and the often very narrow stellar debris streams. Further modelling is required to address these uncertainties.

Another possibility is that the outer halo GC system of M31 is indeed the product of the assimilation of multiple dwarf galaxies, but that these were accreted into the M31 potential well from a preferred direction on the sky.

This would be consistent with the observation that many of the surviving dwarf galaxies associated with M31 lie in a thin rotating planar structure, as reported by Ibata et al. (2013). This plane of dwarfs also appears to be rotating in the same direction as the outer halo GC system, although its rotation axis is inclined by $\sim$ 45 deg with respect to the minor axis of M31. A similar plane of dwarfs is observed in the Milky Way (e.g., Metz et al., 2007), and it has been shown that some of the GCs in the outer Galactic halo share this planar alignment (Keller et al., 2012). It has been hypothesised that the formation of these planes of dwarfs, and by extension the possibility of accretion from a preferred direction, could occur as dwarf galaxies move along large scale dark matter filaments or sheets, in which case they are expected to have aligned angular momenta as seen in some recent cosmological simulations (Libeskind et al., 2005, 2011; Lovell et al., 2011).

3.7 Summary

The global kinematic analysis of the M31 outer halo GC system detected a significant degree of net rotation exhibited by this cluster population. Interestingly, the halo GCs share the same rotation axis and direction as their counterparts located in the inner regions of M31. In addition, evidence for decreasing velocity dispersion as a function of projected distance from the M31 centre is also found, and this is well described with a power law function.

The radial velocity measurements revealed a variety of velocity correlations between the multiple groups of GCs that project on top of distinct stellar debris features in the field halo of M31. Via the use of Monte Carlo methods it was shown that such arrangements are unlikely, implying a common origin for the GCs and the stellar streams.

Finally, using the halo GCs as kinematic tracers, estimated was the total mass of M31 enclosed within a deprojected radius of 200 kpc via the Tracer Mass Estimator. The calculated value, $(1.2 - 1.6) \pm 0.2 \times 10^{12}$ $M_{\odot}$, is in agreement with other recent dynamical mass estimates, but is also likely a subject to several poorly understood biases due to the various assumptions that are built into the Tracer Mass Estimator.

Chapter 4

The globular cluster systems of NGC 147 and NGC 185

Parts of this chapter are published in Veljanoski et al. (2013a)

The outer halo of M31 observed to be full of various stellar substructures, thought to be the remnants of accreted dwarf galaxies (e.g. Ferguson et al., 2002). In addition, the accreted dwarf galaxies have greatly contributed towards to assembly of the outer halo GC system of this galaxy, judging by high spatial correlations between clusters and streams. Thus, a common questions one might ask are what kind of dwarf galaxies contributed towards the build-up of the M31 stellar halo and halo GC population, whether the dwarf galaxies observed today have properties similar to those comprising the stellar substructure features in the M31 halo, and whether the GCs hosted by nearby dwarf galaxies have properties akin to those located in the M31 outer halo. Hence, detailed studies of Local Group dwarf galaxies and their GCs are needed to answer these questions.

Two particularly interesting dwarf galaxies are the M31 satellites NGC 147 and NGC 185. Located in the outer halo of M31, these dwarf elliptical (dE) galaxies are amongst the brightest dwarfs in the Local Group. Their basic properties are summarized in Table 4.1. Given their location and properties, it is possible that these two dwarfs might resemble those that were accreted onto M31, serving as the main motivation behind the work presented in this chapter.

The stellar populations and star formation histories of these two dwarf galaxies have been extensively studied (e.g. Lee et al., 1993; Young & Lo, 1997; Butler & Martínez-Delgado, 2005; McConnachie et al., 2005; Davidge, 2005). It was found that NGC 147 is a typical dE galaxy composed primarily of old stars and it is dust and gas free (Young & Lo, 1997). Its most recent significant star

Table 4.1 *Basic properties of NGC 147 and NGC 185, used for the work presented in this chapter. The data in each row is: (1) and (2) RA and DEC coordinates in the J2000 epoch; (3) absolute visual magnitude; (4) projected distance from the centre of M31; (5) 3D distance from the M31 centre; (6) distance modulus; (7) half-light radius; (8) semi-major axis of the 25th magnitude B-band isophote; (9) mean metallicity from spectroscopic CaT measurements; (10) internal metallicity dispersion;*

	NGC 147	NGC 185	Reference
RA [h:m:s]	00:33:12.1	00:38:58.8	McConnachie (2012)
DEC [d:m:s]	+48:30:32	+48:20:15	McConnachie (2012)
M_{V_0} [mag]	-14.6 ± 0.1	-14.8 ± 0.1	McConnachie (2012)
$R_{\rm proj}$ [kpc]	101.8	97.3	coordinates from McConnachie (2012)
$D_{\rm M31}$ [kpc]	118 ± 15	181^{+25}_{-20}	Conn et al. (2012)
$m - M_0$	24.26 ± 0.06	$23.96^{+0.07}_{-0.06}$	Conn et al. (2012)
r_h [kpc]	0.66	0.48	McConnachie (2012)
B_{25} [kpc]	1.37	1.05	Corwin et al. (1994)
[Fe/H] [dex]	-1.1 ± 0.1	-1.3 ± 0.1	Geha et al. (2010)
$\sigma_{\rm [Fe/H]}$ [dex]	0.4	0.5	Geha et al. (2010)

formation phase occurred $\sim$3 Gyr ago (Davidge, 2005). Conversely NGC 185 has a substantial number of intermediate age stars (Martínez-Delgado et al., 1999), as well as gas and dust (Young, 2001). The highest rate of star formation in the recent past of this galaxy occurred $\sim$1 Gyr ago (Davidge, 2005). Bender et al. (1991) found NGC 147 to be rotating, while NGC 185 to be entirely pressure supported. In contrast, Geha et al. (2010) found both galaxies to have significant internal rotation through study of stars out to 8 effective radii. No evidence for radial metallicity gradient is found in either of these two galaxies (Geha et al., 2010). It has been argued that NGC 147 and NGC 185 may form a physical binary (van den Bergh, 1998; Geha et al., 2010) although this claim has been questioned by Battinelli & Demers (2004) and Watkins et al. (2013).

Earlier studies have discovered 7 GCs around both NGC 147 and NGC 185, all of which lie in or near the main bodies of these systems (Baade, 1944; Hodge, 1976; Ford et al., 1977; Sharina & Davoust, 2009). Thorough photometric (Baade, 1944; Hodge, 1974) and spectroscopic studies (Da Costa & Mould, 1988; Sharina et al., 2006; Sharina & Davoust, 2009) have been undertaken on these clusters, some of which are the brightest GCs known to reside in LG dwarf galaxies. These studies has also shown that in general the GCs hosted by NGC 147 and NGC 185 are old (>7 Gyr) and metal-poor ([Fe/H] < -0.8 dex). However, it is becoming increasingly appreciated that GCs can reside far from their host galaxies (e.g. Galleti et al., 2004; Hwang et al., 2011; Huxor et al., 2011, 2013; Jang et al., 2012) and this has served as a motivation to explore the remote environments of these systems to search for additional members.

This chapter presents the discovery of four outlying GCs, three of which belong to NGC 147 while one is hosted by NGC 185. I derive the first homogeneous optical and near-IR photometry for the entire GC populations of the dEs which I use to constrain their ages and metallicities. In addition, I constrain the kinematic properties of the GC systems of these two dE galaxies, by combining my velocity data of the newly-discovered GCs with that available in the literature for the previously-known clusters. I further use the combined velocity data to constrain the masses of these dwarf galaxies.

4.1 The data

For the work I present in this chapter I have utilised both optical and near-IR imaging, as well as spectroscopic data. The optical imaging, which was used to search for new GCs around NGC 147 and NGC 185, was taken as part of the PAndAS of the M31. I described the technical characteristics of this survey in Section 1.4.2. As a reminder, PAndAS is state-of-the-art survey, which used the *MegaCam* instrument mounted on the 3.6-m *CFHT*. The imaging was done in two optical bands g and i. The observations were taken in good photometric conditions, with typical seeing < 0.8 arcsec, and reaching a depth of $g \sim 25.5$ and $i \sim 24.5$ with S/N of 10. The data were initially reduced by *CFHT* staff via the ELIXIR pipeline which performs the standard bias, flat-field, and fringe corrections, and determines the photometric zero-point. The typical night-to-night variation of the zero-point is around 1-2% (Regnault et al., 2009). The full details of the reduction process are described in McConnachie et al. (2010) and in Ibata et al. (2014).

The near-IR data were taken in October 2008, as part of a survey designed to look at red stellar populations in Local Group galaxies. It used the *Wide-Field Camera* (*WFCAM*, Casali et al., 2007) mounted on the *United Kingdom Infrared Telescope (UKIRT)*. This instrument has a pixel scale of 0.4 arcsec, and the detectors are arranged such that four dithered pointings are aligned to cover a square of 0.75 deg^2. The observations were done in three near-IR bands, J, H and K, with seeing of 0.8 arcsec or better, using the microstepping option to improve the pixel sampling to 0.2 arcsec.

The data were reduced by Mike Irwin, with a pipeline designed by the Cambridge Astronomy Survey Unit, performing the usual dark current correction, flat-fielding, crosstalk removal, systematic noise and sky removal.

Table 4.2 *Journal of the spectroscopic observations for NGC 147 and NGC 185 GCs*

ID	Date of obs.	Number of exposures	Integration time per exposure [s]
PA-N147-1	10/09/2010	4	800
PA-N147-2	10/09/2010	3	800
PA-N147-3	10/09/2010	3	1500
PA-N185	11/09/2010	4	1800

The pipeline, which is part of the VDFS[1], also does full astrometric and photometric calibration based on the *2MASS* point source catalogue and is described in Cioni et al. (2008) and Hodgkin et al. (2009). The nightly zero-point variation on photometric nights is $< 1\%$. The reduced images were stacked and microstepped to produce individual detector frames. These were then resampled to form a 0.333 arcsec per pixel science mosaic (Irwin et al., 2004).

Spectra for the newly-discovered GCs around NGC 147 and NGC 185 were taken during the M31 halo GCs spectroscopic campaign as part of the 2010 *WHT* run. Several exposures were made of each object with varying integration time depending on the brightness of the target. The specifics of these observations are shown in Table 4.2. The reduction of these spectra was done together and in an identical manner as for the M31 halo GCs, as described in 2.2.1. The fully reduced, continuum-normalized spectra of these GCs are displayed in Figure 4.1.

4.2 Discovery of new GCs

At the distance of NGC 147 and NGC 185, GCs are partially resolved into stars at optical wavelengths and can be easily identified. Visual inspection of the area surrounding the two dEs was conducted by three PAndAS members (A. Huxor, D. Mackey and myself) and resulted in the discovery of four new GCs, three belonging to NGC 147, and one to NGC 185. I refer to these objects with the prefix 'PA'. Images of these objects in the g and K bands are shown in Figure 4.2. For completeness and comparison, the previously-known GCs are also included. Table 4.3 lists the coordinates, projected galactocentric radii ($R_{\rm proj}$) and Galactic reddening coefficients, $E(B-V)$, from Schlegel et al. (1998) for all clusters. While conducting the work on these two systems, I found various inconsistencies in the literature regarding the nomenclature of the previously-known GCs in NGC 147 and NGC 185. I describe these

[1] *VISTA* data flow system

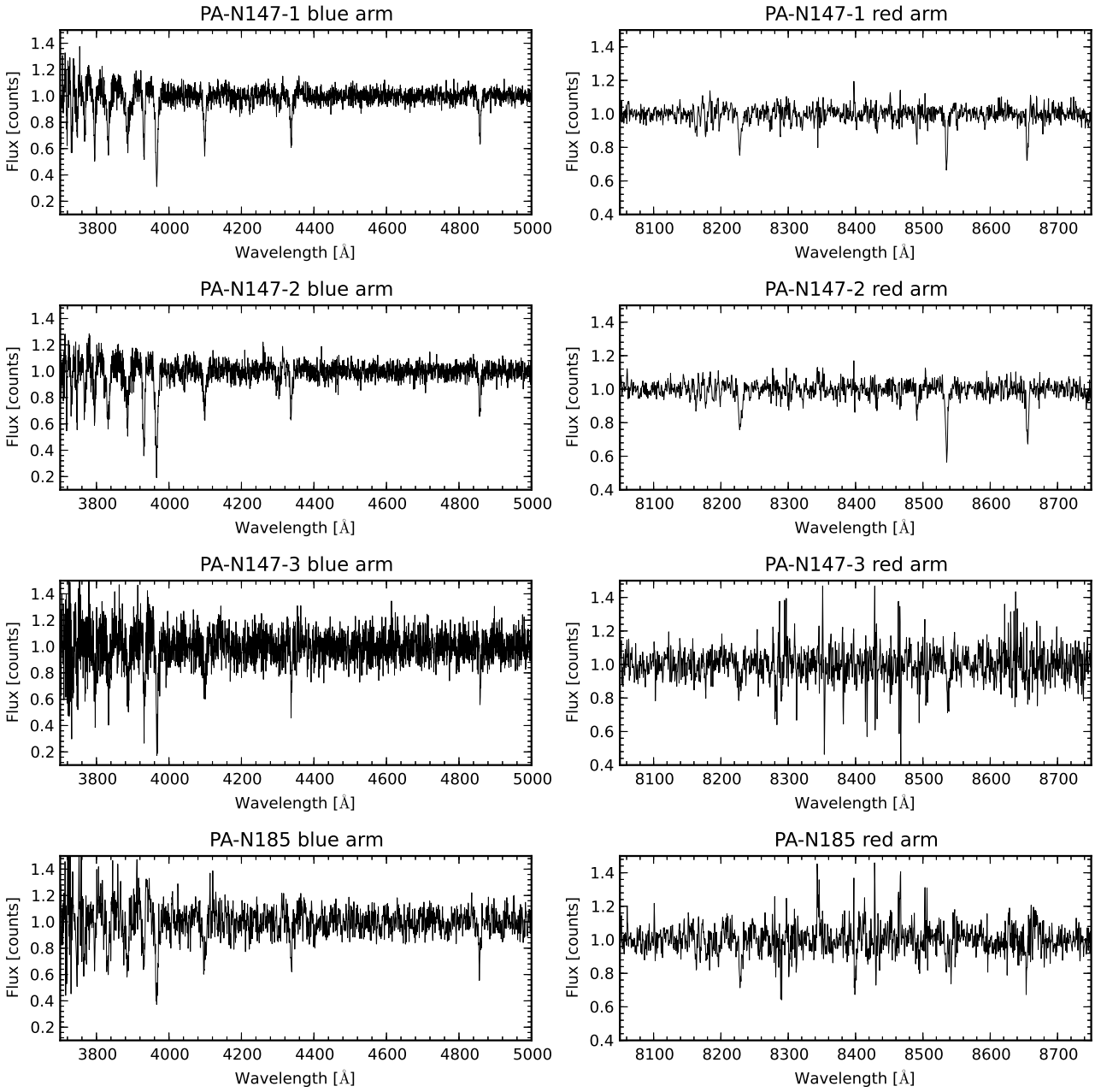

Figure 4.1 *Wavelength calibrated, continuum normalised spectra of the newly-discovered GCs. The left (right) panels show the spectra obtained with the blue (red) arm of the* ISIS *instrument.*

in Appendix B and I have made an effort to rectify these inconsistencies throughout this chapter whenever possible.

The search is based on homogeneous and sensitive imagery covering a very large fraction of the areas around these two dEs. The completeness of the search was quantified in a similar way as for the search of GCs in the M31 halo, as described in Section 1.4.2. The spacial incompleteness, due to the imperfect tiling of the imaging mosaic as well the gaps between the CCD frames in the MegaCam instrument, were quantified by generating a set of randomly located points in a circular area with having a radius of 15 kpc in projection from the centres of each dwarf galaxy. The density of generated points was ~ 100 arcmin^{-2} in each area. Then, the "observed" area was simply calculated by dividing the number of points that fell within the actual imaged regions by the total number of generated points. This test indicates that the fractions of NGC 147 and NGC 185 that are imaged out to a circular radius of 15 kpc are 96.3% and 93.5% respectively. Accounting for the distance to NGC 147 and NGC 185, it was found that the GC recovery is 100(50)% complete down to $M_V \approx -5.3(-4.1)$ around NGC 147, and down to $M_V \approx -5.0(-3.8)$ around NGC 185. For reference, these limits indicate that, if present, most if not all, of the Milky Way Palomar type clusters would be detected. Indeed, of the thirteen such objects known in the Milky Way that have available absolute integrated V magnitudes, 10 of them are brighter than -5.0, while 11 are brighter than -4.0 (Harris, 1996). The Koposov clusters, which have $M_V \sim -1$ (Koposov et al., 2007), would not be detected. However, these objects are difficult to find even in the Milky Way. It thus seems likely that all of the luminous remote GCs around these two systems have been uncovered. Full details on the incompleteness assessment is presented in Huxor et al. (2014).

Figure 4.3 shows the spatial distribution of GCs in the two galaxies where it can readily be seen that the newly-discovered GCs are much more remote than the known populations. Given this, it is possible that some of them might be bound to M31 rather than to NGC 147 or NGC 185. This could be especially true for PA-N147-3 which is located at projected radius of 6.6 kpc from the centre of its host galaxy NGC 147.

To examine this possibility, I calculate the probability of finding a genuine M31 GC projecting as close to NGC 147 and NGC 185 as the newly-found objects. I consider a circular annulus spanning 90–110 kpc in projected radius from M31's centre, the size of which is chosen to comfortably encompass the positions and extents of NGC 147 and NGC 185. Inside the annulus there are 10 M31 GCs excluding the new objects around NGC 147 and NGC 185

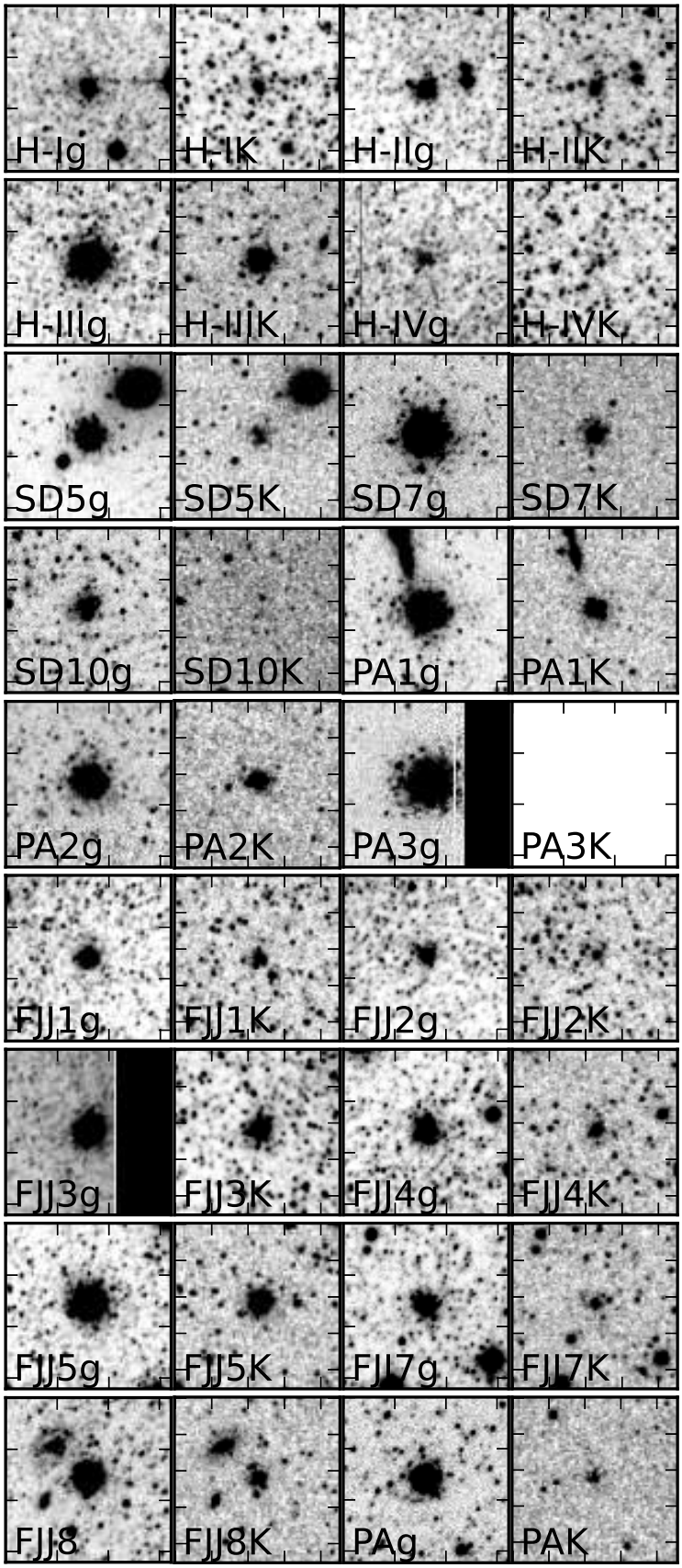

Figure 4.2 *g and K band images of all the clusters in NGC 147 and NGC 185. Each image is 30 × 30 arcsec wide. North is up and east is left. Cluster PA-N147-3 falls outside the near-IR survey and hence no K-band image is shown. Note that the scale in each thumbnail has been manually set to make each cluster easily visible.*

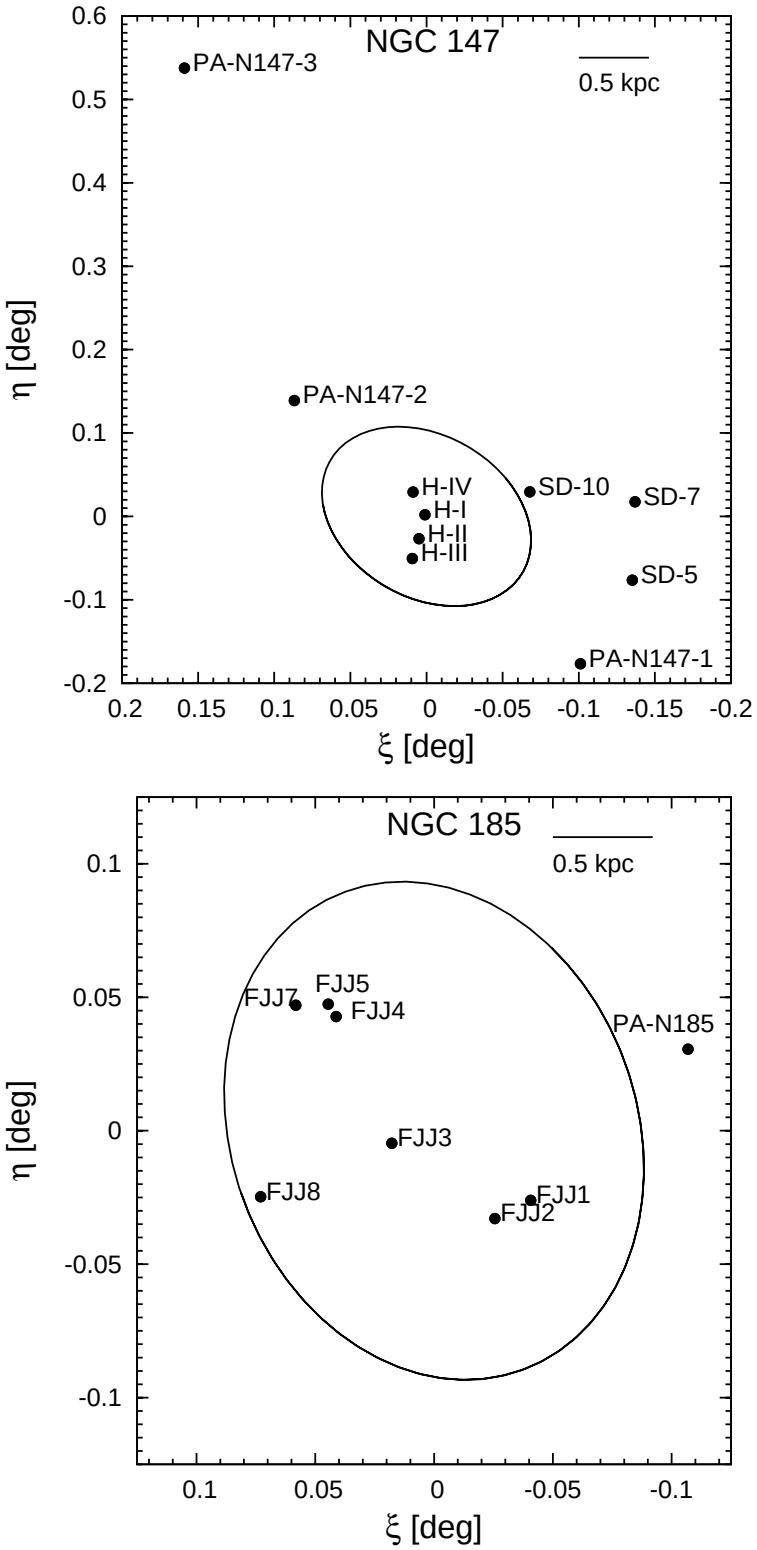

Figure 4.3 *Schematic view of NGC 147 (top panel) and NGC 185 (bottom panel) along with their GCs in standard coordinates. The centres of NGC 147 and NGC 185 are taken to be RA=00:33:12.1, Dec= 48:30:32 and RA=00:38:58.0, Dec=48:20:15 respectively (McConnachie, 2012). The ellipses represent the 25th magnitude B-band isophote taken from Corwin et al. (1994). The new GCs lie further away from the centre of their host galaxies than the known populations. On the top panel "H" stands for "Hodge" and "SD" stands for "GC-SD".*

Table 4.3 *Coordinates, projected radii, position angles and colour excess values of the GCs in NGC 147 and NGC 185.*

ID	RA(J2000) [h m s]	DEC(J2000) [d m s]	PA [deg]	$R_{\rm proj}$ [kpc]	$E(B-V)$ [mag]
Hodge I	00 33 12.2	+48 30 32.3	63	0.03	0.17
Hodge II	00 33 13.6	+48 28 48.7	172	0.34	0.17
Hodge III	00 33 15.2	+48 27 23.1	171	0.64	0.17
Hodge IV	00 33 15.0	+48 32 09.6	16	0.38	0.17
SD-GC5	00 32 22.9	+48 25 49.0	240	1.93	0.18
SD-GC7	00 32 22.2	+48 31 27.0	276	1.72	0.17
SD-GC10	00 32 47.2	+48 32 10.7	292	0.92	0.17
PA-N147-1	00 32 35.3	+48 19 48.0	210	2.53	0.15
PA-N147-2	00 33 43.3	+48 38 45.0	32	2.04	0.16
PA-N147-3	00 34 10.0	+49 02 39.0	16	6.97	0.16
FJJ I	00 38 42.7	+48 18 40.4	238	0.53	0.17
FJJ II	00 38 48.1	+48 18 15.9	220	0.45	0.17
FJJ III	00 39 03.8	+48 19 57.5	106	0.20	0.19
FJJ IV	00 39 12.2	+48 22 48.2	43	0.64	0.19
FJJ V	00 39 13.4	+48 23 04.9	42	0.70	0.19
FJJ VII	00 39 18.4	+48 23 03.6	50	0.81	0.19
FJJ VIII	00 39 23.7	+48 18 45.1	109	0.83	0.17
PA-N185	00 38 18.8	+48 22 04.0	286	1.20	0.18

(Huxor et al., 2014), which in turn equals a number density of 7.0×10^{-4} clusters/kpc^2. I then define a search radius of 7 kpc and 2 kpc around NGC 147 and NGC 185 respectively, chosen to be slightly larger than the GCs that have the largest projected distance from the centres of these systems. On average one would expect to find 0.008 GCs within a circular area of 2 kpc radius and 0.098 GCs within a 7 kpc circular radius. The Poisson probability of finding one or more M31 GCs within a 2 kpc radius of NGC 185 and within a 7 kpc radius of NGC 147 is 1% and 11% respectively. The probability of finding three or more GCs within a 7 kpc radius of NGC 147 drops to 0.01%. The conclusion from this analysis is that, in absence of other information, there is a small chance that at least one of the newly-discovered GCs around NGC 147 could be part of the M31 halo GC system, while the newly-discovered cluster around NGC 185 almost certainly belongs to its apparent host galaxy. It is also worth noting that two of the newly-discovered GCs around NGC 147 appear to lie on top of tidal tails which emanate from this system (Lewis et al., 2013, Irwin et al. in prep).

The measured velocities of the new GCs can be used as another indicator of whether they are bound to the dEs or to M31. The velocity dispersion of the M31 halo GCs that lie beyond 100 kpc in projection is $\sim$80 km s^{-1} (see Section 3.3). As will be discussed in Section 4.5, given the large difference between the radial velocities of the new NGC 147 GCs and that of M31[2], it is

[2]As a reminder, the heliocentric radial velocity of M31 is -301 $\pm$ 4 km s^{-1} (Courteau & van den Bergh, 1999).

likely that they are hosted by the dwarf galaxy. This is not the case for PA-N185, as the difference between it and the M31 velocity is smaller than the M31 outer halo GC velocity dispersion. However, when combined with the probability arguments presented above, the velocity measurements strengthen the conclusion that the new GCs are probably members of the dE systems and not the M31 halo.

It is interesting to point out that the cluster PA-N147-3 projects in position halfway between NGC 147 and the newly-discovered dwarf spheroidal Cass II (Conn et al., 2012, Irwin et al., in prep). Furthermore, it has a similar radial velocity to Cass II, which is measured to be -145 $\pm$ 3 km s^{-1} (Collins et al., 2013). It is therefore possible that this GC could be a satellite of Cass II instead of NGC 147, or else not bound to either system.

4.3 Photometry

I performed integrated photometry on all the GCs in these two dwarf galaxies with the *phot* task within IRAF. The centroid algorithm within the *phot* task was used to determine accurate centres of the clusters by computing the intensity weighted means of the marginal profiles along the physical x and y axes in the *g*-band images. Offsets from nearby bright stars were used to translate the accurately determined centre of each cluster to the rest of the images, both optical and near-IR. I then used circular apertures to sum the total flux coming from each GC. Concentric "sky" annuli around the photometric apertures, with typical width of $\sim$ 7 arcsec, were employed to determine the mean background flux contribution. I carefully selected the exact sizes of the background annuli to avoid pollutants such as bright foreground stars and background galaxies. As some of these clusters lie in very crowded fields, I performed detailed tests to ensure that the background contribution was reliably subtracted.

For each GC, I constructed a curve-of-growth by measuring the flux in concentric apertures of increasing radius. The final photometric aperture size was set to be the point at which the cumulative flux becomes flat. This did not work for clusters in the very dense fields, where I adopted an aperture size based mainly on visual inspection, even though the curve-of-growth was not flat. To reduce background contamination, I used a smaller aperture of 3.5 arcsec when measuring colours, valid if assuming that no colour gradients are present within the GCs. Aperture sizes for both colours and

magnitudes were matched to be the same in the optical and near-IR data. For all photometric measurements, the instrumental magnitudes were zero-point calibrated, corrected for atmospheric extinction and corrected for Galactic reddening using the Schlegel et al. (1998) maps interpolated to the position of each GC. Table 4.4 and 4.5 list the extinction-corrected magnitudes and colours of all GCs in NGC 147 and NGC 185.

Some objects required special treatment. In the cases of Hodge II and SD-GC5, I applied mask consistently across all filters in order to exclude bright contaminating objects that entered the photometric aperture. The cluster PA-N147-3 was split between two separate CCD frames in the optical data. To account for this, I summed the flux within rectangular apertures on each frame and combined them – this strictly represents a lower limit on the total magnitude of this object. This same cluster has the largest projected radius of all GCs in my sample and it falls outside the near-IR survey area, meaning no near-IR measurement is possible. The cluster SD-10 was not detected in the near-IR imaging and the corresponding near-IR magnitudes listed provide upper limits on its brightness. The GC FJJ III lies very close to the edge of the chip in the g band, while it is split between two chips in the i band. For the optical photometry of this cluster, I used previously published data obtained with the *Isaac Newton Telescope Wide Field Camera (INT/WFC)* (McConnachie et al., 2005). This was not possible for PA-N147-3 as it falls outside the area covered by the *INT* survey. The *INT/WFC* survey uses the Johnson V and Gunn i passbands, which are on the Vega scale. Hence the magnitudes of FJJ III were converted to the *CFHT/MegaCam* system, which is on the AB scale, via the following transformations from Ibata et al. (2007):

$$i_{MC} = i_{INT} - 0.105\,, \tag{4.1}$$

$$g_{MC} = \begin{cases} 0.030 + 1.400 \times (V-i)_{INT} + i_{MC} \\ \qquad\qquad\qquad \text{for} \quad (V-i)_{INT} \quad < 1.3\,, \\ \\ 0.491 + 1.046 \times (V-i)_{INT} + i_{MC} \\ \qquad\qquad\qquad \text{for} \quad (V-i)_{INT} \quad > 1.3\,. \end{cases} \tag{4.2}$$

where the subscripts MC and INT refer to the filters employed by the *CFHT/MegaCam* and *INT/WFC* instruments respectively.

Table 4.4 *Photometry for the NGC147 and NGC 185 GCs. $M_{V,0}$ was calculated assuming the line-of-sight distance to the clusters is same as to their host galaxies. Superscripts refer to (1) the presence of masked bright objects in the photometric aperture, (2) the magnitude is a lower limit as the cluster is split between CCD frames and was measured in a rectangular aperture, (3) the optical photometry is measured on* INT *imaging.*

ID	Aperture [arcsecs]	g_0 [mag]	i_0 [mag]	J_0 [mag]	H_0 [mag]	K_0 [mag]	V_0 [mag]	I_0 [mag]	$M_{V,0}$ [mag]
Hodge I	6.5	17.17 ± 0.04	16.31 ± 0.02	14.84 ± 0.02	14.25 ± 0.02	14.13 ± 0.03	16.86 ± 0.03	15.92 ± 0.02	-7.40
Hodge II[1]	4.6	17.79 ± 0.04	17.07 ± 0.04	15.93 ± 0.02	15.30 ± 0.02	15.14 ± 0.02	17.53 ± 0.03	16.71 ± 0.04	-6.73
Hodge III	7.4	16.29 ± 0.03	15.65 ± 0.02	14.71 ± 0.01	14.15 ± 0.01	14.18 ± 0.01	16.05 ± 0.02	15.29 ± 0.02	-8.21
Hodge IV	4.6	18.83 ± 0.04	17.81 ± 0.03	16.55 ± 0.03	15.98 ± 0.03	15.94 ± 0.04	18.48 ± 0.03	17.41 ± 0.03	-5.78
GC-SD5[1]	5.6	17.83 ± 0.02	17.20 ± 0.01	16.36 ± 0.02	15.81 ± 0.02	15.77 ± 0.03	17.60 ± 0.01	16.85 ± 0.01	-6.66
GC-SD7	7.4	16.73 ± 0.01	16.03 ± 0.01	15.03 ± 0.01	14.49 ± 0.01	14.43 ± 0.02	16.47 ± 0.01	15.66 ± 0.01	-7.79
GC-SD10	4.6	19.59 ± 0.01	18.86 ± 0.01	>17.8	>17.3	>17.2	19.32 ± 0.01	18.49 ± 0.02	-4.94
PA-N147-1	6.5	16.72 ± 0.01	16.09 ± 0.01	15.15 ± 0.01	14.69 ± 0.01	14.64 ± 0.02	16.49 ± 0.01	15.74 ± 0.01	-7.77
PA-N147-2	6.5	17.11 ± 0.01	16.44 ± 0.01	15.37 ± 0.01	14.89 ± 0.01	14.86 ± 0.02	16.87 ± 0.01	16.08 ± 0.01	-7.39
PA-N147-3[2]		<17.2	<17.6	...	...	...	<17.48	<17.4	< -6.9
FJJ I	4.6	17.96 ± 0.03	17.22 ± 0.02	15.24 ± 0.02	15.39 ± 0.03	15.06 ± 0.02	17.70 ± 0.03	16.85 ± 0.03	-6.26
FJJ II	4.6	18.28 ± 0.04	17.49 ± 0.03	15.59 ± 0.03	15.75 ± 0.03	15.73 ± 0.04	18.00 ± 0.03	17.12 ± 0.03	-5.96
FJJ III[3]	7.4	16.20 ± 0.29	15.55 ± 0.11	13.80 ± 0.02	14.02 ± 0.02	13.94 ± 0.01	15.99 ± 0.17	15.14 ± 0.11	-7.97
FJJ IV	5.6	17.58 ± 0.03	17.00 ± 0.02	15.24 ± 0.02	15.53 ± 0.03	15.60 ± 0.04	17.37 ± 0.02	16.65 ± 0.02	-6.59
FJJ V	7.4	16.38 ± 0.03	15.66 ± 0.02	13.85 ± 0.01	14.09 ± 0.02	14.00 ± 0.01	16.12 ± 0.02	15.30 ± 0.02	-7.84
FJJ VII	4.6	18.36 ± 0.02	17.62 ± 0.01	15.80 ± 0.02	16.06 ± 0.03	16.07 ± 0.04	18.10 ± 0.02	17.25 ± 0.02	-5.85
FJJ VIII	4.6	17.29 ± 0.01	16.59 ± 0.01	14.82 ± 0.01	15.08 ± 0.02	15.09 ± 0.02	17.04 ± 0.01	16.23 ± 0.01	-6.92
PA-N185	4.6	18.65 ± 0.01	17.98 ± 0.01	16.23 ± 0.03	16.54 ± 0.04	16.39 ± 0.06	18.41 ± 0.01	17.62 ± 0.01	-5.55

Table 4.5 *Colours for the NGC 147 and NGC 185 GCs. All measurements are done within a 3.5 arcsec aperture radius in order to minimise background contamination. Colours of PA-N147-3 cannot be calculated as different portions of the cluster have been measured on the optical imaging and it was not imaged in the near-IR. Superscripts refer to (1) the presence of masked bright objects in the photometric aperture, (2) the photometry is measured on* INT *imaging.*

ID	$(g-i)_0$ [mag]	$(g-J)_0$ [mag]	$(g-H)_0$ [mag]	$(g-K)_0$ [mag]	$(V-I)_0$ [mag]	$(V-K)_0$ [mag]
Hodge I	0.72±0.04	1.97±0.04	2.51±0.04	2.59±0.04	0.83±0.04	2.33±0.03
Hodge II[1]	0.68±0.07	1.75±0.05	2.30±0.05	2.35±0.05	0.79±0.07	2.11±0.04
Hodge III	0.61±0.04	1.57±0.04	2.07±0.04	2.10±0.04	0.73±0.04	1.87±0.03
Hodge IV	0.96±0.05	2.31±0.05	2.89±0.05	2.96±0.05	1.02±0.04	2.62±0.05
GC-SD5	0.60±0.02	1.46±0.03	2.00±0.02	2.03±0.03	0.73±0.01	1.81±0.03
GC-SD7	0.67±0.01	1.69±0.02	2.22±0.01	2.28±0.02	0.78±0.01	2.04±0.02
GC-SD10	0.76±0.02	<1.8	<2.4	<2.3	0.85±0.02	<1.98±0.11
PA-N147-1	0.52±0.01	1.60±0.02	2.04±0.01	2.14±0.02	0.75±0.01	1.91±0.02
PA-N147-2	0.66±0.01	1.70±0.02	2.16±0.02	2.20±0.02	0.79±0.01	1.97±0.02
PA-N147-3	...	...	...	...	...	...
FJJ I	0.73±0.04	2.64±0.04	2.41±0.04	2.55±0.04	0.84±0.04	2.30±0.04
FJJ II	0.75±0.05	2.63±0.05	2.46±0.05	2.52±0.05	0.85±0.04	2.25±0.04
FJJ III[2]	0.67±0.31	2.56±0.29	2.30±0.29	2.42±0.29	0.86±0.19	2.22±0.16
FJJ IV	0.63±0.04	2.39±0.03	2.09±0.04	2.10±0.04	0.75±0.04	1.87±0.04
FJJ V	0.70±0.03	2.52±0.03	2.24±0.03	2.31±0.03	0.81±0.03	2.06±0.02
FJJ VII	0.73±0.03	2.60±0.03	2.34±0.03	2.36±0.04	0.84±0.03	2.10±0.03
FJJ VIII	0.69±0.02	2.48±0.02	2.22±0.03	2.24±0.02	0.80±0.02	2.00±0.02
PA-N185	0.68±0.01	2.50±0.03	2.22±0.03	2.38±0.04	0.80±0.01	2.13±0.04

To allow comparison with other work, Table 4.4 and 4.5 also contain magnitudes and colours converted to the more widely used Johnson/Cousins filters. The *CFHT/MegaCam* data was transformed into the standard V and I system via corrected relations from Huxor et al. (2008)[3]:

$$g_1 = g + 0.092 \tag{4.3a}$$
$$i_1 = i - 0.401 \tag{4.3b}$$
$$V = g_1 - 0.42(g_1 - i_1) + 0.04(g_1 - i_1)^2 + 0.10 \tag{4.3c}$$
$$I = i_1 - 0.08(g_1 - i_1) + 0.06 \tag{4.3d}$$

These relations were derived for the i' filter used with *CFHT/MegaCam* pre-June 2007, while in October 2007 a new i filter was installed on this instrument. The data used in this work were taken with the new i filter and so before transforming the *MegaCam* data to the standard V and I filters, conversion from the new i to the old i filter was done using the relation derived in Ibata et al. (2014):

$$i_{new} = \begin{cases} -0.010 + 0.031 \times (g - i_{old}) + i_{old} \\ \qquad\qquad \text{for} \quad (g - i_{old}) \quad < 1.9\,, \\ \\ -0.081 + 0.069 \times (g - i_{old}) + i_{old} \\ \qquad\qquad \text{for} \quad (g - i_{old}) \quad > 1.9\,. \end{cases} \tag{4.4}$$

In deriving magnitudes and colours, various uncertainties are included and appropriately combined. The instrumental magnitude uncertainties reported by IRAF are small, as the clusters are much brighter than the background sky. For GCs lying within the main optical bodies of their host dwarf galaxies, the main source of uncertainty comes from the local background, which is contaminated by resolved stars from the host galaxy as well as the underlying diffuse light. To assess the uncertainty in the background, I randomly placed 10 apertures around each cluster sampling the local sky. While the apertures include the resolved field star component and the diffuse light of the host dwarf galaxies, I made sure to place them in a way that obvious contaminants such as background galaxies or foreground Milky Way stars are excluded. I set the sky apertures to have the same size as the magnitude and colour apertures that I used to photometer the GCs. I found the standard deviation of all 10

[3]Note that the transformation equations in that paper were incorrectly written, but the magnitudes derived were based on the correct equations.

sky measurements around each cluster, and added this in quadrature to the instrumental and zero-point errors. Furthermore, every conversion between filters introduces an additional uncertainty to the derived magnitudes and colours that I account for as well.

4.4 Ages and metallicities

I derive age and metallicity estimates for the two cluster samples using the integrated optical and near-IR photometry. In principle, one can determine accurate ages and metallicities of GCs with high quality spectroscopic data. However, my spectra have low signal-to-noise, and only two out of the four new GCs have spectra that are suitable for metallicity determination. Furthermore, since my goal is to present a homogeneous analysis of the samples, including objects for which I do not have spectroscopic data, I prefer to base the analysis on integrated photometry alone.

Optical colours are well-known to suffer from an age-metallicity degeneracy, however the addition of near-IR measurements can greatly improve the situation (e.g. Puzia et al., 2002; Hempel et al., 2005; Chies-Santos et al., 2011). This is because of the different sensitivities to age and metallicity of the optical-optical and optical-near-IR colours. The optical g-band is most sensitive to stars near the main sequence turn-off, the magnitudes of which are mostly driven by age. Conversely, the near-IR K band is most sensitive to red giant branch stars (Saviane et al., 2000; Yi et al., 2001). The $g - i$ and $g - K$ colours have similar sensitivity to age, but $g - K$ measures the temperature of the red giant branch which more reflects metallicity than age. Plotting these colours on a colour-colour diagram and comparing to simple stellar population (SSP) model tracks allow one to derive estimates of the age and metal content of each GC.

Various SSP models have been constructed to date (e.g. Maraston, 1998; Bruzual & Charlot, 2003; Marigo et al., 2008; Vazdekis et al., 2010; Bressan et al., 2012). Despite improvements over time, discrepancies still exist between models. One of the largest intrinsic uncertainties in SSP models comes from the limited understanding of certain phases of advanced stellar evolution such as the thermally-pulsating asymptotic giant branch (TP-AGB) phase. Different attempts to implement this phase have led to large differences in the near-IR fluxes. Stars in this phase are short-lived making calibration difficult (Girardi et al., 2010). Models having prominent TP-AGB phases cause the

near-IR luminosity of objects to be overpredicted, but this only affects objects of young to intermediate ages (Kriek et al., 2010). Another problem related to each SSP model is the convergence of the isochrones in the metal-poor regime which produces large uncertainties in the derived properties.

Figure 4.4 shows colour-colour diagrams constructed using the optical and near-IR photometry presented in Table 4.5. The overplotted isochrones span the metallicity range $-2.2 < [\mathrm{Fe/H}] < 0.6$ dex. While the SSP model tracks shown on Figure 4.4 are from Bressan et al. (2012), I have checked that none of the results presented in this section are significantly affected by the chosen SSP model. I resorted to using the native *CFHT/Megacam* rather than the more common Johnson/Cousins system in order to avoid uncertainties arising from the colour transformations, as the SSP model tracks were readily a vailable for the *CFHT/Megacam* system. Figure 4.4 shows that all clusters with the exception of Hodge IV in NGC 147 are metal-poor with $[\mathrm{Fe/H}] \lesssim -1.25$ dex. It would be rather interesting if Hodge IV is indeed as metal-rich as inferred from the SSP diagram. However, it needs to be noted that it is the second faintest cluster in NGC 147 and appears irregular in shape in the MegaCam imaging – see Figure 4.2 – while close to the detection limit in the near-IR data. Although one of the first clusters to be discovered in NGC 147 (Hodge, 1976), high resolution images of this object do not yet exist. Even with high quality ground-based data such as PAndAS, it is difficult to confirm it is a genuine GC and not, for example, an asterism in the NGC 147 field.

The ages of the clusters are more difficult to estimate. At face value, it appears that half of the GCs are old and half are of intermediate age. However, inspecting the clusters that lie on the young to intermediate age tracks, it is found that they are often located in or near the main bodies of their host galaxies. As discussed earlier, these regions are very crowded and often have strong non-linear background gradients that can skew the colours of the GCs. This is certainly an issue for Hodge I in NGC 147 which has a redder $(g - K)_0$ colour than any of the tracks shown. The method of photometric age estimation is not particularly accurate even when free of these complications so I hesitate to claim that I have found evidence for the presence of intermediate age GCs. Furthermore, due to the way the SSP model isochrones are calibrated, small changes in either of the colours used in Figure 4.4 will drastically affect their age estimates, while only minimally impacting their metallicity estimates.

Another outlier in Figure 4.4 is GC-SD10 in NGC 147 which has a redder $(g - i)_0$ and bluer $(g - K)_0$ colour than any of the tracks. This object is the faintest out of all clusters known in the two dEs and was not detected in the K band

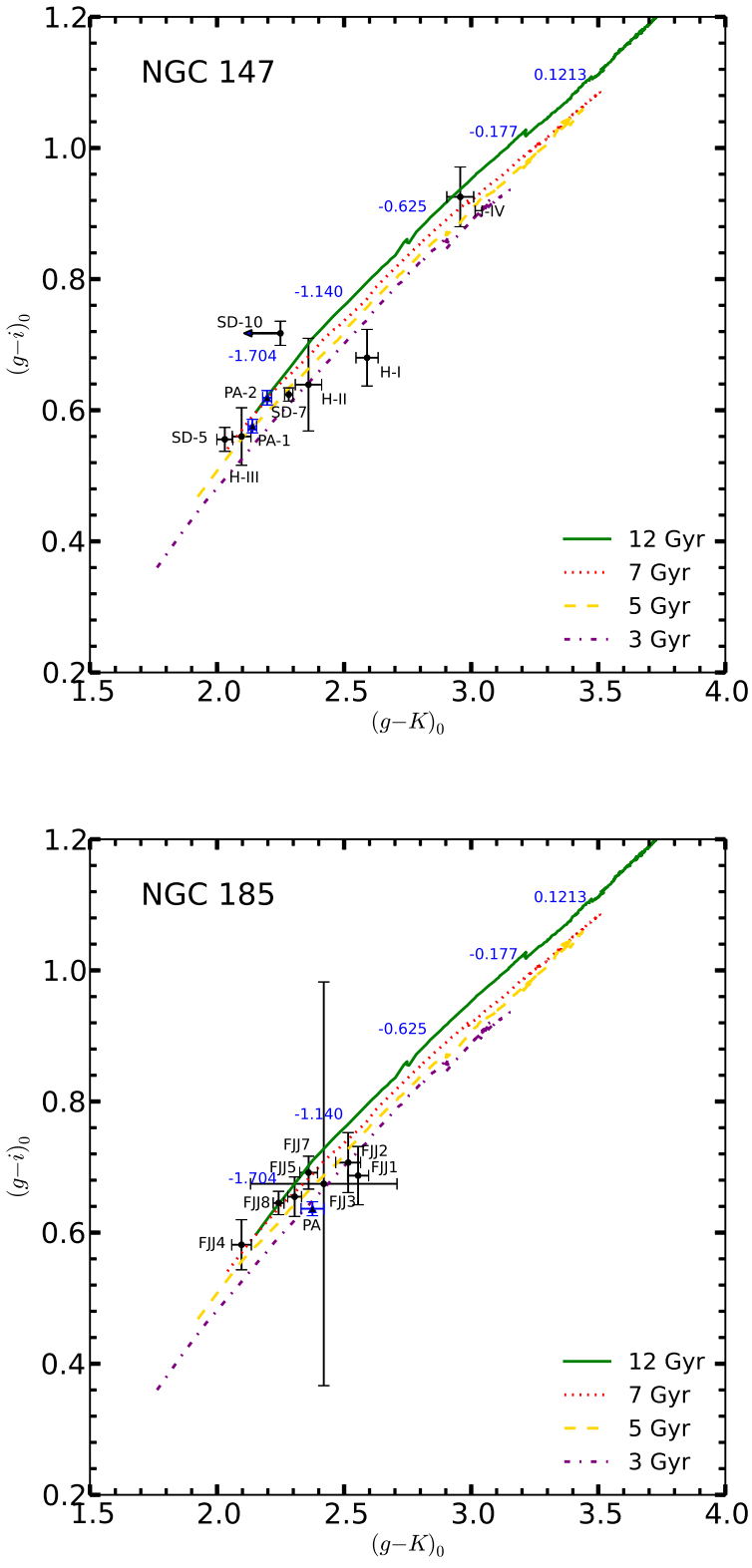

Figure 4.4 *$(g-i)_0$ vs. $(g-K)_0$ colours of GCs in NGC 147 (left) and NGC 185 (right) overlaid on top of isochrones from Bressan et al. (2012). The corresponding metallicity ([Fe/H]) values are indicated. The newly-discovered GCs are marked as blue triangles. All but one cluster is found to be metal-poor, while the ages are more difficult to constrain. The uncertainties of FJJ III are enormous since the data comes from lower quality* INT *imaging.*

Table 4.6 *[Fe/H] values for GCs in NGC 147 and NGC 185. Columns refer to: (a) values obtained using the colour-metallicity relation from Kissler-Patig et al. (2002); (b) Da Costa & Mould (1988); (c) Sharina et al. (2006); Sharina & Davoust (2009); (d) Sharina et al. (2006). Superscripts refer to: (1) spectroscopic study; (2) isochrone fitting. Sharina et al. (2006) originally presented [Z/H] values which were converted to [Fe/H] via the relation from Salaris & Cassisi (2006).*

ID	[Fe/H](a) [dex]	[Fe/H](b)[1] [dex]	[Fe/H](c)[1] [dex]	[Fe/H](d)[2] [dex]
Hodge I	-1.3 ± 0.4	-1.9 ± 0.15	-1.0 ± 0.5	
Hodge II	-1.7 ± 0.4	-2.5 ± 0.25	-1.6 ± 0.5	
Hodge III	-2.1 ± 0.3		-1.8 ± 0.5	-2.0 ± 0.1
Hodge IV	-0.7 ± 0.4			
GC-SD5	-2.2 ± 0.3		-1.7 ± 0.3	
GC-SD7	-1.8 ± 0.3		-1.6 ± 0.2	
GC-SD10	-1.9 ± 0.4			
PA-N147-1	-2.0 ± 0.3			
PA-N147-2	-1.9 ± 0.3			
PA-N147-3				
FJJ I	-1.3 ± 0.4	-1.4 ± 0.10	-1.2 ± 0.4	-1.6 ± 0.2
FJJ II	-1.4 ± 0.4	-1.2 ± 0.25		-2.1 ± 0.2
FJJ III	-1.5 ± 0.5	-1.7 ± 0.15	-1.4 ± 0.6	-2.0 ± 0.1
FJJ IV	-2.1 ± 0.3	-2.5 ± 0.25	-1.6 ± 0.5	-2.0 ± 0.2
FJJ V	-1.8 ± 0.3	-1.8 ± 0.15	-1.1 ± 0.6	-1.5 ± 0.1
FJJ VII	-1.7 ± 0.4		-0.4 ± 0.6	
FJJ VIII	-1.9 ± 0.3		-1.1 ± 0.9	
PA-N185	-1.6 ± 0.4			

imaging. The quoted K band magnitude represents an upper limit, suggesting that the actual $(g-K)_0$ colour must lie blueward of the point in in Figure 4.4. Although these colours seem unusual, GC-SD10 has been spectroscopically confirmed by Sharina & Davoust (2009) as a GC in NGC 147. Finally, even though the measured colours put FJJ III on the model tracks on Figure 4.4, the accompanying uncertainties make constraining the age and metallicity of this cluster nearly impossible.

An alternative way to determine the metallicities of GCs is to use empirical colour-metallicity relations. I adopt the relationship derived by Kissler-Patig et al. (2002) (eq. 4.5), calibrated using 129 M31 GCs that have $E(B-V) < 0.27$, to further constrain the metal content of the NGC 147 and NGC 185 GC systems. This relationship is valid over the interval $-2.3 <$ [Fe/H] < -0.2 dex.

$$[\mathrm{Fe/H}] = (V-K)_0 \times 1.82 \pm 0.11 - 5.52 \pm 0.26 \tag{4.5}$$

Table 4.6 shows the metallicities derived with the Equation 4.5 and affirms my conclusion that all clusters except for Hodge IV are indeed metal-

poor. Although the available spectra are not used to derive metallicities, the similarly strong Balmer lines visible in Figure 4.1 for PA-N147-1 and PA-N147-2 supports the similar metallicities derived from their broadband colours. There is also a hint at a radial metallicity trend in both galaxies, since GCs with projected radii > 0.55 kpc have systematically lower [Fe/H] values by ~ 0.6 dex compared to the central population. For comparison, Table 4.6 also shows metallicities for some of the previously-known GCs derived from spectroscopic studies (Da Costa & Mould, 1988; Sharina et al., 2006; Sharina & Davoust, 2009), and from colour-magnitude diagram isochrone fitting (Sharina et al., 2006). There is generally a good agreement with past studies, lending further confidence to my metallicity estimates. The only exception is FJJ VII in NGC 185 for which a difference larger than 1 dex is seen between the measurements presented here and the spectroscopic measurements of Sharina et al. (2006). I currently have no explanation for this.

4.5 Kinematics

Heliocentric radial velocities for the newly-discovered GCs around NGC 147 and NGC 185 were derived with the same customized χ^2 minimization routine that I developed for their M31 halo counterparts. I used all available template spectra described in Table 2.2 for the minimization process. The measured heliocentric radial velocities for the new GCs are reported in Table 4.7. For reference, the radial velocities of the previously-known clusters, as well as the radial velocities of the dEs themselves are taken from the literature and also shown.

Even though the complete radial velocity data set of the NGC 147 and NGC 185 GC systems is heterogeneous, it can be used to explore the kinematic properties of the clusters in these two dwarf galaxies. In particular, I will test whether the GCs exhibit any measurable rotation signature, as well as constrain their velocity dispersion.

I employ the Bayesian methodology, discussed previously in Chapter 3, to constrain the kinematics of the these two GC systems, in a similar style as for the M31 outer halo GCs. Given the small number of clusters in these dE galaxies – only 10 in NGC 147, and 7 in NGC 185 – I modify the kinematic model $\mathcal{M}$ from Section 3.2 to contain only simple rotation along circular orbits as described in Equation 3.4, and a Gaussian velocity dispersion that does not

Table 4.7 *Heliocentric radial velocities and their uncertainties for the newly-discovered GCs around NGC 147 and NGC 185. For comparison, the heliocentric velocities of the previously known clusters, as well as for NGC 147 and NGC 185 are also shown.*

ID	$V_{\rm helio}$ [km s^{-1}]	$\Delta V_{\rm helio}$ [km s^{-1}]	Reference
NGC 147	−193.1	0.8	Geha et al. (2010)
Hodge I	−147	30	Sharina & Davoust (2009)
Hodge II	−189	25	Sharina & Davoust (2009)
Hodge III	−118	30	Sharina & Davoust (2009)
Hodge IV	−235	35	Sharina & Davoust (2009)
SD-GC5	−187	15	Sharina & Davoust (2009)
SD-GC7	−198	10	Sharina & Davoust (2009)
SD-GC10	−180	30	Sharina & Davoust (2009)
PA-N147-1	−215	10	This work
PA-N147-2	−219	10	This work
PA-N147-3	−133	24	This work
NGC 185	−203.8	1.1	Geha et al. (2010)
FJJ I	−264		Sharina et al. (2006)
FJJ II			Sharina et al. (2006)
FJJ III	−290		Sharina et al. (2006)
FJJ IV	−157		Sharina et al. (2006)
FJJ V	−370		Sharina et al. (2006)
FJJ VII	−217		Sharina et al. (2006)
FJJ VIII	−148		Sharina et al. (2006)
PA-N185	−254	15	This work

change as a function of projected distance from the centre of the two dE:

$$\sigma^2 = (\Delta v)^2 + \sigma_0^2 \tag{4.6}$$

Thus, this model now takes the form:

$$p_{i,\mathcal{M}}(v_i, \Delta v_i | v_{\rm rot}, \sigma) = \frac{1}{\sqrt{2\pi\sigma^2}}\ e^{-\frac{(v_i - v_{\rm rot})^2}{2\sigma^2}} \tag{4.7}$$

where, similar to before, where v_{rot} is the systemic rotation described by Equation 3.4, v_i are the observed heliocentric radial velocities of the GCs as presented in Table 4.7, and σ is a velocity dispersion. Hence, the likelihood function for the above kinematic model is:

$$p_{\mathcal{M}}(D|\Theta) = \mathcal{L}_{\mathcal{M}}\left(v, \Delta v, \theta | A, \theta_0, \sigma_0\right) = \prod_i p_{i,\mathcal{M}} \tag{4.8}$$

where v, Δv, and θ are the observed properties of the GCs, while A, θ_0, and σ_0 are the model free parameters. The priors are left out since formally they are assumed to be flat. Since the non-rotating kinematic model $\mathcal{N}$ described in Section 3.2 is just a special case of model $\mathcal{M}$ for which the amplitude is 0, I will not consider it here.

I systematically calculate the likelihood function via a brute-force method where the parameters A, θ_0 and σ_0 are set on a grid. In the case of NGC 147, the amplitude A and the velocity dispersion σ_0 both range from 0 to 150 km s^{-1} with increments of 2 km s^{-1}, while the rotation axis θ_0 is explored from 0 to 2π rad with a step size of 0.15 rad. For the NGC 185 system, A and σ_0 both range from 0 to 300 km s^{-1} with increments of 5 km s^{-1}, while θ_0 is explored from 0 to 2π rad with a step size of 0.15 rad as before. The parameter grid for NGC 185 is made wider in order to fully sample the posterior distribution functions of the model parameters that would otherwise appear truncated if the same grid as for NGC 147 was used.

The kinematics of NGC 147 GC system

Figure 4.5 shows the results of the kinematic analysis for the NGC 147 GC system. The top panel shows the heliocentric velocities of the GCs, corrected for the systemic motion of NGC 147, versus their position angle around the galaxy. If an obvious rotation were present, the data points would be expected to follow a sinusoidal pattern. One can see from the data presented in this plot that this system does not appear to exhibit any significant rotation. Indeed, this observation is reinforced by looking at the middle left panel where the posterior probability function of the amplitude peaks at 0. This function is truncated at 0, since I only consider positive amplitudes, so calculating the expectation value is not informative in this case. Thus I calculate that the measured value for the amplitude is < 17 km s^{-1} with 68% confidence. Furthermore, the absence of a clear dominant peak in the marginalized posterior distribution function of θ_0 (middle right panel in Figure 4.5) confirms that there is no significant rotation in this system.

On the other hand, the velocity dispersion of this system is well determined. The expectation value is found to be 32^{+20}_{-11} km s^{-1}, while the peak of the distribution is found at 26^{+13}_{-14} km s^{-1}. While it is possible for the GC system of NGC 147 to exhibit a small rotational signature, such a signature will be significantly smaller than the measured velocity dispersion, as well as the errors on the individual GC velocity measurements. It also important to note that the non-detection of a rotation signature is not dependent on the grid sampling, but it is a limitation of the data. It is interesting to note that Geha et al. (2010) found the stellar component of NGC 147 to exhibit an internal rotation of 17 ± 2 km s^{-1} and an average velocity dispersion of 16 ± 1 km s^{-1} out to ~ 3 kpc in projection. If such a rotation is also present in the GC system of this galaxy, it can not be robustly determined with the

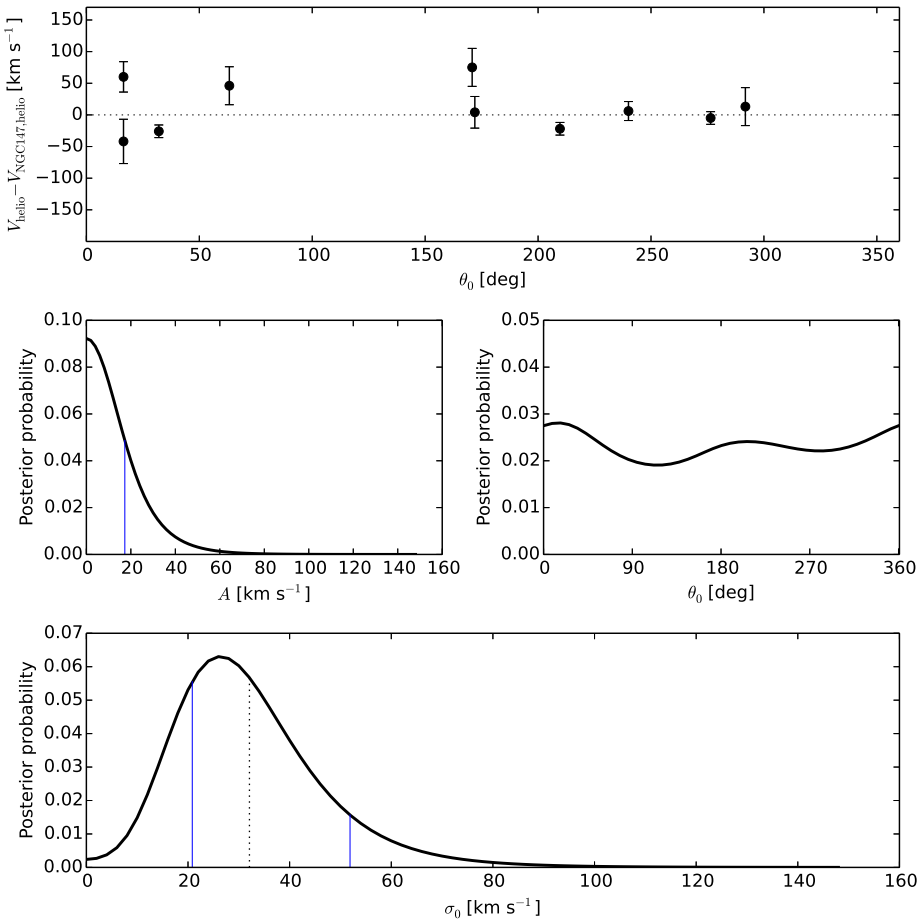

Figure 4.5 *Top panel: heliocentric radial velocity corrected for the systemic motion of NGC 147 vs. position angle of the GCs in this dE. No significant rotation is visible in the data. Middle left panel: marginalized posterior distribution function for the amplitude of this system. The amplitude is consistent with 0. As an upper bound, the amplitude is < 17 km s^{-1} with 68% confidence (blue line). Middle right panel: the posterior function of θ_0. Given no strong peak, reinforces the argument that there is no significant rotation in this system. Bottom panel: the posterior function for σ_0. Also labelled is the expectation value with the 68% confidence intervals.*

current velocity data.

The kinematics of the NGC 185 GC system

I repeat the same analysis for the GC system of NGC 185, the results of which are displayed in Figure 4.6. In this case, I assume an uncertainty of 10 km s^{-1} for the GC velocities adopted from Sharina et al. (2006), since there are no uncertainties published in that study. The top panel in Figure 4.6, shows the velocity of the NGC 185 GCs, corrected for the systemic radial motion of their host, versus their position angle. One can see again that there is no clear evidence for any systemic rotation. However, looking at the posterior

distribution of the amplitude for (middle left panel on Figure 4.6), one can see that even thought the peak of this distribution is consistent with 0, it is very broad. In fact, giving an upper limit, the measured value for the amplitude is < 82 km s^{-1} with 68% confidence. Also, the posterior distribution of the rotation axis θ_0 appears to exhibit a pronounced peak at around 350 deg. However, this peak has a low probability which makes the formal uncertainties quite large as seen on the middle right panel of Figure 4.6. Any possible rotation signature here is most likely induced by the low number statistics combined with most of the clusters having similar position angles.

The marginalized posterior distribution function of the σ_0 of this system is well defined but the value itself is poorly constrained. The expectation value of σ_0 is 102^{+71}_{-20} km s^{-1}, and the posterior function peaks at 79^{+28}_{-32} km s^{-1}. The low number of GCs, as well as the large spread of velocities amongst them, contributes to the large uncertainties. For comparison, it is worth noting that stars in this galaxy are found to rotate with an amplitude of 15 ± 5 km s^{-1} out to $\sim$ 2 kpc in projection, and to have an average velocity dispersion of 24 ± 1 km s^{-1} (Geha et al., 2010).

Testing the kinematic methodology

When deriving the kinematic properties of GC systems such as those of NGC 147 and NGC 185, one faces the immediate issue of low number statistics, and it is important to investigate how this might affect the obtained results. Some parameters might not be well constrained due to insufficient data points, and the parameter space itself may not be sufficiently well populated in order for the analysis to be fruitful. For instance, looking at the top panel of Figure 4.6, it is seen that there are absolutely no data points between $\sim$ 120 to about 240 deg in position angle. Then, from $\sim$ 240 to 40 deg there are only two clusters, while the rest are clustered in the range between 40 and 120 deg. The point here is that, given the potentially high velocity dispersion of a GC system such as that of NGC 185, the few available clusters might be arranged in such a way to mask or artificially induce a rotation signal. Thus, it is important to know and understand the limitation of the method I have employed to constrain the kinematic properties of NGC 147 and NGC 185, and to learn how effective it is when applied to systems which host only a few GCs.

I use a Monte Carlo test to quantify the effectiveness of my Bayesian method in the realm of low number statistics. I generate 10^5 systems of 10 GCs in

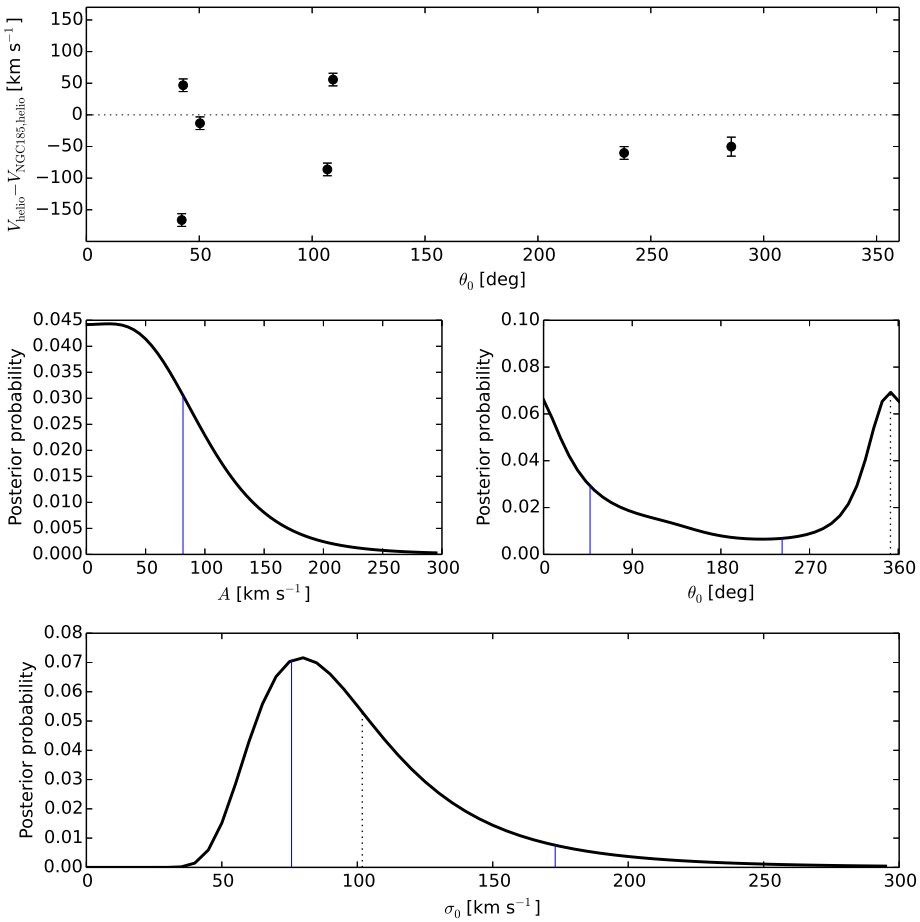

Figure 4.6 *Top panel: heliocentric radial velocity corrected for the systemic motion of NGC 185 vs. position angle of the GCs in this dE. No significant rotation is visible in the data. Notice how most clusters have similar position angles. Middle left panel: marginalized posterior distribution function for the amplitude of this system. Even though the amplitude is consistent with 0, it has a very wide peak, most likely due to the clustering of the GCs in position angle space. Formally, the amplitude is* < 82 *km* s^{-1} *with 68% confidence (blue line). Middle right panel: the posterior function of* θ_0*. The apparent peak has a low probability, making the 68% confidence limits very large (blue lines). Bottom panel: the posterior function for* σ_0*. Labelled is the expectation value with the 68% confidence intervals.*

each system. Each GC has a position angle drawn from a uniform distribution between 0 and 2π rad. The velocity of each GC is a combination of a rotation and a Gaussian dispersion component as per Equation 4.7. The amplitude and the rotation axis of the system are selected from uniform distribution functions between 0 and 70 km $s^{-1}$and 0 and 2π rad respectively. The mean of the Gaussian dispersion is also drawn from a uniform distribution function between 10 and 90 km s^{-1}. The generated data sets are passed through the Bayesian machinery which reports the peak values of the marginalized posterior distribution functions for the amplitude A, the rotation axis θ_0, and the velocity dispersion σ_0. Reporting the peak avoids the bias in the expectation values when the posterior distributions are truncated, and in all previous cases, the peak and mean values were consistent with each other within the 68% confidence limits uncertainties. The parameter grid is identical to the one of the NGC 147 system. Finally, I count the number of times the absolute difference between the true and the recovered values for the free parameters is less than 20 km s^{-1} for A and σ_0, and 20 deg for θ_0. I find that for this set up, the amplitude is recovered 63% of the time, θ_0 is recovered 45% of the time, while σ_0 is recovered 86% of the time. All parameters are simultaneously recovered just 30% of the time.

I also re-run the above experiment, but this time the amplitude is forced to be 0 for each GC set. For this scenario, the amplitude is recovered 73% of the time, while the velocity dispersion is recovered 87% of the time. Both of these parameters are simultaneously recovered 67% of the time. The axis of rotation in this case does not matter, as it can not be recovered since the amplitude is 0. From the above tests I conclude that the velocity dispersion can be well determined despite the low number statistics. The rotation however is not always well constrained. Investigating the cases in which the recovery of the amplitude or the rotation axis has failed, I conclude that this happens when most of the generated GC have similar position angles. For reference, tests with larger GC systems (>70 members) result in a much higher success rate in recovering the kinematic properties, as expected.

4.6 The dynamical masses of NGC 147 and NGC 185

Having derived the general kinematic properties of the GCs hosted by NGC 147 and NGC 185, I further use this information to estimate the total dynamical

mass of both of these galaxies. Since I found the clusters not to exhibit any significant degree of rotation, I assume that the systems are entirely pressure supported, and thus can estimate the mass of their hosts directly from the TME (Evans et al., 2003). The TME was previously described in Equation 3.13 and Equation 3.14.

In this case, I assume the γ parameter – describing the tracer population density distribution – to be 3, which is typical for a spheroidal stellar halo. Using L'Hôpital's rule to avoid the singularity in Equation 3.14, the constant C becomes:

$$C = \frac{4(\alpha+3)(1-\alpha)}{\pi} \frac{\log(r_{\rm out}/r_{\rm in})}{1-(r_{\rm in}/r_{\rm out})^{1-\alpha}}. \tag{4.9}$$

I consider cases were the slope of the underlying gravity field, α, is set to 0, which assumes an isothermal halo potential for NGC 147 and NGC 185, and to 0.55, as for a NFW profile (Navarro et al., 1996; Watkins et al., 2010). As logic dictates, for $r_{\rm in}$ and $r_{\rm out}$ I adopt the smallest and largest projected radius respectively, exhibited by the clusters in each sample that were used for the estimate, respectively.

Since the number of tracer objects in both of these samples is quite small for robust determination of statistical uncertainties via methods such as bootstrapping or jackknifing, I consider two extreme cases in order to put upper and lower limits on the estimated masses. The lower limit is obtained when one assumes the velocity distribution of the tracer objects is isotropic. In this case $C = 16/\pi$. Assuming that all the tracers have radial orbits sets an upper limit on the mass estimate, and in this case $C = 32/\pi$.

When estimating the mass of NGC 147, I exclude Hodge I from the sample. If a tracer object having a projected radius of 0 pc is used in the Tracer Mass Estimator, it will produce a singularity in Equation 4.9. Hodge I has a projected radius of 0.02 kpc which causes the constant C to increase anomalously. In addition, the mass of NGC 147 is calculated twice, once with and once without the inclusion of PA-N147-3. This cluster has a much larger projected radius compared to the other GCs around this galaxy and, as discussed in Section 4.2, it is possible that it might be bound to Cass II, or be a member of the M31 outer halo cluster population.

The results of the mass estimation are presented in Table 4.8, along with

Table 4.8 *Dynamical mass estimates for NGC 147 and NGC 185 within r_{out} as described by Equation 4.9. The lower and upper estimated limits are also shown, arising from assuming isotropic and radial orbit distributions respectively. Mass-to-light ratios are also computed with the newly-derived masses. The index (1) indicates that PA-N147-3 is excluded from the mass estimate.*

Galaxy	N_{GC}	r_{out} [kpc]	α	M [$M_\odot$]	M_{lower} [$M_\odot$]	M_{upper} [$M_\odot$]	M/L[$M_\odot/L_\odot$]
NGC 147	9	6.97	0	10.0×10^9	4.2×10^9	8.5×10^9	169
NGC 147	9	6.97	0.55	6.8×10^9	4.2×10^9	8.5×10^9	115
NGC 147[1]	8	2.53	0	1.8×10^9	1.1×10^9	2.1×10^9	30
NGC 147[1]	8	2.53	0.55	1.4×10^9	1.1×10^9	2.1×10^9	24
NGC 185	7	1.20	0	8.4×10^9	5.0×10^9	10.0×10^9	118
NGC 185	7	1.20	0.55	6.6×10^9	5.0×10^9	10.0×10^9	93

updated mass-to-light ratios using the new mass estimates for these two systems. It is seen that the mass of NGC 147 is considerably inflated when PA-N147-3 is used in the estimation, suggesting that it is either not bound to this galaxy, or the underlying gravitation field is not well described by the assumed values of α.

The masses I obtain for NGC 147 and NGC 185 are significantly higher than the previous estimates. For reference, De Rijcke et al. (2006) found the total mass of NGC 147 within $\sim$ 1 kpc to be $3.0^{+2.4}_{-1.8} \times 10^8$ $M_\odot$ via stellar dynamical modelling. For NGC 185, the same authors found the total mass to be $2.6^{+0.8}_{-0.6} \times 10^8$ $M_\odot$ within $\sim$ 0.6 kpc. Later, Geha et al. (2010) also measured the dynamical mass of NGC 147 and found it to be 5.6×10^8 $M_\odot$ within a $\sim$ 3 kpc radius. The same study found the dynamical mass of NGC 185 to be 7.2×10^8 $M_\odot$ within a radius of $\sim$ 2 kpc. The dynamical masses I estimate out to 2.5 and 1.2 kpc are larger by a factor of 2.5 and 12 for NGC 147 (excluding PA-N147-3) and NGC 185 respectively when compared to those obtained by Geha et al. (2010).

There is another point which is worth discussing briefly. Unlike in the case of M31, the α and γ parameters, as well as the velocity anisotropy (β) are not well constrained for dwarf galaxies such as NGC 147 and NGC 185. For instance, the radial number density distribution of the GCs around M31 was directly measured from the data, and it was found to indeed be a power law with a well determined index, as required by the TME. The result of such an attempt around NGC 147 and NGC 185 will not be reliable due to the small number of GCs around the dwarf galaxies, and thus the radial number density is only assumed to be a power law with index 3, which may or may not be the case. Similar arguments can be made for α. In addition, the velocity distribution is assumed to be isotropic, which is likely not to be true. These poorly

constrained quantities add additional uncertainty to the mass estimates.

Even though such an exercise is not attempted here, it may be possible to better constrain the α, γ and perhaps β parameters, which in turn will provide a less uncertain mass estimate by using the Bayesian framework. Dealing with probabilities, the first step would be to derive the most probable values for the above stated parameters, given the observed data, and only then calculate the mass via the TME. In such an attempt, the complete likelihood function is a product of two likelihood functions. The first such function would give the probability of observing the positions of the GCs around each galaxy given a power law index γ. The second likelihood function would model the probability of observing both the velocities and positions of the GCs given a certain gravitational potential and velocity anisotropy. The final likelihood would have the form of:

$$\mathcal{L} = \mathcal{L}_{\gamma}(R_i|\gamma) \times \mathcal{L}_{\alpha\beta\gamma}(v_i, R_i|\alpha, \beta, \gamma) \tag{4.10}$$

where R_i and v_i are the observed projected radii and line of sight velocities respectively. When deriving the posterior probability distributions for α, β and γ, one can try to use different prior function to include what is previously assumed true for each of those parameters. Once the posterior distributions are determined, one can calculate the mass of the dwarf galaxies using the most probably values of α, β and γ as well as getting better sense of the mass uncertainties.

4.7 Discussion

4.7.1 Comparison to other dwarf elliptical galaxies

The GC specific frequency (S_N) of dwarf galaxies is poorly constrained at present due to incompleteness in terms of imaging and GC detection, but it is critical for understanding what kinds of dwarf galaxies may contribute GCs to the halos of more massive systems. Significant effort has been made to constrain this value for dEs, and past surveys have focused mainly on dwarf galaxies that reside in dense environments, such as the Fornax and Virgo clusters (Durrell et al., 1996; Miller et al., 1998; Lotz et al., 2004; Miller & Lotz, 2007; Peng et al., 2008). The study by Miller & Lotz (2007) found an overall

trend of increasing S_N with increasing M_V (decreasing galaxy luminosity), which has also been found in dwarf irregulars although with smaller samples (Seth et al., 2004; Georgiev et al., 2008, 2010). Peng et al. (2008) found dwarf galaxies with the highest S_N values in their sample to be within 1 Mpc of the Virgo cluster core, which they interpret as an environmental effect. However, these authors also find that dEs within 40 kpc of the most massive galaxies in the Virgo cluster have few or no GCs, suggesting that they have probably been stripped away by the tidal forces from the central hosts.

Using the updated GC census due the efforts presented in this chapter, the specific frequencies for NGC 147 and NGC 185 were recalculated and found to be 8 ± 2 and 5.5 ± 0.5, respectively. This is a slight increase from the previous values which were 6 ± 2 for NGC 147 and 4.8 ± 0.5 for NGC 185. The uncertainties quoted for NGC 147 allow for the possibility of Hodge IV and SD-10 not being genuine GCs, as well as the uncertainty in the galaxy luminosity. In the case of NGC 185, only the uncertainty in the galaxy luminosity was taken into account. Figure 4.7 shows the S_N versus M_V values for dEs observed in the Fornax and Virgo clusters and in the Leo group, taken from the studies of Miller & Lotz (2007) and Peng et al. (2008). The error bars are due to the uncertainty in the host galaxy luminosity and the uncertainty in the total number of GCs found around each galaxy, which has been corrected for background contaminants and spatial incompleteness. On the same figure, the updated S_N values for NGC 147 and NGC 185 are over-plotted. The S_N values are within the range found for dEs of comparable luminosity observed by Miller & Lotz (2007), albeit residing in different environments, and appear to follow the trend of increasing S_N value with decreasing galaxy luminosity.

Another interesting property shared by the GC systems of NGC 147 and NGC 185, and the GC systems of dE galaxies found in rich environments, is their optical colours. The mean $(V-I)_0$ colours of NGC 147 and NGC 185 GCs are 0.85 and 0.84 with standard deviations of 0.09 and 0.03 respectively. In their study of dEs in the Fornax and Virgo galaxy clusters, Lotz et al. (2004) have reported the peak of the mean $(V-I)_0$ colour distribution to be 0.90 for galaxies with absolute magnitudes between -15.0 and -16.0, and 0.85 for galaxies with absolute magnitude between -14.0 and -15.0. This makes the GC systems of NGC 147 and NGC 185 nearly indistinguishable from those hosted by similar luminosity dEs in rich clusters, suggesting that the large-scale present day environment has little impact on either S_N or mean optical colour.

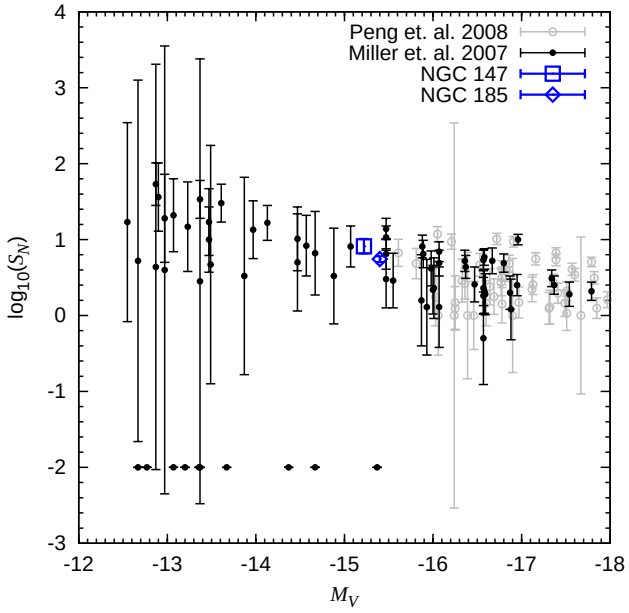

Figure 4.7 *Plot of $log(S_N)$ vs. M_V for dEs in the Fornax and Virgo clusters, and in the Leo group, taken from the studies by Miller & Lotz (2007)(filled points) and Peng et al. (2008)(open gray points). Galaxies which do not host GCs are given $log(S_N) = -2$ in order to distinguish them on the plot. Overplotted are the corresponding S_N values of NGC 147 and NGC 185.*

4.7.2 Comparison to the M31 halo globular clusters

The high spatial correlation between GCs and stellar streams suggest that a significant fraction of the GCs in the M31 halo have been brought by accreted dwarf galaxies. If the captured dwarf galaxies were indeed similar to NGC 147 and NGC 185, some common properties between the GCs hosted by these two dwarfs and those found in the M31 halo are expected to exist. Figure 4.8 displays the $(V-I)_0$ colours as a function of $R_{\rm proj}$ from the centre of M31 for the GCs hosted by NGC 147 and NGC 185. Also shown are confirmed M31 GCs that have $R_{\rm proj} > 30$ kpc taken from the RBC and Huxor et al. (2014). The M31 GCs have been de-reddened using extinction coefficients from Schlegel et al. (1998). One can see that the GCs found around the two dwarf galaxies fit comfortably in the range of $(V-I)_0$ colours measured for their M31 halo counterparts. Although this does not prove that the M31 halo GCs have been accreted from systems like NGC 147 and NGC 185, it demonstrates that this idea is not inconsistent with the data. In terms of the number of GCs they currently host, only about 8 NGC 147 or 185 systems would be needed to create almost the entire M31 halo GC population that consists of ∼80 clusters. Such accretions would also donate $\sim 5.4 \times 10^8$ $L_\odot$ of stellar light, consistent with estimates of the halo luminosity (Irwin et al., 2005).

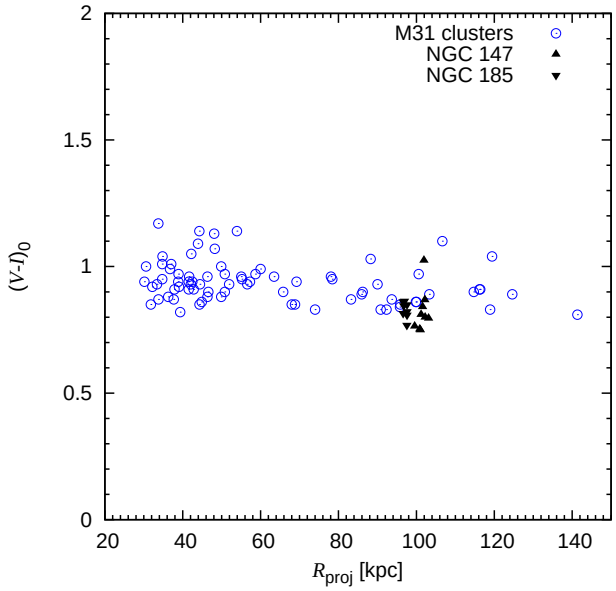

Figure 4.8 *Plot of $(V-I)_0$ vs. $R_{\rm proj}$ showing the M31 GCs that have projected radii larger than 30 kpc, together with the NGC 147 and NGC 185 GCs. Data was taken from the (RBC, Galleti et al., 2004) and Huxor et al. (2014)). The colour similarity supports the suggestion that the M31 outer halo GCs could have been accreted from objects like NGC 147 and NGC 185.*

4.8 Summary

This chapter presentes the discovery of 3 new GCs around NGC 147 and 1 around NGC 185. In addition, homogeneous optical and near-IR photometry of the entire GC systems hosted by these two dwarf galaxies is presented. The photometric measurements are used to constrain the ages and metallicities of the clusters via the use of colour-colour plots and an empirical age-metallicity relation. It is found that all but one cluster are metal-poor ([Fe/H]$\lesssim -1.3$ dex), while their ages were more difficult to estimate. The mean $(V-I)_0$ colours of the two GC systems are very similar to those of the GC systems of dEs in the Virgo and Fornax clusters, as well as the outer halo GC population in M31. The newly-discovered clusters bring the GC specific frequency (S_N) to ~ 9 in NGC 147 and ~ 5 in NGC 185, consistent with values found for dEs of similar luminosity residing in a range of environments.

Radial velocity data are used to examine the kinematic properties of these GC systems as well as to strengthen the membership of the newly-discovered clusters. No significant rotation signature is formally detected in either NGC 147 nor NGC 185. If such coherent motion is present, it can not be detected with the current data. Finally, the kinematic data are used to estimate the dynamical masses of these two dwarf galaxies, finding values considerably

higher than previously published.

Chapter 5

The globular cluster system of NGC 6822

Throughout this thesis, the significance of studying dwarf galaxies and their GC systems as a means to understand galaxy assembly has become quite apparent. In addition, the study of the properties of dwarf galaxies and their formation mechanisms is important in its own right, since these systems dominate the total galaxy population in terms of numbers. Studying dwarf Irregular (dIrr) galaxies is particularly important since they are regarded as the typical building blocks of massive galaxies because they are by far the most common galaxy type at high redshift (e.g. Stiavelli et al., 2004; van der Wel et al., 2011).

One of the most intriguing dwarf galaxies in the Local Group is NGC 6822. Discovered by Barnard (1884), this barred dIrr galaxy exhibits a number of peculiar properties that has made it the focus of over 600 studies. Despite this, the evolutionary history of this galaxy remains poorly constrained.

NGC 6822 is located in the southern hemisphere with Galactocentric coordinates of $l = 25.4°, b = -18.4°$. Given the low Galactic latitude, the observations of this galaxy are quite challenging due to significant reddening and stellar contamination coming from the Galactic disc. NGC 6822 has an absolute magnitude $M_V = -15.2$ and a half-light radius of $\sim$ 0.5 kpc (Mateo, 1998; McConnachie, 2012). With a distance of 472 kpc (Górski et al., 2011), it is the closest dIrr galaxy save for the Magellanic Clouds. It does not appear to be associated with either the Milky Way or M31, and it has no other neighbouring companions. This galaxy contains a spheroid of red giant branch stars out to a radius of at least $\sim$ 5 kpc (Battinelli et al., 2006).

It is found that NGC 6822 also contains large quantities of HI gas, first mapped by Roberts (1972). Subsequent studies (e.g de Blok & Walter, 2000, 2006; Weldrake et al., 2003) found that the semi-major axis of the HI gas disc is perpendicular to the stellar spheroid. In addition, de Blok & Walter (2000) found the outer parts of the HI disc to be dominated by a giant HI shell, the origin of which is best explained by either feedback from an extended star formation phase, or an interaction with a gas cloud lacking an ancient stellar component (Cannon et al., 2012). The inner region of the HI disc has an interesting structure full of shells and holes. The most dominant feature is a large hole spanning $\sim 2 \times 1.4$ kpc (de Blok & Walter, 2000, 2006; Cannon et al., 2012). Demers et al. (2006) presented a kinematic study of 110 carbon stars which comprise the spheroid of NGC 6822. The carbon stars are found to be rotating, but at right angles to the HI disc. This led Demers et al. (2006) to infer that the HI disc is a remnant of a recent strong gravitational interaction.

There have been a number of studies that examined the star formation history of this galaxy (e.g. Hodge, 1980; Gallart et al., 1996b,a; Israel et al., 1996; Mateo, 1998; Cannon et al., 2012). In the most recent study, Cannon et al. (2012) used *HST* to target six positions along the major axis of the HI disc. These authors found that each of their observed fields had a period of increased star formation rate in the last 50 Myr. Given that this interval is considerably shorter than the system's dynamical time-scale of $\sim$ 140 Myr, the heightened star formation most likely occurred on a galaxy-wide scale. This is consistent with the idea that this galaxy experienced a close encounter in its recent past.

Surveying the region within $\sim$ 1 kpc from the centre of NGC 6822, early ground based studies have found this galaxy to be rich in star clusters (e.g. Hubble, 1925; Hodge, 1977, 1980; Wilson, 1992). For a long time, it was thought that Hubble VII, originally discovered by Hubble (1925) was the only true, old GC. Spectroscopic studies (Cohen & Blakeslee, 1998; Chandar et al., 2000) found the [Fe/H] of this cluster to be in the range between ~ -2.0 and -1.5 dex, making it comparable to the metal-poor GCs in the Galaxy. Recently, using data from the wide-field *MegaCam* instrument mounted on the *CFHT* which covered 3×3 deg around NGC 6822, Hwang et al. (2011) discovered 4 new GCs. Later, Huxor et al. (2013) re-examined the data and by complementing it with additional archival *Subaru* imaging uncovered 3 additional GCs, updating the total number of GC to 8. Figure 5.1 shows the positions of all GCs superimposed on an image of NGC 6822, on which also marked are the contours of the HI map (de Blok & Walter, 2000) and the extent of the red giant branch stars forming the galaxy spheroid (Battinelli et al., 2006). The coordinates, position angles, projected radii and Galactic $E(B-V)$

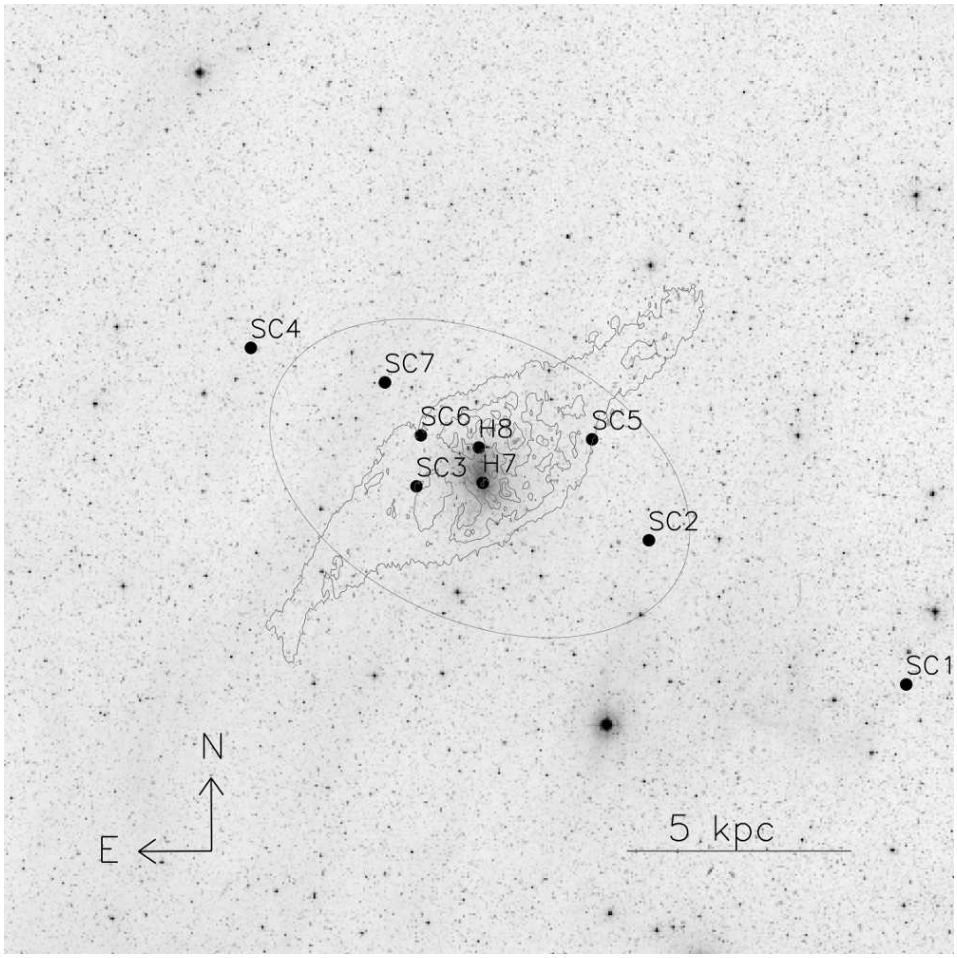

Figure 5.1 *The positions of the GCs are marked on an image from the* Digital Sky Survey (DSS) *of NGC 6822. The ellipse shows the extent of the red giant branch stars of the spheroid where the halo is detected above the noise (Battinelli et al., 2006), with a semi major axis of 36 arcmin and an ellipticity of 0.36. Also shown are contours from the HI map of (de Blok & Walter, 2000). Figure taken from Huxor et al. (2013).*

extinction values are listed in Table 5.1.

Figure 5.1 clearly shows that the GC system of NGC 6822 is quite extended in nature, with the most remote cluster, SC1, having a projected radius of nearly 11 kpc. This once again illustrates the importance of searching for GCs in the remote parts of galaxies. From the same figure, one can also see that the GCs lie in a linear configuration (Hwang et al., 2011; Huxor et al., 2013). Although such an arrangement is unusual, a similar property is found for the clusters in the Large Magellanic Cloud (Grocholski et al., 2009).

Hwang et al. (2014) presented a spectroscopic study of 5 GCs in NGC 6822. They found no evidence of rotation from the radial velocities, despite the presence of the rotating HI disc. In addition, using the Tracer Mass Estimator (Evans et al., 2003), they found the dynamical mass of NGC 6822 to be $7.4^{4.5}_{-0.4} \times 10^9 M_\odot$. The corresponding mass-to-light ratio of $75(M_\odot/L_\odot)$, makes

Table 5.1 *Coordinates, position angles, projected radii, GC type, and the colour excess values due to Galactic interstellar reddening of the GCs in NGC 6822.*

ID	RA(J2000) [h m s]	DEC(J2000) [d m s]	PA [deg]	GC type	$R_{\rm proj}$ [kpc]	$E(B-V)$ [mag]	Reference
Hubble-VII	19 44 55.8	-14 48 56.2	227	GC	0.13	0.24	Hubble (1925)
SC1	19 40 11.9	-15 21 46.6	244	EC	10.71	0.16	Hwang et al. (2011)
SC2	19 43 04.5	-14 58 21.4	250	EC	4.08	0.22	Hwang et al. (2011)
SC3	19 45 40.2	-14 49 25.8	94	EC	1.44	0.19	Hwang et al. (2011)
SC4	19 47 30.4	-14 26 49.3	59	EC	5.96	0.19	Hwang et al. (2011)
SC5	19 43 42.3	-14 41 59.7	290	EC	2.69	0.22	Huxor et al. (2013)
SC6	19 45 37.0	-14 41 10.8	52	GC	1.64	0.19	Huxor et al. (2013)
SC7	19 46 00.7	-14 32 35.0	44	GC	3.04	0.21	Huxor et al. (2013)

this dwarf galaxy highly dominated by dark matter. From their Lick index measurements, Hwang et al. (2014) also found the clusters in their sample to have ages older than 8 Gyr, and metallicities [Fe/H]< -1.5.

What is especially interesting is that this dIrr galaxy is the only dwarf galaxy in the Local Group that is known to be a host of extended GCs. In fact, 5 out of 8 GCs in this galaxy are of the extended variety. This means that galaxies like NGC 6822 could be the source of extended clusters for the halo of M31. However, if M31 accreted similar systems, it must have done so at an early epoch, since the young stellar populations which dominate NGC 6822's main body are not present in the M31 halo.

In this chapter I present uniform optical and near-IR photometry for all 8 GCs in NGC 6822, as a means to constrain their ages and metallicities. Even though deeper optical data exists for some clusters (e.g. Hwang et al., 2011; Huxor et al., 2013), the uniformity of the *PanSTARRS1* imaging ensures no systematic offsets are present in the age and metallicity estimates due to heterogeneous data. In addition, I present a kinematic study of this GC system, which is based on new measurements made for 6 GCs, 2 of which had no previous velocity information. This data is also used to redetermine the dynamical mass and mass-to-light ratio of this galaxy.

5.1 The data

The optical imagery was obtained as part of the *PanSTARRS1* survey. *PanSTARRS – Panoramic Survey Telescope and Rapid Response System* – is a long term project which includes the construction of a four telescope system on Mauna Kea, the peak of Haleakala, a mountain on the Hawaiian island of Maui (Kaiser, 2004). The goal of this system is to perform state-of-the-art surveys addressing

diverse astrophysical topics, from Solar neighbourhood science to cosmology. The 1.8 meter *PanSTARRS1* telescope (Kaiser et al., 2010) is the first one of the four to be built and made fully operational. It is currently operated full time, and the data reduction and publication systems serve as a prototype of the entire array.

The optical system of *PanSTARRS1* features a 1.4 Gigapixel imager (Onaka et al., 2008; Tonry & Onaka, 2009) with a field of view of 7 deg^2. With the 3π Survey – the source of the optical data I use in this chapter – *PanSTARRS1* is covering 3/4 of the total sky in five optical bands ($g_{p1}, r_{p1}, i_{p1}, z_{p1}, y_{p1}$) (Tonry et al., 2012). The entire sky visible from Mauna Kea is observed, four times per band each year, which results in $\sim$1.2 mag deeper imaging on the final stacked images. The typical exposure times of individual frames range between 30 and 45 s, which results in 5σ limiting AB magnitudes of 21.9, 21.8, 21.5, 20.7, and 19.7 for the $g_{p1}, r_{p1}, i_{p1}, z_{p1}, y_{p1}$ bands, respectively (Morganson et al., 2012). The data are automatically processed in real time with the IMAGE PROCESSING PIPELINE (IPP, Magnier, 2006). After the standard reduction processes such as flat-fielding, the pipeline resamples all images to a uniform pixel size of of 0.25 arcsec and aligns them to the equatorial axes onto "skycells" – regular patches on the sky of 6250 pixels across. The resampling conserves the original flux of the images and the final products are called "warps". The stacked images used in this work were retrieved from the postage stamp server by Edouard Bernard, and are from the processing version 1 (PV1).

The near-IR imaging of NGC 6822 was taken as part of the project to survey red stellar populations of Local Group galaxies, previously described in Section 4.1. As a brief reminder, the data were obtained with the *WFCAM* (Casali et al., 2007) mounted on *UKIRT*. *WFCAM* has a pixel scale of 0.4 arcsec, the detectors of which are arranged in way that four dithered pointings cover a square of 0.75 deg^2 when properly aligned. The observations were done in three near-IR bands J, H and K. The data was processed with a pipeline created by the Cambridge Astronomy Survey Unit which performs the standard dark current correction, flat-fielding, crosstalk removal, systematic noise and sky removal. The only difference between the near-IR imaging of NGC 147 and NGC 185, and that of NGC 6822 is that in the latter case the individual pointings were not resampled nor mosaiced and thus they retain the original pixel scale. Figure 5.2 shows 30 $\times$ 30 arcsec wide cutouts of each GC hosted by NGC 6822 in the *PanSTARRS1* g_{p1} and *UKIRT/WFCAM K* bands. I note that in these data the very diffuse clusters (SC4, SC5) are marginally detected.

Spectroscopic data were obtained for 6 GCs. The observations were made

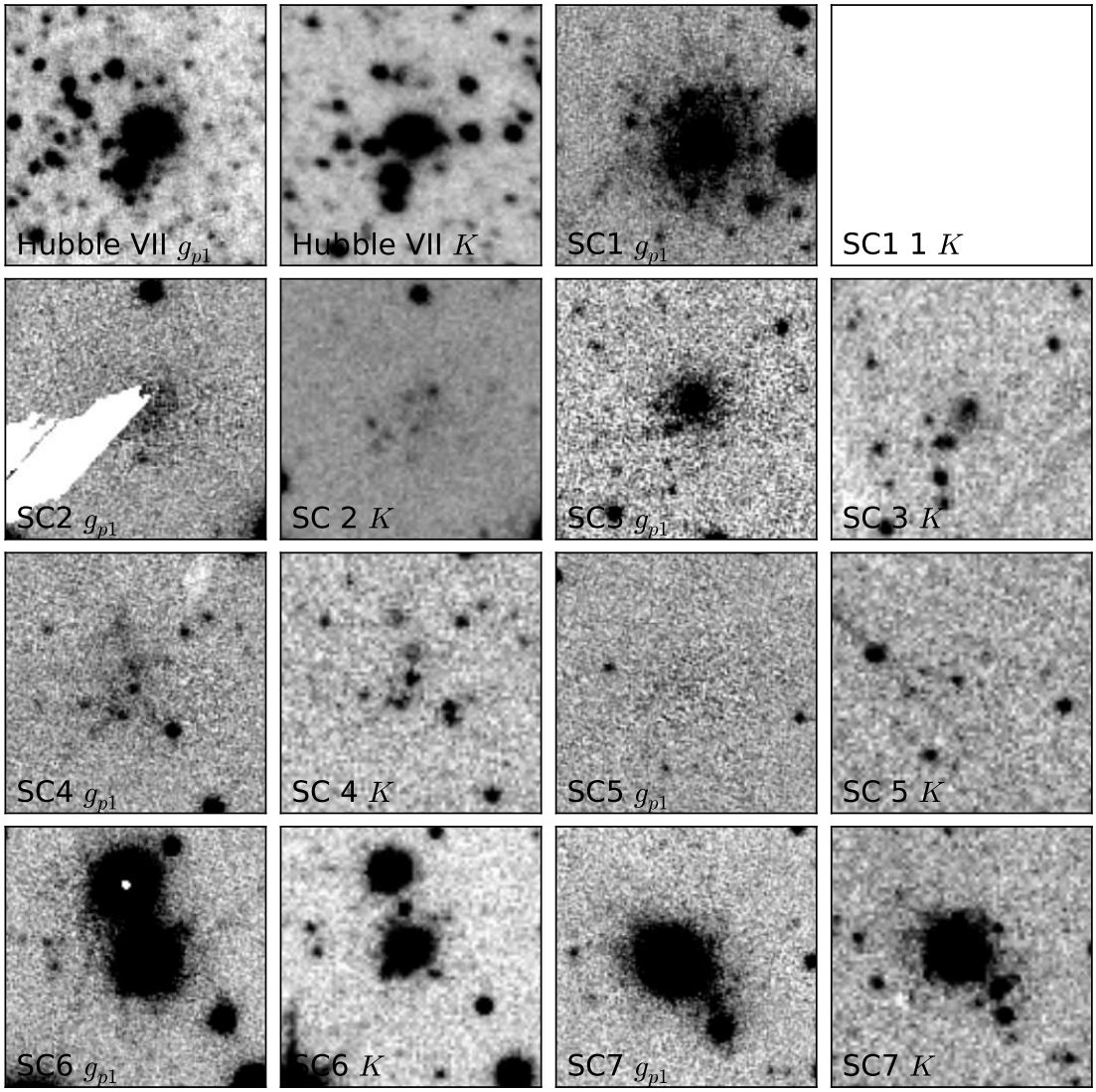

Figure 5.2 *r_{p1} and K band images of the GCs in NGC 6822. Each image is 30 × 30 arcsec wide. North is up and east is left. SC1 falls outside the near-IR survey and hence no K-band image is shown. Part of the thumbnail showing SC2 appears damaged, and this is most likely due to the necessary masking done by the* PanSTARRS1 IPP.

Table 5.2 *Log of spectroscopic observations for GCs around NGC 6822*

ID	Date of obs.	Number of exposures	Integration time per exposure [s]	Instrument
Hubble VII	14/08/2009	3	900	*KPNO*
SC1	16/08/2009	3	1800	*KPNO*
SC3	17/08/2009	3	1800	*KPNO*
SC6	15/08/2009	3	900	*KPNO*
SC7	15/08/2009	3	600	*KPNO*
SC2	16/08/2009	1	1800	*WHT*
SC2	17/08/2009	2	1800	*WHT*
SC7	16/08/2009	2	600	*WHT*

during appropriate intervals throughout the M31 spectroscopic campaign as part of the 2009 *WHT* and *KPNO* runs. The observing log for the clusters in NGC 6822 is show in Table 5.2. The processing of these spectra is identical to that of the M31 halo GCs, the details of which are described in 2.2.1. Examples of calibrated, continuum-normalized spectra are shown in Figure 5.3.

5.2 Photometry

I determined the total magnitudes of each GC in NGC 6822 via aperture photometry in all 8 bands, $g_{p1}, r_{p1}, i_{p1}, z_{p1}, y_{p1}$, J, H, and K. As before, the photometry is done with the *phot* task in IRAF. The centroid algorithm within *phot* is used to pinpoint the centre of each compact cluster. This is done in the r_{p1} band imaging, since the clusters are best seen there. For the diffuse clusters, the centre is determined via visual inspection. An offset from a nearby bright star is used to accurately propagate the cluster centre through the rest of the data.

Circular apertures are used to sum the total flux coming from each cluster. The photometric apertures are chosen such that they enclose the entire light coming from each cluster. The size of each depends on the extent of the cluster being measured, and they are listed in Table 5.3. The background sky is determined between two concentric circular annuli surrounding the photometric aperture. They are placed in a way that excludes unwanted pollutants such as extended background galaxies or foreground Milky Way stars. The reported magnitude uncertainties were formally determined by the *phot* task.

All photometric measurements are zero-point calibrated and corrected for atmospheric extinction. The resulting magnitudes are corrected for Galactic interstellar reddening using colour excess $E(B-V)$ values from Schlegel et al. (1998). The extinction coefficients for the *PanSTARRS1* bands are calculated

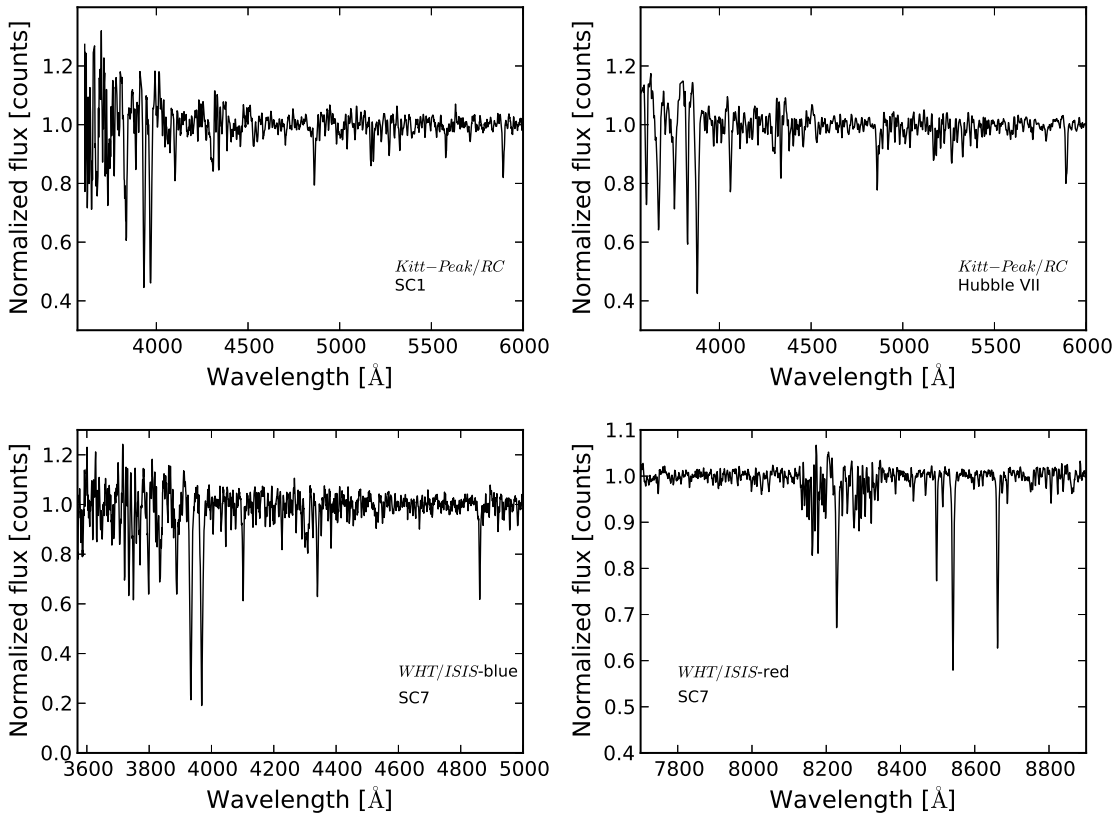

Figure 5.3 *Examples of fully reduced, continuum-normalized spectra of GCs in NGC 6822.*

using the relations presented in Tonry et al. (2012):

$$Ag_{p1}/E(B-V) = 3.613 - 0.0972(g_{p1}-i_{p1}) + 0.0100(g_{p1}-i_{p1})^2 \quad (5.1)$$

$$Ar_{p1}/E(B-V) = 2.585 - 0.0315(g_{p1}-i_{p1}) \quad (5.2)$$

$$Ai_{p1}/E(B-V) = 1.908 - 0.0152(g_{p1}-i_{p1}) \quad (5.3)$$

$$Az_{p1}/E(B-V) = 1.499 - 0.0023(g_{p1}-i_{p1}) \quad (5.4)$$

$$Ay_{p1}/E(B-V) = 1.251 - 0.0027(g_{p1}-i_{p1}) \quad (5.5)$$

Schlafly & Finkbeiner (2011) recalibrated the $E(B-V)$ from Schlegel et al. (1998), and recommend the *PanSTARRS1* reddening coefficients be further multiplied by a factor of 0.88, which I include in the magnitude derivation. Finally, Table 5.3 lists the extinction-corrected total magnitudes of all GCs in NGC 6822.

It needs to be noted that the g_{p1} and r_{p1} magnitudes of SC2 presented in Table 5.3 are lower limits due to masking in the imagery which can be seen in Figure 5.2. SC5 is not detected in the *PanSTARRS1* data, and it is a marginal detection in the near-IR imaging. Thus, the measured values represent upper

Table 5.3 *Optical and near-IR photometry of all GCs hosted by NGC 6822. Superscript (1) denotes that the optical g_{p1} and r_{p1} magnitudes of this cluster are lower limits to masking in the image. Superscript (2) denotes that magnitudes of this cluster are upper limits.*

ID	Aperture [arcsec]	g_0 [mag]	r_0 [mag]	i_0 [mag]	z_0 [mag]	y_0 [mag]	J_0 [mag]	H_0 [mag]	K_0 [mag]
Hubble VII	3.7	15.47 ± 0.03	15.00 ± 0.04	14.72 ± 0.02	14.56 ± 0.04	14.49 ± 0.02	13.44 ± 0.01	12.98 ± 0.02	12.86 ± 0.01
SC1	7.0	16.60 ± 0.03	16.31 ± 0.03	16.00 ± 0.02	15.87 ± 0.07	15.75 ± 0.03	.	.	.
SC2[1]	8.0	< 17.9	< 17.6	16.66 ± 0.02	16.63 ± 0.03	16.50 ± 0.03	15.53 ± 0.03	15.11 ± 0.03	14.86 ± 0.03
SC3	3.0	18.80 ± 0.03	18.36 ± 0.04	18.07 ± 0.02	17.96 ± 0.04	17.80 ± 0.02	16.93 ± 0.04	16.44 ± 0.04	16.32 ± 0.05
SC4	8.0	17.93 ± 0.03	17.38 ± 0.03	17.04 ± 0.03	16.89 ± 0.05	16.96 ± 0.02	15.74 ± 0.04	15.31 ± 0.04	15.11 ± 0.04
SC5[2]	7.5	~ 19.0	~ 18.4	~ 18.4	~ 18.2	~ 17.5	~ 18.0	~ 16.6	~ 16.4
SC6	4.7	15.76 ± 0.04	15.26 ± 0.04	15.02 ± 0.03	14.90 ± 0.04	14.86 ± 0.02	13.89 ± 0.01	13.42 ± 0.02	13.30 ± 0.01
SC7	5.0	15.25 ± 0.04	14.59 ± 0.04	14.28 ± 0.03	14.11 ± 0.04	14.02 ± 0.02	12.93 ± 0.01	12.39 ± 0.02	12.30 ± 0.01

Table 5.4 *Photometry of the NGC 6822 GCs converted to the Johnson/Cousins system using Equation 5.6a and 5.6b taken from Tonry et al. (2012). For convenience, the $(V-I)_0$ colours are also listed. Superscripts are as in Table 5.3.*

ID	V_0 [mag]	I_0 [mag]	$(V-I)_0$ [mag]	$M_{V,0}$ [mag]
Hubble VII	15.07 ± 0.04	14.18 ± 0.03	0.88 ± 0.05	-8.3
SC1	16.34 ± 0.04	15.53 ± 0.03	0.82 ± 0.05	-7.0
SC2[1]	< 17.6	16.17 ± 0.03	< 1.42	< -5.8
SC3	18.45 ± 0.04	17.56 ± 0.03	0.89 ± 0.05	-4.9
SC4	17.52 ± 0.04	16.52 ± 0.03	1.00 ± 0.05	-5.9
SC5[2]	~ 18.7	~ 17.9	~ 0.76	~ -4.7
SC6	15.38 ± 0.04	14.50 ± 0.03	0.88 ± 0.05	-8.0
SC7	14.78 ± 0.04	13.73 ± 0.03	1.04 ± 0.05	-8.6

limits on its magnitudes in all bands. The extended cluster SC1 is the most remote object in this system and is located outside the coverage of the near-IR data.

When deriving the colours of these clusters, I use the magnitudes shown in Table 5.3. Previously, when deriving the colours of the GCs hosted by NGC 147 and NGC 185, smaller apertures were used to decrease any contamination due to the severe crowding. However, the GCs around NGC 147 and NGC 185 are all compact, and sufficiently bright in the centre for accurate photometry to be measured. On the other hand, many clusters in NGC 6822 are quite diffuse, have much lower surface brightness and their centres are not always well defined in the available data. In these cases, larger apertures are needed for sufficient amount of light to be gathered for reliable photometric measurements. The classical GCs SC6 and SC7 are located in regions of low crowding, and using larger apertures for measuring their colours does not introduce unwanted contamination. Finally, Hubble VII is so compact that the size of the aperture adopted for measuring its magnitude is nearly the same as the sizes of the colour apertures used on the NGC 147 and NGC 185 GCs.

To allow for comparison with other studies, I convert the photometry measurements from the *PanSTARRS1* to the classical Johnson/Cousins system. The conversion is made with equations derived in Tonry et al. (2012):

$$V - r_{p1} = 0.005 + 0.462(g - r)_{p1} + 0.013(g - r)^2_{p1} \tag{5.6a}$$

$$I - i_{p1} = -0.366 - 0.136(g - r)_{p1} - 0.018(g - r)^2_{p1} \tag{5.6b}$$

The conversion to the Johnson V band adds an additional 0.012 mag of uncertainty, while the conversion to the Cousins I adds an additional 0.017 mag to the uncertainty. The results of the conversions are listed in Table 5.4. Assuming the clusters have the same distance of 472 kpc as NGC 6822, their absolute M_{V_0} are calculated and also listed in Table 5.4. It is important to note that the $(V - I)_0$ colours and M_{V_0} presented here are not in agreement with those from Hwang et al. (2011), and there is no common systematic offset between the two sets of measurements. On the other hand, I find excellent agreement between my photometric measurements and those presented in Huxor et al. (2013).

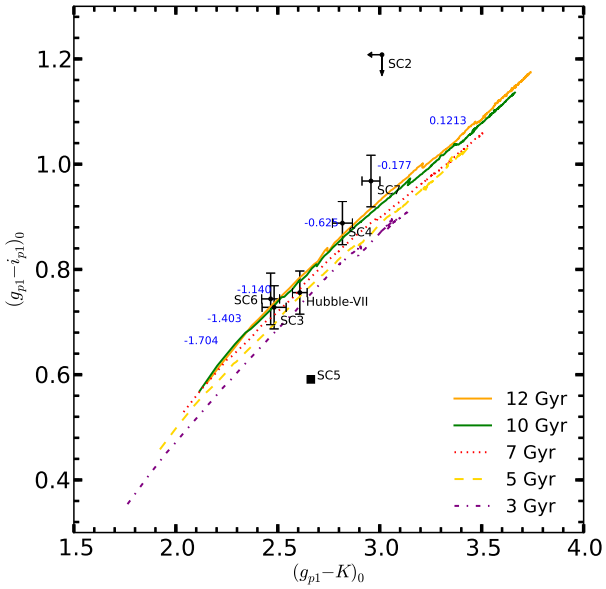

Figure 5.4 $(g_{p1} - i_{p1})_0$ *vs* $(g_{ps1} - K)_0$ *colour-colour diagram of the GCs in NGC 6822, overlaid on top of the PARSEC1.1 isochrones (Bressan et al., 2012). Also shown are [Fe/H] values along the 12 Gyr isochrone. The arrows from SC2 show the direction this point would move if more flux is added to the* g_{p1} *band. SC5 is represented by a square since this cluster is a marginal detection in the imaging. The clusters with reliable photometry are all found to have old ages.*

5.3 Ages and metallicities

In Figure 5.4 I show the $(g_{p1} - i_{p1})_0$ vs $(g_{ps1} - K)_0$ colour-colour diagram constructed with the photometry presented in Table 5.3. The overlaid stellar isochrones are from Bressan et al. (2012) spanning the metallicity range $-2.2 < [\mathrm{Fe/H}] < 0.6$ dex, which are available for the *PanSTARRS1* as well as for the *UKIRT/WFCAM* photometric systems. The diagram shows that all clusters, with the exception of SC2 and SC5 have old ages (> 9 Gyr). This is in complete agreement with the spectroscopic study by Hwang et al. (2014).

Regarding the two outliers, SC2 falls above the isochrones and this is likely a result of the missing flux in the g_{p1} band imaging due to masked areas in the imaging, as seen in Figure 5.2. One can easily imagine that adding more flux to the g_{p1} band will shift the location of this cluster to bluer colours for both colour combinations, thus making it lie on top of the model isochrones. The other outlier, SC5, is the faintest GC in NGC 6822, and it is only marginally detected. The reported fluxes upper bounds, and the estimation of the age and metal content for this cluster is impossible. For completeness, it is shown as a filled square in Figure 5.4.

Table 5.5 *[Fe/H] values for the GCs with reliable photometry in NGC 6822. Columns refer to: (a) values obtained via Equation 4.5, an empirical colour-metallicity relation calibrated on the M31 GC system (Kissler-Patig et al., 2002); spectroscopic metallicity from (b) Hwang et al. (2014); (c) Cohen & Blakeslee (1998); (d) Chandar et al. (2000)*

ID	[Fe/H](a) [dex]	[Fe/H](b) [dex]	[Fe/H](c) [dex]	[Fe/H](d) [dex]
Hubble-VII	-1.5 ± 0.4	-2.34 ± 0.03	-1.95 ± 0.15	-2.0 ± 0.25
SC1		-2.00 ± 0.04		
SC2		-2.53 ± 0.06		
SC3	-1.6 ± 0.4	-1.52 ± 0.06		
SC4	-1.1 ± 0.4	-2.53 ± 0.08		
SC5				
SC6	-1.7 ± 0.4			
SC7	-1.0 ± 0.4			

The estimated metallicities for the clusters that do follow the SSP models are more controversial. I find the GCs to be relatively metal-rich with with significant spread in their metallicities where $-1.5 < [\mathrm{Fe/H}] < -0.4$ dex. For three clusters – SC3, SC6 and Hubble VII – I estimate a similar [Fe/H] ~ -1.3 dex. However, for SC4 and SC7 I find considerably higher [Fe/H] values of -0.7 and -0.4 dex. This is contrary to the results presented in Hwang et al. (2014), which found all of the clusters in their sample – SC1, SC2, SC3, SC4, Hubble VII – to be more metal-poor with [Fe/H]< -1.5 dex.

As an alternative to the colour-colour plot, I use the empirical relation (Equation 4.5) between the [Fe/H] value and $(V-K)_0$ colour, derived by Kissler-Patig et al. (2002) using 129 GCs in M31. The metallicities obtained via this relation are shown in Table 5.5. The same table lists the [Fe/H] values derived via a χ^2 minimisation method applied to 15 Lick indices by Hwang et al. (2014), as well as spectroscopic metallicities for Hubble VII from earlier studies (Cohen & Blakeslee, 1998; Chandar et al., 2000). It is seen that my metallicity estimates are considerably higher than those by Hwang et al. (2014), with only one good agreement between the two data sets. No overall systematic offset is present between these two sets of measurements. In addition, looking at Table 5.5, one can see that the metallicity uncertainties reported by Hwang et al. (2014) are intriguingly small, especially given the large uncertainties these authors assign to the radial velocity measurements derived from the same data (see Section 5.4). Furthermore, note that although my photometric [Fe/H] value for Hubble VII is higher, it is formally in agreement with those derived in Cohen & Blakeslee (1998) and Chandar et al. (2000) within the reported uncertainties.

The reason for this discrepancy is unclear. It is known that NGC 6822 contains

young and more metal rich populations of stars, and they could be the cause of the observed results if they were contaminating the photometric apertures. However, repeating the photometry process with smaller apertures in order to exclude possible contaminants did not change the results displayed in Figure 5.4. In addition, it is strange how the ages are recovered to be old, if there are indeed younger stellar populations contaminating the derived total magnitudes.

Additional checks can be made by comparing the photometry presented here to already published results. In their discovery paper, Huxor et al. (2013) presented optical photometry for SC6 and SC7, measured on *CFHT/MegaCam* archival images. These authors found $(V-I)_0$ values of 0.84 ± 0.04 and 1.05 ± 0.04 for SC6 and SC7, respectively. This is in excellent agreement with the data presented in Table 5.4, adding confidence in the both the photometry and metallicity estimates presented here. Hwang et al. (2011) also presented optical colours for the extended clusters SC1 - SC4 that they uncovered during their work on NGC 6822. Regarding SC1, there is a good agreement between the photometry of Hwang et al. (2011) and that presented in this thesis, while such a comparison for SC2 is not possible due to the masks in the *PanSTARRS1* data for this cluster. However, Hwang et al. (2011) find $(V-I)_0$ colours of 1.31 and 1.12 for SC3 and SC4 respectively, which are redder than those presented in Table 5.4. By looking at Figure 5.4, it becomes apparent that the only way to keep a cluster on the isochrones when its optical colour becomes redder, is by making its optical-near-IR colour also more red. This essentially makes such a cluster more metal-rich.

Another effect to be considered is the internal reddening within NGC 6822 itself. As discussed earlier, this galaxy contains a significant amount of gas, and probably dust, which, if not properly accounted for, could cause the clusters to appear redder and thus more metal-rich than they actually are. Looking at Figure 5.1 this seems to be unlikely since most of GCs found to be metal-rich in this study are located outside the extent of the HI disc. If the spread in metallicity is indeed genuine, it is intriguing that the more metal-poor clusters are more spatially concentrated than their metal-rich counterparts. This is contrary to what is observed in NGC 147 and NGC 185, as well as in most massive galaxies. However, since the uncertainties of the photometric metallicities are large and the clusters with reliable photometry lie within 1 standard deviation of the same metallicity, this observation needs to be taken with caution.

Table 5.6 *Heliocentric radial velocities and their uncertainties for the GCs around NGC 6822. For reference, the systemic velocity of NGC 6822, as well as previous velocity measurements of the clusters are also listed when available.*

ID	$V_{\rm helio}$ [km s^{-1}]	Literature $V_{\rm helio}$ [km s^{-1}]	Reference for literature data
NGC 6822		-57	McConnachie (2012)
Hubble VII	-68 ± 12	-52;-65 ± 20	Cohen & Blakeslee (1998);Hwang et al. (2014)
SC1	-110 ± 28	-61 ± 20	Hwang et al. (2014)
SC2	-82 ± 14	-106 ± 31	Hwang et al. (2014)
SC3	-85 ± 25	-71 ± 17	Hwang et al. (2014)
SC4		-115 ± 58	Hwang et al. (2014)
SC5			
SC6	-71 ± 22		
SC7	-35 ± 7		

5.4 Kinematics

I derived the heliocentric radial velocities of the GCs in Table 5.1 with my dedicated χ^2 minimization routine (see Section 2.3), using all available radial velocity standard stars listed in Table 2.2. Since it was observed with *WHT*, the velocity of the cluster SC2 is the weighted mean of the two independent velocities derived with the blue and red arm of *ISIS*. The cluster SC7 was observed with both arms of *ISIS*, as well as with the *KPNO* telescope. Since all independent measurements agree, the reported velocity of this cluster is the weighted mean of all 3 separate velocity measurements. The final radial velocity measurements are listed in Table 5.6, along with previous velocity measurements taken from the literature. In general, my velocities agree with the literature values within the reported uncertainties, except in the case of SC1 despite it being a bright cluster.

I perform a kinematic analysis with the same Bayesian prescription described in Section 4.5. The kinematic model used is the one described by Equation 4.7. As a reminder, the kinematic model contains a simple rotation along circular orbits, described by Equation 3.4, and a Gaussian velocity dispersion that does not change as a function of projected distance (see Equation 4.6). I calculate the likelihood function systematically, as portrayed by Equation 4.8, over a regular grid shaped by the parameter space of the kinematic model. In this case, the rotation amplitude A and the velocity dispersion parameters σ_0 both range from 0 to 150 km s^{-1} with a resolution of 2 km s^{-1}. The axis of rotation parameter, θ_0, is searched from 0 to 2π rad with a step size of 0.15 rad.

The results of the kinematic analysis are shown in Figure 5.5. Similar to the results obtained in the study by Hwang et al. (2014), I find no evidence for

systemic rotation of the NGC 6822 GCs. This is best seen in the top panel in Figure 5.5, where the GCs radial velocities, corrected for the systemic motion of their host galaxy, are plotted against their position angles. This is reinforced by the posterior probability distribution functions of the amplitude and rotation axis, shown on the middle panels in the same figure. The amplitude is strongly peaked at zero. Formally, the measured value of A is less than 22 km s^{-1} with 68% confidence. From the flatness of the posterior function of θ_0, one can see that no rotation axis is favoured, consistent with the discussion above. However, as discussed in Section 4.5, when analysing the kinematics of systems such as this one, one needs to be aware of the possible issues due to the small number statistics. As seen in the top panel of Figure 5.5, the position angle space of the system is poorly sampled. This is a property of the system and not an observational bias. There are only two known clusters that are not present in my data, the inclusion of which would not remedy this issue. Indeed, assimilating the velocity data of SC4 from Hwang et al. (2014) in the above analysis does not change the results. Thus any possible systemic rotation of the GC system of NGC 6822 is either non existent, or it is considerably smaller than what can be resolved with the current data. The lack of rotation in this GC system is surprising, given the spatial alignment between the GCs and the spheroid of carbon stars in this galaxy (see Figure 5.1), which is found to rotate with an amplitude of ~ 50 km s^{-1} (Demers et al., 2006). The alignment of the GCs is perpendicular to the HI disc, which is also found to rotate with an amplitude of ~ 55 km s^{-1} (Weldrake et al., 2003).

On the other hand, the posterior distribution function of the velocity dispersion of this GC system is well determined. The expectation value, calculated from the posterior probability distribution function shown on the bottom panel in Figure 5.5 is 32^{+37}_{-12} km s^{-1}. As an exercise, I also compute the velocity dispersion of this system using the biweight scale estimator (Beers et al., 1990), and find it to be 23 ± 16 km s^{-1}. This is nearly identical to the peak of my posterior distribution for σ_0 which occurs as 22 km s^{-1}. The reason for this is that the biweight scale estimator calculates the most likely value, even if the underlying distribution is not Gaussian.

5.5 The dynamical mass of NGC 6822

Following the derivation of the GC velocities and their bulk kinematic properties, I proceed to recalculate the dynamical mass of NGC 6822. To achieve this, I once again use the Tracer Mass Estimator (Evans et al., 2003) in the same form

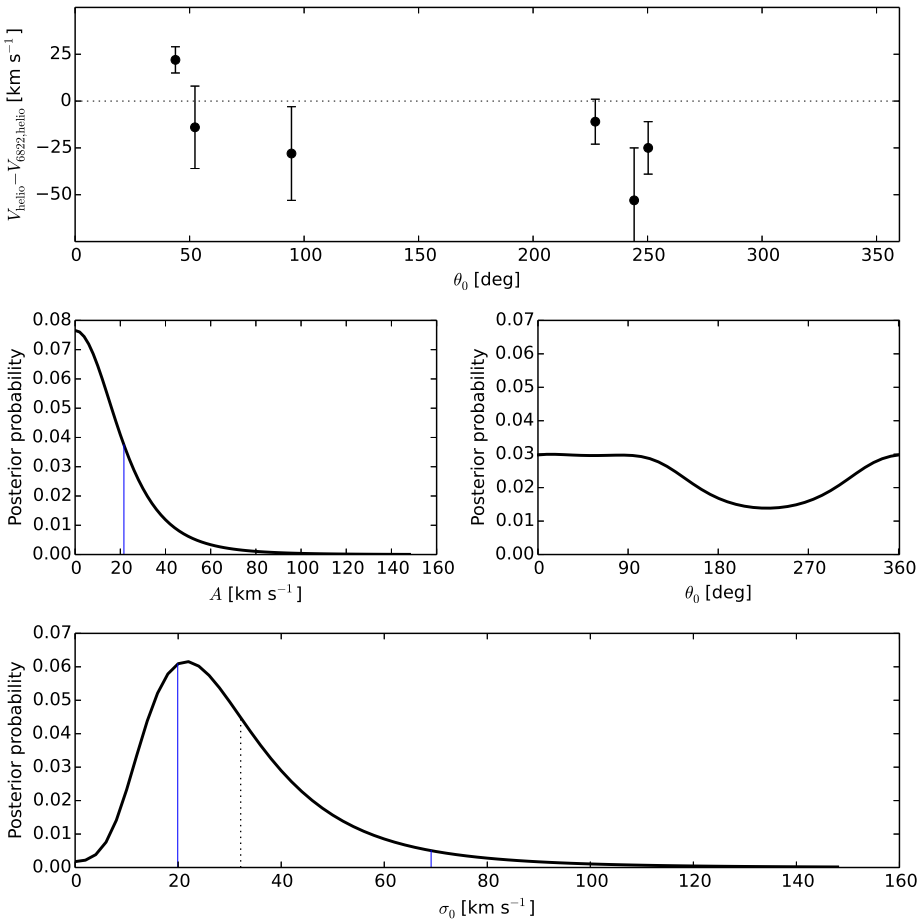

Figure 5.5 *Top panel: heliocentric radial velocity corrected for the systemic motion of NGC 6822 vs position angle of the GC in this dIrr. No evidence for bulk rotation is found in the data. Middle left panel: marginalized posterior distribution function for the amplitude of this system. The amplitude is consistent with 0. As an upper bound, the amplitude is* < 22 *km s*$^{-1}$ *with 68% confidence (blue line). Middle right panel: the posterior function of* θ_0*. The flatness of this probability distribution strengthens the argument that this system exhibits no rotation. Bottom panel: the posterior function for* σ_0*. Also labelled is the expectation value with the 68% confidence intervals.*

as in the case of NGC 147 and NGC 185, which is best described by Equations 3.13 and 4.9. Since no evidence for bulk rotation is found in the currently available data, the Tracer Mass Estimator is applied directly to estimate the total mass of NGC 6822 contained within $\sim$ 11 kpc, i.e. the location of the most distant tracer, SC1. To increase my sample, I also include the velocity of SC4 from Hwang et al. (2014). In addition, Hubble VII is excluded from the calculation since it is located near the centre of NGC 6822, causing the constant C to inflate anomalously.

I consider two cases for slope of underlying gravitational field, α: $\alpha = 0$ as for an isothermal halo potential, and $\alpha = 0.55$ as for the case of a NFW profile (Navarro et al., 1996; Watkins et al., 2010). To estimate the lower and upper limits of the mass, I assume that GCs all have isotropic and radial orbits, respectively.

Table 5.7 lists the results of the mass estimation. In most cases, the mass estimate presented in this work is higher than previous values. It is worth acknowledging the caveats regarding the choice of α and γ parameters which feature in the TME. It is unclear whether their assumed values are indeed the right choices when estimating the mass of NGC 6822, thus adding additional uncertainty, which is not formally included. For instance, using the same method and identical assumptions, but only 4 extended GCs, Hwang et al. (2014) found the total mass of NGC 6822 enclosed within 11 kpc to be $7.5^{+4.5}_{-0.1} \times 10^9$ $M_\odot$. If I exclude the cluster with the velocity I have adopted from Hwang et al. (2014), the upper limit on the mass within the same range is 8.0×10^9 $M_\odot$. This indicates that when dealing with a small samples such as this one, the inclusion or exclusion of a single cluster can have an important effect on the estimated mass. For reference, using the kinematics of the HI gas, Weldrake et al. (2003) found a mass of 3.2×10^9 $M_\odot$ within $\sim$ 5 kpc from the centre of NGC 6822. Using sophisticated models for the evolution of the baryonic and dark matter components, Carigi et al. (2006) obtained a total mass of $1.5 - 4.0 \times 10^{10}$ $M_\odot$.

Using my updated mass estimate, I calculate the mass-to-light ratio of NGC 6822 and find it to be between 141 - 180, depending on the assumed mass. Given that the typical mass-to-light rations for Local Group dwarf galaxies range typically between $\sim$ 1 – 100 (Mateo, 1998; Kirby et al., 2014), NGC 6822 appears to be highly dominated by dark matter.

Table 5.7 *Dynamical mass estimate for NGC 6822. The lower and upper estimated limits, by assuming isotropic and radial orbit distributions respectively, are also shown. The table presents an updated mass-to-light ratio using the newly-derived mass.*

Galaxy	N_{GC}	α	M [$M_\odot$]	M_{lower} [$M_\odot$]	M_{upper} [$M_\odot$]	M/L[$M_\odot/L_\odot$]
NGC 6822	6	0	1.8×10^{10}	1.1×10^{10}	2.1×10^{10}	180
NGC 6822	6	0.55	1.4×10^{10}	1.1×10^{10}	2.1×10^{10}	141

5.6 Discussion

Extended GCs dominate the GC population of NGC 6822 in terms of numbers, suggesting that such galaxies could be the source of extended clusters in haloes of massive galaxies. Comparing the optical colours of the GCs hosted by NGC 6822 and those located in the M31 outer halo, it is found that they are all mutually consistent having $(V-I)_0 \sim 0.9$. This was also true for the GCs in NGC 147 and NGC 185. In addition there is a similarity between the mean absolute magnitudes of the extended GCs hosted by NGC 6822 and by M31, which are found to be $M_{V_0} = -5.7 \pm 0.8$ and $M_{V_0} = -5.6 \pm 0.7$, respectively. This may either be a fundamental property of extended GCs in general, or is a result of a bias arising from the final optical depth of the imaging. Given that some of them lie right at the detection limit, it is possible that the extended GCs have a large range of possible absolute magnitudes, but the currently available data allows only for the bright end of the luminosity function to be observed, resulting in the low spread and similar M_{V_0} values.

A number of studies have focused on GC systems hosted by dIrr galaxies outside the Local Group (e.g. Seth et al., 2004; Sharina et al., 2005; Georgiev et al., 2006, 2008). They have found that GCs have typical optical colours within the range of $0.8 < (V-I)_0 < 1.1$, consistent with my photometry of NGC 6822. In their study, Georgiev et al. (2008) searched for GCs in 19 nearby (2-8 Mpc) dIrr galaxies using archival *HST* data. The galaxies in their sample are members of dwarf galaxy associations only, without a dominant massive galaxy nearby. In their final sample of GC candidates that passed all their selection criteria, Georgiev et al. (2008) found absence of objects having $(V-I)_0 < 1$ and $M_{V_0} \gtrsim -6$, i.e. faint and blue. The authors claim that this effect is not due to a bias in their GC selection criteria, nor a bias due to the depth of the imaging, since they are able to identify clusters down to $M_{V_0} \simeq -4$. In NGC 6822 however, there are 2 extended GCs which satisfy these criteria. If such clusters were present in sample of Georgiev et al. (2008), they were most likely missed because of their low surface brightness as well as their extended morphology. It is also interesting to note that the GCs selected by Georgiev et al. (2008)

exhibit tentative signs for increasingly red optical colours as a function of projected distance from their hosts.

5.7 Summary

This chapter focused on the GC system hosted by the Local Group dIrr galaxy NGC 6822. I presented homogeneous optical and near-IR photometry for all known GCs in this galaxy. Using these data, I constrain the ages and metallicities of the clusters. It is found that all clusters are old with ages typically greater than 9 Gyrs. The estimated photometric metallicities are more controversial, and found to be considerably higher than those derived in previous spectroscopic studies. I compare the optical colours of these GCs to those that reside in the outer halo of M31 and find them to be similar, consistent with the idea that galaxies such as NGC 6822 could be the source of extended GCs in massive galaxy haloes.

Finally, I explore the kinematics of this GC system using new velocities for 6 GCs, 2 of which had no previous velocity information. No strong evidence for systemic rotation is found, meaning that such bulk motion is either not present or is too small to be detected with the current data. Furthermore, the kinematics is used to update the total mass estimate and mass-to-light ratio of this galaxy.

Chapter 6

Summary

The formation and evolution of galaxies through cosmic time are fundamental topics in astrophysics. One way of studying the assembly of a galaxy is through its globular star clusters (GCs). These bright, compact objects are thought to be amongst the oldest stellar systems in the Universe, formed in the most significant phases of galaxy formation. Various correlations have been found between the properties of GC systems and those of their parent galaxies, which makes them valuable tracers of galaxy formation and evolution.

The focus of this thesis is our cosmological backyard, the Local Group of galaxies. Initially the spotlight was laid on the outer halo GC system of M31, and then shifted to the GC systems of the dwarf galaxies NGC 147, NGC 147 and NGC 6822. By conducting photometric and kinematic analysis, important links were found between the GCs hosted by these dwarf galaxies to those located in the M31 outer halo, consistent with the idea that dwarf galaxies such as these are at least partially responsible for the formation of massive galaxies akin to M31.

6.1 Summary of science chapters

Kinematics of the M31 outer halo GC system

This chapter presents a comprehensive kinematic analysis using radial velocities of 78 GCs around M31, 63 of which had no previous spectroscopic information. The sample extends from $\sim$ 20 kpc out to $\sim$ 140 kpc in projection, and at least up to 200 kpc in 3D, enabling the exploration of the true outer halo

GC system of M31.

A significant degree of net rotation is detected in the outer halo GC population of M31. This population shares the the same rotation axis and direction as the GCs located in the inner regions of M31, as well as the M31 disk. Evidence for decreasing velocity dispersion as a function of projected distance from the M31 centre is also found. This behaviour of the velocity dispersion is well described by a power-law. The dispersion profile of the halo GC population is similar to that of the stellar halo, consistent with previous observations that the GCs and stars share similar spatial density profiles.

The velocity measurements further revealed a variety of correlations for the groups of GCs that lie projected on top of distinct stellar debris features in the field halo. This further supports the idea that a significant fraction of the M31 halo GC system has an external origin (e.g. Mackey et al., 2010b).

Finally, using the halo GCs as kinematic tracers, the total mass of M31 enclosed within a 3D radius of 200 kpc was estimated via the Tracer Mass Estimator. The calculated value of $(1.2-1.6)\pm0.2\times10^{12}M_{\odot}$ is in agreement with other recent mass estimates which employed kinematic tracers extending to similar radii.

The GC systems of NGC 147 and NGC 185

The focus of this chapter are the GC systems of NGC 147 and NGC 185. Exploring the PAndAS data resulted in the discovery of 3 new GCs around NGC 147, and one near NGC 185. The new discoveries update the census of GCs to 10 and 8 in NGC 147 and NGC 185, respectively.

Optical and near-IR photometric measurements are made on homogeneous data, as a means to constrain the ages and metallicities of all GCs hosted by these two galaxies. In general, it is found that the clusters are metal-poor ([Fe/H]$\lesssim -1.25$ dex), while their ages are more difficult to constrain. In addition, a hint of decreasing metallicity as a function of projected radius is also tentatively observed.

The close similarity between the $(V-I)_0$ colours of the GCs belonging to NGC 147 and NGC 185 and those belonging to the M31 outer halo is consistent with the idea that accretion of the former could have contributed to the assembly of the latter. In addition, the mean colours of the GCs hosted by these dwarf galaxies are found to lie at the peak of the colour distribution of the GC systems belonging to dEs in the Fornax and Virgo galaxy clusters, despite a

large difference in the environments in which they reside. Their S_N values are consistent with the trend of increasing GC specific frequency with decreasing galaxy luminosity generally observed for dwarf galaxies, regardless of their type, and in a variety of environments.

A kinematic analysis of these two GC systems is done by combining the obtained spectroscopic data of the newly-discovered GCs with the radial velocities of the previously known clusters available in the literature. No significant rotation is detected in either GC system, despite the known rotation of the stellar component in both galaxies. The velocity data is further used to constrain the dynamical masses of NGC 147 and NGC 185 via the Tracer Mass Estimator, finding $(1.4 - 1.8) \times 10^9 M_\odot$ and $(6.7 - 8.4) \times 10^9 M_\odot$ for NGC 147 and NGC 185, respectively. Both of these values are considerably higher than any previous mass estimates.

The GC system of NGC 6822

A uniform optical and near-IR photometric study is presented for the GC system hosted by NGC 6822. The photometric measurements are used to estimate the ages and metallicities of the GCs via colour-colour plots and an empirical colour-metallicity relation. All GCs are found to have old ages (> 9 Gyrs), in agreement with past studies. The clusters are found to exhibit a range of metallicities ($-1.6 \lesssim [\mathrm{Fe/H}] \lesssim -0.4$), contrary to previous studies which found them to be very metal-poor ([Fe/H]<-2.0).

The mean $(V - I)_0$ optical colours of the GCs in NGC 6822 are consistent with those of the GCs located in the M31 outer halo. Thus it is possible that dwarf irregular galaxies akin to NGC 6822 were the source of extended GCs found in the halo of M31.

Finally, the kinematic properties of this GC system are explored using new velocities for 6 GCs, 2 of which had no previous spectroscopic information. The GC system is not found to exhibit any rotation signature, despite the known rotation of the HI disk and the carbon stars spheroid of NGC 6822. Using the GCs as dynamical mass tracers, the total mass of NGC 6822 is recalculated to be $(1.4 - 1.8) \times 10^{10} M_\odot$. The corresponding mass-to-light ratio of this galaxy is between 140 - 180, making NGC 6822 highly dominated by dark matter.

6.2 Future work

The dynamics of the M31 outer halo GC system

The results presented in this work open doors for more detailed study of the dynamics of the M31 outer halo GC system. Through modelling of the orbits of the stellar streams using the GCs that project on top of them as kinematic tracers, one can learn more about the progenitor dwarf galaxies that contributed towards the formation of the M31 halo. Determining the orbits of multiple tidal streams will help deduce whether their formation is consistent with a single, more massive progenitor which got fragmented as it accreted onto M31, if each prominent stream originated from a separately accreted dwarf galaxy, or a combination of the two. In the latter two scenarios, knowledge of the satellite orbits will be an excellent test of the hypothesis that satellites are accreted from few preferred directions on the sky (e.g. Lovell et al., 2011), argument used to explain the planar arrangement of satellite galaxies observed both around M31 and around the Milky Way.

The existence of multiple dynamical tracers – HI gas, planetary nebulae, red and blue globular clusters, stellar streams, dwarf galaxies – which dominate at different projected radii from the centre of M31 presents a unique opportunity to constrain the mass profile of this galaxy.

The metal content of the M31 halo GCs

A good fraction of the spectroscopic data of the M31 outer halo GC system that I have presented in this thesis is appropriate for measurements of Lick indices, through which the ages and metallicities of the clusters can be estimated (e.g. Schiavon et al., 2012). This will enable the search for age and metallicity gradients in the halo GC system of M31, the existence of which will help constrain the origin of the halo GCs. For instance, the GCs that are associated with the Sagittarius dwarf galaxy, currently being accreted onto the Milky Way, are observed to have systematically different metallicities, for their age, compared to the field Galactic GCs (e.g. Dotter et al., 2011). Hence, metallicity information, in addition to spatial location and kinematics, may help to discriminate between GCs accreted along with their parent dwarf galaxies to those formed *in situ*, especially in complicated regions with intersecting stellar streams.

Combining the spectroscopic data with deep proprietary HST observations of the M31 outer halo GCs presents an opportunity for devising a method of determining the horizontal branch morphology via integrated spectra alone. The idea is to identify signature ratios of key indices, primarily the Balmer features. This has been attempted previously with the Milky Way GCs with some success (Schiavon et al., 2004). However, long slit observations of GCs in the Galaxy are challenging because one needs to make the slit width sufficiently large in order to cover significant portion of the cluster. The pursuit of this project with the M31 halo GCs has the advantage that the spectra are virtually unaffected by foreground Milky Way stars, and yet these objects are sufficiently close for the data to be of excellent quality. Such a study represents a crucial step towards the breaking of the age-metallicity degeneracy that arises due to the possible existence of hot old stars, which are hot enough to mimic the young stellar population. This will be of great interest when studying GCs of more distant systems for which obtaining colour-magnitude diagrams in not possible.

6.3 Final words

Modern theory offers a good overall explanation on how the Universe was created and how it grows and evolves with time. And yet, looking in our cosmological backyard, we observe much complexity in galaxies that we do not yet understand. The work presented here serves as a prime example of how studying galaxies through their globular cluster systems can make the picture of their formation and evolution more complete. A true revolution in this field is expected with the launch of the next generation of space observatories, such as the *James Webb Space Telescope*, which would enable us to trace the evolution of globular cluster systems through a larger time span, adding stronger constrains on the assembly processes of their respective hosts.

Appendix A

Radial velocity technique comparison

Radial velocities, and more recently redshifts, are one of the fundamental measurements done when studying astrophysical objects. Knowledge of the motions of celestial objects is extremely important and it has diverse applications in both the local and distant Universe.

It was first recognised by Doppler (1841) that the radial motion would change the observed colour of a star, a process analogous to that of changing the pitch of sound when there is a relative motion between the source and the detector. Fizeau (1841, 1870) realised that this would mean a shift in the positions of the Fraunhofer lines. The first visual attempt to observe these shifts was made by Huggins (1868), who attempted to determine whether a sample of stars and nebulae are moving toward or away from the Earth.

Influenced by radar studies during World War II, Fellgett (1955) suggested correlation techniques for deriving radial velocities, which were then implemented by Griffin (1967).

With the advent of digital detectors and the Fast Fourier Transformation (FFT) algorithm (Cooley & Tukey, 1965), the use of digital power spectrum techniques finally became practical (Blackman & Tukey, 1958). It was then shown by Simkin (1974) that Fourier methods could be used to derive radial velocities from digital spectroscopic data. The method proposed by Simkin (1974) was first put to practical use by Sargent et al. (1977), who used it to determine the redshifts and velocity dispersions of a sample containing 13 galaxies.

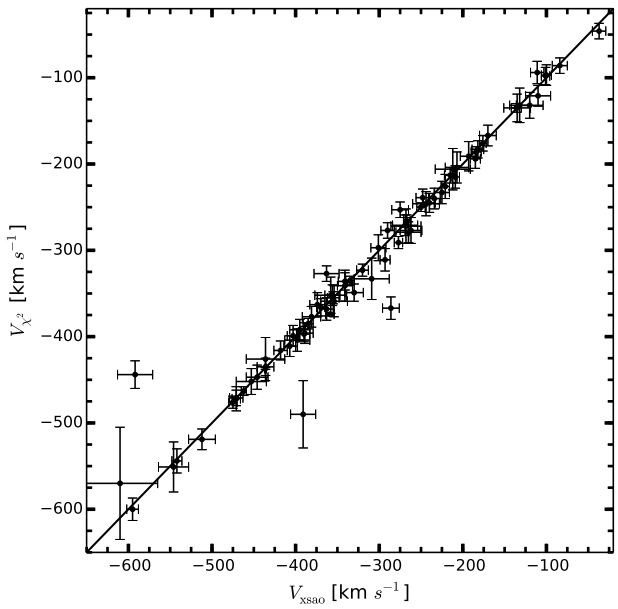

Figure A.1 *Comparing the radial velocities derived with the χ^2 routine to those obtained with* xcsao *task in* IRAF *(Kurtz & Mink, 1998). The comparison is done for the M31 halo GC sample. In general there is excellent agreement between the two sets of measurements with few just a few catastrophic misidentification by the* xcsao *task.*

Tonry & Davis (1979) combined the use of power spectrum techniques along with the use of the FFT algorithm to devise a method for obtaining redshifts and radial velocities from digital spectroscopic data. In addition, they invented the *r* statistic, which is calibrated to give the error of a measurement. Today, this method by Tonry & Davis (1979) is by far the most popular for determining radial velocities for digital spectra, especially for star clusters and galaxies, since it is fast and reliable in many cases.

However, if a noise feature is misidentified to be a real spectral line, the cross correlation FFT method may produce incorrect results. One way to avoid such misidentification is to use the accompanying error spectrum as a means to better determine if a feature in a spectrum is a real line or noise. This served as the motivation behind the construction of the χ^2 technique described in Section 2.3. The χ^2 technique essentially performs the same analysis as the Tonry & Davis (1979) method, but done in real space while also weighting each pixel element of the studied spectrum by the inverse of its accompanying uncertainty, effectively reducing the chances of a noise-induced feature to be misidentified as a real line in the process.

To test the performance of the χ^2 routine, I compare it against the velocities of the M31 halo GCs derived with the *xcsao* task part of the RVSAO pack-

age (Kurtz & Mink, 1998). This task is an advanced implementation of the Tonry & Davis (1979) algorithm coded in the IRAF environment. Figure A.1 shows the comparison between the two techniques, and the data is listed in Table A.1. There is an excellent agreement between the two techniques, with only a few discrepant points. Investigating the corresponding χ^2 and cross correlation functions for the deviant points, I found that in all such cases a series of noise features caused *xcsao* to produce a spurious cross correlation peak resulting in an incorrect velocity. Setting *xcsao* to ignore the noise infested regions produces velocities consistent with those from the χ^2 routine. In addition, the χ^2 routine is found have marginally better precision compared to *xcsao*. Over the whole M31 halo radial velocity sample, the mean uncertainty from the χ^2 routine measurements is 10 km s^{-1}, while for *xcsao* is 13 km s^{-1}.

Table A.1 *Comparison between the radial velocity measurements of the M31 halo GC sample derived with the custom χ^2 code to those derived with the* xcsao *task (Kurtz & Mink, 1998) in* IRAF *which employs the cross correlation method as devised by Tonry & Davis (1979).*

Cluster ID	RA (J2000) [hh:mm:sss]	DEC (J2000) [dd:mm:sss]	$R_{\rm proj}$ [kpc]	PA [deg]	GC type	$V_{\chi^2{\rm routine}}$ [km s^{-1}]	$V_{\rm xcsao}$ [km s^{-1}]
B514	+00:31:09.8	+37:54:00	55	214	GC	-471 $\pm$ 8	-471 $\pm$ 9
B517	+00:59:59.9	+41:54:06	45	78	GC	-277 $\pm$ 13	-262 $\pm$ 15
EXT8	+00:53:14.5	+41:33:24	27	81	GC	-194 $\pm$ 6	-185 $\pm$ 11
G001	+00:32:46.5	+39:34:40	35	229	GC	-335 $\pm$ 5	-335 $\pm$ 5
G002	+00:33:33.7	+39:31:18	34	226	GC	-352 $\pm$ 19	-358 $\pm$ 21
G268	+00:44:10.0	+42:46:57	21	10	GC	-277 $\pm$ 8	-290 $\pm$ 9
G339	+00:47:50.2	+43:09:16	29	26	GC	-97 $\pm$ 6	-100 $\pm$ 12
H1	+00:26:47.7	+39:44:46	46	245	GC	-245 $\pm$ 7	-240 $\pm$ 11
H2	+00:28:03.2	+40:02:55	42	248	GC	-519 $\pm$ 16	-512 $\pm$ 12
H3	+00:29:30.1	+41:50:31	35	284	GC	-86 $\pm$ 9	-84 $\pm$ 9
H4	+00:29:44.9	+41:13:09	33	270	GC	-368 $\pm$ 8	-363 $\pm$ 13
H5	+00:30:27.2	+41:36:19	32	279	GC	-392 $\pm$ 12	-395 $\pm$ 12
H7	+00:31:54.5	+40:06:47	32	242	GC	-426 $\pm$ 23	-000 $\pm$ 25
H8	+00:34:15.4	+39:52:53	29	230	GC	-463 $\pm$ 3	-462 $\pm$ 5
H9	+00:34:17.2	+37:30:43	56	204	GC	-374 $\pm$ 5	-359 $\pm$ 2
H10	+00:35:59.7	+35:41:03	78	194	GC	-352 $\pm$ 9	-356 $\pm$ 12
H11	+00:37:28.0	+44:11:26	42	342	GC	-213 $\pm$ 7	-215 $\pm$ 9
H12	+00:38:03.8	+37:44:00	50	195	GC	-396 $\pm$ 10	-389 $\pm$ 12
H14	+00:38:49.4	+42:22:47	18	327	GC	-271 $\pm$ 15	-269 $\pm$ 12
H15	+00:40:13.2	+35:52:36	74	185	GC	-367 $\pm$ 10	-286 $\pm$ 13
H17	+00:42:23.6	+37:14:34	55	181	GC	-246 $\pm$ 16	-244 $\pm$ 14
H18	+00:43:36.0	+44:58:59	51	2.4	GC	-206 $\pm$ 21	-212 $\pm$ 24
H19	+00:44:14.8	+38:25:42	39	174	GC	-272 $\pm$ 18	-268 $\pm$ 20
H22	+00:49:44.6	+38:18:37	44	155	GC	-311 $\pm$ 6	-293 $\pm$ 13
H23	+00:54:24.9	+39:42:55	37	124	GC	-377 $\pm$ 11	-381 $\pm$ 12
H24	+00:55:43.9	+42:46:15	39	57	GC	-121 $\pm$ 15	-110 $\pm$ 12
H25	+00:59:34.5	+44:05:38	57	46	GC	-204 $\pm$ 14	-207 $\pm$ 18
H26	+00:59:27.4	+37:41:30	66	137	GC	-411 $\pm$ 7	-407 $\pm$ 12
H27	+01:07:26.3	+35:46:48	100	137	GC	-291 $\pm$ 5	-277 $\pm$ 7
HEC1	+00:25:33.8	+40:43:38	45	262	EC	-233 $\pm$ 9	-225 $\pm$ 13
HEC2	+00:28:31.5	+37:31:23	63	217	EC	-341 $\pm$ 9	-98 $\pm$ 18
HEC6	+00:38:35.4	+44:16:51	42	346	EC	-132 $\pm$ 12	-209 $\pm$ 20
HEC10	+00:54:36.4	+44:58:44	59	29	EC	-98 $\pm$ 5	-366 $\pm$ 10
HEC11	+00:55:17.4	+38:51:01	47	134	EC	-215 $\pm$ 5	-341 $\pm$ 13
HEC13	+00:58:17.1	+37:13:49	69	142	EC	-366 $\pm$ 5	-132 $\pm$ 10
MGC1	+00:50:42.4	+32:54:58	116	169	GC	-355 $\pm$ 7	-355 $\pm$ 7

Table A.1 *Continued*

Cluster ID	RA (J2000) [hh:mm:sss]	DEC (J2000) [dd:mm:sss]	R_{proj} [kpc]	PA [deg]	GC type	$V_{\chi^2 routine}$ [km s^{-1}]	V_{xcsao} [km s^{-1}]
PAndAS-01	+23:57:12.0	+43:33:08	119	289	GC	-333 ± 21	-309 ± 24
PAndAS-02	+23:57:55.6	+41:46:49	115	277	EC	-266 ± 4	-267 ± 7
PAndAS-04	+00:04:42.9	+47:21:42	125	315	GC	-397 ± 7	-390 ± 9
PAndAS-05	+00:05:24.1	+43:55:35	101	294	EC	-183 ± 7	-182 ± 10
PAndAS-06	+00:06:11.9	+41:41:20	94	277	GC	-327 ± 15	-363 ± 9
PAndAS-07	+00:10:51.3	+39:35:58	86	257	EC	-452 ± 18	-453 ± 15
PAndAS-08	+00:12:52.4	+38:17:47	88	245	GC	-416 ± 8	-418 ± 11
PAndAS-09	+00:12:54.6	+45:05:55	91	308	GC	-444 ± 21	-592 ± 16
PAndAS-10	+00:13:38.6	+45:11:11	90	309	EC	-435 ± 10	-436 ± 10
PAndAS-11	+00:14:55.6	+44:37:16	83	306	GC	-447 ± 13	-446 ± 14
PAndAS-12	+00:17:40.0	+43:18:39	69	296	EC	-472 ± 5	-471 ± 14
PAndAS-13	+00:17:42.7	+43:04:31	68	293	GC	-570 ± 45	-610 ± 65
PAndAS-14	+00:20:33.8	+36:39:34	86	225	EC	-363 ± 9	-374 ± 14
PAndAS-15	+00:22:44.0	+41:56:14	52	282	GC	-385 ± 6	-385 ± 6
PAndAS-16	+00:24:59.9	+39:42:13	51	247	GC	-490 ± 15	-391 ± 39
PAndAS-17	+00:26:52.2	+38:44:58	54	232	GC	-279 ± 15	-265 ± 12
PAndAS-18	+00:28:23.2	+39:55:04	42	245	EC	-551 ± 18	-546 ± 29
PAndAS-19	+00:30:12.2	+39:50:59	38	240	GC	-544 ± 6	-542 ± 14
PAndAS-21	+00:31:27.5	+39:32:21	38	232	GC	-600 ± 7	-595 ± 13
PAndAS-22	+00:32:08.3	+40:37:31	29	253	GC	-437 ± 1	-436 ± 1
PAndAS-23	+00:33:14.1	+39:35:15	34	228	GC	-476 ± 5	-475 ± 7
PAndAS-27	+00:35:13.5	+45:10:37	57	341	GC	-46 ± 8	-37 ± 9
PAndAS-36	+00:44:45.5	+43:26:34	30	9	GC	-399 ± 7	-403 ± 12
PAndAS-37	+00:48:26.5	+37:55:42	48	161	GC	-404 ± 15	-398 ± 13
PAndAS-41	+00:53:39.5	+42:35:14	33	56	GC	-94 ± 8	-111 ± 13
PAndAS-42	+00:56:38.0	+39:40:25	42	120	GC	-176 ± 4	-176 ± 9
PAndAS-43	+00:56:38.8	+42:27:17	39	64	GC	-135 ± 6	-136 ± 5
PAndAS-44	+00:57:55.8	+41:42:57	39	80	GC	-349 ± 11	-330 ± 10
PAndAS-45	+00:58:37.9	+41:57:11	42	76	GC	-135 ± 16	-135 ± 16
PAndAS-46	+00:58:56.3	+42:27:38	44	67	GC	-132 ± 16	-120 ± 15
PAndAS-47	+00:59:04.7	+42:22:35	44	69	GC	-359 ± 16	-354 ± 18
PAndAS-48	+00:59:28.2	+31:29:10	141	160	EC	-250 ± 5	-250 ± 5
PAndAS-49	+01:00:50.0	+42:18:13	48	72	EC	-240 ± 7	-234 ± 12
PAndAS-50	+01:01:50.6	+48:18:19	107	24	EC	-323 ± 7	-323 ± 7
PAndAS-51	+01:02:06.6	+42:48:06	53	65	GC	-226 ± 5	-226 ± 14
PAndAS-52	+01:12:47.0	+42:25:24	78	76	GC	-297 ± 9	-301 ± 15
PAndAS-53	+01:17:58.4	+39:14:53	96	104	GC	-253 ± 10	-275 ± 9
PAndAS-54	+01:18:00.1	+39:16:59	96	104	GC	-336 ± 8	-341 ± 10
PAndAS-56	+01:23:03.5	+41:55:11	103	82	GC	-239 ± 8	-248 ± 10
PAndAS-57	+01:27:47.5	+40:40:47	116	90	GC	-186 ± 6	-184 ± 6
PAndAS-58	+01:29:02.1	+40:47:08	119	89	GC	-167 ± 10	-170 ± 12
SK255B	+00:49:03.0	+41:54:57	18	61	GC	-191 ± 10	-193 ± 17

Appendix B

Review of the NGC 147 and NGC 185 GC discovery history

The contents of this appendix are published in Veljanoski et al. (2013a)

The following is a short review of the discovery history and the nomenclature of the GCs hosted by NGC 147 and NGC 185. The motivation for this is to highlight some inconsistencies in the literature that were discovered while this thesis was in preparation. This is done in order to minimise the possibility of future confusion when studying the GCs of these two dEs.

The existence of GCs in both NGC 147 and NGC 185 was first reported by Baade (1944), who discovered two GCs in each of the galaxies. In his paper, the clusters were not named and coordinates were provided only for the ones hosted by NGC 185 and in terms of relative positions (measured on photographic plates) from the galaxy centre.

Hodge (1974) reported the discovery and presented photometry of five GCs in NGC 185, two of which were those previously discovered by Baade (1944). These clusters were simply labelled 1-5. While their coordinates were not provided, a finding chart was shown.

Two years later, Hodge (1976) published a paper on the structure of NGC 147, in which the discovery and photometry of two additional GCs bound to this galaxy were presented, alongside the two clusters previously discovered by Baade (1944). Once again, no coordinates for any of these objects were given, but a finding chart was published, on which the clusters are labelled 1-4. In the literature, these clusters are now known as Hodge I-IV.

In an appendix to their paper on planetary nebulae in NGC 147 and NGC 185, Ford et al. (1977) revisited the GC systems of the two dEs. In addition to the

GCs already discovered by Baade and Hodge around NGC 185, they presented the discovery of an additional four clusters from their photographic plates, while also discarding the object labelled by Hodge (1974) as "2" from being a GC. In Ford et al. (1977), the objects are numbered I-VIII but the counting does not follow the pattern started by Hodge (1974). This nomenclature has propagated through the literature, and these clusters are referred to as FJJ I-VIII in recent publications. In addition, equatorial coordinates together with a finding chart were also published for the entire sample of GCs described by Ford et al. (1977).

Ford et al. (1977) also revisited the GC system of NGC 147. They recovered the objects already identified by Hodge (1976) as globulars and did not find any new members belonging to this system. They showed a finding chart and a table with equatorial coordinates for the three brightest globulars in this galaxy. Their finding chart is identical to the one published by Hodge (1976) in terms of the labelling and positions of the GCs: Hodge II is south of Hodge I and Hodge III is south of Hodge II. However, in their Table 9 that lists the clusters' coordinates, the positions of Hodge II and Hodge III are swapped: Hodge II is listed to be south of Hodge III. This unintentional oversight is most probably the main reason for many inconsistencies in the more recent literature.

A paper published by Da Costa & Mould (1988) presented spectroscopic data and metal abundances of the GCs hosted by NGC 147 and NGC 185. Regarding the NGC 185 system, they presented V-band photometry taken from Hodge (1974) and spectroscopic data for clusters FJJ I-V, as well as Hodge 2 that Ford et al. (1977) classified not to be a cluster. For cluster FJJ IV which was not listed amongst the GC candidates by Hodge (1974) the V magnitude was estimated by eye. Analysing the cluster spectra, Da Costa & Mould (1988) showed that Hodge 2 is indeed a galaxy at redshift $z = 0.04$ and not a GC.

Regarding the NGC 147 system, Da Costa & Mould (1988) took spectra only of Hodge I and Hodge III. In their Table 1, they listed the photometric V magnitude of these two clusters as reported by Hodge (1976). They did not list coordinates for any of the clusters but stated that the centres of the clusters were taken from Ford et al. (1977). This probably means that they presented metal abundances of Hodge II rather than Hodge III. There was no indication that Da Costa & Mould (1988) noticed the oversight made by Ford et al. (1977), and in Table 4.6 I have assumed that they have not.

Geisler et al. (1999) observed all but one cluster in NGC 185 with the HST, that

were known at that time. The cluster which was not observed was FJJ VIII. They found that FJJ VI is not a GC but an elliptical galaxy. All other cluster candidates that were observed were confirmed to be genuine GCs.

In more recent literature, Sharina et al. (2006) revisited the GC systems of NGC 147 and NGC 185 using HST/WFPC2 imagery and spectroscopy taken with the SCORPIO spectrograph. They did not provide coordinates for any of the clusters, but they did provide finding charts. In the case of NGC 147, they had the positions of Hodge II and Hodge III reversed compared to the original publication by Hodge (1976), so it is highly likely the data and results presented for Hodge II actually refer to Hodge III and vice versa. In their Table 2, they have taken the V magnitudes of what they label as Hodge I and Hodge III from the original paper by Hodge (1976), while the V magnitude of their Hodge II is taken from Hodge (1974) even though this paper analysed only clusters hosted by NGC 185 and did not list photometric values for any cluster in NGC 147. This made the cluster they label as Hodge II brighter than Hodge III, which is easily seen not to be the case with simple visual inspection of their HST images.

The most recent publication regarding the NGC 147 GC system is by Sharina & Davoust (2009). In their paper they announced the discovery of three new GCs. They presented a coordinate table and a finding chart, both having correct positions compared to the original Hodge (1976) publication regarding the "classical Hodge" clusters. In addition, they also state that the identifiers of Hodge II and Hodge III were inverted by mistake in Sharina et al. (2006), meaning any values cited from the earlier publication are not assigned to the wrong object in Sharina & Davoust (2009).

Finally, in this theis I report the discovery of another three GCs hosted by NGC 147, and one hosted by NGC 185. Interestingly, all three of the new GCs in NGC 147 lie beyond areas previously imaged for GC searches, while the new GC in NGC 185 lies within the photographic plate region searched by Ford et al. (1977). It can be speculated that the outlying nature of this object coupled with its low luminosity caused it to be missed in the original study. The tables presented in this thesis reflect the original naming and correct coordinates for all previously known GCs, as well as these new discoveries.

Bibliography

Abadi M. G., Navarro J. F., Steinmetz M., 2006, MNRAS, 365, 747

Alloin D., Pelat D., Bijaoui A., 1976, AAp, 50, 127

Alves-Brito A., Forbes D. A., Mendel J. T., Hau G. K. T., Murphy M. T., 2009, MNRAS, 395, L34

Anderson J. et al., 2008, AJ, 135, 2055

Armandroff T. E., 1989, AJ, 97, 375

Ashman K. M., Bird C. M., 1993, AJ, 106, 2281

Ashman K. M., Bird C. M., Zepf S. E., 1994, AJ, 108, 2348

Ashman K. M., Carr B. J., 1988, MNRAS, 234, 219

Ashman K. M., Zepf S. E., 1992, ApJ, 384, 50

Ashman K. M., Zepf S. E., 1998, Cambridge Astrophysics Series, 30

Auriere M., Coupinot G., Hecquet J., 1992, AAp, 256, 95

Baade W., 1944, ApJ, 100, 147

Baade W., Arp H., 1964, ApJ, 139, 1027

Barmby P., Huchra J. P., 2001, AJ, 122, 2458

Barmby P., Huchra J. P., Brodie J. P., Forbes D. A., Schroder L. L., Grillmair C. J., 2000, AJ, 119, 727

Barnard E. E., 1884, Astronomische Nachrichten, 110, 125

Barnes J. E., Hernquist L., 1996, ApJ, 471, 115

Bate N. F. et al., 2013, ArXiv e-prints

Battinelli P., Demers S., 2004, AAP, 417, 479

Battinelli P., Demers S., Kunkel W. E., 2006, AAp, 451, 99

Battistini P., Bonoli F., Braccesi A., Federici L., Fusi Pecci F., Marano B., Borngen F., 1987, AApSS, 67, 447

Battistini P. L., Bonoli F., Casavecchia M., Ciotti L., Federici L., Fusi-Pecci F., 1993, AAp, 272, 77

Beasley M. A., Forbes D. A., Brodie J. P., Kissler-Patig M., 2004, MNRAS, 347, 1150

Beers T. C., Flynn K., Gebhardt K., 1990, AJ, 100, 32

Bekki K., 2010, MNRAS, 401, L58

Bekki K., Forbes D. A., Beasley M. A., Couch W. J., 2002, MNRAS, 335, 1176

Bellazzini M., Ferraro F. R., Ibata R., 2003, AJ, 125, 188

Belokurov V. et al., 2006, ApJL, 642, L137

Bender R., Paquet A., Nieto J.-L., 1991, AAp, 246, 349

Bertin E., 2009, MEMSAI, 80, 422

Binney J., Tremaine S., 1987, Galactic dynamics. Princeton, NJ, Princeton University Press

Blackman R. B., Tukey J., 1958, The Measurement of Power Spectra, New York: Dover.

Blakeslee J. P., Cantiello M., Peng E. W., 2010, Apj, 710, 51

Blom C., Forbes D. A., Brodie J. P., Foster C., Romanowsky A. J., Spitler L. R., Strader J., 2012, MNRAS, 426, 1959

Boulade O. et al., 2003, in Iye M., Moorwood A. F. M., eds, Society of Photo-Optical Instrumentation Engineers (SPIE) Conference Series Vol. 4841, Instrument Design and Performance for Optical/Infrared Ground-based Telescopes. pp 72–81

Bressan A., Marigo P., Girardi L., Salasnich B., Dal Cero C., Rubele S., Nanni A., 2012, MNRAS, 427, 127

Brodie J. P., Strader J., 2006, ARAA, 44, 193

Brodie J. P., Usher C., Conroy C., Strader J., Arnold J. A., Forbes D. A., Romanowsky A. J., 2012, ApJL, 759, L33

Bruzual G., Charlot S., 2003, MNRAS, 344, 1000

Burkert A., Smith G. H., 1997, ApJL, 474, L15

Burkert A., Tremaine S., 2010, ApJ, 720, 516

Butler D. J., Martínez-Delgado D., 2005, AJ, 129, 2217

Caldwell N., Schiavon R., Morrison H., Rose J. A., Harding P., 2011, AJ, 141, 61

Cannon J. M. et al., 2012, ApJ, 747, 122

Carigi L., Colín P., Peimbert M., 2006, ApJ, 644, 924

Carretta E., Bragaglia A., Gratton R., D'Orazi V., Lucatello S., 2009, AAp, 508, 695

Casali M. et al., 2007, AAp, 467, 777

Chandar R., Bianchi L., Ford H. C., 2000, AJ, 120, 3088

Chandar R., Whitmore B., Lee M. G., 2004, ApJ, 611, 220

Chapman S. C. et al., 2008, MNRAS, 390, 1437

Chapman S. C., Ibata R., Lewis G. F., Ferguson A. M. N., Irwin M., McConnachie A., Tanvir N., 2006, ApJ, 653, 255

Chies-Santos A. L., Larsen S. S., Kuntschner H., Anders P., Wehner E. M., Strader J., Brodie J. P., Santos J. F. C., 2011, AAP, 525, A20+

Cioni M.-R. L. et al., 2008, AAP, 487, 131

Cohen J. G., 2004, AJ, 127, 1545

Cohen J. G., Blakeslee J. P., 1998, AJ, 115, 2356

Cohen J. G., Blakeslee J. P., Côté P., 2003, ApJ, 592, 866

Collins M. L. M. et al., 2011, MNRAS, 413, 1548

Collins M. L. M. et al., 2009, MNRAS, 396, 1619

Collins M. L. M. et al., 2013, ArXiv e-prints

Collins M. L. M. et al., 2014, ApJ, 783, 7

Conn A. R. et al., 2012, ApJ, 758, 11

Cooley J. W., Tukey J., 1965, Mathematics of Computation, 19, 297

Corwin Jr. H. G., Buta R. J., de Vaucouleurs G., 1994, AJ, 108, 2128

Côté P., 1999, AJ, 118, 406

Côté P., Marzke R. O., West M. J., 1998, ApJ, 501, 554

Côté P. et al., 2001, ApJ, 559, 828

Courteau S., van den Bergh S., 1999, AJ, 118, 337

Da Costa G. S., Held E. V., Saviane I., Gullieuszik M., 2009, ApJ, 705, 1481

Da Costa G. S., Mould J. R., 1988, ApJ, 334, 159

Davidge T. J., 2005, AJ, 130, 2087

de Blok W. J. G., Walter F., 2000, ApJL, 537, L95

de Blok W. J. G., Walter F., 2006, AJ, 131, 343

De Rijcke S., Prugniel P., Simien F., Dejonghe H., 2006, MNRAS, 369, 1321

Deason A. J. et al., 2012, MNRAS, 425, 2840

Demers S., Battinelli P., Kunkel W. E., 2006, ApJL, 636, L85

Deveikis V., Narbutis D., Stonkutė R., Bridžius A., Vansevičius V., 2008, Baltic Astronomy, 17, 351

Di Cintio A., Knebe A., Libeskind N. I., Hoffman Y., Yepes G., Gottlöber S., 2012, MNRAS, 423, 1883

di Tullio Zinn G., Zinn R., 2013, AJ, 145, 50

Doppler C., 1841, Königliche böhmische Gesellschaft der Wissenschaft Abhandlungen, p. 465

Dotter A., Chaboyer B., Jevremović D., Kostov V., Baron E., Ferguson J. W., 2008, ApJS, 178, 89

Dotter A., Sarajedini A., Anderson J., 2011, ApJ, 738, 74

Dotter A. et al., 2010, ApJ, 708, 698

Dubath P., Grillmair C. J., 1997, AAp, 321, 379

Durrell P. R., Harris W. E., Geisler D., Pudritz R. E., 1996, AJ, 112, 972

Eggen O. J., Lynden-Bell D., Sandage A. R., 1962, ApJ, 136, 748

Evans N. W., Wilkinson M. I., 2000, MNRAS, 316, 929

Evans N. W., Wilkinson M. I., Perrett K. M., Bridges T. J., 2003, ApJ, 583, 752

Faifer F. R. et al., 2011, MNRAS, 416, 155

Fardal M. A. et al., 2013, MNRAS, 434, 2779

Faria D., Johnson R. A., Ferguson A. M. N., Irwin M. J., Ibata R. A., Johnston K. V., Lewis G. F., Tanvir N. R., 2007, AJ, 133, 1275

Federici L., Bonoli F., Ciotti L., Fusi-Pecci F., Marano B., Lipovetsky V. A., Niezvestny S. I., Spassova N., 1993, AAp, 274, 87

Federici L., Marano B., Fusi Pecci F., 1990, AAp, 236, 99

Fellgett P., 1955, Optica Acta, 2, 9

Ferguson A. M. N., Irwin M. J., Ibata R. A., Lewis G. F., Tanvir N. R., 2002, AJ, 124, 1452

Feroz F., Hobson M. P., 2008, MNRAS, 384, 449

Feroz F., Hobson M. P., Bridges M., 2009, MNRAS, 398, 1601

Ferraro F. R., Sollima A., Pancino E., Bellazzini M., Straniero O., Origlia L., Cool A. M., 2004, ApJL, 603, L81

Fizeau M. H., 1841, lecture before the Société Philomathique

Fizeau M. H., 1870, Annales de Chimie et de Physique, 19, 217

Forbes D. A., Beasley M. A., Brodie J. P., Kissler-Patig M., 2001, ApJl, 563, L143

Forbes D. A., Brodie J. P., Grillmair C. J., 1997, AJ, 113, 1652

Forbes D. A., Forte J. C., 2001, MNRAS, 322, 257

Ford H. C., Jacoby G., Jenner D. C., 1977, ApJ, 213, 18

Fusi-Pecci F., Clementini G., 2000, Globular Clusters

Gallart C., Aparicio A., Bertelli G., Chiosi C., 1996a, AJ, 112, 2596

Gallart C., Aparicio A., Bertelli G., Chiosi C., 1996b, AJ, 112, 1950

Galleti S., Bellazzini M., Buzzoni A., Federici L., Fusi Pecci F., 2009, AAp, 508, 1285

Galleti S., Bellazzini M., Federici L., Buzzoni A., Fusi Pecci F., 2007, AAp, 471, 127

Galleti S., Federici L., Bellazzini M., Buzzoni A., Fusi Pecci F., 2006, AAp, 456, 985

Galleti S., Federici L., Bellazzini M., Fusi Pecci F., Macrina S., 2004, AAp, 416, 917

Gebhardt K., Kissler-Patig M., 1999, AJ, 118, 1526

Geha M., van der Marel R. P., Guhathakurta P., Gilbert K. M., Kalirai J., Kirby E. N., 2010, ApJ, 711, 361

Geisler D., Armandroff T., da Costa G., Lee M. G., Sarajedini A., 1999, in P. Whitelock & R. Cannon ed., IAU Symposium Vol. 192, The Stellar Content of Local Group Galaxies. p. 231

Georgiev I. Y., Goudfrooij P., Puzia T. H., Hilker M., 2008, AJ, 135, 1858

Georgiev I. Y., Hilker M., Puzia T. H., Chanamé J., Mieske S., Goudfrooij P., Reisenegger A., Infante L., 2006, AAp, 452, 141

Georgiev I. Y., Puzia T. H., Goudfrooij P., Hilker M., 2010, MNRAS, 406, 1967

Gilbert K. M. et al., 2012, ApJ, 760, 76

Girardi L. et al., 2010, ApJ, 724, 1030

Gómez M., Richtler T., 2004, AAp, 415, 499

Górski M., Pietrzyński G., Gieren W., 2011, AJ, 141, 194

Goudfrooij P., Strader J., Brenneman L., Kissler-Patig M., Minniti D., Edwin Huizinga J., 2003, MNRAS, 343, 665

Griffin R. F., 1967, ApJ, 148, 465

Grocholski A. J., Parisi M. C., Geisler D., Sarajedini A., Cole A. A., Clariá J. J., Smith V. V., 2009, in Van Loon J. T., Oliveira J. M., eds, IAU Symposium Vol. 256, IAU Symposium. pp 287–292

Hargis J. R., Rhode K. L., 2012, AJ, 144, 164

Harris G. L. H., Poole G. B., Harris W. E., 2014, MNRAS, 438, 2117

Harris W. E., 1996, AJ, 112, 1487

Harris W. E., 2001, in L. Labhardt & B. Binggeli ed., Saas-Fee Advanced Course 28: Star Clusters. p. 223

Harris W. E., Harris G. L. H., Alessi M., 2013, ApJ, 772, 82

Harris W. E., van den Bergh S., 1981, AJ, 86, 1627

Hartwick F. D. A., Sargent W. L. W., 1974, ApJ, 190, 283

Hempel M., Geisler D., Hoard D. W., Harris W. E., 2005, AAp, 439, 59

Hesser J. E., Harris W. E., Vandenberg D. A., 1987, PASP, 99, 1148

Hodge P. W., 1974, PASP, 86, 289

Hodge P. W., 1976, AJ, 81, 25

Hodge P. W., 1977, ApJS, 33, 69

Hodge P. W., 1980, ApJ, 241, 125

Hodgkin S. T., Irwin M. J., Hewett P. C., Warren S. J., 2009, MNRAS, 394, 675

Hubble E., 1932, ApJ, 76, 44

Hubble E. P., 1925, ApJ, 62, 409

Huchra J., Stauffer J., van Speybroeck L., 1982, ApJL, 259, L57

Huchra J. P., Brodie J. P., Kent S. M., 1991, ApJ, 370, 495

Hudson M. J., Harris G. L., Harris W. E., 2014, ApJL, 787, L5

Huggins W., 1868, Royal Society of London Philosophical Transactions Series I, 158, 529

Hunter J. D., 2007, Computing in Science & Engineering, 9

Huxor A. P. et al., 2011, MNRAS, p. 452

Huxor A. P., Ferguson A. M. N., Veljanoski J., Mackey A. D., Tanvir N. R., 2013, MNRAS, 429, 1039

Huxor A. P. et al., 2014, ArXiv e-prints

Huxor A. P., Tanvir N. R., Ferguson A. M. N., Irwin M. J., Ibata R., Bridges T., Lewis G. F., 2008, MNRAS, 385, 1989

Huxor A. P., Tanvir N. R., Irwin M. J., Ibata R., Collett J. L., Ferguson A. M. N., Bridges T., Lewis G. F., 2005, MNRAS, 360, 1007

Hwang N., Lee M. G., Lee J. C., Park W.-K., Park H. S., Kim S. C., Park J.-H., 2011, ApJ, 738, 58

Hwang N., Park H. S., Lee M. G., Lim S., Hodge P. W., Kim S. C., Miller B., Weisz D., 2014, ApJ, 783, 49

Ibata R., Chapman S., Ferguson A. M. N., Lewis G., Irwin M., Tanvir N., 2005, ApJ, 634, 287

Ibata R., Irwin M., Lewis G., Ferguson A. M. N., Tanvir N., 2001, Nature, 412, 49

Ibata R., Martin N. F., Irwin M., Chapman S., Ferguson A. M. N., Lewis G. F., McConnachie A. W., 2007, ApJ, 671, 1591

Ibata R. A., Gilmore G., Irwin M. J., 1994, Nature, 370, 194

Ibata R. A., Gilmore G., Irwin M. J., 1995, MNRAS, 277, 781

Ibata R. A. et al., 2013, Nature, 493, 62

Ibata R. A. et al., 2014, ApJ, 780, 128

Irwin M. J., Ferguson A. M. N., Huxor A. P., Tanvir N. R., Ibata R. A., Lewis G. F., 2008, ApJL, 676, L17

Irwin M. J., Ferguson A. M. N., Ibata R. A., Lewis G. F., Tanvir N. R., 2005, ApJL, 628, L105

Irwin M. J. et al., 2004, in Quinn P. J., Bridger A., eds, Society of Photo-Optical Instrumentation Engineers (SPIE) Conference Series Vol. 5493, Society of Photo-Optical Instrumentation Engineers (SPIE) Conference Series. pp 411–422

Israel F. P., Bontekoe T. R., Kester D. J. M., 1996, AAp, 308, 723

Jang I. S., Lim S., Park H. S., Lee M. G., 2012, ApJL, 751, L19

Jeffreys H., 1961, The Clarendon Press, Oxford University Press

Jordán A. et al., 2004, ApJS, 154, 509

Kaiser N., 2004, in Oschmann Jr. J. M., ed., Society of Photo-Optical Instrumentation Engineers (SPIE) Conference Series Vol. 5489, Ground-based Telescopes. pp 11–22

Kaiser N. et al., 2010, in Society of Photo-Optical Instrumentation Engineers (SPIE) Conference Series.

Kartha S. S., Forbes D. A., Spitler L. R., Romanowsky A. J., Arnold J. A., Brodie J. P., 2014, MNRAS, 437, 273

Kass R. E., Raftery A. E., 1995, JSTOR, 90, 773

Keller S. C., Mackey D., Da Costa G. S., 2012, ApJ, 744, 57

Kim H.-S., Yoon S.-J., Sohn S. T., Kim S. C., Kim E., Chung C., Lee S.-Y., Lee Y.-W., 2013, ApJ, 763, 40

Kim S. C. et al., 2007, AJ, 134, 706

King I., 1962, AJ, 67, 471

Kinman T. D., 1959, MNRAS, 119, 538

Kirby E. N., Bullock J. S., Boylan-Kolchin M., Kaplinghat M., Cohen J. G., 2014, MNRAS, 439, 1015

Kissler-Patig M., Brodie J. P., Minniti D., 2002, AAp, 391, 441

Koch A., Côté P., 2010, AAp, 517, A59

Koch A., McWilliam A., 2008, AJ, 135, 1551

Koch A., McWilliam A., 2010, AP, 139, 2289

Koposov S. et al., 2007, ApJ, 669, 337

Kravtsov A. V., Gnedin O. Y., 2005, ApJ, 623, 650

Kriek M. et al., 2010, ApJL, 722, L64

Kundu A., Whitmore B. C., 2001, AJ, 121, 2950

Kuntschner H., Ziegler B. L., Sharples R. M., Worthey G., Fricke K. J., 2002, AAp, 395, 761

Kurtz M. J., Mink D. J., 1998, PASP, 110, 934

Larsen S. S., Brodie J. P., Huchra J. P., Forbes D. A., Grillmair C. J., 2001, AJ, 121, 2974

Larson R. B., 1972, Nature Physical Science, 236, 7

Law D. R., Majewski S. R., 2010, ApJ, 718, 1128

Lee M. G., Freedman W. L., Madore B. F., 1993, Aj, 106, 964

Lee M. G., Hwang H. S., Kim S. C., Park H. S., Geisler D., Sarajedini A., Harris W. E., 2008, ApJ, 674, 886

Lewis A., Bridle S., 2002, PhRev, 66, 103511

Lewis G. F. et al., 2013, ApJ, 763, 4

Libeskind N. I., Frenk C. S., Cole S., Helly J. C., Jenkins A., Navarro J. F., Power C., 2005, MNRAS, 363, 146

Libeskind N. I., Knebe A., Hoffman Y., Gottlöber S., Yepes G., Steinmetz M., 2011, MNRAS, 411, 1525

Lotz J. M., Miller B. W., Ferguson H. C., 2004, ApJ, 613, 262

Lovell M. R., Eke V. R., Frenk C. S., Jenkins A., 2011, MNRAS, 413, 3013

Mackey A. D. et al., 2010a, MNRAS, 401, 533

Mackey A. D. et al., 2006, ApJL, 653, L105

Mackey A. D. et al., 2010b, ApJL, 717, L11

Mackey A. D. et al., 2013, MNRAS, 429, 281

Mackey A. D., van den Bergh S., 2005, MNRAS, 360, 631

Magnier E., 2006, in The Advanced Maui Optical and Space Surveillance Technologies Conference.

Mamon G. A., Łokas E. L., 2005, MNRAS, 363, 705

Maraston C., 1998, MNRAS, 300, 872

Marigo P., Girardi L., Bressan A., Groenewegen M. A. T., Silva L., Granato G. L., 2008, AAp, 482, 883

Marín-Franch A. et al., 2009, ApJ, 694, 1498

Martin N. F., Ibata R. A., Irwin M. J., Chapman S., Lewis G. F., Ferguson A. M. N., Tanvir N., McConnachie A. W., 2006, MNRAS, 371, 1983

Martin N. F., Ibata R. A., McConnachie A. W., Dougal Mackey A., Ferguson A. M. N., Irwin M. J., Lewis G. F., Fardal M. A., 2013, ApJ, 776, 80

Martin N. F. et al., 2009, ApJ, 705, 758

Martínez-Delgado D., Aparicio A., Gallart C., 1999, AJ, 118, 2229

Mateo M. L., 1998, ARAA, 36, 435

Mayall N. U., Eggen O. J., 1953, PASP, 65, 24

McConnachie A. W., 2012, AJ, 144, 4

McConnachie A. W., Ferguson A. M. N., Irwin M. J., Dubinski J., Widrow L. M., Dotter A., Ibata R., Lewis G. F., 2010, ApJ, 723, 1038

McConnachie A. W., Irwin M. J., Ferguson A. M. N., Ibata R. A., Lewis G. F., Tanvir N., 2005, MNRAS, 356, 979

McConnachie A. W., Irwin M. J., Ibata R. A. e., 2009, Nature, 461, 66

McMillan P. J., 2011, MNRAS, 414, 2446

Metz M., Kroupa P., Jerjen H., 2007, MNRAS, 374, 1125

Miller B. W., Lotz J. M., 2007, ApJ, 670, 1074

Miller B. W., Lotz J. M., Ferguson H. C., Stiavelli M., Whitmore B. C., 1998, ApJL, 508, L133

Miller B. W., Whitmore B. C., Schweizer F., Fall S. M., 1997, AJ, 114, 2381

Milone A. P. et al., 2008, ApJ, 673, 241

Minniti D., 1995, AJ, 109, 1663

Mochejska B. J., Kaluzny J., Krockenberger M., Sasselov D. D., Stanek K. Z., 1998, Acta Astronomica, 48, 455

Morgan W. W., 1956, PASP, 68, 509

Morgan W. W., 1959, AJ, 64, 432

Morganson E. et al., 2012, AJ, 143, 142

Muratov A. L., Gnedin O. Y., 2010, ApJ, 718, 1266

Nantais J. B., Huchra J. P., 2010, AJ, 139, 2620

Navarro J. F., Frenk C. S., White S. D. M., 1996, ApJ, 462, 563

Newberg H. J. et al., 2002, ApJ, 569, 245

Oliphant T. E., 2007, Computing in Science & Engineering, 9

Olsen K. A. G., Miller B. W., Suntzeff N. B., Schommer R. A., Bright J., 2004, AJ, 127, 2674

Onaka P., Tonry J. L., Isani S., Lee A., Uyeshiro R., Rae C., Robertson L., Ching G., 2008, in Society of Photo-Optical Instrumentation Engineers (SPIE) Conference Series.

Pagel B. E. J., Tautvaisiene G., 1998, MNRAS, 299, 535

Peñarrubia J., Ma Y.-Z., Walker M. G., McConnachie A., 2014, ArXiv e-prints

Peacock M. B., Maccarone T. J., Knigge C., Kundu A., Waters C. Z., Zepf S. E., Zurek D. R., 2010, MNRAS, 402, 803

Peebles P. J. E., 1984, ApJ, 277, 470

Peng E. W. et al., 2011, ApJ, 730, 23

Peng E. W. et al., 2008, ApJ, 681, 197

Pérez F., Granger B. E., 2007, Computing in Science & Engineering, 9

Perina S., Federici L., Bellazzini M., Cacciari C., Fusi Pecci F., Galleti S., 2009, AAp, 507, 1375

Perrett K. M., Bridges T. J., Hanes D. A., Irwin M. J., Brodie J. P., Carter D., Huchra J. P., Watson F. G., 2002, AJ, 123, 2490

Perrett K. M., Stiff D. A., Hanes D. A., Bridges T. J., 2003, ApJ, 589, 790

Peterson R., 1989, in Merritt D., ed., Dynamics of Dense Stellar Systems. pp 161–166

Pierce M., Brodie J. P., Forbes D. A., Beasley M. A., Proctor R., Strader J., 2005, MNRAS, 358, 419

Piotto G. et al., 2007, ApJL, 661, L53

Piotto G. et al., 2012, ApJ, 760, 39

Pota V. et al., 2013, MNRAS, 428, 389

Pota V., Graham A. W., Forbes D. A., Romanowsky A. J., Brodie J. P., Strader J., 2013, MNRAS, 433, 235

Puzia T. H., Kissler-Patig M., Thomas D., Maraston C., Saglia R. P., Bender R., Goudfrooij P., Hempel M., 2005, AAp, 439, 997

Puzia T. H., Zepf S. E., Kissler-Patig M., Hilker M., Minniti D., Goudfrooij P., 2002, AAp, 391, 453

Regnault N. et al., 2009, AAp, 506, 999

Reitzel D. B., Guhathakurta P., Rich R. M., 2004, AJ, 127, 2133

Rhode K. L., 2012, AJ, 144, 154

Richardson J. C. et al., 2011, ApJ, 732, 76

Richtler T., 2003, in D. Alloin & W. Gieren ed., Lecture Notes in Physics, Berlin Springer Verlag Vol. 635, Stellar Candles for the Extragalactic Distance Scale. pp 281–305

Roberts M. S., 1972, in Evans D. S., Wills D., Wills B. J., eds, IAU Symposium Vol. 44, External Galaxies and Quasi-Stellar Objects. p. 12

Rubenstein E. P., Bailyn C. D., 1997, ApJ, 474, 701

Salaris M., Cassisi S., 2006, The Observatory, 126, 306

Sarajedini A., King C. R., 1989, AJ, 98, 1624

Sargent W. L. W., Kowal C. T., Hartwick F. D. A., van den Bergh S., 1977, AJ, 82, 947

Sargent W. L. W., Schechter P. L., Boksenberg A., Shortridge K., 1977, ApJ, 212, 326

Saviane I., Rosenberg A., Piotto G., Aparicio A., 2000, AAp, 355, 966

Schiavon R. P., Caldwell N., Morrison H., Harding P., Courteau S., MacArthur L. A., Graves G. J., 2012, AJ, 143, 14

Schiavon R. P., Rose J. A., Courteau S., MacArthur L. A., 2004, ApJL, 608, L33

Schlafly E. F., Finkbeiner D. P., 2011, ApJ, 737, 103

Schlegel D. J., Finkbeiner D. P., Davis M., 1998, ApJ, 500, 525

Schönrich R., Binney J., Dehnen W., 2010, MNRAS, 403, 1829

Schuberth Y., Richtler T., Hilker M., Salinas R., Dirsch B., Larsen S. S., 2012, AAp, 544, A115

Searle L., Zinn R., 1978, ApJ, 225, 357

Seigar M. S., Barth A. J., Bullock J. S., 2008, MNRAS, 389, 1911

Seth A., Olsen K., Miller B., Lotz J., Telford R., 2004, AJ, 127, 798

Seyfert C. K., Nassau J. J., 1945, ApJ, 102, 377

Sharina M., Afanasiev V., Puzia T., 2006, Monthly Notices of the Royal Astronomical Society, 372, 1259

Sharina M., Davoust E., 2009, AAp, 497, 65

Sharina M. E., Puzia T. H., Makarov D. I., 2005, AAp, 442, 85

Sharov A. S., 1988, Soviet Astronomy Letters, 14, 339

Siegel M. H. et al., 2007, ApJL, 667, L57

Simkin S. M., 1974, AAp, 31, 129

Skilling J., 2004, in Fischer R., Preuss R., Toussaint U. V., eds, American Institute of Physics Conference Series Vol. 735, American Institute of Physics Conference Series. pp 395–405

Spitler L. R., Forbes D. A., 2009, MNRAS, 392, L1

Spitler L. R., Forbes D. A., Strader J., Brodie J. P., Gallagher J. S., 2008, MNRAS, 385, 361

Stetson P. B., 1993, in G. H. Smith & J. P. Brodie ed., Astronomical Society of the Pacific Conference Series Vol. 48, The Globular Cluster-Galaxy Connection. p. 14

Stiavelli M., Fall S. M., Panagia N., 2004, ApJ, 600, 508

Strader J. et al., 2011, ApJS, 197, 33

Tinsley B. M., Larson R. B., 1978, ApJ, 221, 554

Tollerud E. J. et al., 2012, ApJ, 752, 45

Tonry J., Davis M., 1979, AJ, 84, 1511

Tonry J., Onaka P., 2009, in Advanced Maui Optical and Space Surveillance Technologies Conference.

Tonry J. L. et al., 2012, ApJ, 750, 99

Trancho G., Bastian N., Miller B. W., Schweizer F., 2007, ApJ, 664, 284

Udry S. et al., 1999, in Hearnshaw J. B., Scarfe C. D., eds, Astronomical Society of the Pacific Conference Series Vol. 185, IAU Colloq. 170: Precise Stellar Radial Velocities. p. 383

Usher C. et al., 2012, MNRAS, 426, 1475

Usher C., Forbes D. A., Spitler L. R., Brodie J. P., Romanowsky A. J., Strader J., Woodley K. A., 2013, MNRAS, 436, 1172

van den Bergh S., 1969, ApJS, 19, 145

van den Bergh S., 1998, AJ, 116, 1688

van der Marel R. P., Fardal M., Besla G., Beaton R. L., Sohn S. T., Anderson J., Brown T., Guhathakurta P., 2012, ApJ, 753, 8

van der Marel R. P., Guhathakurta P., 2008, ApJ, 678, 187

van der Wel A. et al., 2011, ApJ, 742, 111

Vazdekis A., Sánchez-Blázquez P., Falcón-Barroso J., Cenarro A. J., Beasley M. A., Cardiel N., Gorgas J., Peletier R. F., 2010, MNRAS, 404, 1639

Veljanoski J. et al., 2013a, MNRAS, 435, 3654

Veljanoski J. et al., 2013b, ApJL, 768, L33

Veljanoski J. et al., 2014, ArXiv e-prints

Vetešnik M., 1962, Bulletin of the Astronomical Institutes of Czechoslovakia, 13, 180

Villanova S. et al., 2007, ApJ, 663, 296

Watkins L. L., Evans N. W., An J. H., 2010, MNRAS, 406, 264

Watkins L. L., Evans N. W., van de Ven G., 2013, MNRAS, p. 672

Weldrake D. T. F., de Blok W. J. G., Walter F., 2003, MNRAS, 340, 12

West M. J., Côté P., Marzke R. O., Jordán A., 2004, Nature, 427, 31

Whitmore B. C., Schweizer F., 1995, AJ, 109, 960

Wilson C. D., 1992, AJ, 104, 1374

Woodley K. A., Gómez M., Harris W. E., Geisler D., Harris G. L. H., 2010, AJ, 139, 1871

Woodley K. A., Harris W. E., 2011, AJ, 141, 27

Woodley K. A., Harris W. E., Puzia T. H., Gómez M., Harris G. L. H., Geisler D., 2010, ApJ, 708, 1335

Yencho B. M., Johnston K. V., Bullock J. S., Rhode K. L., 2006, ApJ, 643, 154

Yi S., Demarque P., Kim Y.-C., Lee Y.-W., Ree C. H., Lejeune T., Barnes S., 2001, ApJS, 136, 417

Yoon S.-J. et al., 2011, ApJ, 743, 150

Yoon S.-J., Yi S. K., Lee Y.-W., 2006, Science, 311, 1129

Young L. M., 2001, AJ, 122, 1747

Young L. M., Lo K. Y., 1997, ApJ, 476, 127

Young M. D., Dowell J. L., Rhode K. L., 2012, AJ, 144, 103

Zepf S. E., Beasley M. A., Bridges T. J., Hanes D. A., Sharples R. M., Ashman K. M., Geisler D., 2000, AJ, 120, 2928

Zinn R., 1985, ApJ, 293, 424

Zinn R., 1996, in Morrison H. L., Sarajedini A., eds, Astronomical Society of the Pacific Conference Series Vol. 92, Formation of the Galactic Halo...Inside and Out. p. 211

Zinn R., West M. J., 1984, ApJS, 55, 45